Toward Earth-abundant Metals in Hydrodesulfurization Catalysts

by

Ali Mansouri

A thesis submitted in partial fulfillment of the requirements for the degree of

Doctor of Philosophy

in

Chemical Engineering

Department of Chemical and Materials Engineering

University of Alberta

Abstract

Increasingly stringent environmental regulations for the sulfur content in fuels pose significant technological challenges for refineries. Current single-stage hydrodesulfurization (HDS) technologies are not efficient enough to achieve ultra-deep levels of sulfur, 10 ppmw S for transportation, under non-severe operating conditions. Platinum-group catalysts in the second stage HDS require high hydrogen pressure, which increases capital and operational expenses. Despite a great progress, development of more efficient heterogeneous catalysts for both first and second stage HDS units using earth-abundant elements is still a challenge of paramount importance.

Palladium (Pd) has shown outstanding performance in HDS of refractory sulfur compound 4,6-DMDBT through hydrogenation of aromatic ring. However, Pd is very scarce and sinters in high-temperature applications, which deactivates the catalysts and alters selectivity. The thermal stability of palladium was enhanced in this thesis through the formation of bimetallic nanostructures with yttrium, as a sintering-resistant element, via colloidal synthesis method. The addition of yttrium did not alter the overall HDS rate but doubled the ratio of direct desulfurization (DDS) to hydrogenation (HYD) selectivity and suppressed cracking twice as much as monometallic palladium catalyst did. This enabled the HDS process to be operated at a pressure as low as 1 MPa. The above-mentioned improvements were not achieved by the conventional impregnation synthesis method.

As another alternative to the second-stage HDS catalysts, palladium species were reduced on the surface of colloidal iron (oxide) cores as nanosized islands using galvanic exchange reaction. The synergism between palladium species and iron oxide nanoparticles resulted in a four-fold

enhancement in Pd-mass-based HDS activity at a reduced palladium loading. Pd dispersion and its HDS activity were maximized at the Pd/Fe molar ratio of 0.2. The incorporation of iron also improved the sulfur resistance of hydrogenation sites due to the higher affinity of sulfur to Fe as compared to Pd.

For the first-stage HDS, niobium sulfide (NbS_2) is proposed that is more abundant and intrinsically more active than MoS_2 and WS_2 catalysts in HDS, hydrodenitrogenation, and hydrocracking reactions. However, the formation of NbS_2 via sulfidation of niobium oxides needs a high temperature above 700 °C due to the positive Gibbs free energy of sulfidation. It was shown for the first time that copper reduced the sulfidation/reduction temperature of Nb_2O_5 dramatically that consequently enhanced the HDS activity. The highest HDS activity of bulk NbCu catalysts prepared via coprecipitation technique was achieved at Cu/Nb molar ratio of 0.3. Copper also promoted DDS and HYD selectivities and suppressed hydrocracking.

The strong interaction between Nb_2O_5 and oxide supports such as alumina makes the sulfidation of niobium oxide more difficult than that of bulk material. Among different support materials, carbon and alpha-alumina exhibited higher activities per mole of Nb and carbon support delivered the highest mass-based activity. Raman spectroscopy showed that various niobium oxides formed on the carbon support at different Nb loadings (from 2.0 to 12.0 wt%) exhibiting different sulfidation and catalytic behaviors. Niobium species at low loading (2.0 wt% Nb) showed the least sulfidation degree functioning as coordinatively unsaturated Lewis acid sites. This delivered the highest HDS activity per mole of Nb and an unprecedented hydrocracking selectivity of 71 % at 74 % conversion. Copper reduced sulfidation/reduction temperature of niobium oxide, improved the DDS selectivity, and reduced the hydrocracking selectivity to around 15 % over the entire Nb loadings.

Colloidal synthesis methodology is a powerful technique to control the size and shape of nanostructures in a liquid phase. NbS_2 nanostructures in different shapes such as nanosheets, nanohexagons, nanobars, and nanospheres were prepared in the liquid phase at a low temperature of 300 °C in the presence of (non-)coordinating solvent and capping ligand. The developed NbS_2 nanostructures showed different catalytic behaviors in HDS of DBT depending on their shapes. The highest HDS activity and DDS selectivity were obtained on nanohexagons with abundant corner and edge active sites. This structure was twice more active than carbon-supported NbS_2.

Preface

Chapter 1 as Introduction provides general information about the research topic including a comprehensive literature review on the previous works.

Chapter 2 provides information on the experimental methodology, identification and quantification of the reaction products, and description on the testing system used in this work.

Chapter 3 of this thesis has been published as A. Mansouri, N. Semagina, "Enhancement of palladium-catalyzed direct desulfurization by yttrium addition", Applied Catalysis A: General 543 (2017) 43-50. Long Wu and Hessam Ziaei-Azad built the experimental high-pressure testing system for the hydrodesulfurization reaction. The LabVIEW software to control the setup was prepared by Les Dean from the Instrument Shop at the Department of Chemical and Material Engineering, University of Alberta. Jing Shen collected the TEM images and CO-DRIFT. Dimitre Karpusov acquired the XPS spectra and Anqiang He collected STEM-EDS images at nanoFAB, University of Alberta. Guangcheng Chen performed ICP-MS at the Canadian Centre for Isotopic Microanalysis (CCIM), University of Alberta. I performed the synthesis, HDS reaction and data collection, TPR and CO-chemisorption analyses, and interpretation of the results as well as writing the manuscript.

Chapter 4 of the thesis has been submitted as A. Mansouri, N. Semagina, “Palladium islands on iron oxide nanoparticles for hydrodesulfurization catalysis”, Applied Catalysis B: Environmental. Xuejun Sun collected the TEM images at Alberta Cross-Cancer Institute, University of Alberta. Anqiang He and Shihong Xu performed the XPS analyses at nanoFAB, University of Alberta. NAA analysis was performed at Becquerel Laboratories Inc., Maxxam Analytics, Ontario, Canada. STEM-EDS analysis was performed at the Canadian Centre for Electron Microscopy at McMaster University. Diane Caird at the University of Alberta performed XRD and Lisa Brandt GC-MS. I performed the synthesis, HDS reaction and data collection, TPR and CO-chemisorption analyses, and interpretation of the results as well as writing the manuscript.

Chapter 5 of this thesis is under submission as A. Mansouri, N. Semagina, “Unsupported $Cu_{0.65}NbS_2$ as Hydrodesulfurization Catalyst”. Anqiang He and Shihong Xu performed the XPS and Nancy Zhang measured the BET-BJH at nanoFAB, University of Alberta. Anqiang He

collected the SEM-EDS and Jing Shen took the HRTEM images. Diane Caird at the University of Alberta performed the XRD. Cibele Melo Halmenschlager performed the TGA analysis. I performed the synthesis, HDS reaction, TPR, and DRIFT analyses as well as interpretation of the results and writing the manuscript.

Chapter 6 of this thesis is under submission as A. Mansouri, N. Semagina, "Supported Copper-Niobium Sulfide Layered Structure as Hydrodesulfurization Catalyst". Anqiang He and Shihong Xu performed the XPS and Nancy Zhang measured the BET-BJH at nanoFAB, University of Alberta. Anqiang He collected the STEM-EDS images. Mike Xia and I performed the Raman spectroscopy and Kai Cui collected the TEM images all at the National Institute for Nanotechnology (NINT), University of Alberta. Diane Caird at the University of Alberta performed XRD. I performed the synthesis, HDS reaction and kinetic studies, TPR analyses as well as data interpretation and writing the manuscript.

Chapter 7 of this thesis is under submission as A. Mansouri, N. Semagina, "Shape-controlled Colloidal Niobium Sulfide Nanostructures and their Hydrodesulfurization Activities". Anqiang He and Shihong Xu performed the XPS analyses at nanoFAB, University of Alberta. Anqiang He collected the STEM-EDS images. Pinzhang Gao and I collected the TEM images and Xuejun Sun took the HRTEM images. Diane Caird at the University of Alberta performed XRD. Mike Xia and I performed the Raman spectroscopy at the National Institute for Nanotechnology (NINT), University of Alberta. I performed the synthesis, HDS reaction, and interpretation of the results as well as writing the manuscript.

Dr. Natalia Semagina supervised this research and my Ph.D., provided feedbacks on the experimental design and procedures, data collection, results interpretation and discussions. She also revised the publications, manuscripts, and all parts of the present thesis. The present thesis includes research projects funded by Imperial Oil, Institute of Oil Sands Innovation at the University of Alberta (IOSI), and Natural Sciences and Engineering Research Council of Canada (NSERC).

Dedication

To my beloved Mom and Dad.

Acknowledgements

I would like to thank Dr. Natalia Semagina who supervised me during the Ph.D. program. Thanks for the endless support and giving the opportunity to explore my research ideas and develop my professional skills.

I would like to thank Dr. Jeroen A. van Bokhoven professor of chemistry at ETH Zurich, Switzerland who gave me the opportunity to join his research group and work on a different topic in the field of heterogeneous catalysis. This thesis does not include the obtained data.

I would like to thank external examiner Dr. Nadi Braidy and internal examiner Dr. Douglas Ivey for their valuable comments.

I would also like to express my gratitude to:

Members of NanoFAB at the University of Alberta: Dr. Anqiang He for different measurements he conducted for me including XPS, STEM-EDS, and SEM-EDS. Dr. Shihong Xu who performed many XPS and shared his valuable knowledge on XPS fitting and CasaXPS software. Dr. Dimitre Karpusov for XPS, Dr. Nancy Zhang for BEH-BJH measurements.

Dr. Xuejun Sun and Pinzhang Gao at Alberta Cross-Cancer Institute, the University of Alberta for their support and help to collect the TEM images.

Diane Caird at the Department of Earth and Atmospheric Sciences, the University of Alberta who ran all of my XRD.

Dr. Mike Xia for Raman spectroscopy and Dr. Kai Cui for TEM images at National Institute for Nanotechnology (NINT), the University of Alberta.

Dr. Hessam Ziaeiazad who shared his knowledge and experience on operating the HDS setup.

Dr. Jing Shen for the TEM images she has taken for me.

Dr. Xiaoli Tan, Lisa Brandt, and Brittany Mackinnon at the Institute for Oil Sands Innovations (IOSI), the University of Alberta for the supports they have provided.

Ni Yang in Oil Sands and Coal Interfacial Engineering Facility, the University of Alberta for UV-vis and DRIFTS measurements.

Walter Boddez and Les Dean for the electronic works and programming the LabVIEW software to modify the HDS setup.

Jason Dibbs at chemistry glass shop, the University of Alberta.

Lily Laser, Mia Law, Marion Pritchard, Andree Koenig, Sahofeng Yang, Kevin Heidebrecht, Machine Shop, and all other staffs at the University of Alberta.

My colleagues in the lab and my friends for their constant help and support.

Special thanks to my Mom, Dad, and brothers who have provided me everlasting support and motivation throughout my entire life. Finally, I would like to express my appreciation and love to Arezou who has always encouraged me in everything that I have done.

Financial supports from Imperial Oil, the Institute of Oil Sands Innovation (IOSI) at the University of Alberta, Natural Sciences and Engineering Research Council of Canada (NSERC) are gratefully acknowledged.

Table of Contents

List of Tables

Lists of Schemes

List of Figures

List of Symbols and Abbreviations

α	alpha
Å	angstrom
δ	delta
γ	gamma
θ	theta
μ	micron
0D	zero dimensional
1D	one dimensional
2D	two dimensional
BET	Brunauer-Emmett-Teller
BJH	Barrett-Joyner-Halenda
BP	Biphenyl
CP	Cyclopentane
CH	Cyclohexane
DBT	Dibenzothiophene
DDS	Direct desulfurization
DFT	Density functional theory
DMBCH	Dimethylbicyclohexyl
DMBP	Dimethylbiphenyl
DMCHB	Dimethylcyclohexylbenzene

DMDBT	Dimethyldibenzothiophene
DMHHDBT	Dimethylhexahydrodibenzothiophene
DMPHDBT	Dimethylperhydrodibenzothiophene
DMTHDBT	Dimethyltetrahydrodibenzothiophene
DRIFTS	Diffuse reflectance infrared Fourier transform spectroscopy
EELS	Electron energy loss spectroscopy
EDS	Energy-dispersive spectroscopy
EDX	Energy-dispersive X-ray
EG	Ethylene glycol
EPA	Environmental protection agency
EtOH	Ethanol
EXAFS	Extended X-ray absorption fine structure spectroscopy
f.c.c/fcc	Face-centered cubic
FESEM	Field Emission Scanning Electron Microscopy
FID	Flame ionization detector
$G°_f$	Gibbs Free Energy of formation
GC	Gas chromatography
GC-MS	Gas chromatography coupled with mass spectrometry
HAADF	High angle annular dark field
HCK	Hydrocracking
h.c.p./hcp	Hexagonal close packing

HDA	Hydrodearomatization
HDS	Hydrodesulfurization
HDM	Hydrodemetallation
HDN	Hydrodenitrogenation
HRTEM	High-resolution transmission electron microscopy
HYD	Hydrogenation
ICP-MS	Inductively coupled plasma mass spectrometry
MCH	Methylcyclohexane
MCP	Methylcyclopentane
MS	Mass spectrometry
MW	Molecular weight
NAA	Neutron activation analysis
NO_x	Nitrogen oxides
NP	Nanoparticle
ODE	1-octadecene
OAm	oleylamine
OAc	oleic acid
PAH	Polycyclic aromatic hydrocarbons
PB	Propylbenzene
PDS	Particle size distributions
PM	Particulate matter

ppmw	Parts per million by weight
PVP	Poly-(vinylpyrrolidone)
RO	Ring opening
SAED	Selected area electron diffraction
SCR	Selective Catalytic Reduction
SEM	Secondary electron microscopy
SO_x	Sulfur oxides
SRGO	Straight run gas oil
SSA	Specific surface area
STEM	Scanning transmission electron microscopy
Surf.	Surface
TCD	Thermal conductivity detector
TEM	Transmission electron microscopy
TGA	Thermogravimetric analysis
TMS	Transition metal sulfide
TMDC	Transition metal dichalcogenide
TOF	Turnover frequency
TON	Turnover number
TPD	Temperature programmed desorption
TPR	Temperature programmed reduction
ULSD	Ultra-low sulfur diesel

UV-Vis	Ultraviolet visible spectroscopy
WHSV	Weight hourly space velocity
XANES	X-ray absorption near edge structure
XPS	X-ray photoelectron spectroscopy
XRD	X-ray powder diffraction

Chapter 1. Introduction

1.1 Background and motivation

Due to the higher efficiency of diesel engines (about 25-49 %) than that of gasoline ones, the demand for diesel fuel is extensively growing for transportation and power generation applications.[1] On the other hand, diesel produced from the heavy oil feedstocks or middle distillate is concentrated with harmful and carcinogenic elements such as sulfur and nitrogen, which consequently released into the environment as nitrogen and sulfur oxides (NO_x and SO_x) emissions.[1,2] The produced sulfur trioxide (SO_3), as the main constituent of oxygen-rich diesel exhaust, dissolves in water and releases as sulfuric acid in acidic rains. Note that this can deeply penetrate into the lungs. Sulfur is known as a key cause of particulates or soot formation in engines' exhausts; noxious black exhaust fumes which strongly contributes to air pollution.[1] Even the trace levels of sulfur poison the three-ways oxidation catalysts installed in the engines' exhaust systems for oxidation of carbon monoxide, unburned-hydrocarbons, and volatile organic materials.[3]

It has been shown that SO_x emission and the amount of particulate matter (PM) are linearly increased by the sulfur content of diesel fuel.[1] It has been reported that about 2% of sulfur in diesel fuel is converted to PM emission. Therefore, the worldwide environmental legislation have been regulated to reduce the sulfur content of transportation fuels to around 10-15 ppmw S, termed as ultra-low sulfur diesel (ULSD).[1,4] Reduction of sulfur levels in transportation fuels subsequently decreases harmful emissions through: (i) direct reduction of sulfur dioxide and sulfate PM, (ii) better performance of vehicles' catalytic emissions control systems, and (iii) enabling the use of advanced emission control technologies such as diesel PM filters, NO_x absorbers, and selective catalytic reduction (SCR) systems. Nonetheless, production of transportation fuels with premium quality (ULSD) using current hydrotreating technology is very challenging for refineries. This is because of much poorer quality feedstocks than before that are concentrated with refractory sulfur compounds, which are resistant to existing hydrodesulfurization (HDS) technologies. This reveals the necessity of developing advance-upgrading technologies to meet the required quality. Accordingly, the area of hydrotreating technologies especially the catalysts has received a substantial attention. There are three general approaches to ULSD production such as: designing new catalyst formulation on how to

desulfurize 4,6-DMDBT more effectively at affordable cost, designing new reactor configurations, and developing new processes.[5]

The aim of this thesis is to develop high-performance catalysts for the first and the second stage HDS units with reduced/eliminated Pt-group metals using earth-abundant elements as promoters or main active components. Using advances in nanotechnology, the catalyst performance was improved by controlling the electronic and geometric properties of individual nanoparticles at the atomic level. Such improvements affect the *d*-band structures and thus the catalytic activities of active sites. Therefore, besides the traditional and industrial synthesis method of impregnation, colloidal chemistry was applied in this work to control the size and surface structure of bimetallic nanoparticles. The performances of the developed catalysts were investigated in the HDS of refractory sulfur compounds such as dibenzothiophene (DBT) and its alkyl derivate 4,6-dimethyldibenzothiophene (4,6-DMDBT) under industrially-relevant operating conditions. The focus of this thesis is on the development of niobium- and palladium-based catalysts as two elements with promising performance in the first and second stage HDS unit, respectively. However, utilizing monometallic Pd-based catalysts for HDS is not feasible economically. Furthermore, Pd suffers from thermal instability in such high-temperature applications. For niobium, its sulfidation is only viable at high temperature (above 700 °C) thermodynamically, which is impractical at industrial scales. We hypothesized that the synergism between copper and niobium species could facilitate the reduction/sulfidation of niobium oxides. For palladium, our hypothesis was to increase the dispersion and thus the catalytic activity by decorating Pd species as nanosized islands on earth-abundant metal to reduce palladium contents in the catalysts while enhancing its activity. Addition of sintering-resistant element to Pd enhances its thermal stability. Accordingly, a brief review of the topic is provided in the rest of this chapter.

1.2 Sulfur compounds and their reactivities

The sulfur content of non-hydrotreated middle distillates ranges between 1 and 3 wt% with different reactivities.[6] In general, by increasing the boiling point of a typical feedstock, the complexity of the molecules increases and their reactivities toward hydrotreating reactions decrease. High-resolution analytical techniques showed that a crude oil contains a large number of individual sulfur compounds including (alkyls substituted) benzothiophene (BT) and

dibenzothiophene (DBT).[1] The sulfur compounds can be classified into four groups according to their HDS reactivities. The first group is alkyl BT and the second group DBT and alkyl DBT without alkyl substituents at the 4- and 6-positions. The third group is alkyl DBT with only one alkyl substituent at either 4- or 6-position. The fourth category is alkyl substituents at both 4- and 6-positions. The distributions of sulfur compounds are in accordance with their boiling points. For instance, BT is concentrated in the fractions having boiling points below 300 °C whereas DBT and its alkyl derivatives are in the cuts boiling above 300 °C.[1] Figure 1.1 shows various sulfur compounds and their relative HDS reaction rates as a function of boiling point.[1] As an example, the sulfur distribution in the four above-mentioned groups in the gas oil is 39, 20, 26 and 15 wt.%, respectively, and the relative rate constant of HDS for each of the four groups is 36, 8, 3, and 1, respectively.[7]

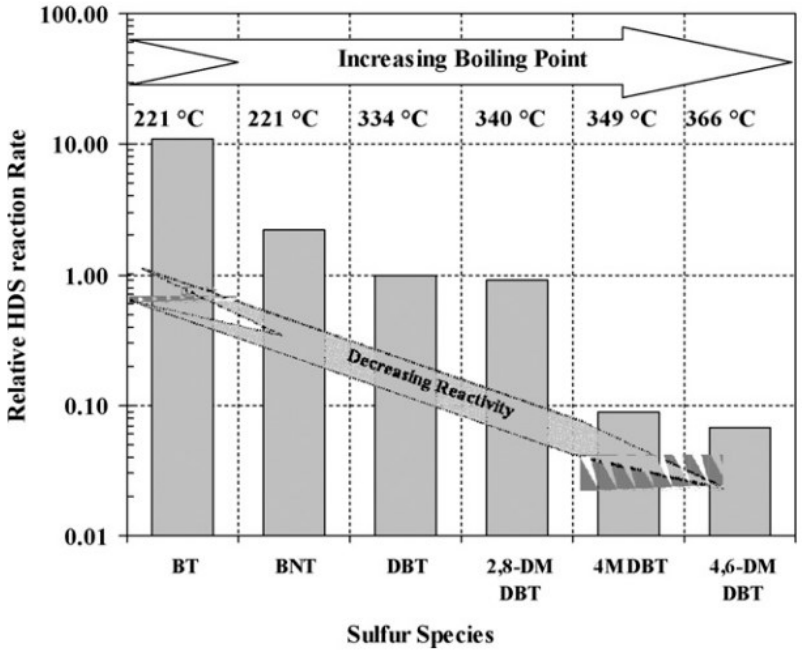

Figure 1.1. Reactivity of different sulfur compounds and their boiling points as a function of diesel sulfur species over $CoMo/Al_2O_3$ catalyst at T=350 °C and P=10 MPa. Reprinted from ref. [1], Copyright (2010) with permission from Elsevier.

The HDS rates of BT and their alkyl derivatives are greater than DBT and alkyl DBTs. Among the various isomers of alkyl DBTs, the ones having alkyl groups close to the sulfur atom such as

4-MDBT, 4,6-DMDBT, and 4,6-MEDBT are less reactive and more resistant to desulfurization. This is due to the steric hindrance effects of alkyl groups preventing an effective interaction between the sulfur atom and the catalytic active sites as illustrated in Scheme 1.1.[6] This preventive effect is further proved by a higher heat of adsorption of 4,6-DMDBT (21 kcal/mole) compare to DBT and 4-MDBT which is 12, 20 kcal/mole, respectively. This suggests that the adsorption of 4,6-DMDBT on the catalyst surface through the π-electrons of aromatic ring is stronger than DBT.[8] Therefore, steric hindrance of the methyl groups disturbs the C–S bond cleavage. The problem of ULSD production is the low reactivity of 4,6-DMDBT. Note that when the sulfur level of diesel is reduced to 500 ppm, 20 wt% of the sulfur species belong to 4,6-DMDBT.[9–11] When the total sulfur content is reduced to 30 ppmw, the sulfur compound remained in the hydrotreated oil is only 4,6-DMDBT.

Scheme 1.1. Steric hindrance effects of alkyl groups on the adsorption of 4,6-DMDBT on the active sites.

1.3 HDS process variables and thermodynamic limitations

Industrial HDS has been carried out on sulfided (Ni)CoMo/γ-Al_2O_3 catalysts in which sulfur anion vacancies associated with exposed Mo cations (as coordinatively unsaturated sites) are believed to be active sites.[6] With the little hydrogenation activity they have, these uncoordinated active sites generally require high hydrogen pressures or long contact times to attain an acceptable HDS rate.[6] Kinetic studies showed that HDS rates could be increased under severe operating conditions such as elevated temperature and hydrogen partial pressure and low space velocity.[12] Figure 1.2 shows the simulated relative volume of catalyst bed required for achieving

various levels of diesel sulfur using conventional HDS process over the commercial CoMo/γ-Al_2O_3 catalyst.[7] For reducing the sulfur level from 500 to 15 ppmw using conventional HDS process, the volume of catalyst bed should be increased at least 3.2 times greater than that of the ordinarily HDS catalyst bed. In order to reach 0.1 ppm as required for fuel cell applications, the volume of the catalyst bed has to be increased by about seven times. This is very costly and energy consuming while many oil refiners are limited by hydrogen pressure and residence time. The severe operating conditions could also change the fuels' quality undesirably.

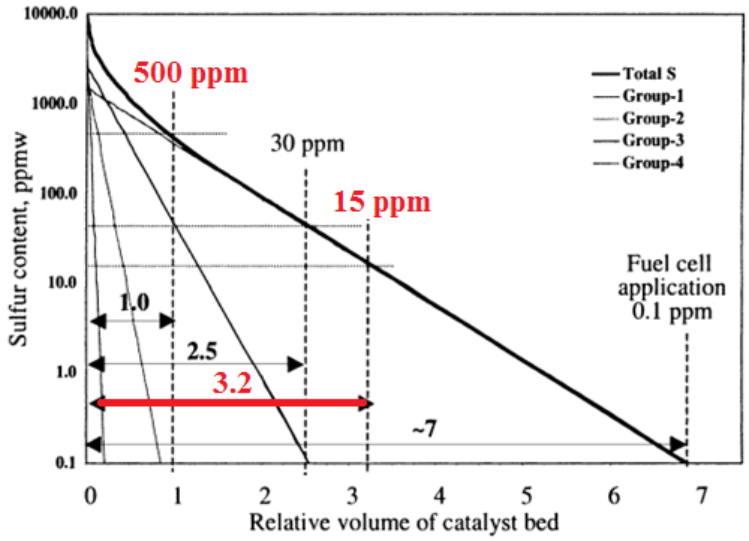

Figure 1.2. Simulated relative volume of the catalyst bed required for achieving various levels of diesel sulfur using conventional single-stage HDS of gas oil having 1.0 wt.% S in feed over a commercial CoMo/γ-Al_2O_3 hydrotreating catalyst. Reprinted from ref. [7], Copyright (2003) with permission from Elsevier.

Despite the unfeasible operation of hydrotreaters under severe conditions, there are some thermodynamics limitations in HDS of refractory sulfur compounds. HDS of DBT and its alkyl derivative proceed via two different reaction ways, which will be fully discussed in section 1.7. Briefly, unlike BT and DBT, the HDS rate of sterically hindered compounds (4,6-DMDBT) is not controlled by reaction temperature but hydrogenation of aromatic ring and thus hydrogen pressure. Therefore, DBT desulfurization can be promoted by temperature, while HDS of 4,6-

DMDBT by hydrogen pressure. This is due to the difference in the activation energies of different reaction routes that for hydrogenation is lower.[13] This has encouraged some process licensors to develop a two-stage HDS process.

1.4 Two-stage hydrodesulfurization process

Two-stage HDS process consists of two series fixed-bed reactors in which HDS reaction is conducted under two different operating conditions as shown in Scheme 1.2. This process has been developed and commercialized by some process licensors such as Shell, ExxonMobil, Topsøe, UOP, and IFP.[1] This process is very effective in reducing both sulfur and polycyclic aromatics in diesel to very low levels while increasing the cetane index by aromatic saturation and hydrodecyclization.[1,14] Typically, gas oil is hydrotreated over conventional CoMo/γ-Al_2O_3 or NiMo/γ-Al_2O_3 catalyst in the first stage and after intermediate stripping of H_2S and NH_3 will be further treated in the second stage over a sulfur-resistant noble metal/zeolite catalyst. IFP uses intermediate fractional distillation. Therefore, diesel with no hydrogen sulfide will be sent to the second stage. When a light cycle oil (LCO) with sulfur content of 1.58 wt.% is subjected to this two-stage process, the sulfur content is lowered to 3 ppm in the first stage, and then the aromatic content is reduced to 1.4% in the second stage.[1] Desulfurization in the second stage relies on hydrogenation of aromatic ring. Therefore, the second stage reactor operates at a lower temperature and a higher hydrogen pressure to promote hydrogenation reaction. The noble metal catalysts in the second stage (Pd and Pt) are highly active in hydrogenation and tolerated to sulfur (up to 1000 ppmw S) and nitrogen (up to 50 ppmw N) compounds.[14] They showed outstanding performance in HDS of refractory sulfur compounds, in particular, 4,6-DMDBT. However, the very high hydrogen pressure required for the second stage HDS and the high price of noble metal catalysts make the process unfeasible economically.

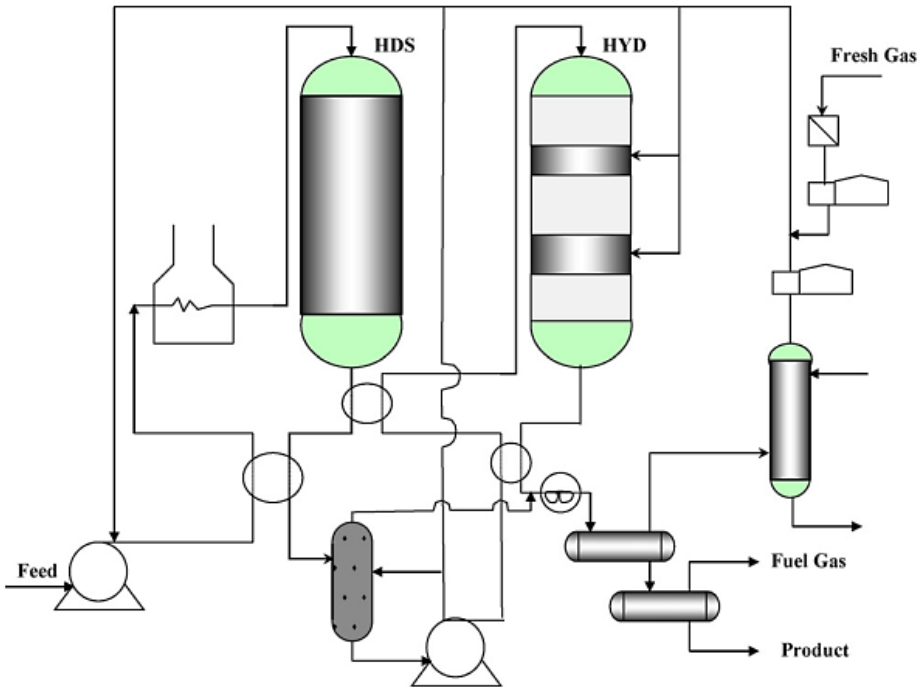

Scheme 1.2. Gas oil hydrotreating, decoupling HDS and aromatic hydrogenation: Shell middle distillate hydrotreating process. Reprinted from ref. [1], Copyright (2010) with permission from Elsevier.

1.5 Transition metal sulfides as hydrotreating catalysts

Transition metal sulfides (TMS) are a class of materials showed exceptional activity in many hydrogenolysis and hydrogenation reactions in the presence of sulfur that is essentially required for the activity maintenance. The field of transition metal sulfides (TMS) catalysts was introduced after the end of First World War (WW-I) to produce liquid fuels via hydrogenation of local coal resources to replace with imported petroleum feedstocks. The researchers realized that following coal hydrogenation the catalytically active metal was converted to the TMS showed catalytic properties as well. This opened up the field of catalysis by TMS. Paul Sabatier, Friedrich Bergius, and M. Pier led the investigations on TMS for production of liquid fuels and chemicals, which resulted in the Nobel Prizes for Sabatier (1912) and Bergius (1931) for their early work on TMS catalysis and coal hydrogenation, respectively.[15] Following this revolutionized finding in catalysis, TMS catalysts have been used for decades in the petroleum hydrotreating units for upgrading and removal of heteroatoms such as sulfur, nitrogen, oxygen, and metals.[16–19] Emphasizing on the production of more cleaner and sustainable fuels as

legislated by stringent environmental regulations, the role of TMS will continue to be an increasingly paramount in fuel processing via hydrodesulfurization (HDS), hydrodenitrogenation (HDN), hydrodemetallation (HDM), and hydrocracking (HCK). Note that the reactions that can be catalyzed by TMS are versatile such as hydrogenation of olefins, ketones, and aromatics (HDA), dealkylation, ring opening of aromatics, isomerization of paraffins, dehydrogenation of alcohols, Fischer–Tropsch and alcohol synthesis, hydration of olefins, amination, and direct coal liquefaction.[15] In addition, the tunable structural and electronic properties of layered TMS make them attractive in optoelectronic,[20] energy storage materials,[21–23] solar cells,[24,25] and recently as photo- and electrocatalyst for hydrogen evolution[26–28] and CO_2 reduction[29,30]. A comprehensive list of the reactions catalyzed by TMS can be found in ref. [31].

Conventional hydrotreating catalysts are gamma-alumina (γ-Al_2O_3) supported molybdenum or tungsten disulfides promoted by Group VIIIB elements mostly Co or Ni at the atomic ratio of Co(Ni)/[Co(Ni)+Mo(W)] between 0.2 and 0.4. CoMo/γ-Al_2O_3 catalyst was found very efficient in HDS, but not highly active for HDN or aromatic hydrogenation (HDA). On the contrary, NiMo/γ-Al_2O_3 is active for HDN and HDA. NiW/γ-Al_2O_3 catalysts are very active for hydrogenation reactions such as HDA but at an unfeasible cost to performance ratio, which simply limits their usage in industrial plants. Hydrotreating units are operated at elevated operating conditions (320–340 °C and 30-100 bar) and consume a large amount of hydrogen. In case of hydrocracking residues as feedstocks, the pressure and temperature further enhance to 100–150 bar and 400–440 °C.[15] Conventional (Ni)Co-(W)Mo/γ-Al_2O_3 sulfide catalysts are not efficient enough to deliver the high-quality fuels under non-severe operating conditions to meet the stringent environmental regulations.[1,5,16,32–36] Note that the quality of feedstocks is also becoming worse with much higher initial impurity levels than before.[37] Therefore, more severe operating temperatures and longer residence times are essentially required for desulfurization of refractory sulfur compounds over existing catalysts that are not economically and operationally viable. On the other hand, the severity of operating conditions can easily change the quality of final products such as the aromaticity and carbon efficiency of fuel besides lowering the lifetime of catalysts.[38] ExxonMobil with Akzo Nobel and Nippon Ketjen have developed a novel unsupported hydroprocessing catalyst called “NEBULA”. The catalyst exhibited a significant improvement in the HDS, HDN, and HDA activities compared to the conventional CoMo/γ-Al_2O_3 and NiMo/γ-Al_2O_3 catalysts enabling refiners to produce ultra-low sulfur diesel in medium

to high-pressure units designed for the production of 500 ppm S.[39–41] However, NEBULA's enhanced performance relies on hydrogenation (HYD) route of HDS that requires elevated hydrogen pressure and consumption, which is very costly and energy consuming.[41] In addition, the catalytic activity per volume of the catalyst is lower for the bulk catalysts. Therefore, larger reactors are required to reach the comparable activity as compared to the supported catalysts. This will increase the reactor fill price significantly.[41]

1.5.1 Periodic trends on the HDS activity of TMS

The catalytic activities of TMS catalysts are related to the surface defects of the crystal lattice. The properties and stability of these defects are determined by the bulk atomic and electronic structure.[15] Pecoraro and Chianelli showed for the first time that the HDS catalytic activity of TMS varies over three orders of magnitude across the periodic table from Group IVB to Group VIIIB.[42] The HDS activities of unsupported TMS are correlated to the position of TMS in the periodic table and the heat of formation of the bulk sulfides that follow a typical "volcano" plots as shown in Figure 1.3. However, Al_2O_3-supported TMS showed different variation probably due to the superimposed effects of the support.[43] As can be seen Figure 1.3, the first-row transition metal sulfides are relatively inactive in HDS of DBT at 400 °C, but the second- and third-row exhibited the highest activities in particular Group VIIIB metal sulfides maximizing with Ru and Os sulfides. The HDS activities for second row TMS ordered as: $RuS_2 > Rh_2S_3 > PdS > MoS_2 > NbS_2 > ZnS$, and third row as $Os^0+S > Ir^0+S > ReS_2 > PtS > WS_2 > TaS$. Despite the highest HDS activates exhibited by the noble metals, their prohibitive costs minimize their usage in the industrial applications.

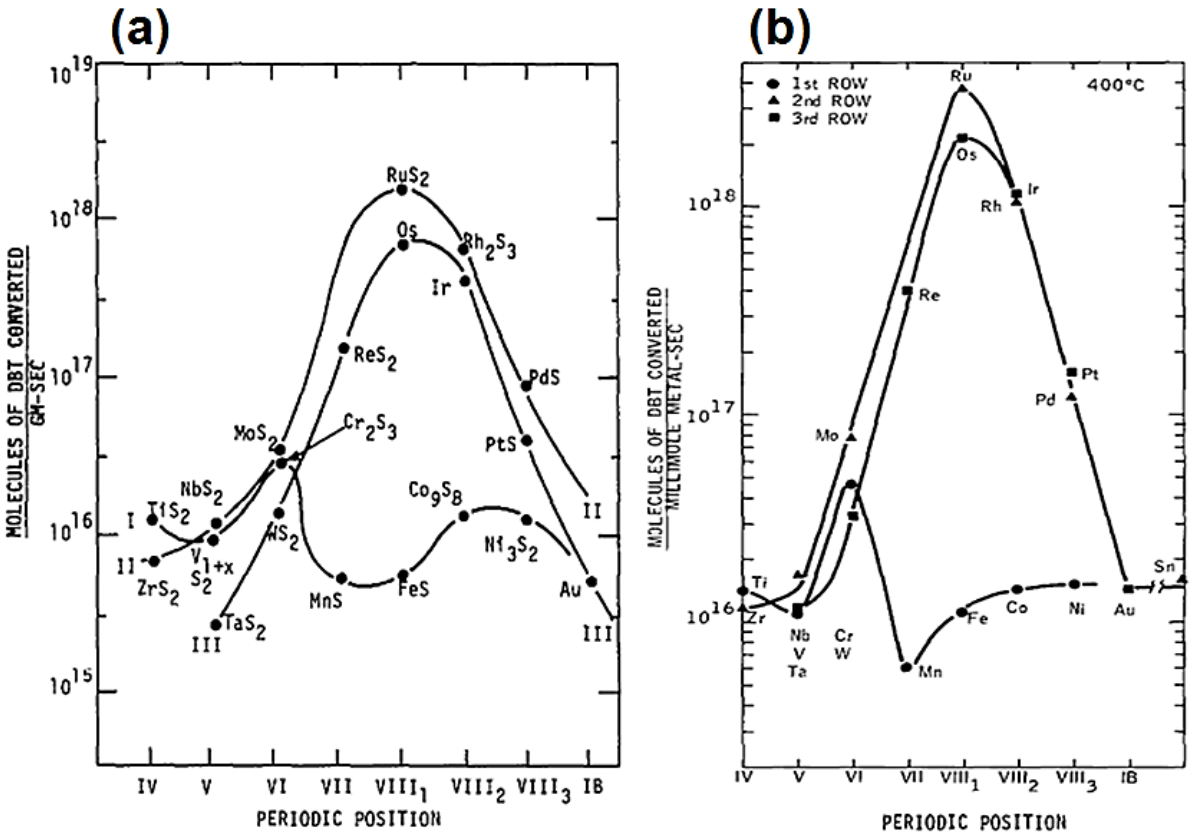

Figure 1.3. Periodic trends for HDS of DBT at 400 °C; (a) per gram of catalyst, (b) per millimole of catalyst. Reprinted from ref. [42], Copyright (1981) with permission from Elsevier.

Unsupported TMS were also examined later in a different study by Lacroix et. al. in hydrogenation of biphenyl (BP) and HDS of DBT at lower temperature of 523-573 K.[44] Figure 1.4 shows the intrinsic activity of unsupported TMS in both HDS of DBT and HYD of BP at 530 K calculated based on the BET surface area of the bulk materials. The same trend as previous one was observed in HDS of DBT except that Nb and V sulfides showed higher activities than the previous study shown in Figure 1.3. For BP hydrogenation reaction, Rh, Ru, and Nb sulfides showed the highest conversions. However, hydrogenation of BP over Nb mostly led to hydrocracking single ring products such as benzene and cyclohexane.

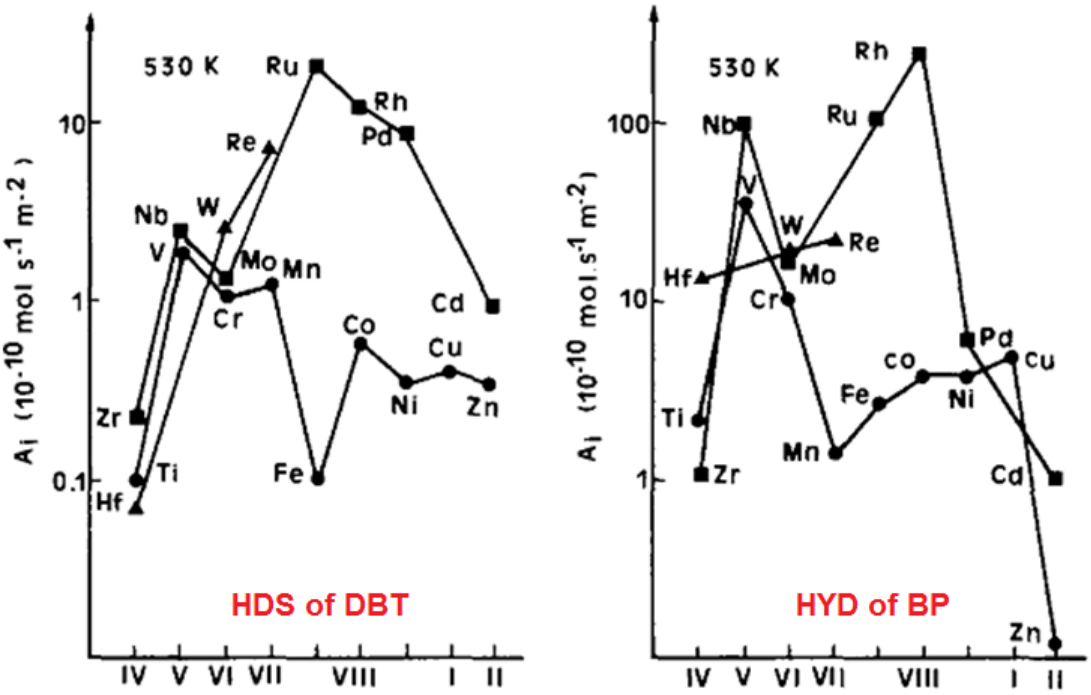

Figure 1.4. Intrinsic activities (Ai) of transition metal sulfides in HDS of DBT and the hydrogenation of biphenyl at 530 K. Reprinted from ref. [44], Copyright (1989) with permission from Elsevier.

Benard et. al. found a correlation between the heats of formation of two-dimensional (2D) and three-dimensional (3D) TMS and the quantity of sulfur adsorption at saturation over the materials.[45] In fact, the heats of formation of the sulfides are linearly correlated with the heats of adsorption of sulfur on transition metals surface. The metal–sulfur (M–S) bond strength is directly proportional to the heat of formation of metal sulfides. Accordingly, Pecoraro and Chianelli interpreted the HDS activities of TMS catalysts by bulk M–S bond strength via determination of the enthalpies of formation.[42,43] Based on the Sabatier principle, a maximum HDS activity corresponds to the moderate interactions between the active site and sulfur compounds corresponding to the moderate heats of formation of sulfides. Figure 1.5 exhibits the HDS activity of TMS versus heats of formation and M-S bond strength of TMS, determined from cohesive energy values.[46,47] The same volcano trend calculated by ab initio was reported in a different study.[48] A range of 29–55 kcal/mol heats of formation corresponds to the highest HDS intrinsic activities of TMS.[46,49] As can be seen in Figure 1.5, the elements located on the left side of the periodic table form very strong bond with sulfur that leads to the poisoning of

active site through permanent deposition of sulfur on active metals. On the other hand, sulfide elements on the right-hand side of the periodic table have very low heats of formation and sulfur-containing reactants bind too weakly on the active site that is not sufficient to promote C–S bond cleavage. This is in agreement with the idea proposed by Tanaka[50] that the surface active sites in HDS are anionic vacancies or coordinately unsaturated sites (CUS).

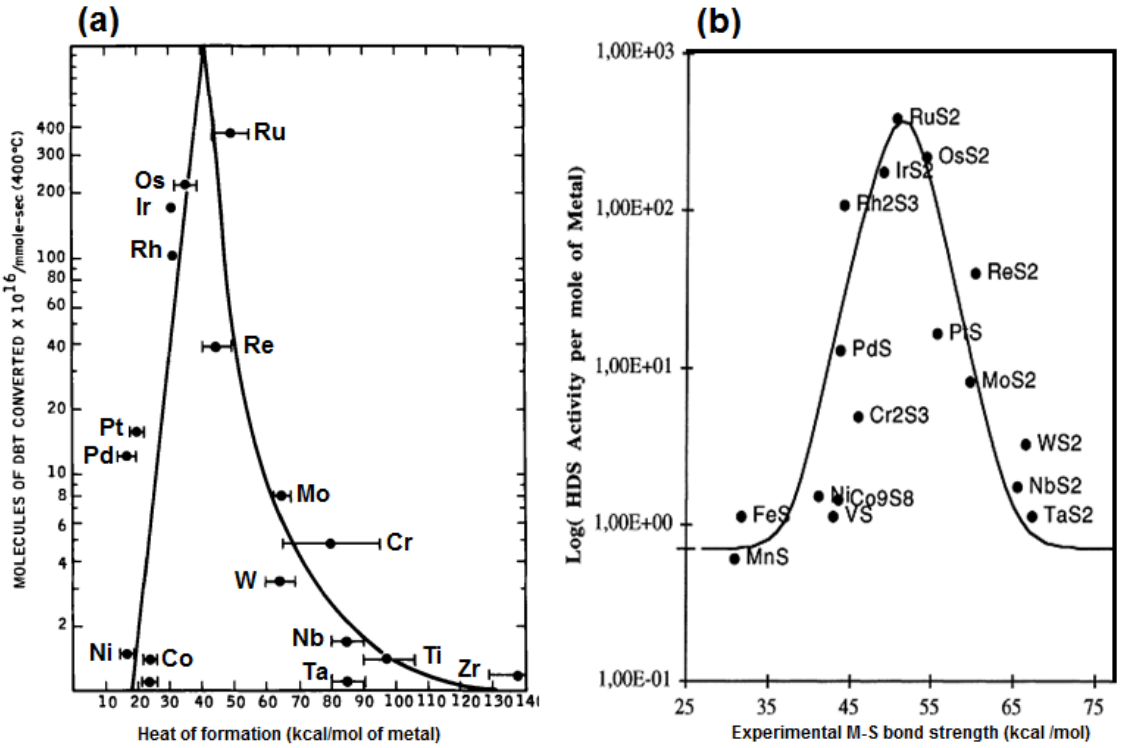

Figure 1.5. (a) Heat of formation of TMS vs HDS activity; (b) Experimental specific activities in DBT HDS versus M-S bond strengths of transition metal sulfides (black dots). Figure (a) reprinted from ref. [15], Copyright (2009) with permission from Elsevier. Figure (b) reprinted from ref. [47], Copyright (1981) with permission from Elsevier.

The M-S bond energies for MoS_2 and NbS_2 are 59.7 kcal/mol[51] and 65.5 kcal/mol, respectively,[52] both out of the optimal range. It has been reported that the average heats of formation of individual sulfides of a synergistic pair fall into an "optimum" range.[49] Table 1.1 lists the average heats of formation of the first-row transition metal sulfides in a synergistic pair (alloy)

with MoS_2 or WS_2. The HDS activities of the promoted TMS versus heats of formation of sulfides are shown in Figure 1.6. As can be seen, elements from the left side of the periodic table, when mixed with MoS_2 or WS_2, located on the right side of the periodic table, decrease the heat of formation of obtained alloyed material. This decrease led to an increase in the HDS reactivity of obtained TMS. Accordingly, doping MoS_2 with Co and Ni can decrease the heats of formation (or M-S bond strength) to the optimum range. Nonetheless, the Sabatier principle is surprisingly hampered at some points by the HDS inactivity of first row TMS (3d TM) and the lowest activity of MnS while the heat of formation of MnS is in the range of moderate metal-sulfur range (51 kJ/mol).[46] Therefore, one could conclude that metal-sulfur bond at the surface of the catalyst is important in determining the HDS activity; however other factors such as the electronic properties and presence of 4d and 5d electrons in the catalyst should be taken into consideration.

Table 1.1 Average heats of formation of pairs of transition metal sulfides. Reprinted from ref. [49], Copyright (1984) with permission from Elsevier.

TMS	Heat of formation (kcal/mol)		
		MoS_2	WS_2
		65.8	62.0
MnS	51.1	58.5	56.6
FeS_2	42.6	54.2	52.3
FeS	24.0	44.9	43.0
Co_9S_8	19.8	42.8	40.9
Ni_3S_2	17.2	41.5	39.6
CuS	12.7	39.3	37.4
ZnS	46.0	57.3	54.0

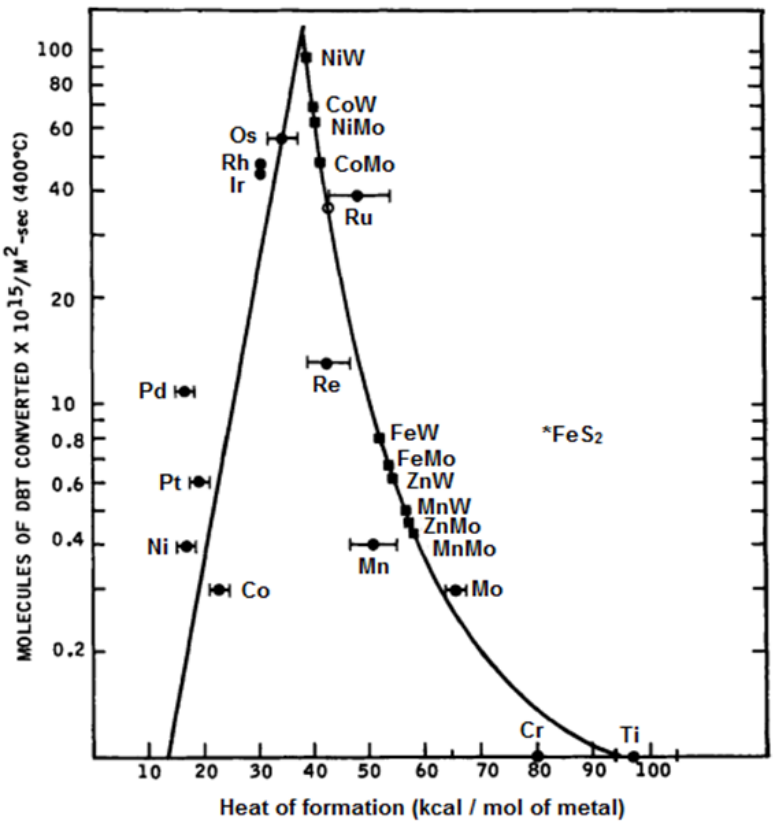

Figure 1.6. HDS activity of the TMS versus average heats of formation of the pairs of binary sulfides. Reprinted from ref. [49], Copyright (1984) with permission from Elsevier.

1.5.2 Niobium sulfide as hydrotreating catalyst

As discussed earlier, Lacroix et. al.[44] showed that the intrinsic HDS and hydrogenation activities of niobium sulfides were higher than that of molybdenum sulfide but lower than those of noble metals sulfides. In a different study later, Hermann et.al.[53] investigated the DBT and 4,6-DMDBT HDS activities of bulk TMS located on the second series of the periodic table and compared with the performance of conventional CoMo/γ-Al_2O_3 catalyst. The absolute DBT and 4,6-DMDBT conversions delivered by TMS at 300 °C are shown in Figure 1.7. NbS_2 exhibited greater conversions than monometallic MoS_2, in agreement with the previous work. In addition, the activity of traditional CoMo/Al_2O_3 catalyst as a reference material was found to be similar to the most active unsupported metal sulfides (RuS_2). Surprisingly, a different trend was reported when the activities were normalized by the BET surface areas of TMS (Figure 1.7b). The activity

of NbS_2 was greater than that of unsupported RuS_2 and $CoMo/\gamma\text{-}Al_2O_3$. However, in general, the HDS activities of the sulfides do not correlate with the BET surface areas as compared to the to morphological effects of active sites.[42] Therefore, normalizing the activity to per gram of active metals or gram of catalysts better reflects the intrinsic activity of TMS.[43]

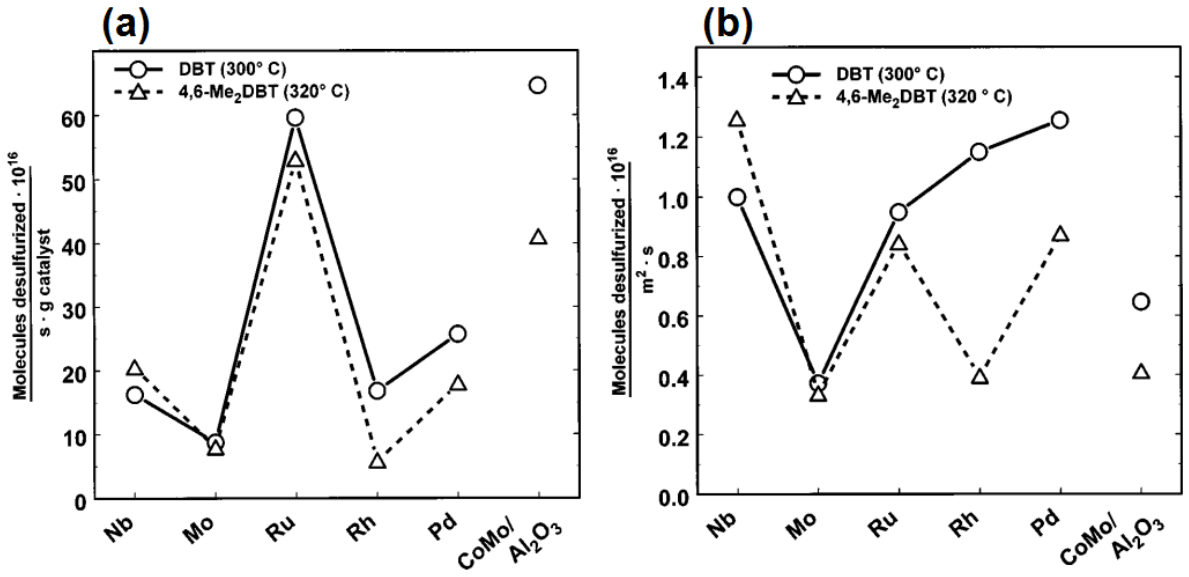

Figure 1.7. (a) Mass activities of catalysts (unsupported second transition series metal sulfides and $CoMo/Al_2O_3$) for HDS of DBT (300 °C) and 4,6- Me_2DBT (320 °C) at $p(H_2) = 38$ atm and $p_0(H_2S) = 0.13$ atm. Even though it appears that DBT is primarily desulfurized by the direct sulfur abstraction pathway and 4,6-Me_2DBT by the prehydrogenation pathway, the two trend curves follow each other; (b) Surface area activities of catalysts (unsupported second transition series metal sulfides and $CoMo/Al_2O_3$) for HDS of DBT (300 °C) and 4,6- Me_2DBT (320 °C) at $p(H_2) = 38$ atm and $p_0(H_2S) = 0.13$ atm. For the $CoMo/Al_2O_3$ catalyst, an active phase surface area of 100 m^2/g has been assumed. Reprinted from ref. [53], Copyright (2000) with permission of Springer.

In the same study,[53] the authors also examined the effects of H_2S partial pressure on the HDS performance of TMS. Figure 1.8 shows that the HDS activities of all TMS were affected when H_2S concentration increased by a factor of five. While the DDS route and durability of the conventional catalysts are strongly inhibited by H_2S,[1,54,55] niobium sulfide is not poisoned by H_2S in HDS of 4,6-DMDBT. Addition of Nb also made MoS_2/Al_2O_3 catalyst insensitive to the H_2S

partial pressure compared to the $NiMo/Al_2O_3$.[35] Furthermore, niobium as dopant improved the DBT HDS and Tetralin HYD activities of industrial $NiMo/Al_2O_3$ catalyst.[56] Niobium catalysts demonstrated a better performance (activity and selectivity) than molybdenum sulfide in cracking and isomerization reactions.[57]

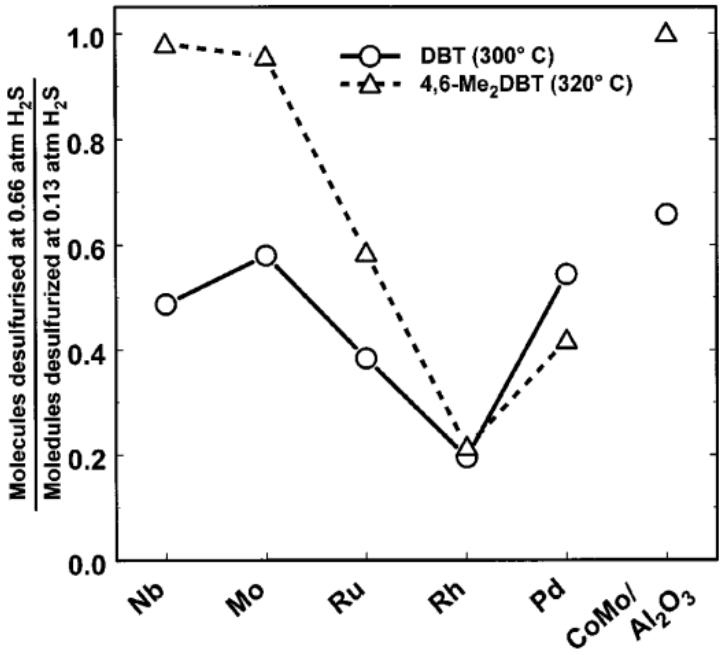

Figure 1.8. Extent of depression of HDS activity as a consequence of increasing the partial pressure of H_2S from 0.13 atm (defining the 1.0 activity level for the catalyst in question) to 0.66 atm (activity level displayed). H_2S inhibition is clearly more pronounced for the more active transition metal sulfides near the center of the second transition series. Reprinted from ref. [53], Copyright (2000) with permission of Springer.

As mentioned above, previous works revealed the promising performance and importance of Nb as a highly active catalyst in the hydrotreating units such as HDS, HDA, HCK, and HDN. The abundance of the metals and thus the catalyst price is also the matter of significant importance, especially for industries.[19,43] Figure 1.9 shows the abundance of periodic table elements in the earth crust in which the major industrially used elements are shown in red. As can be seen, Nb is among the abundant elements in nature, better than conventional W- and Mo-based catalysts.

The ppmw levels of Nb and Mo abundance in the crust are 17 versus 1.1, respectively. For Cu and Co, the abundance values were reported to be 68 vs. 30, respectively.[58,59] Therefore, Nb-based catalysts and more importantly the combination of Nb and Cu are more abundant than existing Co(Ni)-Mo(W)/Al_2O_3 catalysts. The price of Nb is comparable to Mo and Co. These findings imply the great potential of Nb as a hydrotreating catalyst with relatively high abundance.

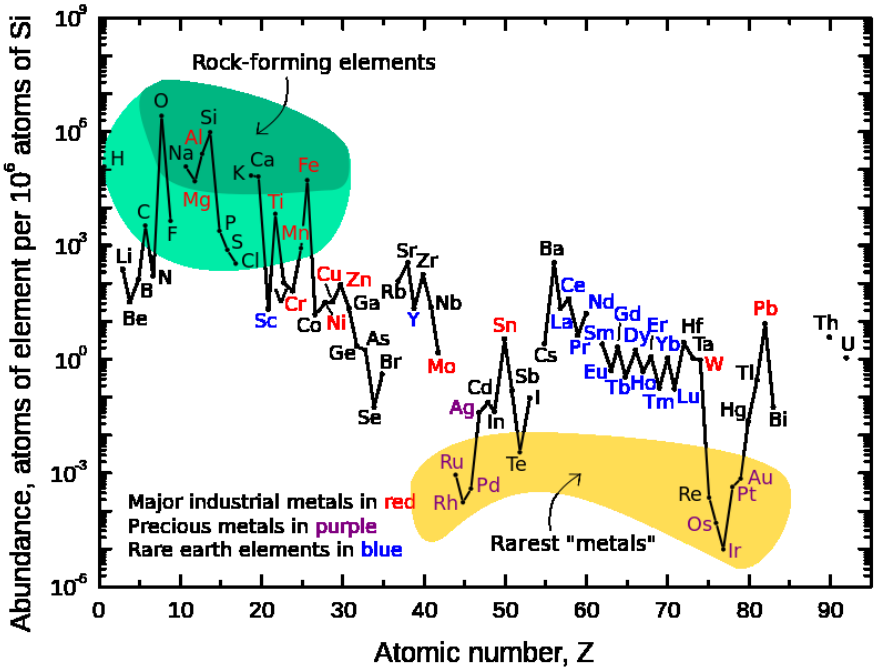

Figure 1.9. Abundance of the elements in the earth crust. Reprinted from ref. [58], with permission from U.S. Geological Survey, Department of the Interior/USGS.

1.5.3 Thermodynamics of sulfidation

Despite the higher intrinsic activity and H_2S tolerance of NbS_2 than MoS_2, sulfidation/reduction of niobium oxide (Nb_2O_5) is not as easy as MoO_3 and WO_3.[34,60,61] However, the sulfidation of transition metals with elemental sulfur is favorable (Table 1.2). Niobium oxides such as Nb_2O_5 and NbO_2 compounds are extremely stable with the heats of formation of -380 and -395 kJ/mol, respectively, greater than MoO_3 (-248 kJ/mol) and WO_3 (-279 kJ/mol).[62] However, the sulfide

materials obtained from dispersed solid elements are not good for catalysis for their very low surface areas of around 1 m^2/g. In addition, in industrial applications, the sulfidation is carried out using sulfurizing agents such as H_2S, CS_2, DMDS, and real sulfur containing feeds over oxidized catalysts. Therefore, the Gibbs free energy of formation of TMS from elements is not a fair comparison for evaluating the sulfidation capability of materials.

Table 1.2. Gibbs free energy of formation of TMS from the elements at 600 K (kJ/mol of metal). Reprinted from ref. [61], Copyright (1988) with permission from Elsevier.

Sulfide phase	$\Delta G°_f$	Sulfide phase	$\Delta G°_f$	Sulfide phase	$\Delta G°_f$
TiS_2	-357	ZrS_2	-594	Hf_2S_3	-133
V_2S_3	-488	NbS_2	-330	TaS_2	-367
CrS	-177	MoS_2	-289	WS_2	-272
$CrS_{1.17}$	-190	MoS_3	-268		
MnS	-239	Tc	–	ReS_2	-186
MnS_2	-258			Re_2S_7	-242
FeS	-119	RuS_2	-214	OsS_2	-154
FeS_2	-180				
Co_9S_8	-105	Rh	–	IrS_2	-154
CoS_2	-170			Ir_2S_3	-125
Ni_3S_2	-61	PdS	-78	PtS	-88
NiS	-105	PdS_2	-102	PtS_2	-124
Cu_2S	-56	Ag_2S	-66	Au	–
CuS	-65				
ZnS	-208	CdS	-157	HgS	-58

The sulfidation behavior of various transition metal oxides using H_2S at 600 K are provided in Table 1.3.[61] Compared to the facile sulfidation by elemental sulfur (Table 1.2), the formation of sulfides using H_2S is thermodynamically less favorable. Among the transition metals, Ti, Zr, Hf, Ta, and Nb form very stable oxides and their sulfidation using H_2S is not favorable

thermodynamically, even though their Gibbs free energies of sulfides formation from elemental sulfur are highly negative as shown in Table 1.2. The heats of sulfidation of these metals are positive indicating that higher temperatures are required to promote the formation of sulfide phases. The Gibbs free energies for the sulfidation of NbO_2 and Nb_2O_5 with H_2S at 600 K are positive, $\Delta G°$= +82 and +108 kJ/mol, respectively, as compared to MoO_3 ($\Delta G°$= -119 kJ/mol).[61]

Table 1.3. Changes in Gibbs free energy and enthalpy in sulfidation of metal oxides at 600 K. Reprinted from ref. [61], Copyright (1988) with permission from Elsevier.

Metal oxide	sulfidation agent	Metal sulfide	$\Delta G°$ (kJ/mol$_{metal}$)	$\Delta H°$ (kJ/mol$_{metal}$)
TiO_2	H_2S	TiS_2	+168	+169
V_2O_3	H_2S	V_2S_3	-157	–
V_2O_5	$H_2S + H_2$	V_2S_3	-258	–
Cr_2O_3	H_2S	Cr_2S_3	+64	+67
MnO	H_2S	MnS	-53	-50
FeO	H_2S	FeS	-41	-38
Fe_2O_3	$H_2S + H_2$	FeS	-49	-20
CoO	$H_2S + H_2$	Co_9S_8	-74	-82
NiO	$H_2S + H_2$	Ni_3S_2	-51	-46
NiO	H_2S	NiS	-74	-77
CuO	$H_2S + H_2$	Cu_2S	-140	-114
CuO	H_2S	CuS	-119	-114
ZnO	H_2S	ZnS	-74	-74
ZrO_2	H_2S	ZrS_2	+79	+77
NbO_2	H_2S	NbS_2	+82	–
Nb_2O_5	$H_2S + H_2$	NbS_2	+108	–
MoO_3	$H_2S + H_2$	MoS_2	-221	-219
MoO_2	H_2S	MoS_2	-119	-130
RuO_2	H_2S	RuS_2	-321	-344
PdO	H_2S	PdS	-180	-180
Ag_2O	H_2S	Ag_2S	-116	-113
CdO	H_2S	CdS	-115	-112

HfO_2	$H_2S + H_2$	Hf_2S_3	+511	–
Ta_2O_5	$H_2S + H_2$	TaS_2	+105	+102
WO_3	$H_2S + H_2$	WS_2	-110	-106
Re_2O_7	$H_2S + H_2$	Re_2S_7	-372	-364
ReO_2	H_2S	ReS_2	-169	-188
OsO_2	H_2S	OsS_2	-278	-296
IrO_2	H_2S	IrS_2	-331	-347
HgO	H_2S	HgS	-182	-184

It was reported that the reduction of bulk Nb_2O_5 initiated at 800 °C which then transformed to bulk Nb_2O_4 at 1300 °C.[63] Such a high-temperature reduction/sulfidation in a reductive atmosphere is not practical industrially and simply hinders the usage of NbS_x in industrial applications. The synthesis of bulk NbS_x from niobium and sulfur elements essentially requires high temperatures, i.e. 700 °C for NbS_3 and above 800 °C for NbS_2, leading to severe sintering of NbS_x species and very low surface areas of less than 3 m^2/g.[54,57,62,64] Although lithium intercalation-deintercalation technique can improve the surface area up to 20 m^2/g, the obtained BET values are still very low for the catalytic reactions.[54,65] The promising performance of unsupported niobium sulfide encouraged researchers to study its transposition to the supported state. Nevertheless, the literature on supported niobium sulfides is very rare. The sulfidation behavior (kinetic and thermodynamic) of niobium oxides is strongly influenced by the nature of the support material.[34,57,61] Although a higher dispersion of the niobium oxide promotes its sulfidation, the strong metal-support interaction on the other hand hinders the sulfidation of niobium oxides, especially in the case of a reactive supports such as alumina and silica.[61] This makes the sulfidation achievable only at the temperatures above 700 °C.[66] Carbon-supported NbS_x was found as efficient material for C-N bond cleavage.[66] A high degree of niobium oxides sulfidation and thus HDS activity was also achieved when carbon employed as a support instead of alumina, because of the weak metal-support interactions.[34,57] Figure 1.10 shows very low HDS activity of NbS_2 when supported on Al_2O_3 compared to the high activity of carbon-supported Nb. Allali et. al. prepared Nb supported on carbon at 10 wt% of Nb via three different Nb precursors as Nb pentachloride, Nb oxalate, and ammonium niobate. They found that the high thiophene

HDS activity at 350 °C was achieved when niobium oxalate was used as Nb precursor via two successive steps impregnation (each time 5 wt%). It was more than twice more active than one pot impregnation.[34] The importance of the factors that affect the degree of sulfidation decreases in the following order: temperature > H_2S partial pressure > duration of sulfidation.[61,67,68]

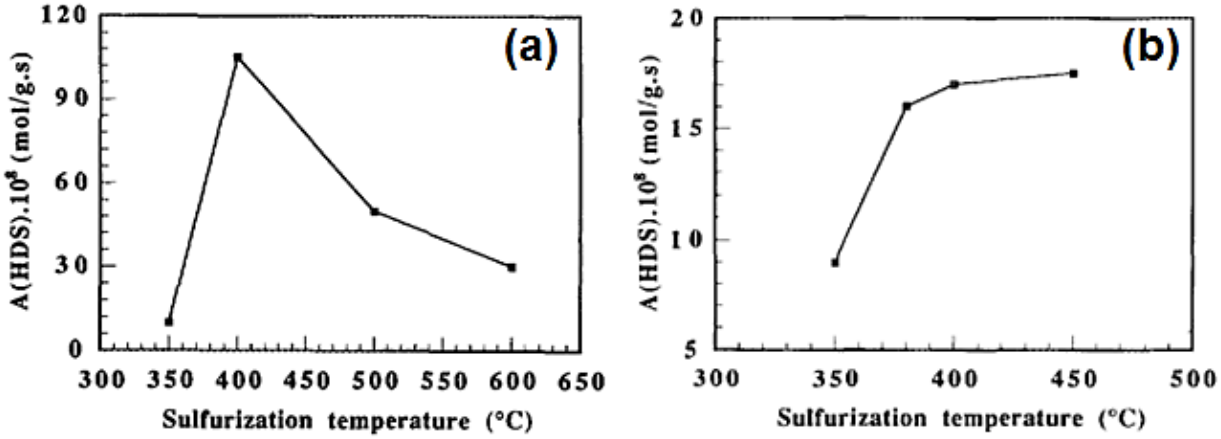

Figure 1.10. Effect of sulfidation temperature on the HDS performance of Nb/C (a) and Nb/Al_2O_3 (b). Reprinted from ref. [34], Copyright (1995) with permission from Elsevier.

1.5.4 Stability of TMS

The stability of sulfide phases during the reaction is important that directly depends on the equilibrium ratios of partial pressures of $p(H_2S)/p(H_2)$ in the gas phase. Table 1.4 displays the order of magnitude of the ratio of partial pressures $p(H_2S)/p(H_2)$ in the gas phase in equilibrium with solid sulfides determined at 600 K. The values in the table are relatively insensitive to the temperature in the range of 450-650 K due to the low heat of reaction. A 100 K increase in the reaction temperature requires about an order of magnitude increase in the equilibrium ratios of partial pressures to keep the metals in the sulfide form. TMS can be divided into two groups of less- and more-stable phases. Unlike the first group, the TMS in the second group (W, Mo, Cd, Cr, Ta, Hf, Nb, Zn, and V) only need less than ppm of H_2S to remain in their sulfide phases. It was reported that the sulfide form of two-dimensional (2D) surface sulfides are much more stable than three-dimensional bulk structures. For instance, the required partial pressure of

$p(H_2S)/p(H_2)$ to keep 2D cobalt sulfide in the sulfide form at 390 °C is three orders of magnitude lower than bulk cobalt sulfide.[61]

Table 1.4. Order of magnitude of ratio of partial pressures $p(H_2S)/p(H_2)$ in the gas phase in equilibrium with solid sulfides at temperature 600 K. Reprinted from ref. [61], Copyright (1988) with permission from Elsevier.

Sulfide phase	$p(H_2S)/p(H_2)$	Sulfide phase	$p(H_2S)/p(H_2)$	Sulfide phase	$p(H_2S)/p(H_2)$
TiS_2	10^{-11}	ZrS_2	10^{-21}	Hf_2S_3	10^{-11}
V_2S_3	10^{-24}	NbS_2	10^{-11}	TaS_2	10^{-11}
CrS	10^{-11}	MoS_2	10^{-8}	WS_2	10^{-7}
MnS	10^{-16}	Tc	–	ReS_2	10^{-3}
FeS	10^{-3}	RuS_2	10^{-5}	OsS_2	10^{-2}
Co_9S_8	10^{-6}	Rh_xS	10^{-1}	IrS_2	10^{-2}
Ni_3S_2	10^{-3}	PdS	10^{-2}	PtS	10^{-3}
Cu_2S	10^{-5}	Ag_2S	10^{-1}	Au	–
ZnS	10^{-13}	CdS	10^{-9}	HgS	10^{0}

1.5.5 Structural features of niobium sulfides

The following phases have been found in niobium-sulfur system: NbS_3, 2s-NbS_2, 3s-NbS_2, 2s-$Nb_{1+x}S_2$, 3s-$Nb_{1+x}S_2$, Nb_3S_4, h.t.-$Nb_{1-x}S$, l.t.-$Nb_{1-x}S$, and $Nb_{21}S_8$. While NbS_3 is a diamagnetic semiconductor, the other niobium sulfides are metallic with nearly temperature-independent paramagnetism.[64] However, two general forms of niobium sulfides as niobium disulfide (NbS_2) and niobium trisulfide (NbS_3) are the most important and stable structures. Electrical and magnetic properties of the sulfides of niobium are quite different from those of the group IV and other group V elements.[69] Nonetheless, NbS_2 exhibited the same structural features as MoS_2; a lamellar arrangement of trigonal prisms [NbS_6] as shown in Figure 1.11.[64,70] Metal layers sandwiched between two sulfur layers within a hexagonal cell.[71] However, the *d*-band filling is

not as same as MoS_2 explaining considerable differences in the electric and chemical properties.[72]

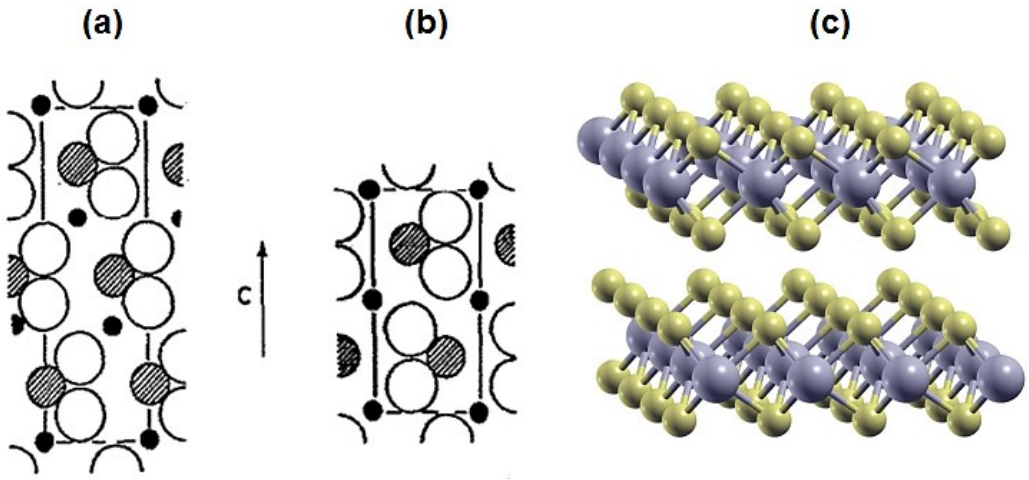

Figure 1.11. Hexagonal (1120) planes of (a) 3s-NbS_2 and (b) 2s-NbS_2; the metal (hatched circles) has trigonal-prismatic coordination by sulfur (open circles). The octahedral interstices between the NbS_2 slabs are indicated by black dots; (c) NbS_2 structure determined by DFT calculation. Figure (a) and (b) reprinted from ref. [64], Copyright (1969) with permission from Elsevier. Figure (c) reprinted from ref. [70], Copyright (2014) with permission from Elsevier.

NbS_3 has a completely different structure, however, is made from the same prismatic units.[34] The infinite fiber Nb-S slabs are formed by sharing the triangular face of [NbS_6] prisms[34] as shown in Figure 1.12.[73,74] Although the atomic arrangement is very complicated in NbS_3, the electronic structure is originated from anion and cation pairing as $Nb^{4+}S^{2-}(S_2)^{2-}$.[34] NbS_3 is more active than NbS_2 likely due to the presence of anionic vacancies as active sites.[34,44,54,57] However, in general, the thermal stability of trisulfides (NbS_3, MoS_3, WS_3) is low that leads to the structural transformation to disulfides (NbS_2, MoS_2, WS_2) under hydrotreatment conditions.[44,54] Allali et. al.[34] used EXAFS for structural investigation of Nb/C prepared from niobium oxalate precursor. EXAFS data of dried impregnated sample showed that Nb deposited as oxalate form, which the corresponding peak was disappeared after sulfidation. Nb-S distance is not a good indicator to distinguish the nature of Nb sulfides because of the similarity in both NbS_2 and NbS_3. Both Nb sulfide structures were found on the carbon-supported catalyst, however at very poor

crystallinity. For alumina-supported sample prepared under the same conditions, no Nb-S was identified using EXAFS indicating insufficient sulfidation temperature of 400 °C using H_2S. This was further confirmed by a very poor HDS activity of the material.[34] However, a stronger sulfurizing agent like CS_2 provided some degrees of sulfidation. In that case, NbS_2 or $Nb_{1-x}S$-like entities were found on alumina depending on the sulfidation temperature and duration. However, the later structure was not identified on the carbon support.

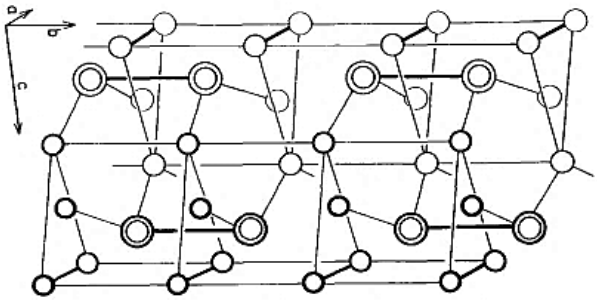

Figure 1.12. Schematic picture of the NbS_3 structure. Eight S atoms (open circles) form a bicapped trigonal prism around Nb atoms (double circles). Nb-Nb and S-S bonds are shown by thick lines. Reprinted from ref. [73], Copyright (1978) with permission from Elsevier.

1.5.6 Effects of copper on niobium sulfide

As discussed before, the elements on the left side of the periodic table, unlike the elements on the right side, form a very strong bond with sulfur that leads to the poisoning of the active sites. The average heats of formation of individual sulfides of a synergistic pair fall into an "optimum" range that results in the highest HDS activity.[49] Copper from the right side of the periodic table, when mixed with MoS_2, located on the left side of the periodic table, decreases the heat of formation of obtained alloyed material. Accordingly, the Mo-S bond energy in MoS_2 decreased from 59.7 to 53.1 kcal/mol in case of $Cu_{3.2}Mo_6S_8$ and to 54.1 kcal/mol for $Fe_{1.5}Mo_6S_8$ catalysts.[51,72,75] However, the improved HDS and HDN activities were not reported for these bimetallic catalysts.[19,72] Similarly, Nb and Cu are respectively located on the right and the left sides of the periodic table, however, in two different rows. Therefore, the reduction of the heat of formation of niobium sulfides by the addition of copper can be expected. In addition, the

enthalpy of vaporization of copper is lower than niobium, 300 versus 690 kJ/mol. Thus, it is also expected that copper concentrates on the surface of bimetallic structure. Sulfidation of copper is easier than niobium, but due to the higher stability of NbS_2 than Cu_2S or CuS (ΔG°_f = -330 kJ/mol for NbS_2, and ΔG°_f = -56 kJ/mol for Cu_2S), sulfur migrates from Cu to Nb and facilitates its sulfidation. Literature shows that $Cu_{0.5}NbS_2$ is the most abundant Cu-Nb-S species.[76] Figure 1.13 shows the structural feature of the Cu intercalated NbS_2 ($Cu_{0.5}NbS_2$).[76] Nb ions are present in the centers of the trigonal prisms of S ions similar to NbS_2. However, the stacking of the NbS_2 sandwiches in the intercalated copper compounds is similar to that of pure NbS_2 crystal. Therefore, the catalytic performance of the structure should be similar to that of NbS_2.

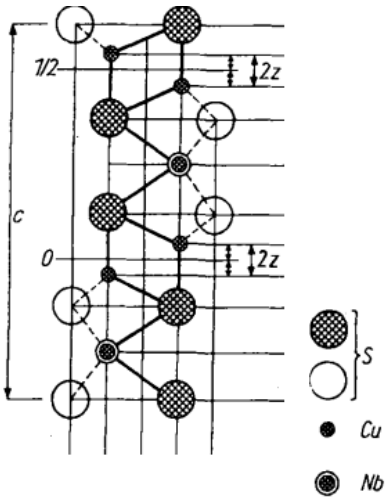

Figure 1.13. Schematic representation of the structures of the Cu intercalated NbS_2. The small circles represent Cu, whereas the larger ones represent sulfur in two levels. In this projection, the niobium positions coincide partly with the Cu positions. Reprinted from ref. [76], Copyright (1976) with permission from John Wiley and Sons.

1.5.7 On the structure of TMS active sites

The catalytic activity of TMS catalysts is related to surface defects of the lattice structure, which can be different from bulk properties due to the high-temperature sulfidation leading to the surface reconstructing. TMS, in general, have two types of structures: isotropic and layered sulfides. Metals in Group VIII are dominated by isotropic sulfides with octahedral coordination

to sulfur except for Co_9S_8 that contain mixed six- and four-fold tetrahedral coordination. Layered sulfides predominate in Groups IV to VII except for MnS that is isotropic.[15] Several models have been developed for the structure of active sites in TMS. Schuit and Gates[77] for the first time proposed a "monolayer" model for MoS_2 and WS_2 as active sites in HDS reaction in which molybdenum atoms were bonded to the sulfur and two oxygen atoms located in the upper and the same layers, respectively. Upon reduction of molybdenum atoms from Mo^{5+} to Mo^{3+} the sulfur atoms removed from the layer creating the HDS active sites, called sulfur anion vacancies. Simultaneously, Voorhoeve and Stuiver proposed "pseudo-intercalation" model in which promoters (Fe, Co, Ni) reduce Mo^{4+} and W^{4+} to Mo^{3+} and W^{3+} by occupying the octahedral spaces between the layers of MoS_2 and WS_2.[78,79] However, it was assumed that Co^{2+} and Ni^{2+} only occupy the sites located on the edges of the MoS_2 crystallites. Delmon's group introduced the idea of synergy between MoS_2 and Co_9S_8 instead of promotional effects of cobalt as a second catalytic metal. They proposed that sulfur molecule adsorbs on MoS_2 and hydrogen molecule simultaneously dissociates on Co_9S_8 followed by transferring H atom toward MoS_2 to desulfurize the sulfur molecule.[79] Topsøe et. al.[80] showed, using *in situ* Emission Mössbauer spectroscopy (EMS), that there are three phases of cobalt species in CoMo catalysts. These are spinel cobalt-alumina ($CoAl_2O_4$), Co_9S_8, and CoMoS which the latter is a small amount of cobalt species located inside or on the edges of MoS_2 crystallites as shown in Figure 1.14.[81] In addition, the amount of CoMoS phase increases by Co content correlating linearly with the HDS activity of the catalyst. However, the promoter atoms that present on the support as spinel structure or as separate sulfide phases are inactive and their formation should be eliminated.[80,82,83] As a key discovery, they have also identified two types of CoMoS sites with different electronic or geometric properties leading to different HDS activities: Type I in which cobalt atoms are located on monolayer slabs while in Type II occurs on multilayered slabs.[84] Type I sites were found less active than Type II[15,82,84] because of the Mo–O–Al bonds between the Co– Mo–S structures and the support, which will be broken by a high-temperature sulfidation transforming Type I to Type II active phases.[82] Therefore, most of the existing industrial hydrotreating catalysts are based on Type II structures.[82] Daage and Chianelli[85] proposed a model called ''rim–edge'', as shown in Figure 1.15, to correlate the morphology of the MoS_2 to the hydrogenation and direct desulfurization selectivity. They found that the ratio of HYD to DDS selectivity is linearly correlated with the reciprocal of the stacking height adjusted by the annealing

temperature. The ‘‘rim sites’’ have metallic character and are able for both hydrogenation and desulfurization, while ‘‘edge sites’’ only do desulfurization. The catalysts with single unstacked layers are selective to the HYD route as compared to the stacked layered catalysts. This model was proved by experimental reaction results and STM images[86] revealing that the brim sites play a key role in the catalysis. They are open sites suitable for desulfurization of the refractory sterically hindered sulfur compounds, and not being poisoned by H_2S. On the other hand, they interact strongly with nitrogen compounds.[80,82] The high-resolution atom-resolved scanning tunneling microscopy (STM) was conducted to investigate the structures and morphologies of individual Co–Mo–S and Ni–Mo–S nanoclusters.[36,37,86–88] The STM results confirmed that promoter atoms are located at the edges. In addition, it was found that the promoter atoms prefer to occupy very specific types of edge sites (the so-called S edges) as shown in Figure 1.16.

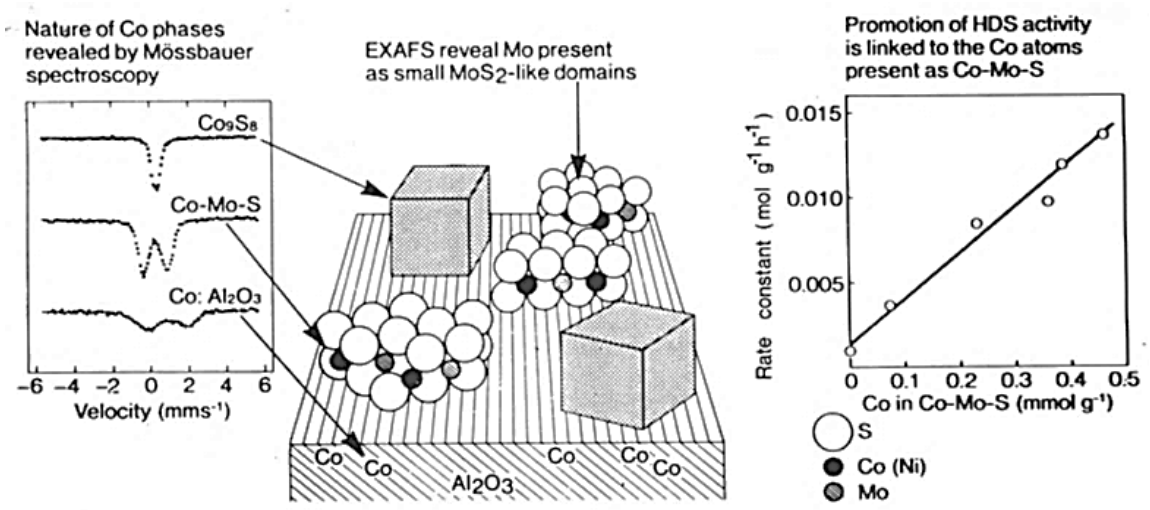

Figure 1.14. Schematic illustration of a typical $CoMo/Al_2O_3$ catalyst revealed by *in situ* MES and EXAFS measurements. Reprinted from ref. [84], Copyright (1986) with permission from Elsevier.

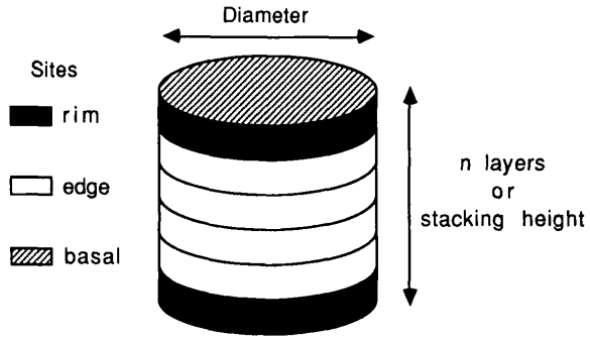

Figure 1.15. Physical model of a MoS_2 particle. Reprinted from ref. [15], Copyright (2009) with permission from Elsevier.

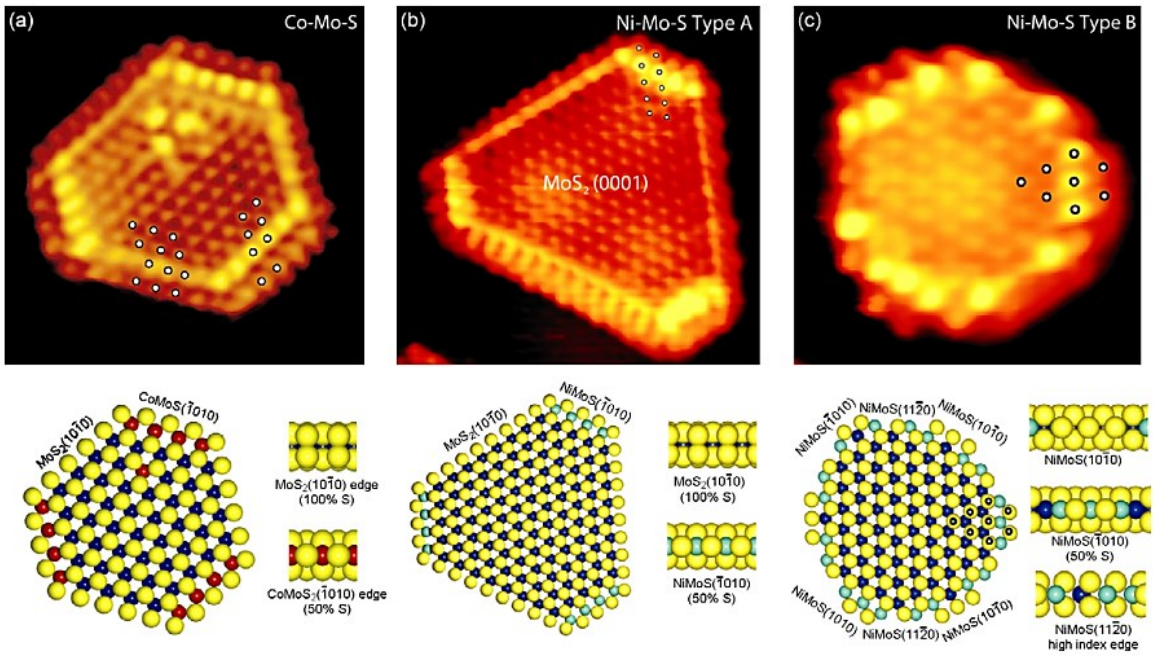

Figure 1.16. (a) Top: Atom-resolved STM image of a hexagonally truncated Co–Mo–S nanocluster. The superimposed white dots illustrate the registry of protrusions on both types of edges. Bottom: A ball model (top and side views, respectively) of the Co–Mo–S nanocluster based on DFT calculations. (b) Top: Atom-resolved STM image of a hexagonally truncated type A Ni–Mo–S nanocluster. Bottom: A ball model (top and side views, respectively) of the Ni–Mo–S type A nanocluster based on DFT calculations. (c) Top: Atom-resolved STM image dodecagonally shaped type B Ni–Mo–S nanocluster. Bottom: A ball model (top and side views, respectively) of the Ni–Mo–S type B nanocluster based on DFT calculations. (Mo: blue; S: yellow; Co: red; Ni: cyan). Reprinted from ref. [89], Copyright (2009) with permission from Elsevier.

1.6 HDS reaction mechanism

HDS of radioactive ^{35}S-labeled dibenzothiophene (DBT) was carried out over a series of sulfide Mo/Al_2O_3 and $CoMo/Al_2O_3$ catalysts in a pressurized flow reactor to estimate the behavior of sulfur on the working catalysts.[90,91] A ^{35}S radioisotope tracer method is an approach to determine the state of the sulfide in the catalyst under real operating conditions (*in situ*). A mechanism of the HDS reaction of DBT is shown in Figure 1.17.[92] It was found that sulfur on the catalyst can be exchanged by the sulfur in H_2S. After the catalyst was labeled with ^{35}S during HDS of [^{35}S]DBT, ^{35}S remaining on the catalyst was also exchanged by ^{32}S in [^{32}S]H_2S and released as [^{35}S]H_2S again. There are two routes where labile sulfur present in the form of bimetallic sulfur species "Co–Mo–S phases" desorbs as H_2S from the catalyst and formed a vacancy as an active site. In the sulfur exchange pathway with H_2S (Route II), when one vacancy is occupied by sulfur of H_2S formed in the HDS reaction, a labile sulfur in another site is released as H_2S to form another new vacancy. In HDS (Route I), when a sulfur compound is adsorbed on a vacancy, the C–S bond is subsequently cleaved and the sulfur remains on the catalyst. Simultaneously, labile sulfur is released as H_2S and a new active site is formed. In the two routes, the migration of vacancies on the catalyst always occurs due to the transformation between labile sulfur and vacancies on the catalyst surface. Therefore, it was assumed that a rapid adsorption/desorption of H_2S will always take place in the presence of H_2S under typical hydrotreating conditions. This leads to a rapid interconversion of the active site and labile sulfur and reveals that the vacancies under reaction are mobile.[91,92] The same exchangeable behavior and mobility of sulfur were observed in HDS of DBT over supported Pt- and Pd-based catalysts.[93] Moreover, it was found that almost all sulfur accommodated on the noble metal catalyst was labile sulfur participating in the reaction, although the amount of this labile sulfur was much smaller than that experienced with conventional Mo- or W-based catalysts. The sulfur mobility on the catalyst depends on the bond strength of the metal sulfide that is weaker in the case of Pt and Pd than Mo-S and Co-Mo-S.[94]

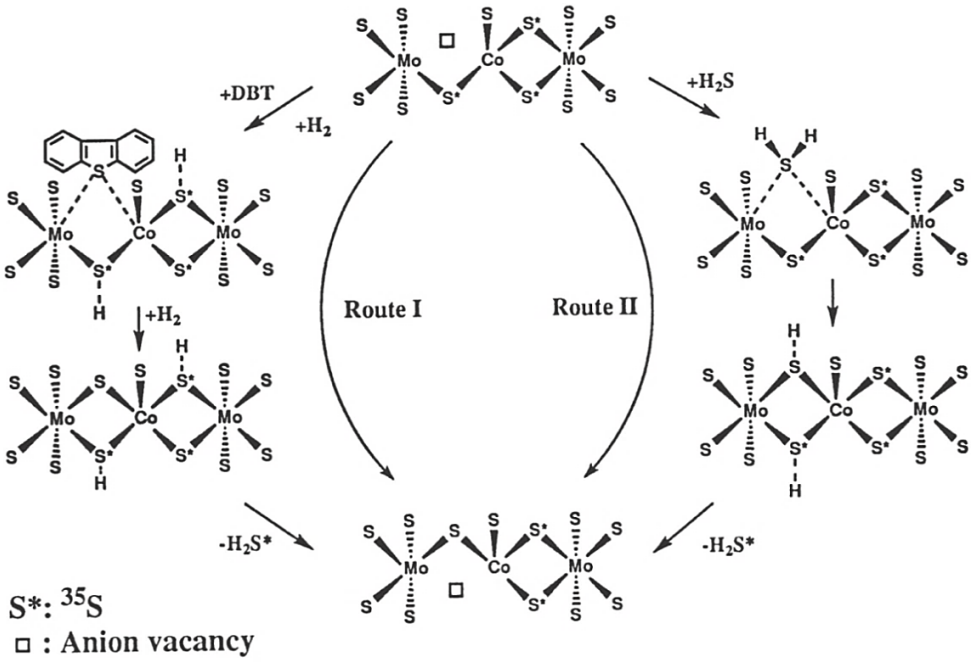

Figure 1.17. Transformation between labile sulfur and vacancies on the sulfided Co-Mo/Al_2O_3 in HDS. Route I: hydrodesulfurization; Route II: sulfur exchange. Reprinted from ref. [92], Copyright (1997) with permission from Elsevier.

1.7 Platinum group-based catalysts for ultra-deep hydrodesulfurization

When sulfur content in fuels has been pre-reduced to 500 ppm, 20 wt% of all remaining sulfur species belong to 4,6-dimethyldibenzothiophene (4,6-DMDBT) while CoMo or NiMo catalysts are not able to remove sulfur from this compound to reach the ultra-low levels of sulfur and aromatics.[9–11,95–97] The sterically hinderance effects of adjacent alkyl groups to sulfur atom prevent desulfurization of this refractory sulfur compound. There are four possible pathways such as hydrogenation, isomerization, demethylation, and C–C carbon session to lessen the steric hindrance of the methyl groups.[98] Among these pathways, partial hydrogenation of the aromatic rings has received a significant attention (Scheme 1.3). All other routes are mainly promoted by the acidic properties of the catalyst.[99]

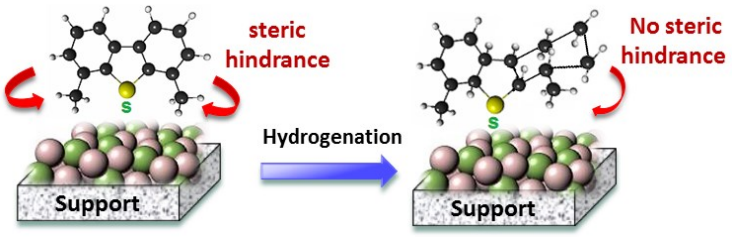

Scheme 1.3. Steric hindrance effects of methyl groups removed by hydrogenation of aromatic.

Pt-group catalysts that are known for their outstanding hydrogenation properties attracted considerable attention as potential catalysts for a second stage ultra-deep desulfurization of fuels.[9,100,101] Thermodynamically, HDS over conventional CoMo or NiMo catalysts is more favorable at higher temperatures whereas HDA essentially requires lower temperatures as shown in Figure 1.18. On the other hand, noble meal-based catalysts conduct both HDS and HDA at lower temperatures.[97] Therefore, an integrated two-stage hydrotreatment was set up, in which conventional CoMo or NiMo sulfide catalysts are used in the first stage and sulfur-tolerant noble metal catalysts are used in the second stage.

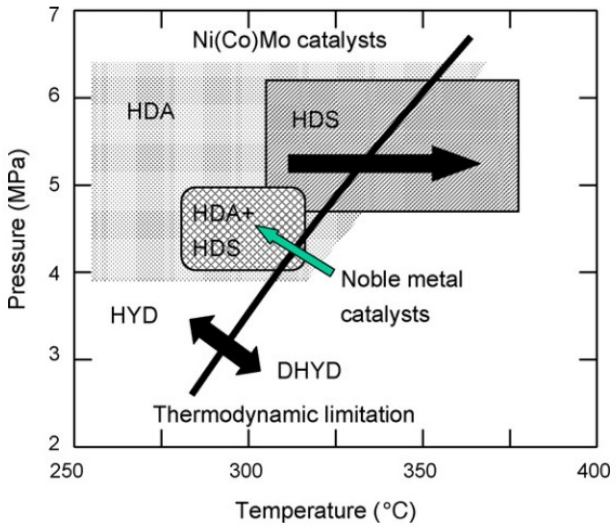

Figure 1.18. Thermodynamic limitations in simultaneous reduction of sulfur and aromatics. HDA: hydrodearomatization; HDS: hydrodesulfurization; HYD: hydrogenation; DHYD: dehydrogenation. Activity losses in HDS are usually compensated by an increase in reaction temperature. Reprinted from ref. [97], Copyright (2007) with permission from Elsevier.

Although metals have much better hydrogenation activities than metal sulfides, they can transform into inactive sulfides in the presence of sulfur-containing molecules and H_2S.[90] The strong interaction between noble metals and sulfur- and nitrogen-containing compounds leads to sulfidation of the metal particle surface and thus hindering their hydrogenation activity.[102] Several investigations have shown that the noble metals on the right-hand side of the periodic table are less sensitive to sulfur, especially Pt-Pd alloys that are more resistant than other metals against transformation into inactive sulfide.[97,101] However, in the two-stage hydrotreating, after removal of the H_2S formed in the first reactor, the amount of sulfur entering the second reactor may be low enough for the noble metals to maintain sufficient activity.[101] Pd is the most resistance noble metal to H_2S poisoning,[93,103] which also showed the highest activity in HDS of 4,6-DMDBT.[4,104,105] The catalytic activity of noble metals decreases in the order Pd ~ Pt-Pd > Pt > Rh > Ru-Rh ≫ Ru for HDS of 4,6-DMDBT.[104] The HDS reaction network of 4,6-DMDBT over Pd/γ-Al_2O_3 consists of two reaction routes, direct desulfurization (DDS) and hydrogenation (HYD)[103] and hydrocracking (HCK) as shown in Scheme 1.4.

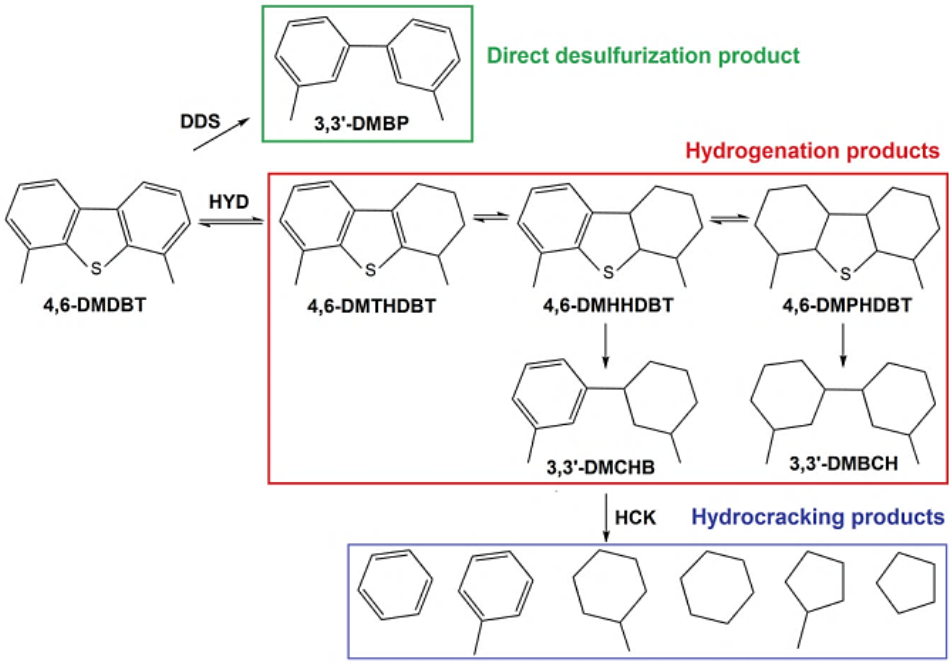

Scheme 1.4. HDS reaction network of 4,6-DMDBT over Pd/γ-Al_2O_3. Reprinted from ref. [103], Copyright (2005) with permission from Elsevier.

A perpendicular adsorption of molecules on the active sites via the sulfur atom (σ-mode) leads to the hydrogenolysis sulfur elimination (DDS) and flat adsorption of the molecule leads to the hydrogenation of aromatic ring and then sulfur removal, termed as HYD.[101] The HYD pathway as the dominant route for HDS of 4,6-DMDBT over noble metal catalysts, leads to sulfur-containing intermediates such as 4,6-dimethyl-tetrahydrodibenzothiophene (4,6-DM-THDBT), 4,6-dimethyl-hexahydrodibenzothiophene (4,6-DM-HHDBT), and 4,6-dimethyl-perhydrodibenzothiophene (4,6-DM-PHDBT), as well as desulfurized products 3,3'-dimethyl-cyclohexylbenzene (3,3'-DM-CHB) and 3,3'-dimethyl-bicyclohexyl (3,3'-DM-BCH). The DDS route yields 3,3'-dimethyl-biphenyl (3,3'-DM-BP).[101] The hydrocracking selectivity (HCK) includes single-ring products such as benzene, toluene, cyclohexane, cyclopentane, and methylcyclopentane. In contrast to 4,6-DMDBT, dibenzothiophene (DBT) converts predominantly via the DDS pathway. This difference is attributed to the steric hindrance of the methyl groups adjacent to the sulfur atom in 4,6-DMDBT.[101,103,106–111] It has been reported that hydrogenolysis (DDS) reactivities are governed by the electron density on the S atom and alkyl steric hindrance, while the hydrogenation route involves the order of the bond which is hydrogenated prior to the S elimination.[111] Quantum chemical calculations showed that the hydrogenation of one aromatic ring of DBT enhances the electron density on the S atom from 5.758 to 5.924 facilitating the sulfur removal from the molecule.[111] The DDS and HYD pathways are governed by different types of active sites. Due to the nature of perpendicular σ–adsorption in DDS mode, DDS selectivity can be promoted by low-coordinated active sites[38] such as those located on the edges and corners of NPs governed by decreasing the size of NPs.[112,113] Interestingly, higher DDS selectivity was observed over smaller Pt[112], Ru[114], and Pd[105] NPs. For example, when Ru NPs size decreased from 6 to 1 nm, a four-fold increase was observed in the DDS/HYD turnover rates of thiophene HDS.[114] The size of catalytic NPs affects the poisoning resistance of active sites.[105,115,116] It was reported that Pd and Pt NPs when smaller than 2 nm showed the highest sulfur tolerance while increasing the size of NPs decreased their sulfur resistance especially in the case of Pd.[116] Investigation of different supports showed the importance of NPs' size rather than the support effects on the sulfur tolerance of Pt.[115] A recent study showed an unprecedented DDS selectivity in the HDS of 4,6-DMDBT when the size of Pd NPs decreased to 4 nm.[105] It was also shown that the 4 nm Pd NPs were highly poisoned with sulfur than larger NPs. However, the electronic properties of active metals play an important role

to determine the resistance of metals to sulfur. It was reported that the higher resistance of bimetallic Pt-Pd catalysts toward sulfur poisoning compared to their monometallic Pt counterparts obtained from the weakened metal–sulfur bond on the electron-deficient Pt atoms.[102] Thus, increasing the fraction of electron-deficient Pt on the surface of the bimetallic clusters increases the hydrogenation efficiency of the catalyst in the presence of sulfur-containing compounds. Accordingly, acidic oxides are often used as supports for noble metals to withdraw electrons from the metal and creating electron-deficient metals,[117–121] which decreases the interaction with H_2S and form weaker sulfur–metal bond.[102,122,123] However, compared to alloying of active metal, the approach of using acidic supports can be confined to the feedstocks contain nitrogen-containing compounds.[97]

The outstanding performance of noble metals catalysts does not compensate the price of the catalysts for HDS reaction, termed as unfeasible price to performance ratio. Moreover, they occur at very low levels of abundance in the earth crust. Since catalytic activity depends on the surface fraction of metal nanoparticle atoms,[124,125] enhancing the utilization of the noble metal atoms has been a scientific and technological matter of paramount importance.[124,126,127]

1.8 Structure-controlled synthesis of catalytic nanoparticles

The most common traditionally and industrially methods for the preparation of heterogeneous catalysts are impregnation and precipitation.[128] The metallic precursors dissolved in a liquid directly introduced in the void of the support via impregnation or precipitated using a precipitating agent. Then, a high-temperature post-treatment decomposes the metallic precursors to form bimetallic NPs. However, the metal-support electronic and ligand interactions affect the formation and growth of NPs.[81,128] For instance, the strong metal-support interactions can lead to the formation of spinel structures such as nickel aluminate ($NiAl_2O_4$) that decreases the number of active sites. In addition, these synthesis methods result in the formation of both mono- and bimetallic particles of inhomogeneous composition coexisting on the support besides the poor control of particles' size.[129,130] In addition, since catalytic activity depends on the surface fraction of metal nanoparticle atoms,[124,125] enhancing the utilization of the noble metal atoms is crucial for the catalytic processes.[124,126,127] This can be achieved by surface engineering of active sites.

Structure-controlled synthesis of nanoparticles provides the possibility of tailoring the size, structure, and chemical properties of multiple components at atomic levels within individual NPs. This may improve the interaction between reactant and active sites as shown in Scheme 1.5. The metal-support interaction can also be controlled largely. In this way, bimetallic NPs are synthesized with desired structure and thus catalytic properties in a separate step and then deposit on a support material.

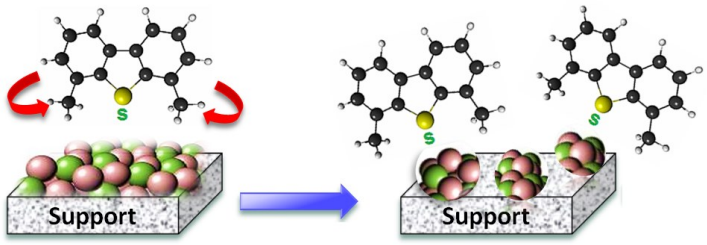

Scheme 1.5. Effects of size and structure control on the interactions between active centers and reactant.

1.8.1 Metal-based core-shell structures in catalysis

Several approaches have been applied to increase the number of surface active atoms such as downsizing nanoparticles (NPs) to sub-nanometers and single atoms,[124,131–139] introducing high-index crystallographic planes,[140–143] and decorating active metal as small particles (dumbbell-like)[144,145] or thin shell (core-shell)[126,146–148] over individual nanoparticles. The core-shell structures have received a significant attention owing to the possibility of tailoring structural and chemical properties of multiple components at atomic levels within individual NPs.[126,147–153] The idea of using core-shell NPs in heterogeneous catalysis is to dispersing precious active metals on a cheap and earth-abundant core such as iron. Depending on the combination of elements and their interactions, the synergism between core and shell metals can enhance the performance of active species (activity, selectivity, and durability) offering new properties beyond the monometallic counterparts. Accordingly, one can tune the catalytic properties of NPs on demand by controlling the structure like shell thickness, porosity, and degree of core surface coverage.

The exceptional reactivity of core-shell can be ascribed to the modification of electronic properties and the lattice strain of active metal atoms.[154–156] The electronic defects of reducible

metal oxides provide anchoring sites for active metals,[157,158] where the degrees of their interactions control dispersion, morphology, and metal reactivity.[157] However, the electronic impacts of core on the shell properties are limited to the first few layers and decline with layer thickness.[155] The lattice strain affects the *d*-band structure and hence the catalytic activity of nanoparticles by modifying the adsorption energy of reactants.[154] However, by increasing the layer thickness above a critical value, the overgrown layer dislocates to recover the strain-free prime-crystal structure, which can also change the morphology of NPs.[159] Therefore, the activity of core-shell structures essentially maximizes at a threshold shell thickness.

The bottom-up approach to fabricate the core-shell nanoparticles can be categorized into three methods which will be discussed thoroughly in section 1.31: 1) simultaneous fabrication of core and shell, 2) sequential fabrication of core and shell, and 3) galvanic exchange (displacement) reaction.[160]

1.8.2 Increasing dispersion and thermal stability of nanoparticles

As the particle size decreases, a larger fraction of active metal atoms with enhanced catalytic activities is exposed to the surface. On the other hand, the high surface energy of nanoparticles[161,162] results in a severe sintering (thermal deactivation) of nanoparticles during high-temperature reactions, causing a serious decline in their dispersion and catalytic performance.[150,163–165] This is more serious for the sintering-prone metals such as palladium and copper, which even grows at room temperature.[166] The sintering of nanoparticles can occur through migration and then coalescence of nearby NPs. However, the Ostwald ripening is the dominant mechanism in which coordinatively unsaturated atoms located in the edges and corners of small particles migrate toward larger particles.[163]

Controlling the thermal deactivation of catalysts has been a scientific and technological matter of paramount importance. Therefore, vast efforts have been invested worldwide to control the particle growth and enhancing their thermal stability. Different strategies have been introduced such as encapsulation of nanoparticles in the robust shell such as silica[150,167,168] or alumina[169,170] shell or using hollow zeolite (i.e. ZSM-5) as a nanoreactor to host single crystals.[171] However, all above-mentioned methods accompany with some mass transfer limitations especially for the

bulky reactant such as DBT to reach the active centers to take part in the reaction leading to an activity decrease. In addition, silica or alumina provides strong acidic sites resulting in deep cracking of the reactant molecules and coking. A strong metal-support interaction can prevent metal sintering, even in the case of sub-nanometers and single atoms catalysts,[124] but on the other hand, may diminish the catalytic activity.

A promising approach to constraining the mobility of metal NPs is alloying of the active metal with sintering-resistant elements. For instance, bimetallic Pt−Rh showed good thermal stability up to 850 °C in contrast to the monometallic counterparts sintered at about 500 °C.[172] It was reported that iridium promote the thermal stability of palladium in HDS.[4] However, iridium is one of the rarest elements in the earth crust. Yttrium as one of most abundant elements in nature provides the most thermally stable alloys; for example, Y stabilizes zirconia for high-temperature fuel cell applications.[173] Yttrium significantly increased the mechanical stability and hydrogen permeability of Pd-based membrane.[174] Accordingly, it can be considered as a promising candidate to promote the thermal stability of active metals having low stability.

1.8.3 Colloidal chemistry: liquid phase synthesis of nanostructures

Colloidal chemistry offers a great opportunity to design and fabricate uniform catalytic NPs with controlled size (1-10 nm), shape, and chemical properties. It is based on the reduction or thermal decomposition of the metallic precursor in the presence of electrostatic (inorganic) or steric (organic) stabilizers to make colloidal metal (oxide) NPs dispersed in a liquid. Electrostatic stabilization is based on the Coulombic repulsion force between individual particles. It occurs by the adsorption of ions on the electrophilic metal surface creating an electrical double layer. On the other hand, in steric stabilization, metal center is surrounded by layers of material that are bulky such as polymers or surfactant providing a steric barrier for intimate contact of the metal particles.[175] A reductant solvent such as alcohols or an external reducing agent such as sodium (potassium) borohydride carries out the reduction. An alcohol with α-hydrogen atoms oxidizes to the aldehyde and simultaneously reduces metallic precursors.[130,176] The type of alcohol affects the size and morphology of synthesized particles. Smaller Pd NPs were obtained in the order of methanol> ethanol>1-propanol.[175] However, external reducing agent are mostly used for the

reduction of non-noble metals such as nickel, iron, and copper.[177] Colloidal synthesis consists of three components: reactive precursors for particle formation, surfactants to direct particle size and shape, and solvent as a reaction medium.[143] The surfactants (ligand) bind onto particles through a surface-interacting functional group and contain a solvent-soluble chain that extends into the solution for solubility. LaMer et. al.[178] developed a model for the particle formation consisting three separate stages of super-saturation, nucleation, and growth as shown in Figure 1.19. In Stage I, monomers are added to the solution without forming the particles. Once the concentration of monomers reaches the critical saturation point ($S=S_c$), particles are nucleated that decreases the monomer concentration (Stage II). When the concentration of monomers drops below the critical point (Stage III), nucleation of new particles and simultaneous growth cause a further decrease in monomer concentration. Due to the simultaneous nucleation and growth of the particles, a rapid and short nucleation phase and slow growth kinetics minimize the particle size broadening.[143,178,179] Surfactant concentration can adjust the size of the nanoparticles.[105,143,180,181] A solution concentrated with surfactant results in smaller particle sizes, whereas larger particles are normally obtained in a dilute surfactant solution.[143]

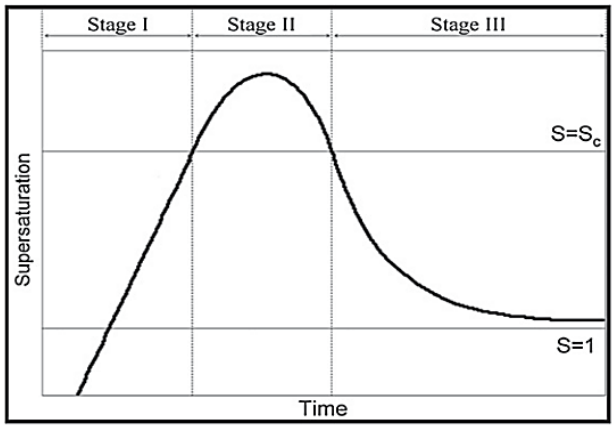

Figure 1.19. LaMer model: variation of the supersaturation as a function of time. Reprinted from ref. [143], Copyright (2012) with permission from Elsevier.

Besides controlling the shape of NPs, a proper choice of surfactant promotes the formation and growth of specific crystallite facets. For example, Pt nanoparticles with cube and cuboctahedron

shapes can be manufactured using cationic tetradecyltrimethylammonium bromide (TTABr) surfactant, while octahedron shape prepared by poly-(N-vinyl-2-pyrrolidone) polymer (PVP) as stabilizer.[143] PVP promotes the growth of (111) plane of palladium NPs. It was reported that regardless of the type of stabilizing polymer, the dominant shape of Pt nanoparticles was controlled by changing the reduction rate of Pt^{4+} ions. Tetrahedral particles predominated by using H_2 reduction, while methanol reduction generated mainly truncated octahedral particles.[179] In a different study, octopods Pt_3 showed higher turnover frequency (TOF) than nanocubes.[142]

In addition to the above-mentioned benefits, colloidal synthesis enables a controlled production of high-index planes that showed exceptional reactivity in versatile catalytic reactions than that of the most common stable planes. For instance, bulk Pt(410) surface exhibits unusual activity for catalytic decomposition of NO.[182] This is because of the higher density of atomic steps, ledges, and kinks on the high-index planes that usually serve as active sites for the catalytic reactions.[140,183,184]

1.8.4 Hydrogen sacrificial and galvanic exchange reaction techniques

As mentioned above, the colloidal synthesis relies on the reduction or decomposition of metallic precursors. In the case of bimetallic nanoparticles, the difference in the reduction potentials of each element results in the formation of different structures. The metal with higher redox potential reduces first and serves as a core for the second metal with lower redox potential leading to the formation of core-shell structures if they reduce simultaneously in the synthesis liquid. However, in the case of similar values, an alloy will be formed. In this way, an active metal could be easily inactive if serving as a core instead of being concentrated on the surface of the nanoparticles to do the catalysis. Then, these kinds of bimetallic core-shell structures should be inverted. Therefore, a successive reduction should be used for the synthesis of inverted core-shell structures. Hydrogen sacrificial protective strategy is a kind of successive reduction technique that can be used for the controlled-synthesis of inverted core-shell structure.[130,185] A schematic view of this method is presented in Figure 1.20. In this method, the core metal should be able to dissociate hydrogen and form metal-hydride at moderate synthesis temperature (50-200 $^{\circ}$C). This is because of the strong reducing capability of hydrogen to reduce the second metal

and decorate it as a shell. In that way, when the second metal ion contacts, i.e. Pt, the metal hydride cores, i.e. Pd, adsorbed hydrogen atoms will provide the electron and leaves the structure as a proton, providing the deposition of the second metal atoms on the surface of the first ones.[94]

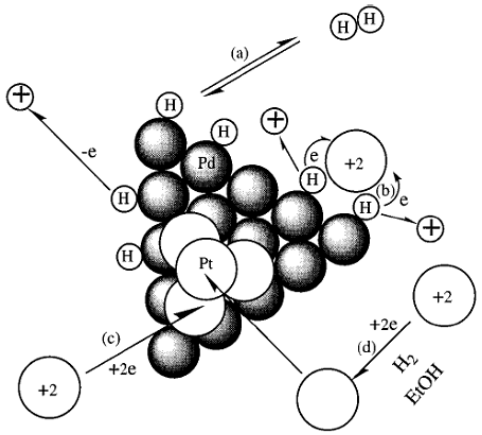

Figure 1.20. Hydrogen-sacrificial protective strategy for the preparation of bimetallic colloids in a core-shell structure. Reprinted from ref. [185], Copyright (1997) with permission from American Chemical Society.

Note that several transition metals are not able to for metal-hydride at a moderate synthesis temperature such as iron and cobalt.[186] Galvanic exchange reaction (also known as transmetalation) is a promising method for the synthesis of NPs with complex morphologies.[187–190] This can be also considered as an alternative method for the formation of inverted core-shell structures in which cores are not able to form metal hydride structures. This redox process involves the oxidation of one metal (which is often referred to as a sacrificial template) by the ions of another metal having a higher reduction potential. This reaction can be employed to generate a wide range of nanostructures which is only limited by a difference in the reduction potentials of the two metals.[187–190] Galvanic exchange reactions should be carried out in a precisely controlled manner to reach the desired nanostructures. During galvanic exchange reactions between the more and less noble metals, initially, alloy shells usually grow on the less noble metal NPs as a core template. As the reaction proceeds, dealloying may occur, where the less noble metal is removed from the alloy leading to the morphological changes and formation of hollow nanostructures and nanoframes. The final stage of dealloying can lead to breakup of

the nanostructure by completion of vigorous galvanic exchange reaction as shown in Figure 1.21.[190] However, it is possible to control or prevent galvanic exchange reaction by introduction of a strong antioxidant or reductant agent.[187]

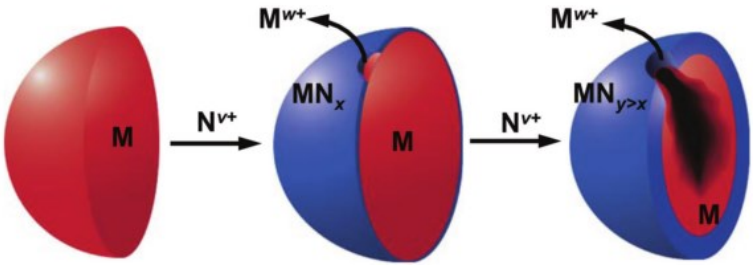

Figure 1.21. Galvanic exchange: reduction of ions (N^{v+}) of a more noble metal (N) drives oxidation of a less noble metal (M), which dissolves into solution (M^{w+}) through pinholes formed in the shell. Reprinted from ref. [190], Copyright (2014) with permission of The Royal Society of Chemistry.

1.9 Objectives and outline of the thesis

The objective of this thesis is to design and to fabricate high-performance hydrodesulfurization (HDS) catalysts based on earth-abundant elements for the two-stage HDS units to remove refractory sulfur compounds for clean fuels production. Recent advances in nanotechnology were applied for size-, shape-, and structure-controlled synthesis of catalytic nanostructures. Niobium-based catalysts were developed for the first-stage HDS unit. Niobium sulfide is more abundant and intrinsically more active in HDS reaction than molybdenum sulfide. Nonetheless, the formation of niobium sulfide requires an extremely high sulfidation temperature (above 700 °C), which simply hinders its usage in industrial applications. The novelty of the present thesis in this part is the use of copper for the first time to decrease the reduction/sulfidation temperature of niobium oxide. Copper also improved the product distribution of Nb-based catalysts. It reduced undesirable cracking products in both bulk and supported catalysts. Furthermore, size- and shape-controlled colloidal niobium sulfide structures were synthesized in a liquid phase at a low temperature of 300 °C.

For the second stage HDS, palladium-based catalysts were developed with a focus to reduce Pd usage in the catalyst formulation and to improve its activity, thermal stability, and sulfur tolerance. The bimetallic catalyst with a better performance than monometallic Pd catalyst can mediate the operating conditions (pressure and temperature), which can bring large Capex and Opex savings. Colloidal chemistry was used for tailoring the size, structure, and surface composition of the developed bimetallic catalysts.

Chapter 3 and 4 of the current thesis discuss the Pd-based catalysts. In Chapter 3, the synthesis and HDS performance of a series of bimetallic palladium-yttrium are discussed. The study addressed the issue of thermal deactivation of palladium nanoparticles in high-temperature applications. Monometallic Pd catalysts are prone to sintering which consequently reduces the activity and alters the selectivity to undesired products. We showed that addition of yttrium to palladium improved its thermal stability and dispersion of palladium nanoparticles even after a high-temperature treatment. TPR and XPS verified the formation of bimetallic palladium-yttrium nanostructures and CO-DRIFT showed the surface modification of Pd by yttrium. Accordingly, yttrium enhanced the ratio of direct desulfurization to hydrogenation selectivity without altering the overall HDS rate at 350 °C and 1 MPa. Moreover, yttrium suppressed the cracking reaction significantly. This allows operation of HDS reaction at low-pressures. The work exhibits the importance of colloidal synthesis method in the preparation of bimetallic Pd-Y catalysts. All mentioned improvements only observed for the catalysts prepared by the colloidal method.

We observed in Chapter 3 that smaller Pd nanoparticles promoted the desired direct desulfurization (DDS) selectivity, in agreement with literature. In Chapter 4, Pd species were preferentially reduced as nanosized metallic islands on the surface of 12-nm iron oxide nanoparticles using colloidal chemistry. The synthesized bimetallic structures were evaluated in HDS of refractory 4,6-DMDBT at 270 and 350 °C and 3 MPa and sulfur-free hydrogenation of biphenyl at 350 °C and 3 MPa. A wide range of Pd/Fe molar ratios was examined and the highest Pd dispersion and a four-fold enhancement in the Pd mass-based HDS activity were observed for the Pd/Fe ratio of 0.2. The interaction between Fe and Pd resulted in the change of electronic properties of Pd as revealed by TPR, XPS, and XRD. Iron improved the sulfur resistance of hydrogenation sites due to the higher affinity of sulfur to Fe as compared to Pd. Pd catalyst prepared from commercial iron oxide did not provide activity enhancement and catalyzed

significant cracking. The study demonstrates the advantages of the used colloidal preparation method to improve palladium dispersion and ensure beneficial Pd-Fe interactions for hydrodesulfurization.

Niobium sulfide (NbS_2) is intrinsically more active than MoS_2 and WS_2 structures in HDS, hydrogenation, and hydrodenitrogenation. Nonetheless, it has not found many catalytic applications due to the extreme stability of niobium oxides toward reduction and sulfidation, which is greater than molybdenum and tungsten oxides. The Gibbs free energy for the formation of niobium disulfide (NbS_2) is positive meaning that an extremely high temperature (more than 700 °C) is required for reduction and sulfidation. Chapter 5 explains the facilitative effect of copper on reduction and sulfidation of niobium oxides when alloyed as bimetallic NbCu structure. Thermodynamic calculations showed that copper could reduce the Gibbs free energy of sulfidation significantly. Accordingly, bulk bimetallic catalysts with different Cu/Nb molar ratios were prepared by coprecipitation method. TPR profiles revealed that copper reduced the reduction temperature of niobium oxide significantly. XPS data of sulfided samples showed the enhanced sulfidation of Nb in the presence of Cu correlating with Cu content in the samples. XRD revealed that $Cu_{0.65}NbS_2$ structure was formed after sulfidation at 400 °C. The HDS activity was maximized at the Cu/Nb of 0.3. The synergism between Nb and Cu improved the direct desulfurization and hydrogenation selectivities and reduced hydrocracking.

As explained in Chapter 6, mono- and bimetallic NbCu species were supported on different support materials such as mesoporous carbon and different phases of alumina at different metal loadings via incipient wetness impregnation method. In contrast to the carbon support, the strong interactions between niobium oxide species and oxide-supports made their sulfidation more difficult than bulk niobium oxide. Similar to the bulk catalysts, copper and niobium formed bimetallic $Cu_{0.65}NbS_2$ structure, as revealed by XRD and electron microscopy results. Copper reduced the reduction and sulfidation temperatures of supported niobium oxide species. The highest HDS activity was obtained on the carbon support and then alpha-alumina. Raman spectroscopy showed that various niobium oxide species formed on the carbon support at different Nb loadings with different sulfidation and catalytic behaviors. Niobium species at low loading of 2.0 wt% showed the least sulfidation degree functioning as coordinatively unsaturated Lewis acid sites in the HDS of DBT and delivered the highest HDS activity per mole of Nb. This

high acidic catalyst resulted in a high hydrocracking selectivity of around 70 % at the DBT conversion of 74 % at 325 °C and 3 MPa pressure. Although Cu did not enhance the activity, the improvement in selectivities was significant. Copper enhanced the direct desulfurization selectivity and reduced the hydrocracking selectivity over the whole range of Nb loadings.

Chapter 7 deals with a low-temperature shape-controlled synthesis of monometallic NbS_2 in a liquid phase. Colloidal NbS_2 nanostructures were synthesized in a coordinating solvent in the presence of natural capping ligands. In contrast to the solid-gas sulfidation that requires a high temperature of more than 700 °C, NbS_2 was formed very fast at 300 °C upon injection of the sulfur source (CS_2). In the absence of capping ligand (oleic acid), NbS_2 was formed as single layer nanosheets. Increasing the sulfidation time, increased the number of layers and then finally aggregated them as a flower-like structure after 3 h sulfidation reaction. In contrast, oleic acid as a capping ligand reduced the number of layers significantly even after 3 h sulfidation. The amount of the ligand in the solution and the sulfur content affected the structural properties of NbS_2 remarkably. An increased amount of CS_2 formed nanohexagons, and a further amount of CS_2 led to the formation of nanobars. A non-coordinating solvent such as 1-octadecene resulted in the formation of NbS_2 nanospheres. The synthesized structures were supported on γ-Al_2O_3 and evaluated in HDS of DBT at 325 °C and 3 MPa without a high-temperature pre-sulfidation. The monolayer nanosheets showed better performance than multilayers in HDS. On the other hand, nanohexagons delivered the highest activity and DDS selectivity most likely because of the higher fraction of corners and edges it possesses.

Chapter 8 provides concluding remarks as well as some suggestions for future works.

1.10 References

(1) Stanislaus, A.; Marafi, A.; Rana, M. S. Catal. Today 2010, 153, 1–68.

(2) Mariq, M. M.; Chase, R. E.; Xu, N.; P.M. Laing. Environ. Sci. Technol. 2002, 36, 283-289.

(3) Corro, G. Catal. Lett. 2002, 75, 89-106.

(4) Ziaei-Azad, H.; Semagina, N. Appl. Catal. B, Environ. 2016, 191, 138–146.

(5) Song, C. Catal. Today 2003, 86, 211–263.

(6) Ho, T. C. Catal. Today 2004, 98, 3–18.

(7) Song, C.; Ma, X. Appl. Catal. B, Environ. 2003, 41, 207–238.

(8) Kabe, T.; Ishihara, A.; Zhang, Q. Appl. Catal. A, Gen. 1993, 97, L1-L9.

(9) Prins R. in Handbook of heterogeneous catalysis; Ertl, G., Knozinger, H., Schuth, F., Weitkamp, J., (Eds.) Wiley-VCH, Weinheim, 2008, 2695–2718.

(10) Ito, E.; van Veen, J. A. R. Catal. Today 2006, 116, 446–460.

(11) Ma, X.; Sakanishi, K.; Isoda, T.; Mochida, I. Energy & Fuels 1995, 9, 33–37.

(12) Andari, M. K.; Abu-Seedo, F.; Stanislaus, A.; Qabazard, H. M. Fuel 1996, 75, 1664–1670.

(13) Knudsen, K. G.; Cooper, B. H.; Topsøe, H. Appl. Catal. A, Gen. 1999, 189 (1999), 205–215.

(14) van den Berg, J. P.; Lucien, J. P.; Germaine, G.; Thielemans, G. L. B. Fuel Process. Technol. 1993, 35, 119–136.

(15) Chianelli, R. R.; Berhault, G.; Torres, B. Catal. Today 2009, 147, 275–286.

(16) Aray, Y.; Zambrano, D.; Cornejo, M.; Ludeña, E. V.; Iza, P.; Vidal, A. B.; Coll, D. S.; Jímenez, D. M.; Henriquez, F.; Paredes, C. J. Phys. Chem. C 2014, 118, 27823–27832.

(17) Gutiérrez, O. Y.; Singh, S.; Schachtl, E.; Kim, J.; Kondratieva, E.; Hein, J.; Lercher, J. A.

ACS Catal. 2014, 4, 1487–1499.

(18) Bara, C.; Plais, L.; Larmier, K.; Devers, E.; Digne, M.; Lamic-Humblot, A. F.; Pirngruber, G. D.; Carrier, X. J. Am. Chem. Soc. 2015, 137, 15915–15928.

(19) Eijsbouts, S.; Anderson, G. H.; Bergwerff, J. A.; Jacobi, S. Appl. Catal. A, Gen. 2013, 458, 169–182.

(20) Wang, Q. H.; Kalantar-Zadeh, K.; Kis, A.; Coleman, J. N.; Strano, M. S. Nat. Nanotechnol. 2012, 7, 699–712.

(21) Pang, Q.; Liang, X.; Kwok, C. Y.; Nazar, L. F. Nat. Energy 2016, 1, 16132-16143.

(22) Lai, C.-H.; Lu, M.-Y.; Chen, L.-J. J. Mater. Chem. 2012, 22, 19–30.

(23) Ou, X.; Xiong, X.; Zheng, F.; Yang, C.; Lin, Z.; Hu, R.; Jin, C.; Chen, Y.; Liu, M. J. Power Sources 2016, 325, 410–416.

(24) Montoya, J. H.; Seitz, L. C.; Chakthranont, P.; Vojvodic, A.; Jaramillo, T. F.; Nørskov, J. K. Nat. Mater. 2016, 16, 70–81.

(25) Tsai, M.-L.; Su, S.-H.; Chang, J.-K.; Tsai, D.-S.; Chen, C.-H.; Wu, C.-I.; Li, L.-J.; Chen, L.-J.; He, J.-H. ACS Nano 2014, 8, 8317–8322.

(26) Kibsgaard, J.; Chen, Z.; Reinecke, B. N.; Jaramillo, T. F. Nat. Mater. 2012, 11, 963–969.

(27) Ha, E.; Liu, W.; Wang, L.; Man, H.-W.; Hu, L.; Tsang, S. C. E.; Chan, C. T.-L.; Kwok, W.-M.; Lee, L. Y. S.; Wong, K.-Y. Sci. Rep. 2017, 7, 39411-39419.

(28) Staszak-Jirkovský, J.; Malliakas, C. D.; Lopes, P. P.; Danilovic, N.; Kota, S. S.; Chang, K.-C.; Genorio, B.; Strmcnik, D.; Stamenkovic, V. R.; Kanatzidis, M. G.; Markovic, N. M. Nat. Mater. 2015, 15, 197–203.

(29) Asadi, M.; Kumar, B.; Behranginia, A.; Rosen, B. a; Baskin, A.; Repnin, N.; Pisasale, D.; Phillips, P.; Zhu, W.; Haasch, R.; Klie, R. F.; Král, P.; Abiade, J.; Salehi-Khojin, A. Nat. Com. 2014, 5, 4470-4478.

(30) Asadi, M.; Kim, K.; Liu, C.; Addepalli, A. V.; Abbasi, P.; Yasaei, P.; Phillips, P.;

Behranginia, A.; Cerrato, J. M.; Haasch, R.; Zapol, P.; Kumar, B.; Klie, R. F.; Abiade, J.; Curtiss, L. A.; Salehi-Khojin, A. Science 2016, 353, 467–470.

(31) Topsøe, H.; Clausen, B.S.; Massoth, F.E. Hydrotreating Catalysis Science and Technology,, 11, Anderson, J.R; Boudart, M. (Eds.), Springer Verlag Berlin, New York, 1996.

(32) Shafi, R.; Hutchings, G. J. Catal. Today 2000, 59, 423–442.

(33) Babich, I. V.; Moulijn, J. A. Fuel 2003, 82, 607–631.

(34) Allali, N.; Marie, A. M.; Danot, M.; Geantet, C.; Breysse, M. J. Catal. 1995, 156, 279–289.

(35) Gaborit, V.; Allali, N.; Danot, M.; Geantet, C.; Cattenot, M.; Breysse, M.; Diehl, F. Catal. Today 2003, 78, 499–505.

(36) Lauritsen, J. V.; Kibsgaard, J.; Olesen, G. H.; Moses, P. G.; Hinnemann, B.; Helveg, S.; Nørskov, J. K.; Clausen, B. S.; Topsøe, H.; Lægsgaard, E.; Besenbacher, F. J. Catal. 2007, 249, 220–233.

(37) Walton, A. S.; Lauritsen, J. V.; Topsøe, H.; Besenbacher, F. J. Catal. 2013, 308, 306–318.

(38) Oyama, S. T.; Zhao, H.; Freund, H. J.; Asakura, K.; Włodarczyk, R.; Sierka, M. J. Catal. 2012, 285, 1–5.

(39) Plantenga, F. L.; Cerfontain, R.; Eijsbouts, S.; van Houtert, F.; Anderson, G. H.; Miseo, S.; Soled, S.; Riley, K.; Fujita, K.; Inoue, Y. Stud. Surf. Sci. Catal. 2003, 145, 407–410.

(40) Eijsbouts, S.; Plantenga, F.; Leliveld, B.; Inoue, Y.; Fujita, K. ACS Div. Fuel Chem. Prepr. 2003, 48, 494–495.

(41) Eijsbouts, S.; Mayo, S. W.; Fujita, K. Appl. Catal. A, Gen. 2007, 322, 58–66.

(42) Pecoraro, T. A.; Chianelli, R. R. J. Catal. 1981, 67, 430–445.

(43) Chianelli, R. R. Catal. Rev. 1984, 26, 361–393.

(44) Lacroix, M.; Boutarfa, N.; Guillard, C.; Vrinat, M.; Breysse, M. J. Catal. 1989, 120, 473–477.

(45) Benard, J.; Oudar, J.; Barbouth, N.; Margot, E.; Berthier, Y. Surf. Science 1979, 88, L35-L41.

(46) Chianelli, R. R.; Berhault, G.; Raybaud, P.; Kasztelan, S.; Hafner, J.; Toulhoat, H. Appl. Catal. A, Gen. 2002, 227, 83–96.

(47) Toulhoat, H.; Raybaud, P.; Kasztelan, S.; Kresse, G.; Hafner, J. Catal. Today 1999, 50, 629–636.

(48) Raybaud, P.; Kresse, G.; Hafner, J.; Toulhoat, H. J. Phys. Condens. Matter 1999, 9, 11085–11106.

(49) Chianelli, R. R.; Pecoraro, T. A.; Halbert, T. R.; Pan, W. H.; Stiefel, E. I. J. Catal. 1984, 86, 226–230.

(50) Tanaka, K. I. Adv. Catal. 1985, 33, 99–158.

(51) Karroua, M.; Ladrie`re, J.; Matralis, H.; Grange, P.; Delmon, B. J. Catal. 1992, 138, 640–658.

(52) P. Afanasiev, L. Fischer, F. Beauchesne, M. Danot, V. Gaborit, M.; Breysse. Catal. Lett. 2000, 64, 59.

(53) Hermann, N.; Brorson, M.; Topsøe, H. Catal. Letters 2000, 65, 169–174.

(54) Danot, M.; Afonso, J.; Des, C. T.; Portefaix, J. L.; Breysse, M. Catal. Today 1991, 10, 629–643.

(55) Egorova, M.; Prins, R. , J. Catal. 2004, 225, 417–427.

(56) Gaborit, V.; Allali, N.; Geantet, C.; Breysse, M.; Vrinat, M.; Danot, M. Catal. Today 2000, 57, 267–273.

(57) Geantet, C.; Afonso, J.; Breysse, M.; Allali, N.; Danot, M. Catal. Today 1996, 28, 23–30.

(58) Haxel, G. B.; Hedrick, J. B.; Orris, G. J. Rare Earth Elements—Critical Resources for High Technology; 2002.

(59) WebElements.com. Archived from the original on 9 March 2007. Retrieved 2007-04-14.

(60) Ziolek, M. Catal. Today 2003, 78, 47–64.

(61) Zdražil, M. Catal. Today 1988, 3, 269–365.

(62) Dash, J. K.; Chen, L.; Dinolfo, P. H.; Lu, T. M.; Wang, G. C. J. Phys. Chem. C 2015, 119, 19763–19771.

(63) Wachs, I. E.; Briand, L. E.; Jehng, J.-M.; Burcham, L.; Gao, X. Catal. Today 2000, 57, 323–330.

(64) Kadijk, F.; Jellinek, F. J. Less Common Met. 1969, 19, 421–430.

(65) Allali, N.; Prouzet, E.; Michalowicz, A.; Gaborit, V.; Nadiri, A.; Danot, M. Appl. Catal. A Gen. 1997, 159, 333–354.

(66) Breysse, M.; Courieres, T. D.; Danot, M.; Geantet, M.; Portefaix, J.-L., US patent, 1992, US5157009 A.

(67) Gissy, H.; Bartsch, R.; Tanielian, C. J. Catal. 1980, 65, 150–157.

(68) de Beer, V. H. J.; Bevelander, C.; van Sint Fiet, T. H. M.; Werter, P. G. A. J.; Amberg, C. H. J. Catal. 1976, 43, 68–77.

(69) Rao, C. N. R.; Pisharody, K. P. R. Prog. Solid State Chem. 1976, 10, 207–270.

(70) Liu, Z. L.; Cai, L. C.; Zhang, X. L. J. Alloys Compd. 2014, 610, 472–477.

(71) Jellinek, F.; Brauer, G.; Müller, H. Nature 1960, 185, 376–377.

(72) Afanasiev, P.; Bezverkhyy, I. Appl. Catal. A, Gen. 2007, 322, 129–141.

(73) Rijnsdorp, J.; Jellinek, F. J. Solid State Chem. 1978, 25, 325–328.

(74) Bullett, D. W. J. Solid State Chem. 1980, 33, 13–16.

(75) McCarty, K. F.; Anderegg, J. W.; Schrader, G. L. J. Catal. 1985, 93, 375–387.

(76) Ridder, R. De; Tendeloo, G. Van; Landuty, J. Van; Dyck, D. Van; Amelince, S. Phys. Stat. Sol. 1976, 37, 591–606.

(77) Schuit, G. C. a; Gates, B. C. AIChE J. 1973, 19, 417–438.

(78) Voorhoeve, R. J. H.; Stuiver, J. C. M. J. Catal. 1971, 23, 243–252.

(79) Hagenbach, G.; Courty, P.; Delmon, B. J. Catal. 1973, 31, 264–273.

(80) Topsøe, H.; Clausen, B. S.; Candia, R.; Wivel, C.; Mørup, S. J. Catal. 1981, 68, 433–452.

(81) Sørensen, O.; Clausen, B. S.; Candia, R.; Topsøe, H. Appl. Catal. 1985, 13, 363–372.

(82) Topsøe, H. Appl. Catal. A, Gen. 2007, 322, 3–8.

(83) Breysse, M.; Bennett, B. A.; Chadwick, D.; Vrinat, M. Bull. Soc. Chim. Belg. 1981, 90, 1271.

(84) Topsøe, H.; Clausen, B. S. Appl. Catal. 1986, 25, 273–293.

(85) Daage, M.; Chianelli, R. R. J. Catal. 1994, 149, 414–427.

(86) Lauritsen, J. V; Nyberg, M.; Nørskov, J. K.; Clausen, B. S.; Topsøe, H.; Laegsgaard, E.; Besenbacher, F. J. Catal. 2004, 224, 94–106.

(87) Lauritsen, J. V.; Helveg, S.; Lægsgaard, E.; Stensgaard, I.; Clausen, B. S.; Topsøe, H.; Besenbacher, F. J. Catal. 2001, 197, 1–5.

(88) Helveg, S.; Lauritsen, J. V; Laegsgaard, E.; Stensgaard, I.; Nørskov, J. K.; Clausen, B. S.; Topsøe, H.; Besenbacher, F. Phys. Rev. Lett. 2000, 84, 951-955.

(89) Besenbacher, F.; Brorson, M.; Clausen, B. S.; Helveg, S.; Hinnemann, B.; Kibsgaard, J.; Lauritsen, J. V.; Moses, P. G.; Nørskov, J. K.; Topsøe, H. Catal. Today 2008, 130, 86–96.

(90) Kabe, T.; Ishihara, A.; Qian, W.; Godo, M. Catal. Today 1998, 45, 285–291.

(91) Kabe, T.; Qian, W.; Ishihara, A. Catal. Today 39 1997, 39, 3–12.

(92) Qian, W.; Ishihara, A.; Wang, G.; Tsuzuki, T.; Godo, M.; Kabe, T. J. Catal. 1997, 170, 286–294.

(93) Kabe, T.; Qian, W.; Hirai, Y.; Li, L.; Ishihara, A. J. Catal. 2000, 190, 191–198.

(94) Nørskov, J. K.; Clausen, B. S.; Topsøe, H. Catal. Letters 1992, 13, 1–8.

(95) Song, C. Catal. Today 2002, 77, 17–49.

(96) Ma, X.; Sakanishi, K.; Mochida, A. Ind. Eng. Chem. Res. 1996, 35, 2487–2494.

(97) Yoshimura, Y.; Toba, M.; Matsui, T.; Harada, M.; Ichihashi, Y.; Bando, K. K.; Yasuda, H.; Ishihara, H.; Morita, Y.; Kameoka, T. Appl. Catal. A, Gen. 2007, 322, 152–171.

(98) Bej, S. K.; Maity, S. K.; Turaga, U. T. Energy & Fuels 2005, 18, 1227–1237.

(99) Landau, M. V.; Berger, D.; Herskowitz, M. J. Catal. 1996, 159, 236–245.

(100) Qian, E. W.; Otani, K.; Li, L.; Ishihara, A.; Kabe, T. J. Catal. 2004, 221, 294–301.

(101) Niquille-Röthlisberger, A.; Prins, R. J. Catal. 2006, 242, 207–216.

(102) Yu, Y.; Gutiérrez, O. Y.; Haller, G. L.; Colby, R.; Kabius, B.; Rob Van Veen, J. A.; Jentys, A.; Lercher, J. A. J. Catal. 2013, 304, 135–148.

(103) Niquille-Röthlisberger, A.; Prins, R. J. Catal. 2005, 235, 229–240.

(104) Ishihara, A.; Dumeignil, F.; Lee, J.; Mitsuhashi, K.; Qian, E. W.; Kabe, T. Appl. Catal. A, Gen. 2005, 289, 163–173.

(105) Shen, J.; Semagina, N. ChemCatChem 2016, 8, 2565–2571.

(106) Niquille-Röthlisberger, A.; Prins, R. Catal. Today 2007, 123, 198–207.

(107) Girgis, M. J.; Gates, B. C. Ind. Eng. Chem. Res. 1991, 30, 2021–2058.

(108) Whitehurst, D. D.; Isoda, I. Mochida, I. Adv. Catal. 1998, 42, 345.

(109) Houalla, M.; Broderick, D. H.; Sapre, A. V.; Nag, N. K.; de Beer, V. H. J.; Gates, B. C.; Kwart, H. J. Catal. 1980, 61, 523–527.

(110) Ishihara, A.; Tajima, H.; Kabe, T. Chem. Lett. 1992, 21, 669–670.

(111) Ma, X.; Sakanishi, K.; Mochida, I. Fuel 1994, 73, 1667-1671.

(112) Wang, H.; Iglesia, E. ChemCatChem 2011, 3, 1166–1175.

(113) Zhu, W.; Michalsky, R.; Metin, Ö.; Lv, H.; Guo, S.; Wright, C. J.; Sun, X.; Peterson, A. A; Sun, S. J. Am. Chem. Soc. 2013, 135, 16833–16836.

(114) Wang, H.; Iglesia, E. J. Catal. 2010, 273, 245–256.

(115) Jackson, S. D.; Willis, J.; Mclellan, G. D.; Webb, G.; Keegan, M. B. T.; Moyes, R. B.; Simpson, S.; Wells, P. B.; Whyman, R. J. Catal. 1993, 139, 191–206.

(116) Matsui, T.; Harada, M.; Ichihashi, Y.; Bando, K. K.; Matsubayashi, N.; Toba, M.; Yoshimura, Y. Appl. Catal. A Gen. 2005, 286, 249–257.

(117) Betta, R. A. D.; Boudart, M.; Gallezot, P.; Weber, R. S. J. Catal. 1981, 69, 514–515.

(118) Figueras, F.; Mencier, B.; De Mourgues, L.; Naccache, C.; Trambouze, Y. J. Catal. 1970, 19, 315–321.

(119) Gallezot, P. Catal. Rev. 1979, 20, 121–154.

(120) Guo, H.; Sun, Y.; Prins, R. Catal. Today 2008, 130, 249–253.

(121) Sachtler, W. M. H.; Stakheev, A. Y. Catal. Today 1992, 12, 283–295.

(122) Sun, Y.; Prins, R. Angew. Chemie - Int. Ed. 2008, 47, 8478–8481.

(123) Cooper, B. H.; Donnis, B. B. L. Appl. Catal. A, Gen. 1996, 137, 203–223.

(124) Qiao, B.; Wang, A.; Yang, X.; Allard, L. F.; Jiang, Z.; Cui, Y.; Liu, J.; Li, J.; Zhang, T. Nat. Chem. 2011, 3, 634–641.

(125) Choi, C. H.; Kim, M.; Kwon, H. C.; Cho, S. J.; Yun, S.; Kim, H.-T.; Mayrhofer, K. J. J.; Kim, H.; Choi, M. Nat. Commun. 2016, 7, 10922–10931.

(126) Hunt, S. T.; Milina, M.; Alba-rubio, A. C.; Hendon, C. H.; Dumesic, J. A.; Román-

leshkov, Y. Science 2015, 352, 974–978.

(127) Hu, G.; Nitze, F.; Gracia-Espino, E.; Ma, J.; Barzegar, H. R.; Sharifi, T.; Jia, X.; Shchukarev, A.; Lu, L.; Ma, C.; Yang, G.; Wågberg, T. Nat. Commun. 2014, 5, 1–9.

(128) Marceau, E.; Carrier,X.; Che M. Synthesis of solid catalysts; de Jong, K. P., (Ed.), Wiley-VCH, 2009.

(129) Coq, B.; Figueras, F. J. Mol. Catal. A Chem. 2001, 173, 117–134.

(130) Ziaei-Azad, H. Bimetallic Ir-based Catalysts for Ring Opening and Hydrodesulfurization Reactions, University of Alberta, Edmonton, Canada, PhD thesis, 2014.

(131) Lei, Y.; Mehmood, F.; Lee, S.; Greeley, J.; Lee, B.; Seifert, S.; Winans, R. E.; Elam, J. W.; Meyer, R. J.; Redfern, P. C.; Teschner, D.; Schloegl, R.; Pellin, M. J.; Curtiss, L. A.; Vajda, S. Science 2010, 328, 224–228.

(132) Herzing, A. A; Kiely, C. J.; Carley, A. F.; Landon, P.; Hutchings, G. J. Science 2008, 321, 1331–1335.

(133) Turner, M.; Golovko, V. B.; Vaughan, O. P. H.; Abdulkin, P.; Berenguer-Murcia, A.; Tikhov, M. S.; Johnson, B. F. G.; Lambert, R. M. Nature 2008, 454, 981–983.

(134) Wei, H.; Liu, X.; Wang, A.; Zhang, L.; Qiao, B.; Yang, X.; Huang, Y.; Miao, S.; Liu, J.; Zhang, T. Nat. Commun. 2014, 5, 5634–5642.

(135) Vilé, G.; Albani, D.; Nachtegaal, M.; Chen, Z.; Dontsova, D.; Antonietti, M.; López, N.; Pérez-Ramírez, J. Angew. Chemie - Int. Ed. 2015, 54, 11265–11269.

(136) Liu, P.; Zhao, Y.; Qin, R.; Mo, S.; Chen, G.; Gu, L.; Chevrier, D. M.; Zhang, P.; Guo, Q.; Zang, D.; Wu, B.; Fu, G.; Zheng, N. Science 2016, 352, 797–801.

(137) Ranocchiari, M.; Lothschutz, C.; Grolimund, D.; van Bokhoven, J. A. Proc. R. Soc. A Math. Phys. Eng. Sci. 2012, 468, 1985–1999.

(138) Duarte, R. B.; Krumeich, F.; Van Bokhoven, J. A. ACS Catal. 2014, 4, 1279–1286.

(139) Fujiwara, K.; Müller, U.; Pratsinis, S. E. ACS Catal. 2016, 6, 1887–1893.

(140) Tian, N.; Zhou, Z.-Y.; Sun, S.-G.; Ding, Y.; Wang, Z. L. Science 2007, 316, 732–735.

(141) Chen, C.; Kang, Y.; Huo, Z.; Zhu, Z.; Huang, W.; Xin, H. L.; Snyder, J. D.; Li, D.; Herron, J. A.; Mavrikakis, M.; Chi, M.; More, K. L.; Li, Y.; Markovic, N. M.; Somorjai, G. A.; Yang, P.; Stamenkovic, V. R. Science 2014, 343, 1339–1343.

(142) Khan, M. U.; Wang, L.; Liu, Z.; Gao, Z.; Wang, S.; Li, H.; Zhang, W.; Wang, M.; Wang, Z.; Ma, C.; Zeng, J. Angew. Chemie - Int. Ed. 2016, 55, 9548 –9552.

(143) An, K.; Alayoglu, S.; Ewers, T.; Somorjai, G. A. J. Colloid Interface Sci. 2012, 373, 1–13.

(144) Wang, C.; Daimon, H.; Sun, S. Nano Lett. 2009, 9, 1493–1496.

(145) Sun, X.; Guo, S.; Liu, Y.; Sun, S. Nano Lett. 2012, 12, 4859–4863.

(146) Wang, D.; Xin, H. L.; Hovden, R.; Wang, H.; Yu, Y.; Muller, D. a.; DiSalvo, F. J.; Abruña, H. D. Nat. Mater. 2012, 12, 81–87.

(147) Zhang, X. B.; Yan, J. M.; Han, S.; Shioyama, H.; Xu, Q. J. Am. Chem. Soc. 2009, 131, 2778–2779.

(148) Alayoglu, S.; Nilekar, A. U.; Mavrikakis, M.; Eichhorn, B. Nat. Mater. 2008, 7, 333–338.

(149) Tao, F.; Grass, M. E.; Zhang, Y.; Butcher, D. R.; Renzas, J. R.; Liu, Z.; Chung, J. Y.; Mun, B. S.; Salmeron, M.; Somorjai, G. A. Science 2008, 322, 932–934.

(150) Joo, S. H.; Park, J. Y.; Tsung, C. K.; Yamada, Y.; Yang, P.; Somorjai, G. A. Nat. Mater. 2009, 8, 126–131.

(151) Sasaki, K.; Naohara, H.; Choi, Y.; Cai, Y.; Chen, W.-F.; Liu, P.; Adzic, R. R. Nat. Commun. 2012, 3, 1115–1124.

(152) Liang, W. I.; Zhang, X.; Zan, Y.; Pan, M.; Czarnik, C.; Bustillo, K.; Xu, J.; Chu, Y. H.; Zheng, H. J. Am. Chem. Soc. 2015, 137, 14850–14853.

(153) Gawande, M. B.; Goswami, A.; Asefa, T.; Guo, H.; Biradar, A. V; Peng, D.; Zboril, R.; Varma, R. S. Chem. Soc. Rev. 2015, 44, 7540–7590.

(154) Strasser, P.; Koh, S.; Anniyev, T.; Greeley, J.; More, K.; Yu, C.; Liu, Z.; Kaya, S.; Nordlund, D.; Ogasawara, H.; Toney, M. F.; Nilsson, A. Nat. Chem. 2010, 2, 454–460.

(155) Schlapka, A.; Lischka, M.; Groß, A.; Kasberger, U.; Jakob, P. Phys. Rev. Lett. 2003, 91, 016101/1-016101/4.

(156) Zhang, S.; Zhang, X.; Jiang, G.; Zhu, H.; Guo, S.; Su, D.; Lu, G.; Sun, S. J. Am. Chem. Soc. 2014, 136, 7734–7739.

(157) Kwak, J. H.; Hu, J.; Mei, D.; Yi, C.-W.; Kim, D. H.; Peden, C. H. F.; Allard, L. F.; Szanyi, J. Science 2009, 325, 1670–1673.

(158) Chen, M. S.; Goodman, D. W. Science 2004, 306, 252–255.

(159) Kwon, S. G.; Krylova, G.; Phillips, P. J.; Klie, R. F.; Chattopadhyay, S.; Shibata, T.; Bunel, E. E.; Liu, Y.; Prakapenka, V. B.; Lee, B.; Shevchenko, E. V. Nat. Mater. 2015, 14, 215–223.

(160) Wei, S.; Wang, Q.; Zhu, J.; Sun, L.; Lin, H.; Guo, Z. Nanoscale 2011, 3, 4474-4502.

(161) Tschöpe, A.; Birringer, R. Acta Metall. Mater. 1993, 41, 2791–2796.

(162) Bryden, K. J.; Ying, J. Y. Acta Mater. 1996, 44, 3847–3854.

(163) Hansen, T. W.; Delariva, A. T.; Challa, S. R.; Datye, A. K. Acc. Chem. Res. 2012, 46, 1720–1730.

(164) Campbell, C. T. Acc. Chem. Res. 2013, 46, 1712–1719.

(165) An, K.; Zhang, Q.; Alayoglu, S.; Musselwhite, N.; Shin, J. Y.; Somorjai, G. A. Nano Lett. 2014, 14, 4907–4912.

(166) Weissmiiller, J.; Loffler, J.; Martin, K. Nanostruetured Mater. 1995, 6, 105–114.

(167) Ge, J.; Zhang, Q.; Zhang, T.; Yin, Y. Angew. Chemie - Int. Ed. 2008, 47, 8924–8928.

(168) Wang, Y.; Biradar, A. V.; Duncan, C. T.; Asefa, T. J. Mater. Chem. 2010, 20, 7834-7841.

(169) Zhang, W.; Chi, Z. X.; Mao, W. X.; Lv, R. W.; Cao, A. M.; Wan, L. J. Angew. Chemie -

Int. Ed. 2014, 53, 12776–12780.

(170) Wang, Y.; Tseng, W. J. J. Am. Ceram. Soc. 2009, 92, 32–37.

(171) Fodor, D.; Ishikawa, T.; Krumeich, F.; van Bokhoven, J. A. Adv. Mater. 2015, 27, 1919–1923.

(172) Cao, A.; Veser, G. Nat. Matter. 2010, 9, 75-81

(173) Courtin, E.; Boy, P.; Rouhet, C.; Bianchi, L.; Bruneton, E.; Poirot, N.; Laberty-Robert, C.; Sanchez, C. Chem. Mater. 2012, 24, 4540–4548.

(174) Fort, D.; Farr, J. P. G.; Harris, I. R. J. Less-Common Met. 1975, 39, 293–308.

(175) Semagina, N.; Kiwi-Minsker, L. Catal. Reviews 2009, 51, 147-219.

(176) Helmut, B.; Kyatanahalli S., N. in Metal Nanoclusters in Catalysis and Materials Science, Corain, B.; Schmid, G.; Toshima, N. (Eds.), 2008, 21–48.

(177) Shi, G.; Franzke, T.; Sánchez, M. D.; Xia, W.; Weis, F.; Seipenbusch, M.; Kasper, G.; Muhler, M. ChemCatChem 2012, 4, 760–765.

(178) LaMer, V.; Dinegar, R. J. Am. Chem. 1950, 72, 4847–4854.

(179) Teranishi, T.; Kurita, R.; Miyake, M. J. Inorg. Organomet. Polym. 2000, 10, 145–156.

(180) Mpourmpakis, G.; Caratzoulas, S.; Vlachos, D. G. Nano Lett. 2010, 10, 3408–3413.

(181) Jana, N. R.; Chen, Y.; Peng, X. Chem. Mater. 2004, 16, 3931–3935.

(182) Banholzer, W. F.; R.I. Masel. J. Catal. 1984, 85, 127–134.

(183) Somorjai, G. a.; Blakely, D. W. Nature 1975, 258, 580–583.

(184) Sun, S. G.; Chen, A. C.; Huang, T. S.; Li, J. B.; Tian, Z. W. J. Electroanal. Chem. 1992, 340, 213–226.

(185) Wang, Y.; Toshima, N. J. Phys. Chem. B 1997, 101, 5301–5306.

(186) Kleperis, J.; Wójcik, G.; Czerwinski, A.; Skowronski, J.; Kopczyk, M.; Beltowska-

Brzezinska, M. J. Solid State Electrochem. 2001, 5, 229–249.

(187) Xia, X.; Wang, Y.; Ruditskiy, A.; Xia, Y. Adv. Mater. 2013, 25, 6313–6332.

(188) Park, T.-H.; Lee, H.; Lee, J.; Jang, D.-J. RSC Adv. 2017, 7, 7718–7724.

(189) Alia, S. M.; Yan, Y.; Pivovar, B. Catal. Sci. Technol. 2014, 4, 3589–3600.

(190) Tracy, B. J.; Anderson, B. D. Nanoscale 2014, 6, 12195–12216.

Chapter 2. Methodology

This chapter provides information on the experimental testing system including procedure and equations used to verify kinetic regime, plug flow behavior, and catalytic performance. In addition, identification and quantification of the reaction products are provided.

2.1 HDS experimental setup and reaction procedure

A continuous fixed-bed flow reactor was used in this work to evaluate the catalytic activity and kinetic study of the synthesized catalysts in hydrodesulfurization process under industrially relevant operating conditions. Scheme 2.1 shows schematic of the experimental setup for the HDS reaction. A LabVIEW program was designed to control the reaction from start to finish. Two liquid containers were considered for sulfidation and main liquid feed streams. Identification and quantification of the reaction products was performed off-line by gas chromatograph (GC) equipped with a mass spectrometry and a calibrated FID detector. All the HDS tests were studied for at least 18 h including overnight stabilization at reaction conditions. Two parallel stainless steel condensers were used to collect liquid samples for quantification analyses. In this way, pressure fluctuations inducing system instability were prevented during sampling. For each point, we let the system to treat at least 40 ml of the liquid feed to make sure that the sample is taken at new condition.

2.2 Sulfidation procedure

A solution of 10 wt% CS_2 in *n*-decane at 0.05 ml/min was used as sulfidation feed under the desired reaction conditions with 100 sccm ultra-high purity hydrogen gas. The sulfidation procedure was optimized to achieve the highest activity in HDS of 1000 ppmw S as DBT at 325 °C and 3 MPa hydrogen pressure. For a typical sulfidation method, the loaded catalyst inside the pressurized reactor is heated up to 170 °C at 8 °C/min under hydrogen flow rate of 100 sccm. Then, CS_2 solution was injected into the reactor at 0.05 ml/min, and then the temperature increased to 400 °C at 5 °C/min and kept at this temperature for 20 h.

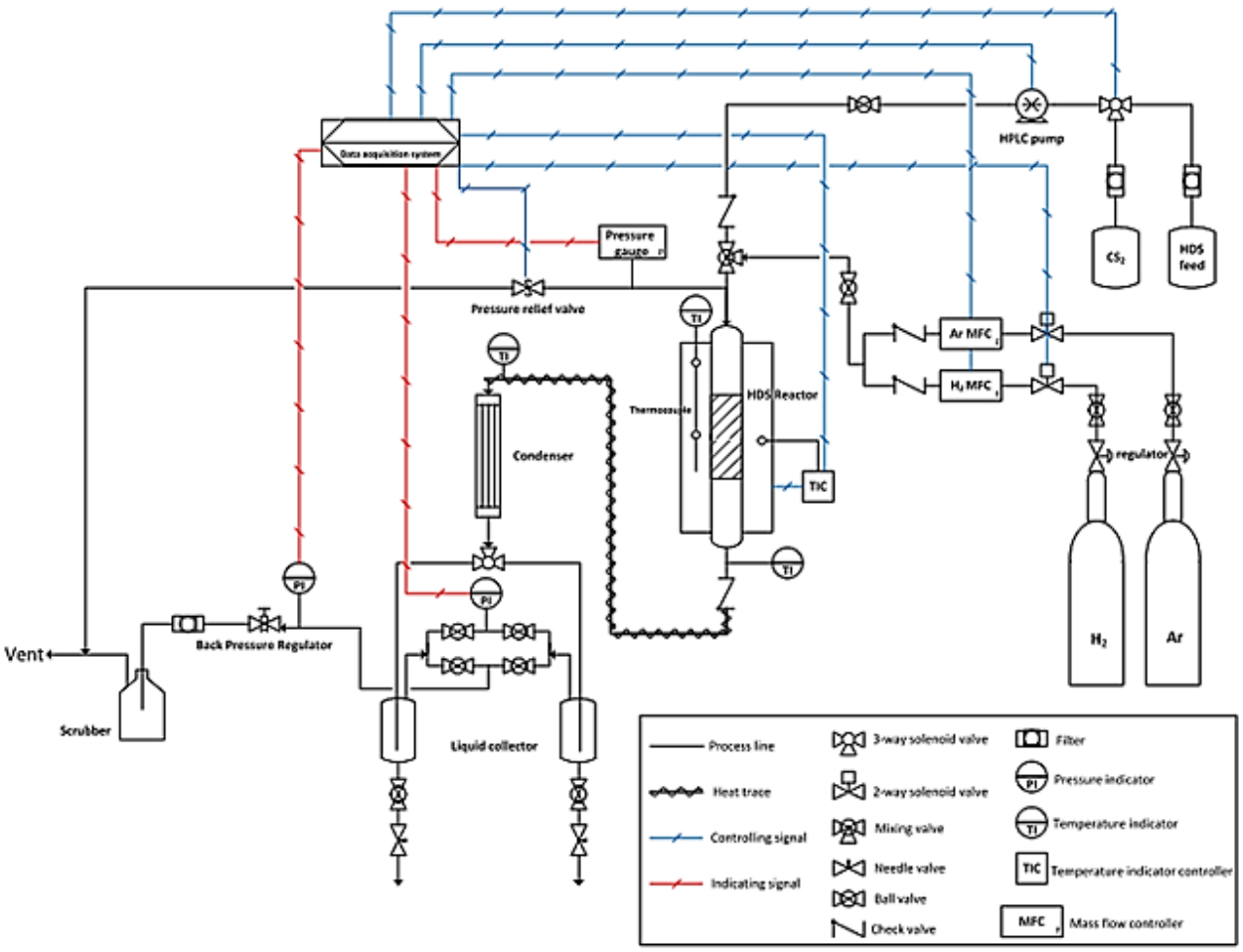

Scheme 2.1. Hydrodesulfurization (HDS) experimental setup.

2.3 Calculations of initial rates and turn over frequency (TOF)

Following equations have beed used to calculate initial rates and TOF.

Rate constant for the first order reaction:

$$k_i = \frac{\mathrm{Ln}\left(\frac{1}{1-X_i}\right) \times F_i \times 1000}{C_i \times m_{cat.}} , \left(\frac{L}{kg_{cat.}\,.\,s}\right) \qquad (2.1)$$

F: molar flow rate , m: mass of catalyst , X: conversion (mol) , C: initial concentration , i: DMDBT or BP

Initial rate:

$$r_i = k_i \times C_i \ , \left(\frac{mol_i}{kg_{cat.} \cdot s}\right) \tag{2.2}$$

TOF$_i$:

$$r'_i = \frac{r_i \times MW_{Pd}}{wt\%_{Pd}} \ , \left(\frac{mol_i}{mol_{Pd} \cdot s}\right) \tag{2.3}$$

$$TOF_{DMDBT} = \frac{r'_{DMDBT} \times mol_{Pd}}{mol_{CO}} \ , \left(\frac{mol_{DMDBT}}{mol_{surf.\ Pd} \cdot s}\right) , \text{mol CO} = \text{mol surf. Pd} \tag{2.4}$$

$$TOF_{BP} = \frac{r'_{BP} \times mol_{Pd}}{mol_{CO}} \ , \left(\frac{mol_{BP}}{mol_{surf.\ Pd} \cdot s}\right) , \text{mol CO=mol surf. Pd} \tag{2.5}$$

TOF$_{DDS}$, TOF$_{HYD}$:

$$Y_{DDS} = \frac{X_{DMDBT} \times F_{DMDBT} \times S_{DMBP}}{mol_{surf.\ Pd}} \ , \left(\frac{mol_{DMBP}}{mol_{surf.\ Pd} \cdot s}\right) \tag{2.6}$$

$*$ S: selectivity (mol %)

$$Y_{HYD} = \frac{X_{DMDBT} \times F_{DMDBT} \times S_{HYD}}{mol_{surf.\ Pd}} \ , \left(\frac{mol_{HYD}}{mol_{surf.\ Pd} \cdot s}\right) \tag{2.7}$$

$$Y_{HCK} = \frac{Y_{HYD}}{2} \ , \left(\frac{mol_{HCK}}{mol_{surf.\ Pd} \cdot s}\right) \tag{2.8}$$

$$TOF_{DDS} = \frac{Y_{DDS} \times TOF_{DMDBT}}{Y_{HYD} + Y_{DDS} + Y_{HCK}} \ , \left(\frac{mol_{DMBP}}{mol_{surf.\ Pd} \cdot s}\right) \tag{2.9}$$

$$TOF_{HYD} = \frac{(Y_{HYD} + Y_{HCK}) \times TOF_{DMDBT}}{Y_{HYD} + Y_{DDS} + Y_{HCK}} \ , \left(\frac{mol_{HYD}}{mol_{surf.\ Pd} \cdot s}\right) \tag{2.10}$$

2.4 Verification of kinetic regime and plug-flow behavior in HDS reaction

Mass and heat transfer limitations play an important role in heterogeneous catalysis. The reaction rate is influenced by diffusion or mass transfer of species (reactants or products) involved in the reactions. The reaction competes with internal diffusion and external mass transfer inside the pore and outer layer of solid catalysts, respectively. To be in the kinetic regime, mass transfer from the bulk to the particle surface and diffusion from the surface to the pore should be very fast as compared to the reaction rate. Table 2.1 shows the equations to verify the absence of diffusion, heat, and mass transfer limitations as well as axial dispersion and wall effects. The calculations were provided for $FeO_x@Pd_{0.2}/Al_2O_3$ catalyst in Chapter 4 of this thesis. The required data are provided in Table 2.2.

Table 2.1. Calculations on the absence of internal and external mass and heat transfer limitations; the required parameters and calculation procedure are listed in Table 2.2.

Phenomenon	**criterion**	**calculated value for the criterion**
external heat transfer limitations[1]	$\Delta T_{film} = \frac{-r_{A(obs)} \times \rho_b \times R \times E_a \times (-\Delta H_{rxn})}{R_g \times h \times T^2} < 0.15$	$2.6 \times 10^{-6} < 0.15$
external mass transfer limitations (Mears criterion)[1]	$\frac{-r_{A(obs)} \times R \times n \times \rho_b}{k_c \times C_{Ab}} < 0.15$	$7.8 \times 10^{-4} < 0.15$
internal mass transfer limitations (Weisz-Prater criterion for the 1st order reaction)[1]	$\frac{-r_{A(obs)} \times R^2 \times \rho_c}{D_e \times C_{As}} < 0.3$	$0.03 < 0.3$
plug-flow behavior (no axial dispersion and wall effects)[2, 3]	$\frac{d_t}{d_p} > 8.0$ $\frac{L_{bed}}{d_p} > 50.0$	$127.0 > 8.0$ $800.0 > 50.0$

Table 2.2. Parameters used to estimate heat and mass transfer limitations for $FeO_x@Pd_{0.2}/Al_2O_3$ catalyst.

Parameter	Definition and Unit	Equation and Value
$k_{i(obs)}$	Observed rate constant @ 623 K and X_{DMDBT} = 35.9 % [L/kg.s]	$k_i = \frac{\mathrm{Ln}\left(\frac{1}{1-X_i}\right) \times F_i}{C_i \times m_{cat.}} = 2.06 \times 10^{-3}$
$-r_{A(obs)}$	Observed reaction rate @ 623 K and X_{DMDBT} = 35.9 % [mol/kg.s]	$-r_{A(obs)} = k_i \times C_i = 3.5 \times 10^{-5}$
$m_{cat.}$	Weight of catalyst [g]	0.18
F_i	DMDBT molar flow rate [mol/s]	1.41×10^{-8}
C_i	Initial concentration of DMDBT [mol/L]	0.017
ρ_c	Catalyst density [kg/m^3]	4000
ϕ	Bed porosity	0.4
ρ_b	Catalyst bed density [kg/m^3]	$\rho_b = (1-\varepsilon) \times \rho_c = 2400$
R	Catalyst particle radius [m]	0.00005
E_a	Activation energy for the 1st order gas phase reaction [kJ/mol]	200 [1]
ΔH_{rxn}	Heat of reaction calculated from the enthalpies of formation of each compounds in Scheme 1 provided in ref. [4], [kJ/mol]	-148.5
Rg	Universal gas constant [J/mol.K]	8.314
T	Reaction temperature [K]	623
d_p	Catalyst particle diameter [m]	0.0001
ρ_g	Density at 623 K and 30 bar [kg/m^3]	1.17
μ	Viscosity at 623 K [kg/m.s]	1.42×10^{-5}
Re	Reynolds number at 623 K for the fluid velocity of 0.022 m/s (in the reactor i.d. 0.5") assuming the bed porosity of 0.4	$\mathrm{Re} = \frac{U \times \rho_g \times d_p}{(1-\phi) \times \mu} = 0.18$
Sh, Nu	Sherwood and Nusselt numbers	2.0
k_{H2}	Thermal conductivity of hydrogen at 623 K, [W/m.K]	0.25

h	Heat transfer coefficient [kW/m^2.K]	$h = \frac{Nu \times k_{H2}}{d_p} = 1.5$
n	Reaction order, HDS of 4,6-DMDBT on Pd-based catalyst is known to follow a pseudo-first-order kinetics[5]	1.0
$C_{Ab} \approx C_{As}$	Bulk DMDBT gas phase concentration considering hydrogen gas [mol/m^3]	0.107
M	DMDBT molecular weight [g/mol]	212.3
D_{AB}	Estimated gas phase DMDBT diffusivity in H_2 at 623 K and 30 bar [m^2/s]; the molar volumes of H_2 and 4,6-DMDBT are 7.07 and 271.76 cm^3/mol, respectively.	$D_{AB} = \frac{10^{-3}\ T^{1.75}\left[\frac{1}{M_A}+\frac{1}{M_B}\right]^{0.5}}{P\left[\left(\sum v_i\right)_A^{1/3}+\left(\sum v_i\right)_B^{1/3}\right]^2} = 2.61 \times 10^{-6}$
k_c	Mass transfer coefficient [m/s]	$k_c = \frac{D_{AB} \times Sh}{d_p} = 0.05$
d_{pore}	Catalyst pore diameter [nm]	5.8
D_k	Knudsen diffusivity [m^2/s]	$D_K = 48.5 \times d_{pore} \times \sqrt{\frac{T}{M}} = 4.8 \times 10^{-7}$
D_{pore}	Diffusivity in a pore [m^2/s]	$D_{pore} = \left(\frac{1}{D_{AB}}+\frac{1}{D_K}\right)^{-1} = 4.1 \times 10^{-7}$
S	BET surface area [m^2/g]	155
ε_p	Particle porosity	$\varepsilon_p = \frac{S \times \rho_c \times d_{Pore}}{4} = 0.9$
τ	Tortuosity	3.9
D_e	Effective diffusivity [m^2/s]	$D_{eff} = \frac{\varepsilon_P \times D_{pore}}{\tau} = 9.5 \times 10^{-8}$
d_t	Reactor diameter [m]	0.0127
L_{bed}	Catalyst bed length [m]	0.08

2.5 Mass spectrometry (GC-MS)

Hydrocracking products identified by GC-MS are shown in Figure 2.1.

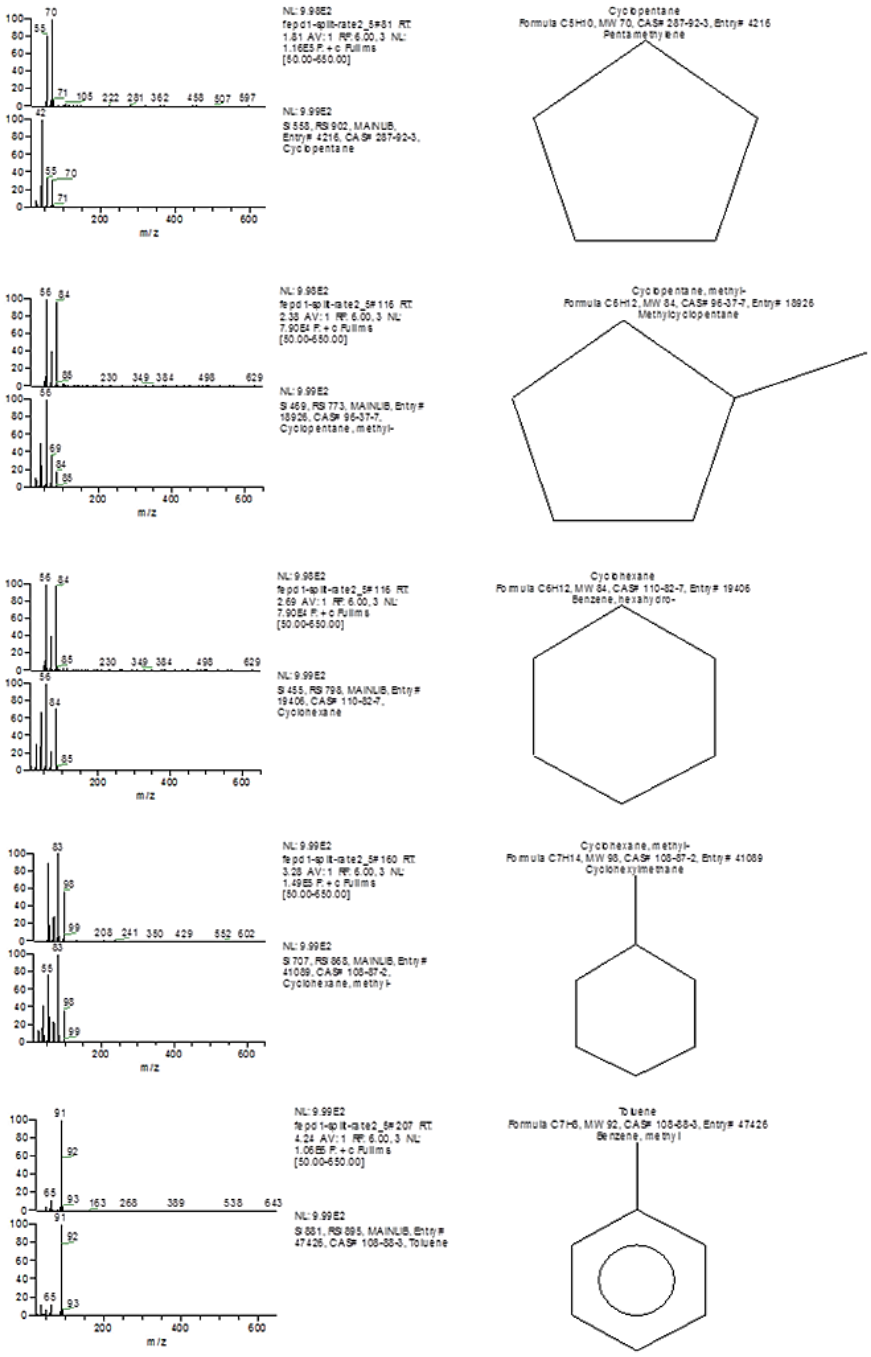

Figure 2.1. Hydrocracked products identified in HDS of 4,6-DMDBT on Pd/Al_2O_3 catalyst.

2.6 References

(1) Fogler, H.S. Elements of chemical reaction engineering, 4th Ed., Prentice Hall, 2005.R.E.

(2) Perez-Ramirez, J.; Berger, R.J.; Mul, G.; Kapteijn, F.; Moulijn, J. A. Catal. Today 2000, 60, 93-109.

(3) Le Page, J.F. Applied heterogeneous catalysis, TechniP, 1987.

(4) Q. Yu, Q.; Zhang, L.; Guo, R.; Sun, J.; Fu, W.; Tang, T.; Tang, T. Fuel Process. Technol. 2017, 159, 76-87.

(5) Niquille-Röthlisberger, A.; Prins, R. J. Catal. 2006, 242, 207–216.

Chapter 3. Enhancement of palladium-catalyzed direct desulfurization by yttrium addition[1]

3.1 Introduction

Tuning product selectivity in complex reactions is of paramount importance in increasing the carbon atom economy through the formation of desired products.[1–3] Selectivity control by operating parameters such as temperature, pressure, and residence time is not always feasible due to equipment, safety and economic limitations. Development of heterogeneous catalysts with desired active sites enables such technologies.[1,4] Increasingly stringent environmental regulations for the sulfur content in fuels pose significant technological challenges for refineries.[5-7] To achieve ultra-deep levels of sulfur in transportation fules (10 ppmw S), the most refractory 4,6-dialkyldibenzothiophenes must be desulfurized[5–8] because they constitute around 20 wt% of total sulfur species in a conventionally pre-desulfurized fuel with 500 ppmw S.[9] The steric hindrance of alkyl groups prevents perpendicular σ-adsorption through sulfur atom for direct sulfur elimination, termed the direct desulfurization (DDS) pathway.[5–7,9–12] However, this hindrance can be reduced by changing the spatial configuration of the molecule through hydrogenation of flat π-adsorbed phenyl rings, known as the hydrogenation (HYD) pathway.[7,11–13] Accordingly, NEBULA catalysts rely on the HYD route, which requires elevated hydrogen pressure.[14,15]
The DDS pathway requires lower operating pressure than the HYD route.[16,17] The aromaticity of desulfurized products via the DDS path is higher[17], giving the possibility of product quality control based on demand. On the other hand, low-pressure operations could accelerate ring opening and cracking of naphthenic compounds, resulting in lower fuel quality and yield. This reveals the challenges to proper design and development of an active catalyst for low-pressure hydrodesulfurization (HDS).

Oyama et al.[17] reported 85% DDS selectivity (at 99% conversion) in HDS of 4,6-dimethyldibenzothiophene (4,6-DMDBT) at 340 °C and 3 MPa over NiFeP/SiO_2 catalyst.

---

[1] Chapter 3 of this thesis has been published as A. Mansouri and N. Semagina, "Enhancement of palladium-catalyzed direct desulfurization by yttrium addition", Applied Catalysis A: General 543 (2017) 43-50. Reprinted with permission from Elsevier Copyright © 2017.

However, the catalyst showed low volumetric activity, implying larger required reactor volume and increased energy consumption as compared to conventional HDS catalysts. Pt-group metals have also shown promising activity in HDS of refractory compounds in pre-desulfurized fuels due to their outstanding hydrogenation and hydrogenolysis properties.[10,11,18–27] Palladium and platinum and their bimetallic PtPd combinations promote the hydrogenation pathway in HDS of 4,6-DMDBT.[10,20,27,28] Pd is known for its high resistance to sulfur poisoning and high activity in HDS of 4,6-DMDBT.[20,23,28] In contrast to iridium, Pd does not significantly catalyze ring opening and cracking at low pressure[25] and thus represents a promising candidate for a low-pressure HDS. Since the DDS pathway proceeds via perpendicular σ–adsorption, the DDS selectivity can be promoted by decreasing the size of the Pd nanoparticles and thus increasing the fraction of low-coordinated active sites[17] (edges and corners of Pd nanoparticles).[21,29] Higher DDS selectivity has been observed over smaller Pt[21], Ru[30], and Pd[31] nanoparticles. However, the thermal instability of smaller nanoparticles is a matter of significant concern[32–35], especially for sintering-prone metals such as palladium[36]. Nanoparticle growth deactivates catalysts and may alter selectivity. A promising strategy for constraining the sintering of metal nanoparticles is to create alloys with sintering-resistant elements such as iridium; however, this is a scarce and expensive metal.[37]

It is desirable to use earth-abundant elements as a textural promoter. Yttrium provides the most thermally stable alloys; for example, Y stabilizes zirconia for high-temperature fuel cell applications.[38] An early study showed that yttrium significantly increased the mechanical stability and hydrogen permeability of Pd-based membranes.[39] In addition, nanostructured Pd-Y alloys prepared by ball-milling exhibited stability against grain growth up to 400 °C.[40] Palladium and yttrium can form various alloy structures at different Pd/Y ratios, from Pd_7Y to PdY_3, according to the Pd-Y phase diagram.[41] The palladium lattice is expanded upon alloying with yttrium due to the larger atomic size of yttrium than palladium[40,42], 1.82 Å vs. 1.37 Å [43], accompanied by a change in the filling and level of the Pd *d*-band.[4,43,44] Although the surface energies of Pd and Y are 2.050 $J \cdot m^{-2}$ and 1.125 $J \cdot m^{-2}$, respectively[45], an ab initio density functional theory (DFT) study showed that Y tends to occupy the inner near-surface layers[43]. Depending on the distribution of Y atoms in the near-surface layers, the *d*-band center positions of surface atoms shift up- or downward.[43] The energy level of the *d*-band is known to affect the

adsorption energies of surface species, leading to the changes in the reaction rates and selectivities.[49-52]

The promising combination of yttrium and transition metals, especially noble metals, has been verified in a variety of catalytic applications, such as partial oxidation of methane[46], CO_2 and autothermal reforming of methane[47,48], oxygen reduction reaction (ORR)[43,49,50], and electrooxidation reaction[43,51]. The enhanced oxygen electroreduction activity and stability of platinum catalyst when alloyed with yttrium was also shown by DFT calculations.[51] The higher ORR and ethanol electrooxidation activity of Pd_3Y alloy relative to monometallic Pd was attributed to the modified electronic structures of Pd by Y.[43] Yttrium was found to increase the surface area and dispersion of Ni_2P.[52] Adding Y to Pd/Al_2O_3 and Ni/Al_2O_3 catalysts for CO_2 and autothermal reforming of CH_4, respectively, enhanced the stability of the catalysts by suppressing particle sintering and coking.[47,48] This behavior was attributed to the formation of an intermediate surface compound between Ni and Y_2O_3.[48] A similar explanation was provided for the enhanced stability of the Pt/Y_2O_3 system in partial oxidation of methane, which was that an intermetallic compound formed between the Pt and the yttria.[46]

PdY catalysts have thus attracted our attention as promising catalysts that could potentially increase the direct desulfurization selectivity in 4,6-DMDBT HDS. The increased sintering resistance as compared to the monometallic Pd should provide a higher fraction of edge and corner Pd atoms and thus facilitate perpendicular 4,6-DMDBT adsorption for direct sulfur removal. The introduction of larger Y atoms into the Pd surface (or near-surface) layer should also alter the chemisorption strength of flat π-adsorbed species in the hydrogenation path. Increased DDS contribution is favorable for the development of low-pressure desulfurization technologies. The reported study herein thus provides an experimental validation of this hypothesis as relates to the hydrodesulfurization of 4,6-DMDBT at 350 °C and 1 MPa hydrogen pressure. As demonstrated below, compared to a monometallic Pd catalyst, the bimetallic PdY nanoparticles that were developed demonstrated enhanced DDS selectivity to the formation of 3,3'-dimethybiphenyl while reducing the hydrogenation and hydrocracking selectivity. A control study conducted with Pd nanoparticles deposited on Y-impregnated Al_2O_3 revealed the crucial importance of the PdY alloy formation to achieve the desired catalytic performance. To the best of our knowledge, this is the first report on the catalytic performance of PdY bimetallic

nanoparticles in an HDS reaction to demonstrate their superior selectivity to direct desulfurization of 4,6-DMDBT.

3.2 Experimental methods

3.2.1 Materials

Palladium (II) chloride solution ($PdCl_2$, 5 wt%), yttrium (III) nitrate hexahydrate ($Y(NO_3)_3 \cdot 6H_2O$), gamma-alumina (γ-Al_2O_3, Mesh size 150, average pore diameter of 58 Å, BET surface area of 155 m^2/g) and polyvinylpyrrolidone (PVP, average molecular weight of 29,000) were purchased from Sigma–Aldrich and used as received to prepare the catalysts. Milli-Q water, ethanol (95 vol.%, Fisher Scientific), and acetone (≥99.7%, Fisher Scientific) were used for synthesis. Ultra-high purity (99.999%) hydrogen, nitrogen, helium, and argon were purchased from Praxair. A diesel model compound containing 720 ppmw sulfur as 4,6-dimethyldibenzothiophene (4,6-DMDBT, $C_{14}H_{12}S$, Sigma-Aldrich) dissolved in *n*-decane (Fischer Scientific) with 3.5 wt% *n*-dodecane (Fischer Scientific) as internal standard was used for the HDS reactions.

3.2.2 Catalyst preparation

Bimetallic palladium-yttrium nanoparticles were prepared using the hydrogen-sacrificial method as reported by X. Liu et al.[50]. This technique for bimetallic nanoparticle synthesis relies on the capability of the core metal to dissociate hydrogen to form metal hydride at a moderate temperature (50-200 $^{\circ}C$), which is capable to reduce the reduction-resistant elements, such as yttrium, to form bimetallic structures.[53,54] In the present modification of the method, first, PVP-stabilized Pd nanoparticles were synthesized in a colloidal dispersion using the alcohol reduction method.[55] 500 µl of Pd precursor was dissolved in 40 ml ethanol and then diluted with 60 ml milli-Q water containing 0.47 g of PVP (PVP-to-metal molar ratio of 30) in a 500-ml three-neck flask. The mixture was then stirred rigorously and refluxed for 1 h under nitrogen, followed by cooling to room temperature. Next, Pd seeds were hydrogenated by purging the colloidal solution with hydrogen gas for 2 h under stirring to create palladium hydride, so that it can

reduce yttrium precursor on the surface of Pd nanoparticles. Then, a mixture of yttrium nitrate hexahydrate in 25 ml ethanol (at variable Pd/Y molar ratios) was added to this solution dropwise over the course of 2 h followed by an additional 2 h stirring under H_2. No precipitation was observed. The synthesized mono- and bimetallic nanoparticles were deposited on γ-Al_2O_3 by mixing the colloidal solution and the support with excess acetone, termed as acetone precipitation method, in which acetone fractionated the PVP-stablized nanoparticles from the aqueos solution on γ-Al_2O_3. As a control catalyst, a Pd_2/Y-Al_2O_3 sample was prepared via incipient wetness impregnation of yttrium precursor on γ-Al_2O_3 followed by calcination at 400 °C to obtain Y-Al_2O_3. Pd nanoparticles prepared by the alcohol reduction method were then precipitated on Y-Al_2O_3 using acetone at a Pd-to-Y molar ratio of 2 to obtain Pd_2/Y-Al_2O_3. All the catalysts were dried at room temperature for 2 h and then at 100 °C overnight with subsequent calcination at 400 °C for 4 h in a static air furnace to remove the organic stabilizer.

3.2.3 Catalyst characterization

Inductively coupled plasma mass spectrometry (ICP-MS) analysis was used to determine the paladium and yttrium contents of synthesied catalysts. Transmission electron microscopy (TEM) images were taken with JEOL JEM2100 operating at 200 kV. The TEM samples were prepared by dispersing the solid sample in ethanol to obtain a clear solution. Next, a few drops of the solution were added to the TEM grid and then dried it at room and then 60 °C for 2 h. Scanning transmission electron microscopy (STEM) coupled with energy dispersive X-ray spectroscopy (EDS) was conducted by a CM20FEG/STEM operated at 200kV. The EDS spectra were obtained by an Oxford EDS detector. Particle size distributions (PSD) were measured by considering 500 particles.

High resolution X-ray photoelectron spectroscopy (XPS) of calcined and spent catalysts (after the HDS reaction for 18 h on stream) was acquired using a Kratos Axis 165 X-ray photoelectron spectrometer using a mono Al Kα source operating at 14 kV and15 mA. The CasaXPS software package was used for data analysis including background subtraction and peak fitting. All the acquired XPS spectra were corrected with C 1s at 284.8 eV.

CO chemisorption analyses were performed using an Autochem II 2920 apparatus (Mircomeritics). About 260 mg of calcined catalyst was reduced at 350 °C under hydrogen for 1

h. The catalysts were then purged with He at the same temperaure for 1 h and then cooled down to room temperature. A 5 mol% CO/He was micropulsed 15 times to measure the amount of adsorbed CO. Temperature-programmed reduction (TPR) was performed using the same device. About 200 mg of the calcined catalysts was degassed by Ar at 200 °C for 2 h. After the catalyst cooled down to room temperature, TPR analysis was performed using 10 ml/min of 10 mol% H_2/Ar at the heating rate of 10 °C/min from room temperature up to 800 °C.

Diffuse-reflectance infrared Fourier-transform spectra of adsorbed carbon monoxide (CO-DRIFTS) were collected using NEXUS 670 FT-IR fitted with a smart diffuse reflectance accessory. For this, the catalysts were prepared with a high palladium loading of 2 wt %. Calcined catalysts were reduced in H_2 at 350 °C for 2 h, then purged with Ar at the same temperature for 30 min and left to cool down to room temperature under Ar. A flow of 3% CO/He at 50 ml/min was passed over the sample for 30 min, and then the system was purged by Ar for 30 min. DRIFT spectra were recorded three times against a KBr standard with 256 scans and a resolution of 4 cm^{-1}. The resolution enhancement and data processing were performed with OMNIC software.

3.2.4 Hydrodesulfurization

HDS of 4,6-DMDBT was performed at 350 °C and 1 MPa H_2 pressure in a fixed-bed continuous flow reactor, as described previously.[37] For each test, about 0.14-0.15 g of Pd/γ-Al_2O_3 and 0.18 g of bimetallic Pd_xY/γ-Al_2O_3 catalysts were diluted with 4 g of silicon carbide(120 mesh) and loaded in a stainless steel reactor (L=22", i.d.=0.5"). The length of the catalyst bed was about 3.5". The wall effects and the effects of axial dispersion were insignificant,[56] and the absence of external and internal mass transfer limitations was verified by Mears and Weisz-Prater criteria, respectively. Because of the low metal loading in the synthesized catalysts, which was also diluted with inert silicon carbide, the heat transfer limitations were assumed to be negligible. Before each HDS reaction, the catalysts were pre-reduced *in situ* with 100 ml/min (STP) H_2 at 350 °C and 1 MPa for 1 h. Next, 4,6-DMDBT (720 ppmw of S) in *n*-decane (with 3.5 wt% *n*-dodecane as internal standard) was fed to the reactor at 0.05 ml/min using a Series II high

pressure pump 350 °C and 1 MPa (at H_2-to-liquid molar ratio of 16). The HDS experiments were performed for 18 h on stream including overnight stabilization.

The reaction products were identified by gas chromatography coupled with mass spectrometry (GC-MS) and quantified off-line by a flame ionization detector (FID) detector based on the amount of internal standard in the feed. According to the reaction mechanism in Scheme 1, selectivity to the direct desulfurization (DDS) path was calculated by the amount of dimethyl biphenyl (DMBP) divided by the amount of converted 4,6-DMDBT. Selectivity to hydrogenation (HYD) is the summation of selectivities to dimethylcyclohexylbenzene (DMCHB), dimethylbicyclohexyl (DMBCH), perhydro-dibenzothiophene (PHDBT), hexahydro-dibenzothiophene (HHDBT) and tetrahydrodibenzothiophene (THDBT). Selectivity to hydrocracking (HCK) is based on the amount of single ring products such as toluene, benzene, cyclohexane, methylcyclopentane, and cyclopentane. The reported conversions are subject to 15% experimental error. Two standard deviations in selectivities are 3%. The carbon mass balance was 97%.

3.3 Results and Discussion

3.3.1 Characterization of catalysts

Table 3.1 summarizes some physicochemical properties of γ-Al_2O_3-supported monometallic Pd, Y, bimetallic PdY_n/Al_2O_3 and Pd/Y-Al_2O_3 catalysts, where "n" is the molar ratio of yttrium to palladium measured by ICP-MS. Figure 3.1 shows TEM images of the colloidal Pd and bimetallic PdY nanoparticles, as well as of the supported catalysts after 18 h on stream in the HDS reaction. The bimetallic nanoparticles in the colloidal dispersion revealed larger particle size implying that yttrium was deposited on the Pd surface as expected in the applied hydrogen-sacrificial method.[50] After calcination at 400 °C and 18-h HDS reaction at 350 °C, the monometallic Pd catalyst sintered to a more significant extent than the PdY samples, which shows that Y addition is beneficial in improving the sintering resistance of Pd. EDS mapping of a spent bimetallic catalyst (Figure 3.2) confirms the spatial association of yttrium and palladium species. XRD data also showed the coexistence of Pd and Y in the samples (Figure S2, Supporting Information). The peaks' intensity reduced in the XRD patterns of PdY NPs, as

compared to the monometallic Pd, correlating with the Y/Pd molar ratio. This suggests that Y addition changed the crystallographic properties of Pd NPs. As seen i the high-resolution TEM images of the spent catalysts (Figure 3.1g-i), the Pd(111) lattice spacing of 0.23 nm in monometallic Pd catalyst increased to 0.25 nm and 0.28 nm in PdY_2/Al_2O_3 and $PdY_{5.5}/Al_2O_3$ catalysts, respectively. These values are different from that of γ-Al_2O_3 (0.35 nm). This systematic change of the lattice spacing of host material (Pd) by adding guest atoms (Y) suggests the interaction between Y and Pd,[4] i.e., the incorporation of yttrium atoms as solute into palladium crystal structure.[44,49] However, Y could not not completely substitute into Pd lattice due to the limited solubility of Y in Pd lattice structure. The lattice mismatch between Pd and Y results in Pd lattice expansion because yttrium atoms are larger than palladium[42], 1.82 Å vs. 1.37 Å, respectively.[43] The expansion of the Pd lattice by alloying with Y was also attributed to the filling of d-states.[44]

Table 3.1. Physicochemical properties of synthesized catalysts.

Catalyst	Pd/Y loading (wt%)[a]	Y/Pd (mol)	CO uptake		Particle size[b] (nm)	
			$\mu mol_{CO}/g_{cat}$	mol_{CO}/mol_{Pd}	colloid	Supported
Al_2O_3	0.00/0.00	0	–	–	-	–
Y-Al_2O_3	0.0/0.68	0	0.3	–	-	–
Pd/Y_2-Al_2O_3	0.41/0.58	2.0	–	–	-	–
Pd/Al_2O_3	0.41/0.00	0	2.0	0.05	1.8	16.3
PdY_2/Al_2O_3	0.35/0.58	2.0	5.7	0.17	3.2	13.7
$PdY_{5.5}/Al_2O_3$	0.38/1.75	5.5	4.0	0.11	3.5	13.2

[a] the metal loadings were determined by ICP and were found to be the same as used in the synthetic procedure within 7% error; [b] measured by counting 500 nanoparticles from TEM images of colloidal dispersions and supported catalysts after 18 h on stream in the HDS.

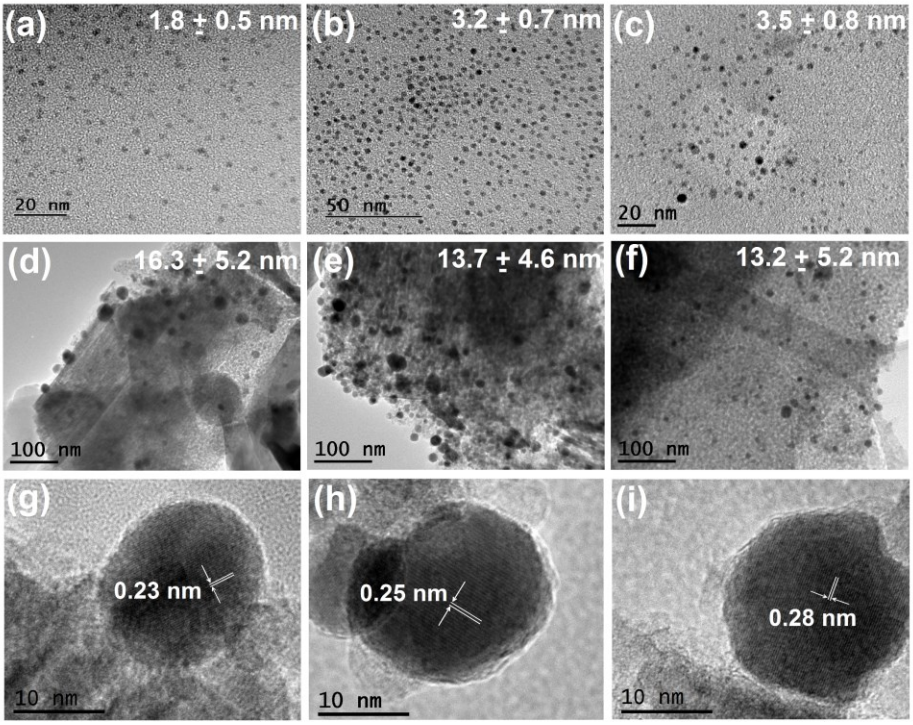

Figure 3.1. Bright-field TEM and HRTEM images of colloidal Pd (a), PdY_2 (b) and $PdY_{5.5}$ (c) nanoparticles, as well as supported catalysts after 18 h on stream in the HDS reaction: Pd/Al_2O_3 (d, g), PdY_2/Al_2O_3 (e, h), and $PdY_{5.5}/Al_2O_3$ (f, i). Multiple fringes in different particles were measured for d-spacing. The corresponding size distribution histograms can be found in the Supplementary Material.

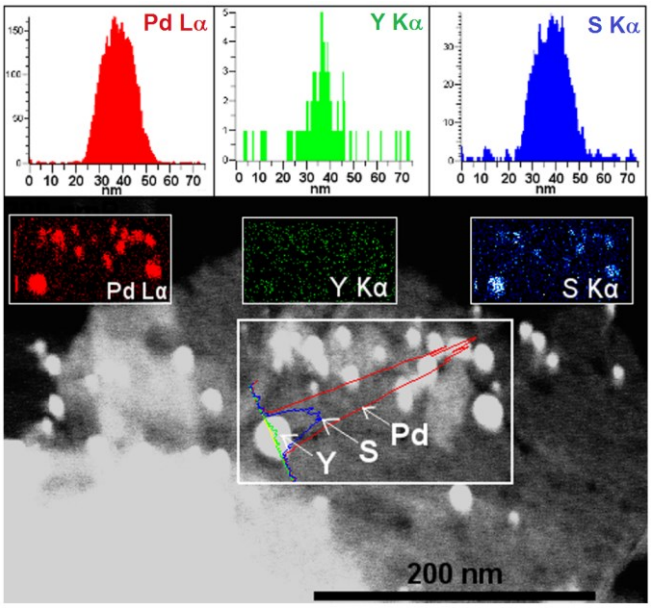

Figure 3.2. STEM-EDS mapping and line scan signals of spent $PdY_{5.5}/Al_2O_3$ catalyst.

Figure 3.3 shows experimental and deconvoluted XPS spectra of spent catalysts after 18 h on stream in the HDS reaction at 350 °C. Binding energies (BE), surface atomic ratios Y/Pd and Pd^{2+}/Pd^{0} are presented in Table 3.2. The BEs of Pd 3d doublet at 335.1 and 340.4 eV (Figure 3.3) were assigned to Pd(0), and those at 336.6 eV and 342.1 eV were attributed to Pd(II).[57–59] Yttrium was found in the oxidized state in the Y 3d spectra, where the BEs maximize at 158.07 and 160.05 eV, which differ from those of metallic yttrium (156.0 and 158.5 eV).[50,43] The broader characteristic peaks of Pd 3d core levels of bimetallic samples, in which full width at half maximum increased from 1.8 eV (Pd/Al_2O_3) to 2.4 eV (PdY/Al_2O_3), can be attributed to the presence of Pd species with a different chemical environment.[60] The contribution of oxidized surface Pd in PdY samples also increased (Table 3.2), which is in line with the lower particle size of PdY nanoparticles as observed by TEM (Table 3.1, Figure 3.1). Compared to the Pd/Al_2O_3 catalyst, the Pd 3d doublet in bimetallic PdY catalysts shifted toward the higher BEs that correlate with yttrium content (Table 3.2). In the bimetallic samples, Y 3d spectra exhibited a negative shift in BEs with respect to Y_2O_3/Al_2O_3, indicating partial reduction of yttrium species on the surface of Pd seeds in agreement with TPR profiles. The Y/Pd surface atomic ratio in both samples is higher than the bulk composition as expected by the applied synthetic method.

Table 3.2. Binding energy values of Pd 3d and Y 3d in spent catalysts. Quantification was done by the ratio of Y to Pd doublets and deconvoluted peaks corresponding to Pd^{2+} and Pd^{0}.

Catalyst	Binding energy (eV)				Y/Pd atomic ratio	Pd^{2+}/Pd^{0} atomic ratio
	Pd $3d_{5/2}$	Pd $3d_{3/2}$	Y $3d_{5/2}$	Y $3d_{3/2}$		
Pd/Al_2O_3	335.09	340.36	–	–	-	22
PdY_2/Al_2O_3	335.13	340.40	157.58	159.63	3.5	30
$PdY_{5.5}/Al_2O_3$	335.25	340.52	157.58	159.63	7.4	30
Y_2O_3/Al_2O_3	–	–	158.29	160.37		–

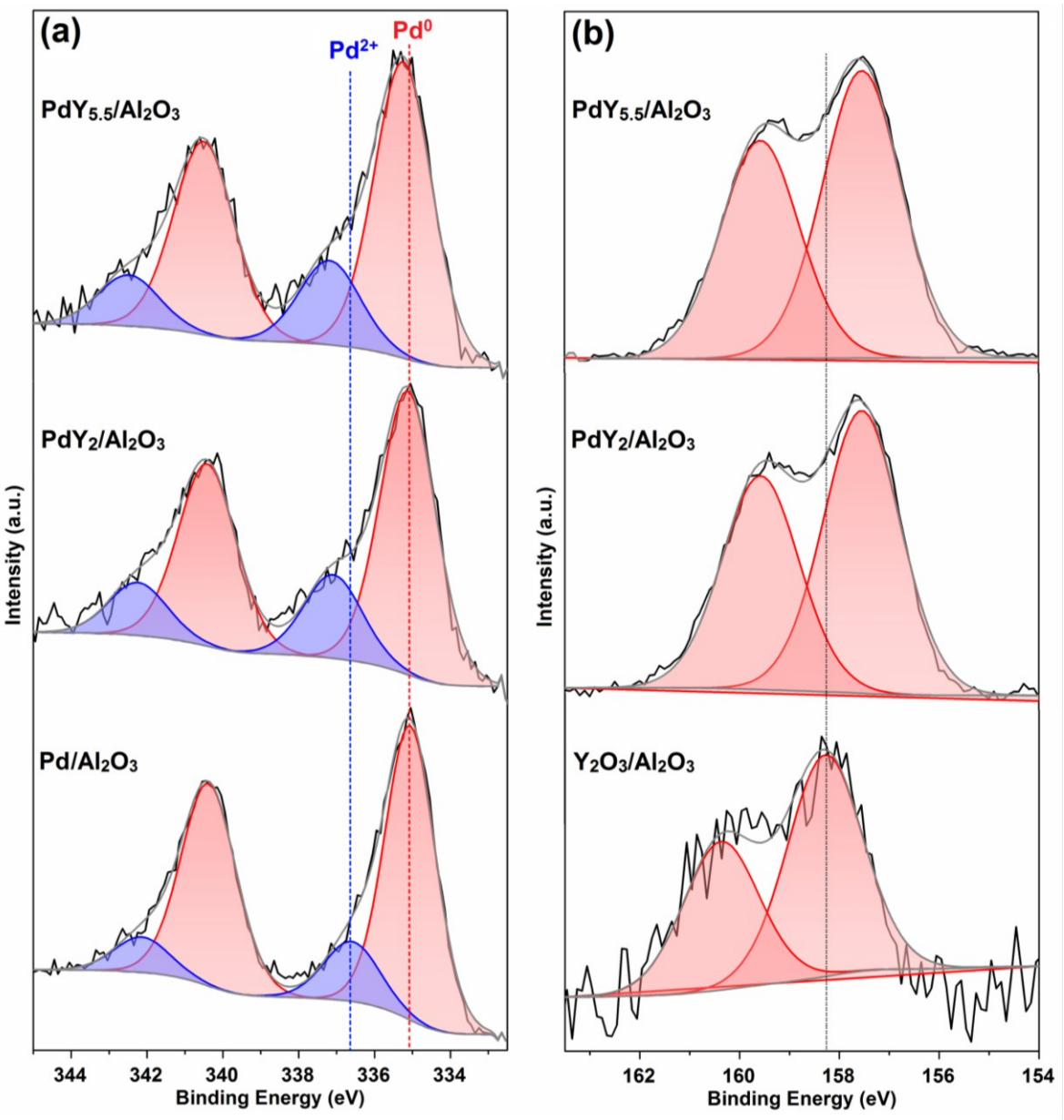

Figure 3.3. XPS spectra; Pd 3d (a) and Y 3d (b) of HDS spent catalysts.

TPR profiles of the calcined catalysts are shown in Figure 3.4. Monometallic Y_2O_3/Al_2O_3 catalyst exhibited a reduction peak at 508 °C, similarly to the reported values.[46,47] PdO reduction in the monometallic Pd/Al_2O_3 in a relatively high temperature region (340 °C) has been previously assigned to Pd species strongly interacting with the alumina support.[68-70] The impregnation of alumina with yttrium, followed by calcination and Pd nanoparticle deposition (sample Pd/Y_2-Al_2O_3 catalyst) resulted in the peak disappearance. The origin of Pd species and

alumina properties are known to affect significantly the temperature and even existence of such a peak reflecting strong metal-support interactions.[68-70] For the bimetallic PdY_2/Al_2O_3 sample, the peak corresponding to yttria shifted to a lower temperature by 100 °C and merged with the PdO reduction peak, suggesting the formation of a bimetallic structure such as $Pd_xY_yO_z$ as reported previously.[61]

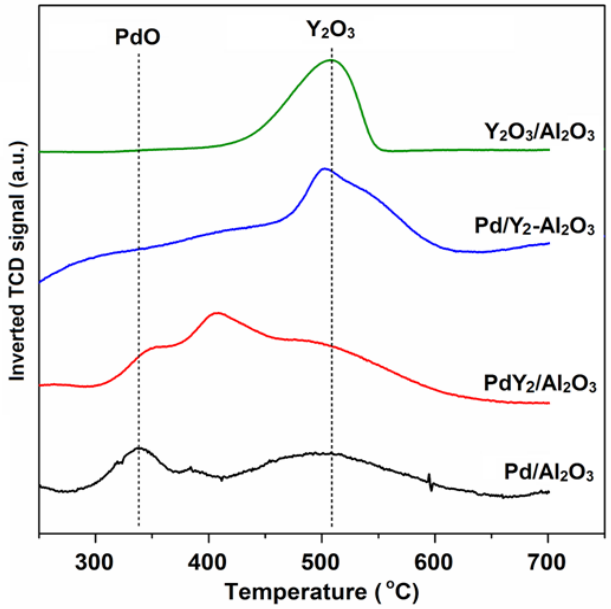

Figure 3.4. TPR profiles of calcined supported catalysts. The inverted TCD signal reveals hydrogen consumption.

CO chemisorption performed on the reduced samples showed that the Pd-Y catalysts adsorbed 2 to 3 times higher CO amounts (Table 3.1), which did not correlate with an incremental increase in dispersion, as observed from TEM (Figure 3.1). The Y/Al_2O_3 sample prepared by impregnation of yttrium precursor on γ-Al_2O_3 adsorbed a negligible amount of CO because yttria (Y_2O_3) does not have affinity toward CO molecules,[62] but CO can chemisorb on metallic yttrium [63]. According to the XPS and TPR data, Pd does promote partial reduction of yttrium oxide. Therefore, the higher CO uptakes of bimetallic structures can be attributed to the adsorption of CO molecules on reduced Y present on the bimetallic nanoparticle surface as well as a higher Pd dispersion.

CO-DRIFTS analysis confirms that the presence of Y affects the adsorption sites on a Pd nanoparticle surface (Figure 3.5). The gas-phase CO band occurs at 2143 cm^{-1}, while the adsorbed CO may display linear (2000−2130 cm^{-1}), bridged (1800−2015 cm^{-1}), and 3-fold hollow (1915 and 1923 cm^{-1}) adsorption modes.[64–68] The linear (2130 cm^{-1}) and bridged (ca. 2015 cm^{-1}) modes are present in all the samples (Figure 3.5), but the addition of Y to Pd significantly increased the contribution of the bridged adsorption mode and also developed a weak shoulder at around 1915 cm^{-1} that was associated with the 3-fold adsorption. Alternatively, the "bridged" peak in the PdY species could refer to the linear adsorption of CO on reduced Y species, which could explain the doubled CO chemisorption on the bimetallic samples (Table 3.1). Thus, the characterization results indicate that the addition of Y to Pd using the applied hydrogen-sacrificial technique led to the deposition of reduced Y atoms on the Pd nanoparticle surface, which resulted in improved thermal stability and modified surface electronic properties.

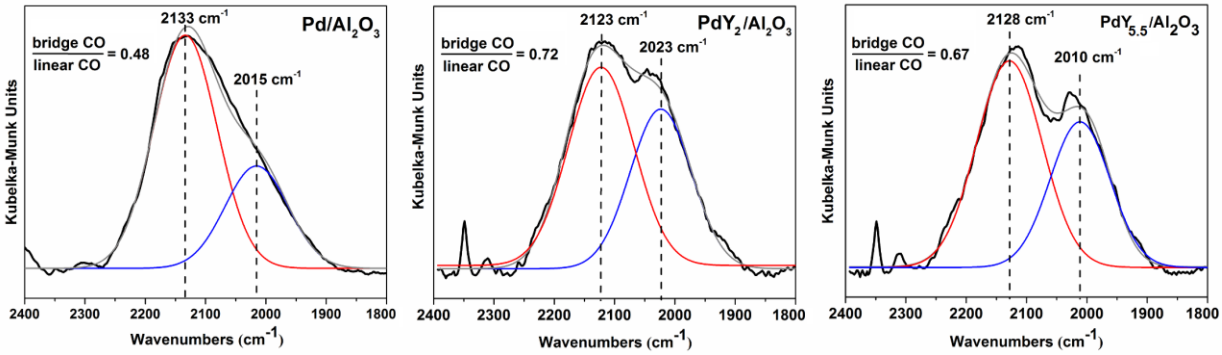

Figure 3.5. CO-DRIFT spectra for reduced catalysts.

3.3.2 Catalytic performance

The catalytic performance of the synthesized catalysts was evaluated in HDS of 4,6-DMDBT. The amounts of catalysts in the reactor were adjusted to achieve comparable 4,6-DMDBT conversions for a fair selectivity comparison. The products were grouped as the products of direct desulfurization (DDS), hydrogenation (HYD) and hydrocracking (HCK), the latter of which included 5- and- 6-membered sulfur-free compounds (Scheme 3.1). Note that the formation of yttrium sulfide is thermodynamically unfavorable at the reaction temperature.[69]

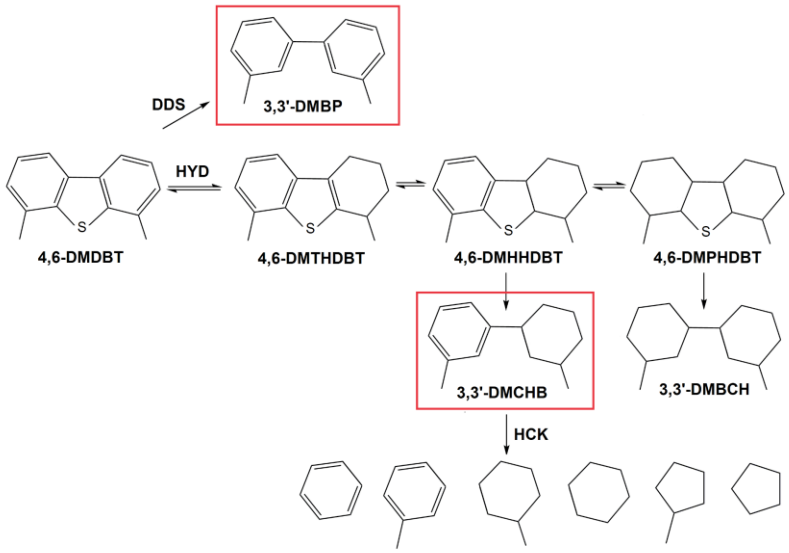

Scheme 3.1. Reaction mechanism of HDS of 4,6-DMDBT [22,70].

Table 3.3 and Table 3.4 list the activities and selectivities of the synthesized catalysts determined after 18 h on stream (the steady state was achieved after 2 hours on stream). Intrinsic rates were calculated using the initial DMDBT concentration and rate constants calculated from conversions assuming a first-order reaction.[22] As seen from the obtained rates, deposition of Y on the Pd nanoparticle surface did not decrease the 4,6-DMDBT conversion, but it affected the product distribution. The presence of Y almost doubled the selectivity ratio of direct desulfurization to hydrogenation products by increasing the selectivity to 3,3-DMBP from 71% to 84% and decreasing the hydrogenation selectivity from 24% to 15%. In the hydrogenation path, the major product for all the catalysts was desulfurized partially hydrogenated 3,3'-dimethylcyclohexylbenzene (DMCHB). Since its content was reduced with the addition of Y, the PdY catalysts also exhibited lower hydrocracking selectivity (2% vs. 5% for the monometallic Pd). In contrast, the Pd/Y_2-Al_2O_3 catalyst, prepared by deposition of monometallic Pd nanoparticles on a binary (Table 3.3 and Table 3.4), which is likely due to the modified metal-support interactions observed from the TPR (Figure 3.4). This finding shows the importance of the applied synthetic method and requirement of reduced Y deposition on Pd for enhanced catalytic performance in HDS. The presence of Y on the Pd surface thus affects the ratio of adsorption modes of 4,6-DMDBT: perpendicular adsorption via S atoms is required for direct desulfurization, and flat adsorption leads to the hydrogenation products.[7,9–11] First of all, Y

increases the sintering resistance of Pd nanoparticles and provides a higher fraction of edge atoms, which are known to benefit DDS selectivity.[21,30,31] In addition, Y atoms were shown in a previous work to stabilize in the second layer from the Pd surface, increasing the Pd interatomic distances in the surface layer and also affecting the Pd *d*-band and reactant's chemisorption strength.[43] In the case of 4,6-DMDBT, these effects lead to the enhanced direct desulfurization. The Pd-Y catalysts thus represent a promising candidate for low-pressure desulfurization occurring with the same overall HDS rate but lower hydrogen consumption and suppressed cracking as compared to the Pd-only catalyst.

Table 3.3. Catalytic performance in HDS of 4,6-DMDBT at 350 °C and 1 MPa at 18 h on stream.

Catalyst[a]	Mass of catalyst (g)	DMDBT X(%)	Rate ($mmol_{DMDBT}/mol_{Pd}/s$)		Selectivity (mol%)			DDS/ HYD	S-free (mol%)
			Integral	Intrinsic	DDS	HYD	HCK		
Pd/Al_2O_3	0.15	34	0.86	1.1	71	24	5	2.9	97
PdY_2/Al_2O_3	0.18	35	0.82	1.0	84	15	1	5.4	98
$PdY_{5.5}/Al_2O_3$	0.18	37	0.81	1.0	80	17	3	4.7	98
Pd/Y_2-Al_2O_3	0.18	9	0.2	–	34	28	38	0.5	81

[a] Al_2O_3 and Y_2-Al_2O_3 showed no activity.

Table 3.4. Individual product selectivities (mol%) for the catalysts in Table 3.3.

Catalyst[a]	DMBP	Main HYD		HCK[b]				Other HYD		
		BCH	CHB	CP	MCP	CH	BZ	PHDBT	HHDBT	THDBT
Pd/Al_2O_3	70.5	1.2	20.0	3.4	0.5	0.5	0.4	<0.1	0.5	3.0
PdY_2/Al_2O_3	83.5	0.1	13.2	1.0	<0.1	<0.1	<0.1	<0.1	<0.1	2.2
$PdY_{5.5}/Al_2O_3$	80.0	0.4	15.0	1.8	0.7	<0.1	<0.1	<0.1	<0.1	1.8
Pd/Y_2-Al_2O_3	34.1	5.6	3.2	16.1	2.5	13.0	6.0	2.4	6.7	10.4

[a] refer to Scheme 3.1 for the full product abbreviation.

[b] selectivities to methylcyclohexane and toluene were below 0.1-0.3.

3.4 Conclusions

- Bimetallic PdY/Al_2O_3 catalysts were developed via the colloidal synthesis method. Yttrium species were reduced on the surface of Pd nanoparticles via reduction by Pd hydride.
- Yttrium improved the thermal stability of Pd nanoparticles against sintering and also altered the surface chemistry, which was revealed by boosted CO chemisorption and modified CO adsorption mode and strength.
- The supported bimetallic nanoparticles were evaluated in hydrodesulfurization of 4,6-dimethydibenzothiophene at 350 $^{\circ}$C and 1 MPa. Yttrium addition did not alter the overall hydrodesulfurization rate but increased direct desulfurization selectivity from 71% to 84% and suppressed cracking twice as much as the monometallic Pd catalyst.
- The study demonstrates that PdY structures can be a promising candidate for low-pressure hydrodesulfurization of refractory sulfur compounds.

Acknowledgements

Financial support from NSERC Discovery grant (RGPIN 371888-09) is appreciated. We gratefully thank Dr. Dimitre Karpusov for XPS, Dr. Anqiang He for STEM-EDS, and Dr. Jing Shen for CO-DRIFT data acquisition (all from U of A).

3.5 Supporting Information

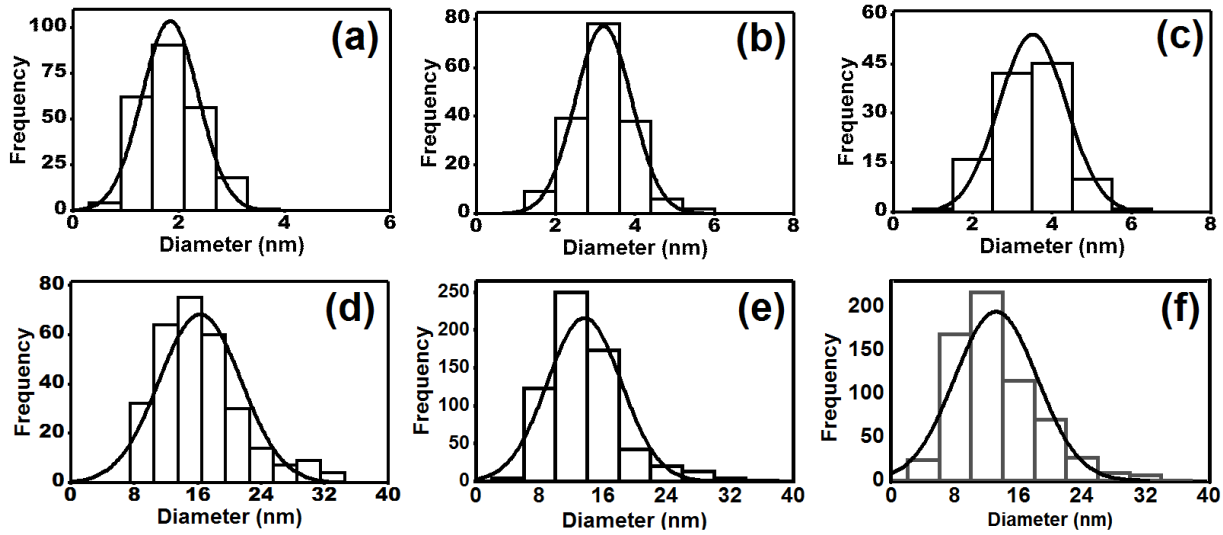

Fig. S1. Size distribution histograms obtained from TEM analyses of colloidal Pd (a), PdY_2 (b) and $PdY_{5.5}$ (c) nanoparticles, as well as supported catalysts after 18 h on stream in the HDS reaction: Pd/Al_2O_3 (d), PdY_2/Al_2O_3 (e), and $PdY_{5.5}/Al_2O_3$ (f). The corresponding TEM images can be found in the main text in Fig. 3.1.

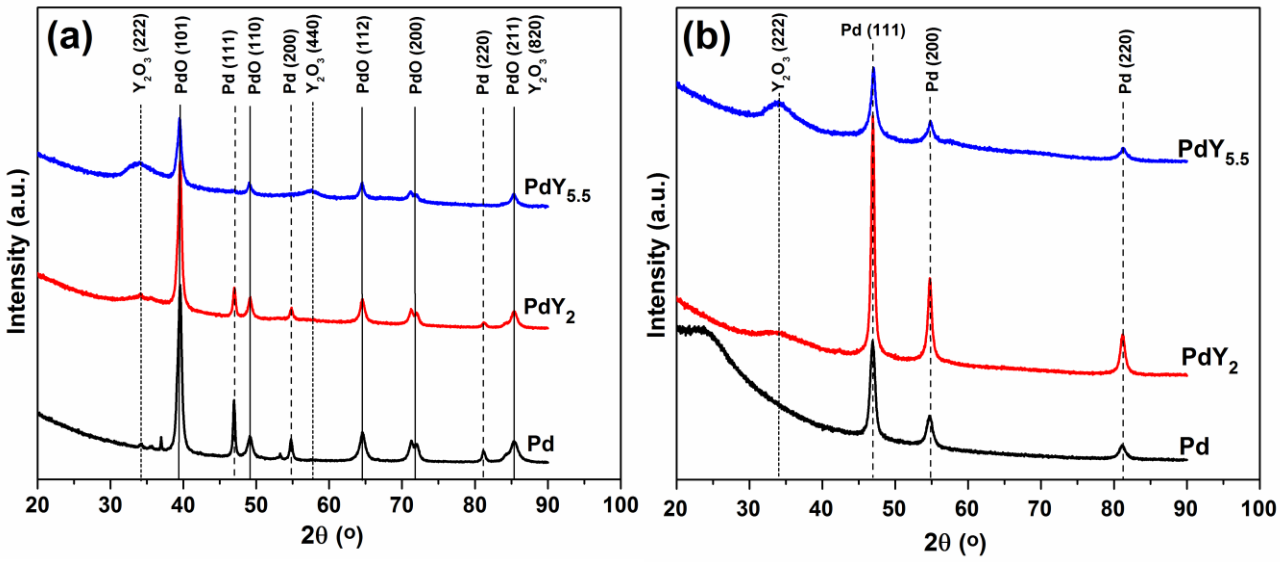

Fig. S2. XRD of unsupported nanoparticles after calcination at 400 C (a) and reduction at 350 °C (b). Peaks assignment based on the powder diffraction file numbers of 97-018-0870 for metallic palladium, 00-006-0515 for PdO, and 97-001-6394 for yttrium oxide.

3.6 References

(1) Gross, E.; Liu, J. H.-C.; Toste, F. D.; Somorjai, G. a. Nat. Chem. 2012, 4, 947–952.

(2) Lee, I.; Delbecq, F.; Morales, R.; Albiter, M. a; Zaera, F. Nat. Mater. 2009, 8, 132–138.

(3) Chen, G.; Xu, C.; Huang, X.; Ye, J.; Gu, L.; Li, G.; Tang, Z.; Wu, B.; Yang, H.; Zhao, Z.; Zhou, Z.; Fu, G.; Zheng, N. Nat. Mater. 2016, 15, 564–569.

(4) Wu, J.; Li, P.; Pan, Y.-T. F.; Warren, S.; Yin, X.; Yang, H. Chem. Soc. Rev. 2012, 41, 8066–8074.

(5) Yang, R. T.; Hernández-Maldonado, A. J.; Yang, F. H. Science 2003, 301, 79–81.

(6) Shafi, R.; Hutchings, G. J. Catal. Today 2000, 59, 423–442.

(7) Babich, I. V.; Moulijn, J. A. Fuel 2003, 82, 607–631.

(8) Stanislaus, A.; Marafi, A.; Rana, M. S. Catal. Today 2010, 153, 1–68.

(9) Song, C.; Ma, X. Appl. Catal. B, Environ. 2003, 41, 207–238.

(10) Sun, Y.; Prins, R. Angew. Chemie - Int. Ed. 2008, 47, 8478–8481.

(11) Prins, R.; Egorova, M.; Niquille-Röthlisberger, A.; Zhao, Y.; Sivasankar, N.; Kukula, P. Catal. Today 2006, 111, 84–93.

(12) Ma, X.; Sakanishi, K.; Mochida, I. Ind. Eng. Chem. Res. 1996, 2487–2494.

(13) Ma, X.; Sakanishi, K.; Isoda, T.; Mochida, I. Energy & Fuels 1995, 9, 33–37.

(14) Plantenga, F. L.; Cerfontain, R.; Eijsbouts, S.; van Houtert, F.; Anderson, G. H.; Miseo, S.; Soled, S.; Riley, K.; Fujita, K.; Inoue, Y. Stud. Surf. Sci. Catal. 2003, 145, 407–410.

(15) Eijsbouts, S.; Plantenga, F.; Leliveld, B.; Inoue, Y.; Fujita, K. ACS Div. Fuel Chem. Prepr. 2003, 48, 494–495.

(16) Alsolami, B.; Carneiro, J. T.; Moulijn, J. A.; Makkee, M. Fuel 2011, 90, 3021–3027.

(17) Oyama, S. T.; Zhao, H.; Freund, H. J.; Asakura, K.; Włodarczyk, R.; Sierka, M. J. Catal. 2012, 285, 1–5.

(18) Hermann, N.; Brorson, M.; Topsøe, H. Catal. Letters 2000, 65, 169–174.

(19) Niquille-Röthlisberger, A.; Prins, R. Catal. Today 2007, 123, 198–207.

(20) Ishihara, A.; Dumeignil, F.; Lee, J.; Mitsuhashi, K.; Qian, E. W.; Kabe, T. Appl. Catal. A, Gen. 2005, 289, 163–173.

(21) Wang, H.; Iglesia, E. ChemCatChem 2011, 3, 1166–1175.

(22) Niquille-Röthlisberger, A.; Prins, R. J. Catal. 2006, 242, 207–216.

(23) Kabe, T.; Qian, W.; Hirai, Y.; Li, L.; Ishihara, A. J. Catal. 2000, 190, 191–198.

(24) Navarro, R.; Pawelec, B.; Fierro, J. L. G.; Vasudevan, P. T.; Cambra, J. F.; Arias, P. L. Appl. Catal. A, Gen. 1996, 137, 269–286.

(25) Ziaei-Azad, H.; Yin, C. X.; Shen, J.; Hu, Y.; Karpuzov, D.; Semagina, N. J. Catal. 2013, 300, 113–124.

(26) Reinhoudt, H. R.; Troost, R.; Van Schalkwijk, S.; Van Langeveld, A. D.; Sie, S. T.; Van Veen, J. A. R.; Moulijn, J. A. Fuel Process. Technol. 1999, 61, 117–131.

(27) Vít, Z.; Gulková, D.; Kaluža, L.; Kupčík, J. Appl. Catal. B, Environ. 2015, 179, 44–53.

(28) Niquille-Röthlisberger, A.; Prins, R. J. Catal. 2005, 235, 229–240.

(29) Zhu, W.; Michalsky, R.; Metin, Ö.; Lv, H.; Guo, S.; Wright, C. J.; Sun, X.; Peterson, A. a; Sun, S. J. Am. Chem. Soc. 2013, 135, 16833–16836.

(30) Wang, H.; Iglesia, E. J. Catal. 2010, 273, 245–256.

(31) Shen, J.; Semagina, N. ChemCatChem 2016, 8, 2565–2571.

(32) Hansen, T. W.; Delariva, A. T.; Challa, S. R.; Datye, A. K. Acc. Chem. Res. 2012, 46, 1720–1730.

(33) Campbell, C. T. Acc. Chem. Res. 2013, 46, 1712–1719.

(34) An, K.; Zhang, Q.; Alayoglu, S.; Musselwhite, N.; Shin, J. Y.; Somorjai, G. A. Nano Lett. 2014, 14, 4907–4912.

(35) Joo, S. H.; Park, J. Y.; Tsung, C. K.; Yamada, Y.; Yang, P.; Somorjai, G. A. Nat. Mater. 2009, 8, 126–131.

(36) Weissmiiller, J.; Loffler, J.; Martin, K. NanoStruetured Mater. 1995, 6, 105–114.

(37) Ziaei-Azad, H.; Semagina, N. Appl. Catal. B, Environ. 2016, 191, 138–146.

(38) Courtin, E.; Boy, P.; Rouhet, C.; Bianchi, L.; Bruneton, E.; Poirot, N.; Laberty-Robert, C.; Sanchez, C. Chem. Mater. 2012, 24, 4540–4548.

(39) Fort, D.; Farr, J. P. G.; Harris, I. R. J. Less-Common Met. 1975, 39, 293–308.

(40) Bryden, K. J.; Ying, J. Y. Acta Mater. 1996, 44, 3847–3854.

(41) ASM Handbook, Volume 3: Alloy Phase Diagrams; 2004.

(42) Doyle, B. M. L.; Harris, I. R. Platin. Met. Rev. 1988, 32, 130–140.

(43) Seo, M. H.; Choi, S. M.; Seo, J. K.; Noh, S. H.; Kim, W. B.; Han, B. Appl. Catal. B, Environ. 2013, 129, 163–171.

(44) Harris, I. R.; M. Norman. J. Less-Common Met. 1970, 22, 127–130.

(45) Vitos, L.; Ruban, A. V.; Skriver, H. L.; Kollár, J. Surf. Sci. 1998, 41, 186–202.

(46) Passos, F. B.; Oliveira, E. R.; Mattos, L. V.; Noronhe, F. B. Catal. Letters 2006, 110, 261–267.

(47) Shi, C.; Zhang, P. Appl. Catal. B, Environ. 2012, 115–116, 190–200.

(48) Santos, D. C. R. M.; Madeira, L.; Passos, F. B. Catal. Today 2010, 149, 401–406.

(49) Jeon, M. K.; McGinn, P. J. J. Power Sources 2011, 196, 1127–1131.

(50) Liu, X.; Yu, E. H.; Scott, K. Appl. Catal. B, Environ. 2015, 162, 593–601.

(51) Greeley, J.; Stephens, I. E. L.; Bondarenko, S.; Johansson, T. P.; Hansen, H.; Jaramillo, T. F.; Rossmeisl, J.; Chorkendorff, I.; Nørskov, J. K. Nat. Chem. 2009, 1, 552–556.

(52) Song, H.; Xu, X. W.; Song, H. L.; Jiang, N.; Zhang, F. Y. Catal. Commun. 2015, 63, 52–55.

(53) Wang, Y.; Toshima, N. J. Phys. Chem. B 1997, 101, 5301–5306.

(54) Ziaei-Azad, H. Bimetallic Ir-based Catalysts for Ring Opening and Hydrodesulfurization Reactions, University of Alberta, Edmonton, Canada, PhD thesis, 2014.

(55) Teranishi, T.; Miyake, M. Chem. Mater. 1998, 10, 594–600.

(56) Pérez-Ramírez, J.; Berger, R. J.; Mul, G.; Kapteijn, F.; Moulijn, J. A. Catal. Today 2000, 60, 93–109.

(57) Guo, X.; Brault, P.; Zhi, G.; Caillard, A.; Jin, G.; Guo, X. J. Phys. Chem. C 2011, 115, 24164–24171.

(58) Niemantsverdriet, J. W.; van Kaam, J. A. C.; Flipse, C. F. J.; van der Kraan, A. M. J. Catal. 1985, 96, 58–71.

(59) Pillo, T.; Zimmermann, R.; Steiner, P.; Hüfner, S. J. Phys. Condens. Matter 1999, 9, 3987–3999.

(60) Otto, K.; Haack, L. P.; deVries, J. E. Appl. Catal. B, Environ. 1992, 1, 1–12.

(61) Oemar, U.; Hidajat, K.; Kawi, S. Int. J. Hydrogen Energy 2015, 40, 12227–12238.

(62) Köck, E.-M.; Kogler, M.; Bielz, T.; Klötzer, B.; Penner, S. J. Phys. Chem. C 2013, 117 (34), 17666–17673.

(63) Zhao, W.; Li, X.; Shao, X.; Xu, B.; Yao, J. Eur. Phys. J. D 2013, 67, 1–8.

(64) Scheffler, M. Surf. Sci. 1979, 81, 562–570.

(65) Shen, J.; Semagina, N. ACS Catal. 2014, 4, 268–279.

(66) Zeinalipour-Yazdi, C. D.; Willock, D. J.; Thomas, L.; Wilson, K.; Lee, A. F. Surf. Sci. 2016, 646, 210–220.

(67) George, C.; Genovese, A.; Casu, A.; Prato, M.; Povia, M.; Manna, L.; Montanari, T. Nano Lett. 2013, 13, 752–757.

(68) Lear, T.; Marshall, R.; Lopez-Sanchez, J. A.; Jackson, S. D.; Klapötke, T. M.; Bäumer, M.; Rupprechter, G.; Freund, H. J.; Lennon, D. J. Chem. Phys. 2005, 123.

(69) Wagman, D. D.; Evans, W. H.; Parker, V. B.; Schumm, R. H.; Halow, I.; Bailey, S. M.; Churney, K. L.; Nuttall, R. L. Journal of Physical and Chemical Reference Data. 1982, 1, 407.

(70) Richard, F.; Boita, T.; Pérot, G. Appl. Catal. A, Gen. 2007, 320, 69–79.

Chapter 4. Palladium islands on iron oxide nanoparticles for hydrodesulfurization catalysis

4.1 Introduction

Platinum group-based heterogeneous catalysts are known for their outstanding catalytic properties among other transition metals, but they occur at very low levels of abundance in the earth crust. Since catalytic activity depends on the surface fraction of metal nanoparticle atoms,[1,2] enhancing the utilization of the noble metal atoms has been a scientific and technological matter of paramount importance.[1,3,4] Vast efforts have been invested to increase the number of surface active atoms by downsizing nanoparticles (NPs) to subnanometers and single atoms,[1,5–13] introducing high-index crystallographic planes,[14–17] and structuring active metal as small particles (dumbbell-like)[18,19] or thin shell (core-shell)[3,20–22] over individual nanoparticles. The core-shell architecture is highly desirable due to the possibility of tailoring structural and chemical properties of multiple components at atomic levels within individual NPs.[3,21–27]

The surface availability of precious metals for catalysis can be remarkably increased by decorating them on low-cost non-noble metal cores.[3,4,28] Iron (Fe), as one of the utmost earth-abundant and environmentally benign elements, is a promising candidate for a core in core-shell structures[21,29–32] that can also facilitate recovery of spent catalysts via magnetic separation.[21,33,34] The combinations of Fe with Pt-group metals have shown a superior performance in a variety of catalytic applications such as electrooxidation catalysis,[17,19,38] oxygen reduction reaction,[18,29–31,39] CO oxidation,[1,40] hydrodechlorination,[41] methane combustion,[32] and non-syngas-route methanol production.[42] Even a mixture of Pd and iron oxide NPs exhibited higher activity than Pd NPs in the hydrogenation of alkyne alcohols.[34] The promising combination of iron with either platinum or palladium has encouraged researchers to develop different hetero-configurations such as iron-oxide-supported Pd,[42,43] dumbbells,[18,19] urchin-like NPs,[44] Pt single atoms on FeO_x,[1,8] and cluster-in-cluster Pt-Fe_xO_y NPs[45] besides their alloys[35,36,39,46] and in different controlled shapes.[47] The exceptional reactivity of core-shell NPs was ascribed to the modification of electronic properties and the lattice strain of active metal atoms.[28,31,48] The electronic defects of reducible metal oxides provide anchoring sites for active metals,[49,50] where the degrees of their interactions control dispersion, morphology, and metal reactivity.[49] For example, Pt shell that formed on

lattice-defect-rich amorphous Fe NPs showed better catalytic performance than crystalline Fe NPs,[21] and in another study, the strong metal-support interactions stabilized more reactive Pt single atoms over iron oxide support.[1] The electronic impacts of core on the shell properties are limited to the first few layers and decline with layer thickness,[48] whereas the lattice strain effects resulting from the mismatch remain for thicker layers[28,48] with the possibility of being tuned by altering the structural properties of core NPs.[31] The lattice strain affects the *d*-band structure and hence the catalytic activity of heterostructured NPs by modifying the adsorption energy of reactants.[28] However, by increasing the layer thickness above a critical value, the overgrown layer dislocates to recover the strain-free prime-crystal structure, which can also change the morphology of NPs.[51] This explanation elucidates the fact that the activity of core-shell structures is essentially maximized at a threshold shell thickness, which in some cases is hardly adjustable and/or stable under reaction conditions, especially for metals such as Pd that have a high tendency to thermal sintering. For instance, a core-shell structure of Fe@Pd has changed into FePd alloy after catalytic combustion of methane over 530 °C.[32] A previous work by Hu et al.[4] showed the increased electrocatalytic activity of segregated Pd islands in bimetallic palladium-tungsten NPs suggesting the lack of necessity of a complete shell configuration for enhanced catalysis.

Herein, we report the design of bimetallic FeO_x@Pd nanoparticles in which palladium atoms forming nanosized islands on the surface of iron oxide nanoparticles as core using colloidal chemistry techniques followed by annealing for a high-temperature catalytic application. The synthesis uses a galvanic reaction of Pd^{2+} reduction by Fe^0 and/or Fe^{2+} on preformed iron oxide seeds, which was shown earlier to produce small Pd nanoparticles attached to FeO_x[52] or FeO_x likely decorated with Pd(0) ultra-small clusters undetectable by standard imaging techniques.[53] The developed configuration allowed for the improved palladium dispersion compared to the monometallic Pd catalysts and modified catalytic properties. The catalytic performance was evaluated in hydrodesulfurization of 4,6-dimethyldibenzothiophene (HDS of 4,6-DMDBT, Scheme 1) and sulfur-free hydrogenation of biphenyl. HDS of 4,6-DMDBT is a model reaction in the production of fuels with ultra-low sulfur level for either transportation or fuel cell applications.[54–60] When sulfur content in fuels has been pre-reduced to 500 ppm, 20 wt% of all sulfur species belong to 4,6-dialkyldibenzothiophenes.[61–65] Their desulfurization is hindered by the steric constrains from the alkyl groups, which can be lessened by partial preliminary

hydrogenation of the aromatic rings (hydrogenation path in Scheme 1). Pt-group metals are highly efficient hydrogenation catalysts; that is why they attract considerable attention as potential catalysts for a second-stage ultra-deep desulfurization of fuels.[61,66,67] However, their low sulfur tolerance and high price impede their commercialization. In the current work, the target was to improve Pd dispersion by decorating Pd atoms on the low-cost iron oxide core, which at the same time may serve as a promoter to improve Pd sulfur tolerance since the affinity of sulfur to Fe is higher than to Pd (Gibbs free energy of formation of FeS_2, FeS and PdS at 600 K is -180, -119 and -78 kJ/mol_{metal},[68] respectively). The Pd-Fe system is especially suitable for high-temperature applications requiring palladium because of the lower Pd surface energy and higher atomic diameter as compared to Fe, which causes large surface segregation of Pd and similar total surface-based activities of Pd and Pd-Fe systems in hydrogenations.[69] To the best of our knowledge, this is the first report to produce Pd islands on FeO_x nanoparticles for low-sulfur hydrodesulfurization catalysis. The synthesized materials can also be recommended for a variety of reactions catalyzed by Pt-group metals, where the efficiency of costly and scarce active metal is paramount.

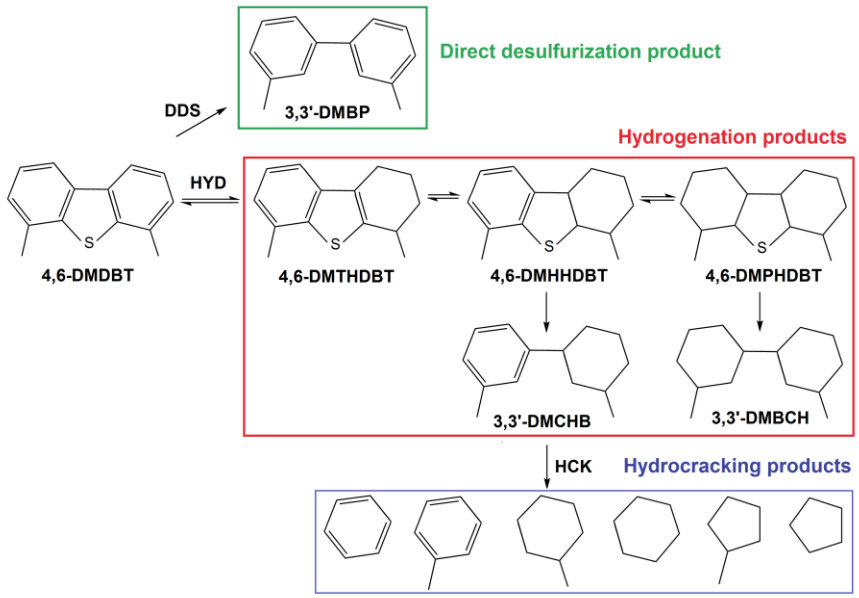

Scheme 4.1. Pathways of 4,6-DMDBT hydrodesulfurization, modified from ref. [67] for the formation of HCK products.

4.2 Experimental

4.2.1 Materials

Palladium (II) chloride solution ($PdCl_2$, 5 wt%), iron (III) chloride hexahydrate ($FeCl_3 \cdot 6H_2O$), polyvinylpyrrolidone (PVP, average molecular weight of 29,000), sodium borohydrate ($NaBH_4$), gamma-alumina (γ-Al_2O_3, 150 mesh, average pore diameter of 58 Å, BET=155 m^2/g), and Fe_2O_3 (<5 μm), all from Sigma–Aldrich were used for the catalyst preparation. Ethanol (95 vol.%, Fisher Scientific), Milli-Q water, ethylene glycol (≥99.7%, Fisher Scientific), and acetone (≥99.7%, Fisher Scientific) were used as received. 720 ppmw sulfur as 4,6-dimethyldibenzothiophene (4,6-DMDBT, $C_{14}H_{12}S$, Sigma-Aldrich) was dissolved in *n*-decane (Fisher Scientific) as a solvent containing 3.5 wt% *n*-dodecane (Fisher Scientific) as the internal standard and was used as a model fuel for HDS reactions. For biphenyl hydrogenation reaction, 400 ppmw of biphenyl was dissolved in *n*-decane as solvent with 3.5 wt% *n*-dodecane as internal standard. Ultra-high purity (99.999%) argon and hydrogen gases were purchased from Praxair.

4.2.2 Catalyst synthesis

Monometallic palladium and bimetallic iron-palladium nanoparticles ($FeO_x@Pd_n$, iron oxide as a core) were synthesized as colloidal dispersions in the presence of PVP as a stabilizer followed by deposition on γ-Al_2O_3 by acetone precipitation. An alcohol reduction method with some modifications was used for the synthesis of Pd nanoparticles.[70] 500 μl of the Pd precursor solution with 0.47 g of PVP (PVP-to-Pd molar ratio of 30) were dissolved in 40 ml ethanol. The mixture was diluted with 60 ml Milli-Q water in a 500-ml three-neck flask and was stirred rigorously at room temperature while purging with ultra-high purity nitrogen gas. After obtaining a transparent solution, the temperature of mixture was then increased to its boiling temperature, was refluxed for 1 h, and was then cooled down to room temperature.

For the synthesis of bimetallic $FeO_x@Pd_n$ catalysts, 0.14 mmol of iron(III) chloride hexahydrate was dissolved in 100 ml of ethylene glycol containing 0.47 g PVP. The mixture was stirred rigorously for 30 min at room temperature in a 500-ml three-neck flask while purging with ultra-high purity nitrogen. After obtaining a transparent yellowish solution, the temperature was gently increased to 140 °C while purging with nitrogen. Excess amount of sodium borohydrate was

added to the solution, changing the color to black first and then dark-green. The mixture was then refluxed for 2 h while purging with nitrogen. After cooling down to room tempeature, hydrogen was flown for 2 hours followed by drop-wise addition of palladium chloride in ethylene glycol (40 ml) within 1 h. The system was then purged with hydrogen for an additional 2 h. No precipitation was observed at the end of the synthesis procedure, and the obtained colloids were clear and macroscopically homogeneous. All the synthesized nanoparticles were precipitated on dried γ-Al_2O_3 using acetone. For comparison, monometallic Pd nanoparticles were prepared with the same alcohol reduction method in the presence of PVP and were deposited on commercial Fe_2O_3 (<5 μm). All the synthesized catalysts were dried at room temperature for 2 h and then 100 °C overnight with subsequent calcination at 400 °C for 4 h to remove the polymer stabilizer. The synthesis repeatability was verified for the most representative $FeO_x@Pd_{0.2}/Al_2O_3$ and $FeO_x@Pd_{0.6}/Al_2O_3$ catalysts, with identical characterization results for two different batches of each.

4.2.3 Catalyst characterization

The palladium and iron content of the calcined catalysts were determined using neutron activation analysis NAA (Becquerel Laboratories – Maxxam Company, Ontario, Canada). Gamma-ray spectrometer with a high resolution coaxial germanium detector was used to irradiate the samples. Transmission electron microscopy (TEM) images were recorded using a JEOL JEM2100 device operating at 200 kV. Scanning transmission electron microscopy (STEM) coupled with energy dispersive X-ray spectroscopy (EDS) was performed using a field emission JEOL 2010F Transmission Electron Microscope operating at 200 kV. Particle size distributions (PDS) were measured by counting 200 particles.

Powder X-ray diffraction (XRD) patterns of unsupported synthesized nanoparticles were recorded using Rigaku Ultima IV diffractometer equipped with a D/Tex detector, an Fe Filter, and Co Kα radiation (λ = 1.78899 Å). The synthesized nanoparticles were first washed with Milli-Q water and were then dried at 60 °C in air before XRD measurements. The diffraction patterns were collected over 5° to 90° on continuous scan at 2 degrees 2θ per minute with a step size of 0.02°. Data interpretation was done using JADE 9.6 with the 2014 ICDD and 2015 ICSD databases.

X-ray photoelectron spectroscopy (XPS) of the calcined and spent catalysts (after the HDS reaction for 18 h on stream) was performed using Kratos Axis 165 X-ray photoelectron spectrometer using Mono Al Kα source operating at 14 kV and15 mA. Background subtraction and peaks fitting were performed using CasaXPS software package. All the XPS core–level spectra were corrected with C 1s at 284.8 eV.

CO chemisorption analyses were carried out using a Micromeritics Autochem II 2920 apparatus equipped with a TCD detector. About 300 mg of calcined catalysts were reduced by hydrogen at the temperatures used for HDS reactions (270 - 350 °C) for 1 h. The catalysts were then purged with helium at the same temperature for 1 h. After cooling down to room temperature, 5 mol% CO in He was micropulsed to measure the amount of CO uptake. Temperature-programmed reduction (TPR) was performed using the same device. About 100 mg of the calcined catalysts were degassed by Ar at 200 °C for 2 h. After cooling down to room temperature, TPR analysis was performed using a 10 ml/min of 10 mol% H_2/Ar at the heating rate of 10 °C/min from room temperature up to 800 °C.

4.2.4 Catalytic experiments

Hydrodesulfurization of 4,6-dimethyldibenzothiophene (4,6-DMDBT) was studied under 3 MPa hydrogen pressure using a continuous-flow fixed bed reactor, as described in detail previously.[60] The calcined catalysts were diluted with silicon carbide (mesh 120, 22:1 weight ratio) and were then loaded in a stainless steel reactor (L=22”, i.d.=0.5”). The absence of external and internal mass transfer limitations were verified by Mears and Weisz-Prater criterion, respectively. The wall effects and effects of axial dispersion were found to be negligible.[71] The heat transfer limitations were assumed to be negligible because of the low loading of metals in the catalysts and the dilution with inert silicon carbide. The catalysts were reduced *in situ* for 1 h before the HDS reaction using 100 ml/min hydrogen at the catalytic reaction temperature (270 - 350 °C) and operating pressure of 3 MPa. A model liquid fuel containing 720 ppmw sulfur as 4,6-DMDBT with 3.5 wt% *n*-dodecane as the internal standard in *n*-decane (as solvent) was then introduced into the reactor at 0.05 ml/min downward continuous flow using a Series II high pressure pump. Before feeding to the reactor, the liquid feed was mixed with 100 ml/min

hydrogen gas to reach the hydrogen-to-liquid molar ratio of 16. All the HDS experiments were performed for 18 h on-stream including overnight catalyst stablization to reach steady-state indicated by a maximum of 5% deviation in the conversions at 2 and 18 h on stream. Hydrogenation of biphenyl was carried out at sulfur-free conditions at 350 °C and 3MPa hydrogen pressure for 18 h on stream.

Indentification of the reaction products was carried out off-line by a gas chromatography coupled with mass spectrometry (GC-MS) using a Thermo Scientific Trace GC Ultra, equipped with a Thermo Scientific TR-5 column (30m, 0.25mm, 0.25um, μm film thickness). The quantitative analyses of 4,6-DMDBT and all of the reaction products were performed using a calibrated Agilent 7890A gas chromatograph equipped with a H-PONA Agilent capillary column (50 m, 0.25 mm, 0.25 μm film thickness) with high purity helium as the carrier gas and a flame ionization detector. The injector and detector temperatures were maintained at 300 °C. The oven temperature was held at 40 °C for 2 min, and then ramped up to 300 °C at 10 °C/min, and it remained at this temperature for 20 min. According to the reaction mechanism in Scheme 1, the selectivity to the direct desulfurization (DDS) path was calculated based on the amount of dimethyl biphenyl (DM-BP) divided by the amount of converted 4,6-DMDBT. Selectivity to hydrogenation (HYD) path is the summation of selectivities to dimethylcyclohexylbenzene (DM-CHB), dimethylbicyclohexyl (DM-BCH), perhydro-dibenzothiophene (PH-DBT), hexahydro-dibenzothiophene (HH-DBT), and tetrahydrodibenzothiophene (TH-DBT). Hydrocracking selectivity (HCK) includes single-ring products such as benzene, toluene, cyclohexane, cyclopentane and methylcyclopentane. The product amounts were identified with the aid of the internal standard in the feed. The reported conversions are subject to 15% experimental error. Two standard deviations in selectivities are 3%. The carbon mass balance was above 95%.

4.3 Results and Discussion

4.3.1 Catalysts characterization

Table 4.1 illustrates the physicochemical characteristics of monometallic Pd, Fe, and bimetallic $FeO_x@Pd_n$ catalysts, where n is the molar ratio of Pd to Fe measured by neutron activation analysis (NAA). The bimetallic $FeO_x@Pd_n/Al_2O_3$ structures exhibited higher CO uptakes than

those of monometallic Pd catalysts, which also increase with the decreasing Pd concentration in the catalyst. The CO uptake of $Pd_{0.2}/Fe_2O_3$ catalyst, prepared by deposition of Pd NPs on commercial Fe_2O_3, was significantly lower than that of the synthesized $FeO_x@Pd_{0.2}/Al_2O_3$ catalyst. These results reveal the greater dispersion of Pd species in bimetallic $FeO_x@Pd_n/Al_2O_3$ catalysts, which could not be achieved using commercial Fe_2O_3 with the particle size <5 μm.

Table 4.1. Physicochemical properties of synthesized catalysts.

Catalyst	Pd/Fe loading[a] (wt%)	CO uptake[b]		Pd lattice parameter[d] (Å)
		$\mu mol_{CO}/g_{cat}$	mol_{CO}/mol_{Pd}	
Pd/Al_2O_3	0.410/0.0	2.03	0.053	3.893
$FeO_x@Pd_{1.5}/Al_2O_3$	0.410/0.160	5.92	0.153	–
$FeO_x@Pd_{0.6}/Al_2O_3$	0.180/0.160	3.02	0.179	3. 885
$FeO_x@Pd_{0.2}/Al_2O_3$	0.060/0.160	3.43	0.608	3.826
$FeO_x@Pd_{0.05}/Al_2O_3$	0.012/0.160	0.60	0.532	–
$Pd_{0.2}/Fe_2O_3$	0.060/65.7	1.34[c]	0.150	–
FeO_x/Al_2O_3	0.0/0.160	0.097	–	–

[a] measured by NAA

[b] CO uptakes for the catalysts reduced at 270 °C and 350 °C were found identical, most likely due to the higher precalcination temperature of 400 °C

[c] CO uptake of commercial Fe_2O_3 is 0.44 $\mu mol_{CO}/g_{cat}$

[d] calculated from the Pd(111) peak position on the XRD profiles of as-prepared unsupported nanoparticles

Figure 4.1a-c show the TEM images of the colloidal FeO_x, unsupported and supported $FeO_x@Pd$ nanoparticles. The image of the colloidal $FeO_x@Pd$ in Figure 4.1b shows preferential association of ca. 2 nm Pd nanoparticles to FeO_x particles of ca. 12 nm size. Remarkably, after the calcination at 400 °C and an 18-h catalytic HDS reaction at 350 °C, no agglomerates were observed for the supported $FeO_x@Pd_{0.6}$ catalyst (Figure 4.1c), while the FeO_x-free Pd/Al_2O_3 catalyst exhibited sintered Pd nanoparticles up to 30 nm in size (refer to the TEM images in the Supporting Information). EDS mapping (Figure 4.2) confirmed the spatial association of Pd and Fe. Thus, the colloidal FeO_x serves as a high-surface area support for the Pd species, which

prevents their sintering as opposed to Al_2O_3 and commercial Fe_2O_3 supports and explains the observed CO uptakes (Table 4.1). High-resolution TEM images of FeO_x@Pd/Al_2O_3 catalysts, taken after the catalytic reaction, show different modes of Pd-Fe association (Figure 4.1d-f). The fringes on grey areas of 0.24–0.26 nm belong to magnetite[34,72] and the fringe of 0.35 nm to alumina[40]. XRD revealed that FeO_x was present as a mixture of magnetite and hematite (Fig. S2 in the Supporting Information). Monometallic Pd nanoparticles exhibited lattice spacing of 0.23 nm, which is characteristic of Pd(111) planes (Fig. S1 in the Supporting Information). Figure 4.1d-f for the bimetallic samples demonstrate that Pd partially covers the FeO_x surface forming islands. In the bimetallic samples, the black Pd-containing areas exhibit fringes with spacing of 0.20–0.23 nm. The decreased spacings are characteristic of Pd alloyed with Fe.[32,36,37] The lattice parameter decrease for the FeO_x@Pd samples, as compared to the monometallic Pd, was also evidenced by XRD (Table 4.1). The Pd(111) XRD peak for the FeO_x@Pd structures became broader and shifted to higher angles as compared to the monometallic Pd nanoparticles (Fig. S2 in the Supporting Information), thereby confirming the smaller nanoparticle size for the bimetallic samples and the Pd lattice compression due to the alloying with Fe.[36,37] The lattice compression of Pd in the FeO_x@$Pd_{0.2}$ sample was greater than FeO_x@$Pd_{0.6}$ suggesting that more Pd atoms were involved in the interaction with Fe probably by formation of thinner Pd layers. This finding is in line with CO chemisorption uptakes (Table 4.1): 61% of all Pd species are located in the outermost shell in FeO_x@$Pd_{0.2}$ sample vs. 18% for FeO_x@$Pd_{0.6}$ and only 5% for the monometallic Pd. It is known[51] that when the shell layer thickness increases above a critical value, the overgrown layer recovers the strain-free prime-crystal structure. Thus, the shell metal dispersion is maximized at a threshold shell thickness. The highest dispersion in this work was found for Pd/Fe molar ratio of 0.2 as compared to 0.05, 0.6, 1.5 and pure Pd (Table 4.1).

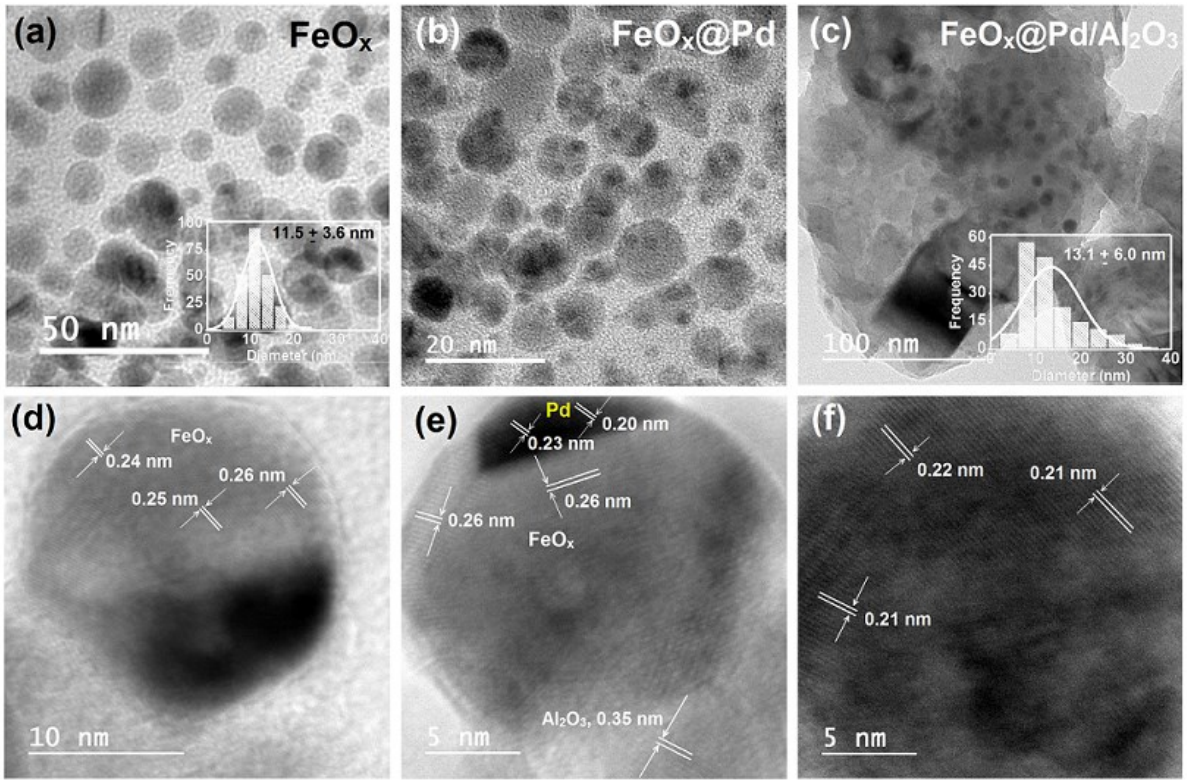

Figure 4.1. Electron microscopy images of fresh colloidal FeO_x (a) and FeO_x@Pd nanoparticles (b) and spent $FeO_x@Pd_{0.6}/\gamma\text{-}Al_2O_3$ after HDS reactions at 350 ^oC (c-f).

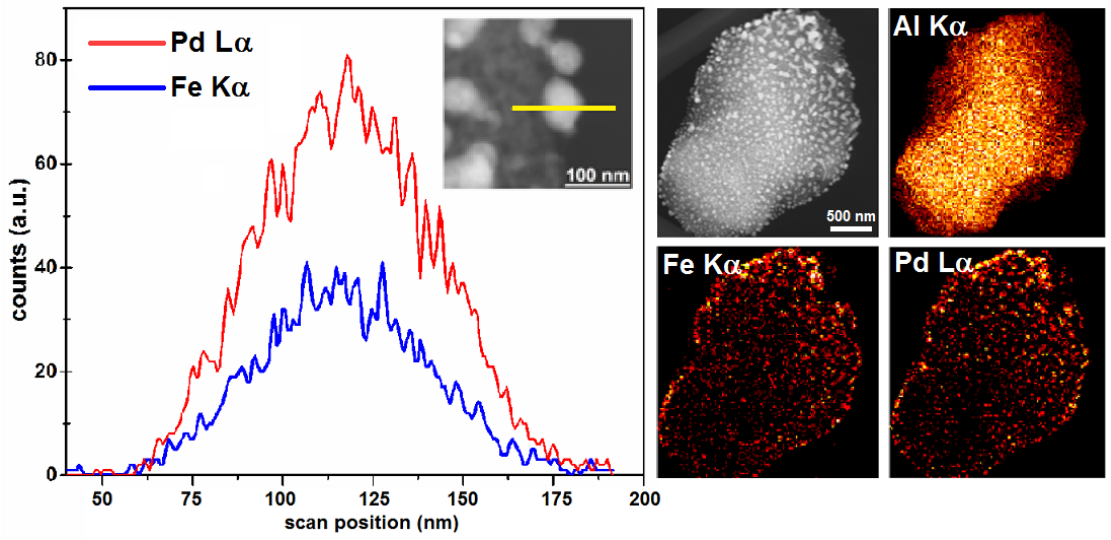

Figure 4.2. STEM-EDS mapping of spent $FeO_x@Pd_{0.6}/Al_2O_3$.

XPS analyses were performed on the fresh catalysts after calcination in air and on the spent catalysts (after calcination, reduction, and HDS reaction at 350 ^{o}C) (Figure 4.3 and Table 4.2). As expected, oxidized Pd was found in the calcined catalysts, and mostly reduced Pd was found in the spent catalysts. Typically, if Pd dispersion increases, such as in the case of the bimetallic catalysts in the presented work, a decrease in Pd(0) contribution and an increase in oxidized surface Pd should be expected. This was not the case for the spent FeO_x@Pd catalysts as a result of the galvanic exchange reaction between FeO_x and Pd^{2+}, which maintains palladium in the reduced form. Similar Pd(0) species were found by XPS in an earlier reported FeO_x@Pd system with highly dispersed Pd.[53] In both reduced and calcined states, binding energies for Pd species shifted to higher values for FeO_x@Pd as compared to monometallic Pd catalysts. Similar Pd BE shifts to the higher values were observed for PdFe systems by Wang et al. and were explained by the electron transfer from Fe to Pd and modification of Pd *d*-band.[36] This suggests the change in the electronic properties of Pd in the presence of Fe.[42] Iron sulfides were not expected to be formed because the HDS reaction was conducted at a $p(H_2S)/p(H_2)$ ratio of 10^{-4}, while metallic Fe is thermodynamically stable at the ratio below 10^{-3} at 600 K.[68] Indeed, $2p_{3/2}$ peaks of iron sulfides at BE of 706-710 eV were not observed in the spent samples.

In the fresh monometallic FeO_x catalyst, the shape of the Fe 2p core level with the Fe $2p_{3/2}$ centroid at 710.6 eV accompanied by a shake-up satellite peak at 719.7 eV is a typical feature of Fe_2O_3.[74,75] Compared to the spectra of calcined samples, the Fe 2p peaks shifted slightly toward higher BEs in spent catalysts, i.e., from 710.6 to 711.7 eV as a characteristic BE of Fe^{3+} in Fe_2O_3 and Fe_3O_4, respectviely.[75] These small changes and the depletion in the intensity of Fe^{3+} shake-up satellite peaks in the spent samples suggest that a limited reduction of Fe_2O_3 to Fe_3O_4 might occur during reduction pretreatment and HDS reaction. Although the XPS spectra are noisy for any distinctive conclusions to be drawn, the facilitated iron oxide reduction in the presence of Pd is also evident from the TPR of the calcined materials. The 500 $^{\circ}$C peak in the TPR of Fe/Al_2O_3, corresponding to hematite reduction, shifted to lower temperatures for FeO_x@Pd/Al_2O_3 samples (Figure 4.4). The TPR profiles also illustrate Pd-Fe interaction in the synthesized FeO_x@Pd/Al_2O_3 bimetallic catalysts. The palladium reduction peak at 330 $^{\circ}$C for Pd/Al_2O_3 and Pd/Fe_2O_3 samples was not observed (or shifted to lower temperatures) for the FeO_x@Pd_n/Al_2O_3 materials.

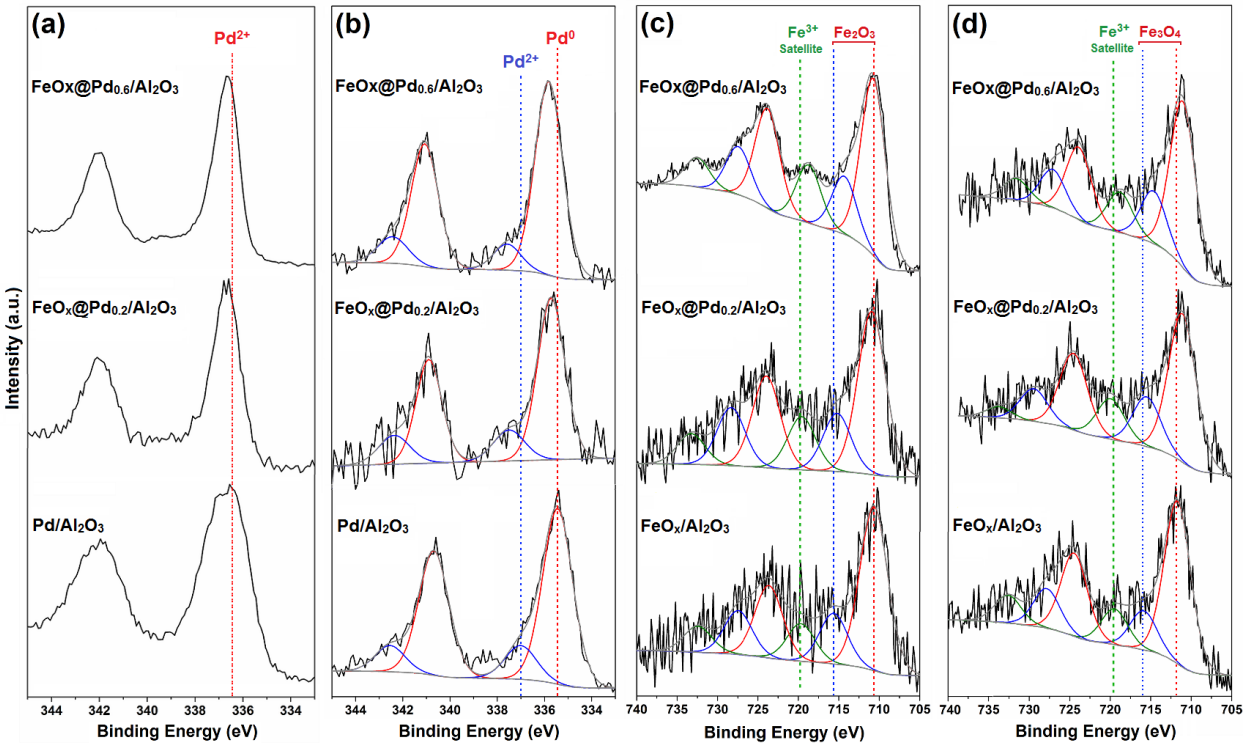

Figure 4.3. XPS profiles of Pd/Al_2O_3, FeO_x/Al_2O_3 and $FeO_x@Pd_n/Al_2O_3$ catalysts: Pd 3d of (a) calcined and (b) spent catalysts; Fe 2p of (c) calcined and (d) spent catalysts.

Table 4.2. Binding energy values of Pd 3d and Fe 2p in the fresh and spent catalysts.

Catalyst	Binding Energy (eV)							
	Pd $3d_{5/2}$		Pd $3d_{3/2}$		Fe $2p_{3/2}$		Fe $2p_{1/2}$	
	fresh	spent	fresh	spent	fresh	spent	fresh	spent
Pd/Al_2O_3	336.3	335.4	341.5	340.6	–	–	–	–
$FeO_x@Pd_{0.2}/Al_2O_3$	336.7	335.7	341.9	340.9	710.9	711.1	724.0	724.1
$FeO_x@Pd_{0.6}/Al_2O_3$	336.6	335.8	341.9	341.1	710.8	711.0	723.8	723.9
FeO_x/Al_2O_3	–	–	–	–	710.6	711.7	723.6	724.5

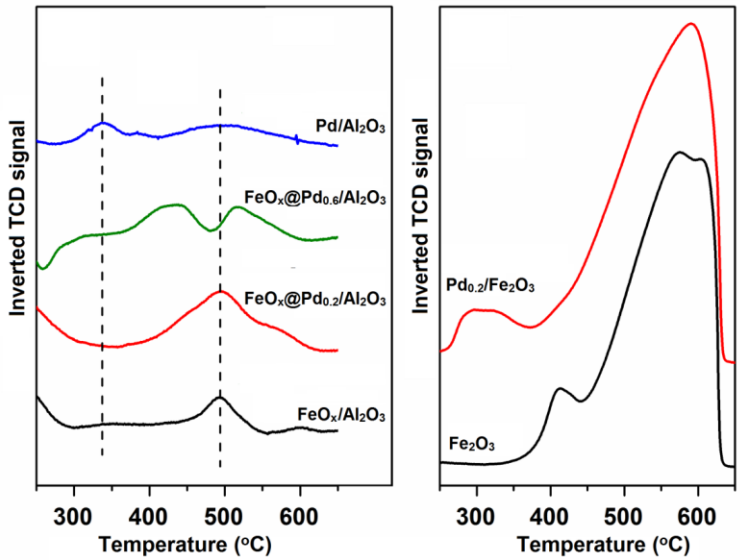

Figure 4.4. TPR profiles of calcined supported catalysts. The inverted TCD signal reflects hydrogen consumption.

Thus, the characterization results provide evidence of preferential Pd species reduction on the surface of FeO_x nanoparticles, as expected from the galvanic exchange reaction.[53] The thus-formed Pd islands preferentially nucleated and grew on the surface of FeO_x NPs instead of being formed as individual particles. The intimate Fe-Pd contact resulted in a change of the electronic properties of Pd. Pd dispersion increased greatly compared to monometallic Pd catalysts and was maximized at Pd/Fe molar ratio of 0.2. The catalytic section below explores how the increased Pd dispersion and its modified electronic properties affected the catalytic function in the example of a high-temperature low-sulfur hydrodesulfurization and sulfur-free hydrogenation reactions.

4.3.2 Catalytic performance in hydrodesulfurization and hydrogenation

The catalytic activity and selectivity of the synthesized catalysts were assessed in the continuous hydrodesulfurization of 4,6-DMDBT and sulfur-free hydrogenation of biphenyl for 18 hours on stream. The catalytic performance stabilized after 2 h on stream. As seen in the HDS reaction scheme (Scheme 4.1), the detected reaction products include the products of direct desulfurization (DDS), hydrogenation products with and without extracted sulfur and sulfur-free hydrocracking products with 6- or 5-membered rings. HDS of 4,6-DMDBT on Pd catalysts is

known to follow a pseudo-first-order kinetics.[67] The measured reactor exit conversions were used to calculate rate constants for a first-order reaction in a packed-bed reactor; this was followed by the calculation of the initial reaction rates at the initial 4,6-DMDBT concentration for a fair comparison of the catalysts. Figure 4.5 demonstrates that the catalyst activity depends on the Pd/Fe ratio in the FeO_x@Pd_n/Al_2O_3 catalysts and is maximized at the ratio of 0.2, which is in line with the maximized Pd dispersion as measured by CO chemisorption (Table 4.1). Pd/Fe_2O_3, prepared from commercial iron oxide with the same Pd/Fe ratio of 0.2, did not provide any enhancement as compared to the Al_2O_3-supported Pd. This demonstrates the advantage of the used colloidal preparation method to improve the dispersion and enhance the Pd-mass-based activity. Table S1 (Supporting Information) reports selectivities to individual products for the HDS reaction at 350 °C. Pd/Al_2O_3 and FeO_x@Pd_n/Al_2O_3 catalysts showed 23±2% selectivity to 3,3'-DMBP (direct desulfurization DDS product), 45±1% selectivity to hydrogenation (HYD) products (Scheme 4.1) and 32±2% selectivity to hydrocracking (HCK) products at similar ca. 33% 4,6-DMDBT conversion at 350 °C. As compared to Pd/Al_2O_3, the FeO_x@Pd_n/Al_2O_3 catalysts suppressed the formation of 5-membered ring HCK products in favor of 6-membered ring products. Pd/Fe_2O_3 catalyst showed 77% hydrocracking selectivity with only 11% DDS and 12% HYD selectivities, confirming the importance of Pd-Fe interactions in the FeO_x@Pd_n/Al_2O_3 catalysts. Iron catalysts are known for high cracking selectivity, as reported for thiophene hydrodesulfurizaion.[76]

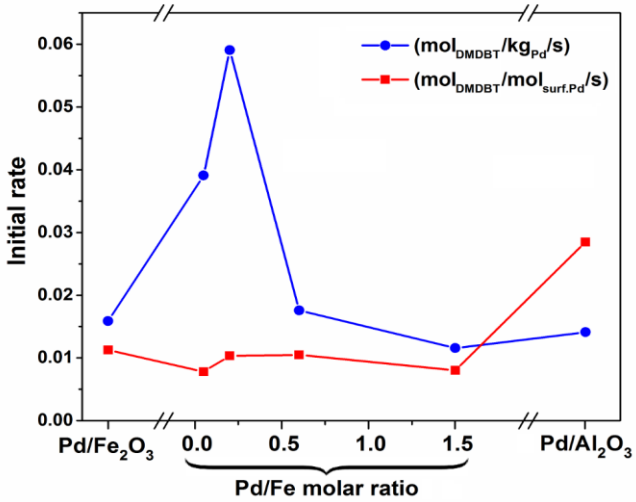

Figure 4.5. Initial rate of 4,6-DMDBT HDS at 350 °C and 3 MPa as a function of Pd/Fe ratio.

For further analysis and comparison, three catalysts were selected: the iron-free Pd/Al_2O_3, the most efficient $FeO_x@Pd_{0.2}/Al_2O_3$ and $FeO_x@Pd_{0.6}/Al_2O_3$. Conventionally, the kinetic analysis of 4,6-DMDBT HDS considers separately the direct desulfurization path (formation of 3,3'-DMBP) and hydrogenation path, as a lumped formation of all products other than 3,3'-DMBP.[67,77] Both paths follow a pseudo-first-order kinetics on Pd catalysts for 4,6-DMDBT HDS,[67] which enables calculation of rate constants and turnover frequencies for DDS and HYD paths. Table 4.1 compares turnover frequencies (TOF) for the selected catalysts calculated from initial reaction rates at 350 °C (Figure 4.5) and amount of surface Pd atoms, as determined by CO chemisorption (Table 4.1) assuming CO:Pd stoichiometry of 1. TOFs for DDS and TOFs for HYD paths were calculated based on two first-order parallel reactions of 4,6-DMDBT conversion to DDS and HYD products with 1:1 stoichiometry (Scheme 4.1), where HCK products were accounted for in the HYD path with 1:2 stoichiometry. Table 4.3 also includes TOFs for sulfur-free hydrogenation of biphenyl (BP) to assess the effect of Fe on sulfur tolerance of the hydrogenation sites. Table S2 (Supporting Information) provides more details on the BP hydrogenation. Biphenyl hydrogenation on supported Pt-group catalysts is known to follow a pseudo-first-order kinetics[78], which was used to calculate TOFs from initial reaction rates at 350 °C.

As seen in Table 4.3, the introduction of Fe resulted in the decreased turnover frequencies at 350 °C, both for direct desulfurization and hydrogenations with and without sulfur. An order of magnitude higher TOF for HYD path than for DDS path in 4,6-DMDBT HDS is known for Pt-group catalysts[67] because of methyl groups hindering the reactant's σ mode adsorption via the sulfur atom for DDS. The 4,6-alkyl groups do not pose constrains for the HYD path which occurs via π adsorption of a benzene ring.[67,79] Thus, although the use of $FeO_x@Pd_n$ structures allowed for higher dispersion and four-fold higher Pd mass-based catalyst activity (Figure 4.5), Pd-Fe interactions led to the decreased intrinsic site activity at 350 °C. Similarly, the formation of bimetallic Pd-Fe nanoparticles supported on SiO_2, along with large bimetallic particle size, suppressed phenylacetylene hydrogenation as compared to monometallic Pd catalyst.[80] Thiophene hydrodesulfurization at 400 °C was also inhibited when Pd was diluted with Fe, which was assigned to the formation of less active Fe-Pd alloy.[76] However, the ratio of hydrogenation TOFs in the presence and absence of sulfur (Table 4.3) improved upon addition of

Fe. This justifies the choice of iron core for Pd deposition based on the higher sulfur affinity to Fe than to Pd, leading to the improved catalyst's sulfur resistance.

Table 4.3. Turnover frequencies (mmol/$mol_{surface\ Pd}$/s) in hydrodesulfurization of 4,6-DMDBT and sulfur-free hydrogenation of biphenyl (BP) at 350 °C and 3 MPa at 18 h on stream.

Catalyst	4,6-DMDBT HDS				TOF_{BP} in BP HYD	$TOF_{HYD\ in\ HDS}$ / $TOF_{BP\ in\ BP\ HYD}$
	TOF_{DMDBT}	TOF_{HYD}	TOF_{DDS}	TOF_{HYD}/TOF_{DDS}		
Pd/Al_2O_3	29	20	8	3	47	0.4
$FeO_x@Pd_{0.6}/Al_2O_3$	11	7	3		1	7
$FeO_x@Pd_{0.2}/Al_2O_3$	11	8	2.5		2	4

4,6-DMDBT HDS at a lower temperature (270 °C, Table 4.4 and Table S3 in the Supporting Information) showed that the HYD path is in stronger preference to the DDS path as compared to the 350 °C HDS, which was also observed for 4,6-DMDBT HDS on Co-Mo catalysts.[77] Table 4.4 and Figure 4.6 reveal the beneficial effect of Pd-Fe interactions on the intrinsic site activities at 270 °C (the enhancement factors refer to the ratio of TOF for Fe-containing catalysts to the Pd-only catalyst), which is contrary to the inhibiting effect at 350 °C (Table 4.3). A controversial effect of Pd-Fe interactions has been reported for phenylacetylene hydrogenation, with PdFe alloy inhibiting[80] or promoting[81] the activity of Pd-only catalysts. The inhibition effect in thiophene HDS could not be decoupled from the change in Pd dispersion.[76] In the current study, Pd dispersion, as measured by CO chemisorption, remained the same after the reduction at 270 °C as at 350 °C (Table 4.1), most likely, because all catalysts were precalcined at 400 °C. Thus, the beneficial effect of Fe addition to Pd for the reaction at 270 °C, as opposed to the inhibiting effect for the reaction at 350 °C, is not related to the change of available Pd atoms for catalysis. As was shown by DFT calculations for molybdenum sulfide, flat adsorption of 4,6-DMDBT for hydrogenation via benzene ring and perpendicular adsorption for desulfurization occur on two types of active sites.[79] An experimental study of 4,6-DMDBT HDS on Pd nanoparticles of different sizes and shapes confirmed the defect sites being active sites for the

DDS path.[82] Fe improves sulfur tolerance of Pd HYD sites (Table 4.3), but at the same time consumes active Pd for the formation of less active (or inactive) PdFe.

Table 4.4. Turnover frequencies (mmol/mol$_{surface\ Pd}$/s) in HDS of 4,6-DMDBT at 270 °C.

Catalyst	TOF_{HYD}	TOF_{DDS}	TOF_{HYD}/TOF_{DDS}
Pd/Al_2O_3	2.5	0.3	9
$FeO_x@Pd_{0.6}/Al_2O_3$	3.1	0.5	6
$FeO_x@Pd_{0.2}/Al_2O_3$	3.3	0.4	8

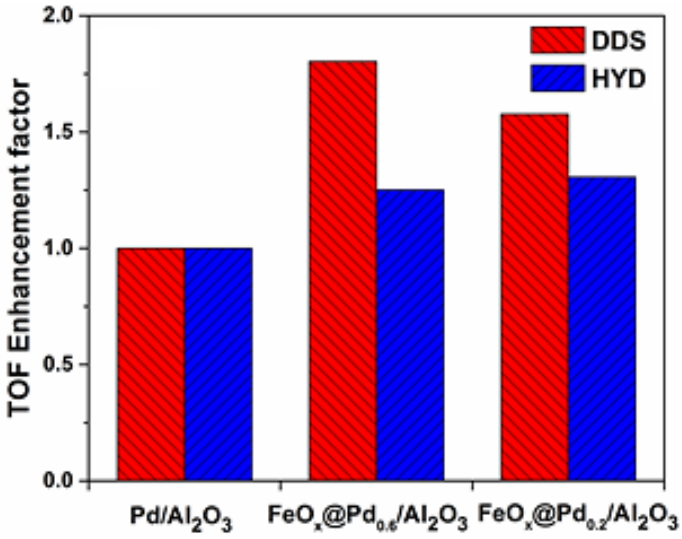

Figure 4.6. TOF enhancement factors in HDS of 4,6-DMDBT at 270 °C.

4.4 Conclusions

$FeO_x@Pd_n/Al_2O_3$ catalysts were developed via colloidal synthesis followed by annealing for high-temperature catalysis (270-350 °C). Pd species preferentially reduced on the surface of FeO_x nanoparticles and formed Pd(0) islands rather than forming individual nanoparticles. The

Fe-Pd interaction resulted in the change of electronic properties of Pd. The highest Pd dispersion was found for Pd/Fe molar ratio of 0.2 as compared to 0.05, 0.6, 1.5 and pure Pd. The catalytic behavior was assessed in the continuous hydrodesulfurization of 4,6-DMDBT and sulfur-free hydrogenation of biphenyl.

The introduction of Fe nanocores for Pd deposition provided a number of advantages for 4,6-DMDBT hydrodesulfurization. The Pd mass-based HDS activity increased four-fold at 350 $^{\circ}$C, but the effect on the intrinsic site activities varied with temperature. Fe-Pd interactions led to a drop in the number of active sites for both direct desulfurization and hydrogenation pathways. The incorporation of Fe also improved the sulfur resistance of hydrogenation sites due to the higher affinity of sulfur to Fe as compared to Pd. Pd/Fe_2O_3, prepared from commercial iron oxide with the optimal Pd/Fe ratio of 0.2, did not provide activity enhancement as compared to the alumina-supported Pd and led to significant cracking. This demonstrates the advantage of the used colloidal preparation method to improve the dispersion and ensure beneficial Pd-Fe interactions.

Acknowledgements

Financial support from NSERC Discovery grant (RGPIN 371888-09) is appreciated. We thank Becquerel Laboratory-Maxxam Company (Ontario, Canada) for the NAA analyses. Dr. Xuejun Sun, Dr. Anqiang He, Diane Caird, and Lisa Brandt (GC-MS) are gratefully acknowledged for TEM, XPS, XRD and GC-MS data acquisition at the U of A. The STEM-EDS research described in this paper was performed at the Canadian Centre for Electron Microscopy at McMaster University, which is supported by NSERC and other government agencies.

4.5 Supporting Information

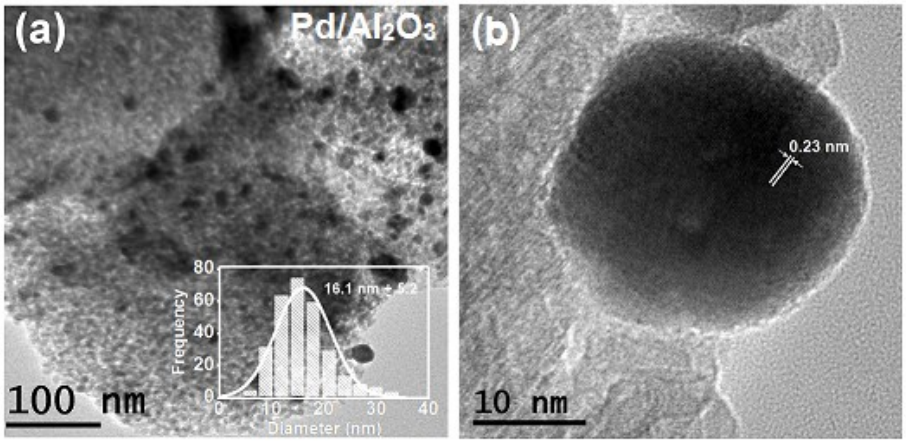

Figure S1. (a) TEM and (b) HRTEM images of spent Pd/Al_2O_3 catalyst.

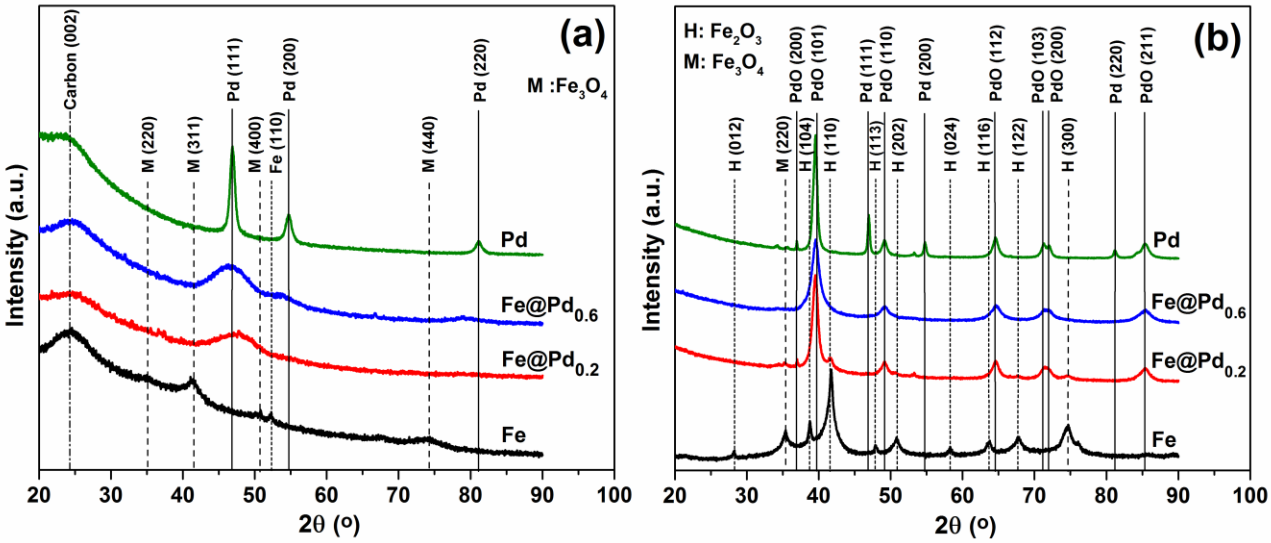

Figure S2. (a) XRD patterns of unsupported FeO_x, Pd, and FeO_x@Pd nanoparticles after synthesis, and (b) after 4 h of calcination at 400 °C; M and H represent magnetite (Fe_3O_4) and hematite (Fe_2O_3), respectively. The peaks were assigned based on the powder diffraction file numbers 00-019-0629 for magnetite, 97-002-2505 for hematite, 00-006-0696 for metallic iron, 97-018-0870 for metallic palladium, and 00-006-0515 for PdO. Figure S2(a) was used to calculate the lattice parameters in Table 4.1. The high intensities at 20-30° range in Figure S2(a) are due to carbon in PVP (stabilizer), which disappeared after calcination in Figure S2(b).

Table S1. Products distribution in HDS of 4,6-DMDBT at 350 °C and 3 MPa.

Catalyst	DMDBT conversion (%)	Selectivity (mol %)														
		DDS	HYD						Total HYD	HCK						Total HCK
		DMBP	DM-CHB	DM-BCH	DM-THDBT	DM-HHDBT	DM-PHDBT		CP	MCP	CH	Benzene	MCH	Toluene	
Pd/Al_2O_3	30.5	24.4	9.9	23.5	10.5	0.6	0.7	45.3	14.1	1.1	10.8	0.7	2.7	1.0	30.3
$FeO_x@Pd_{1.5}/Al_2O_3$	44.9	22.5	43.3	11.3	8.4	0.6	<0.1	63.6	1.9	2.1	3.1	3.6	3.2	<0.1	13.9
$FeO_x@Pd_{0.6}/Al_2O_3$	32.8	24.4	24.2	3.5	15.0	0.7	<0.1	43.3	5.2	5.3	5.3	<0.1	9.6	6.8	32.3
$FeO_x@Pd_{0.2}/Al_2O_3$	35.9	20.2	26.4	4.6	15.0	0.1	0.1	46.1	4.8	4.5	6.8	1.9	10.0	5.6	33.6
$FeO_x@Pd_{0.05}/Al_2O_3$	5.7	29.6	13.0	<0.1	21.1	<0.1	<0.1	34.1	8.0	4.3	8.0	4.6	9.7	1.7	36.3
$Pd_{0.2}/Fe_2O_3$	11.3	10.7	0.4	0.6	1.3	4.3	5.7	12.3	34.6	8.0	16.7	2.7	15.0	<0.1	77.1

Table S2. Sulfur-free hydrogenation of biphenyl at 350 C and 3MPa after 18 h on stream.

Catalyst	Cat. (mg)	Biphenyl conversion (%)	Initial rate ($mol_{BP}/kg_{Pd}/s$)	TOF ($mmol_{BP}/mol_{surface\ Pd}/s$)
Pd/Al_2O_3	25	69.9	0.023	47
$FeO_x@Pd_{0.6}/Al_2O_3$	60	11.3	0.002	1.3
$FeO_x@Pd_{0.2}/Al_2O_3$	49	12.4	0.011	2.0

Table S3. Products distribution in HDS of 4,6-DMDBT at 270 °C and 3 MPa.

Catalyst	DMDBT conversion (%)	Selectivity (mol %)														
		DDS	HYD						Total HYD	HCK						Total HCK
		DMBP	DM-CHB	DM-BCH	DM-THDBT	DM-HHDBT	DM-PHDBT		CP	MCP	CH	Benzene	MCH	Toluene	
Pd/Al_2O_3	4.7	9.4	34.6	4.0	29.9	14.0	0.0	82.5	0.0	0.0	8.1	0.0	0.0	0.0	8.1
$FeO_x@Pd_{0.6}/Al_2O_3$	13.0	12.2	18.4	1.7	34.5	11.8	1.2	67.6	0.0	0.0	20.2	0.0	0.0	0.0	20.2
$FeO_x@Pd_{0.2}/Al_2O_3$	15.0	10.7	19.5	0.0	38.5	14.8	0.0	72.8	0.0	0.0	7.7	8.8	0.0	0.0	16.5

4.6 References

(1) Qiao, B.; Wang, A.; Yang, X.; Allard, L. F.; Jiang, Z.; Cui, Y.; Liu, J.; Li, J.; Zhang, T. Nat. Chem. 2011, 3, 634–641.

(2) Choi, C. H.; Kim, M.; Kwon, H. C.; Cho, S. J.; Yun, S.; Kim, H.-T.; Mayrhofer, K. J. J.; Kim, H.; Choi, M. Nat. Commun. 2016, 7, 10922–10931.

(3) Hunt, S. T.; Milina, M.; Alba-rubio, A. C.; Hendon, C. H.; Dumesic, J. A.; Román-leshkov, Y. Science 2015, 352, 974–978.

(4) Hu, G.; Nitze, F.; Gracia-Espino, E.; Ma, J.; Barzegar, H. R.; Sharifi, T.; Jia, X.; Shchukarev, A.; Lu, L.; Ma, C.; Yang, G.; Wågberg, T. Nat. Commun. 2014, 5, 1–9.

(5) Lei, Y.; Mehmood, F.; Lee, S.; Greeley, J.; Lee, B.; Seifert, S.; Winans, R. E.; Elam, J. W.; Meyer, R. J.; Redfern, P. C.; Teschner, D.; Schloegl, R.; Pellin, M. J.; Curtiss, L. A.; Vajda, S. Science 2010, 328, 224–228.

(6) Herzing, A. a; Kiely, C. J.; Carley, A. F.; Landon, P.; Hutchings, G. J. Science 2008, 321, 1331–1335.

(7) Turner, M.; Golovko, V. B.; Vaughan, O. P. H.; Abdulkin, P.; Berenguer-Murcia, A.; Tikhov, M. S.; Johnson, B. F. G.; Lambert, R. M. Nature 2008, 454, 981–983.

(8) Wei, H.; Liu, X.; Wang, A.; Zhang, L.; Qiao, B.; Yang, X.; Huang, Y.; Miao, S.; Liu, J.; Zhang, T. Nat. Commun. 2014, 5, 5634–5642.

(9) Vilé, G.; Albani, D.; Nachtegaal, M.; Chen, Z.; Dontsova, D.; Antonietti, M.; López, N.; Pérez-Ramírez, J. Angew. Chemie - Int. Ed. 2015, 54, 11265–11269.

(10) Liu, P.; Zhao, Y.; Qin, R.; Mo, S.; Chen, G.; Gu, L.; Chevrier, D. M.; Zhang, P.; Guo, Q.; Zang, D.; Wu, B.; Fu, G.; Zheng, N. Science 2016, 352, 797–801.

(11) Ranocchiari, M.; Lothschutz, C.; Grolimund, D.; van Bokhoven, J. A. Proc. R. Soc. A Math. Phys. Eng. Sci. 2012, 468, 1985–1999.

(12) Duarte, R. B.; Krumeich, F.; Van Bokhoven, J. A. ACS Catal. 2014, 4, 1279–1286.

(13) Fujiwara, K.; Müller, U.; Pratsinis, S. E. ACS Catal. 2016, 6, 1887–1893.

(14) Tian, N.; Zhou, Z.-Y.; Sun, S.-G.; Ding, Y.; Wang, Z. L. Science 2007, 316, 732–735.

(15) Chen, C.; Kang, Y.; Huo, Z.; Zhu, Z.; Huang, W.; Xin, H. L.; Snyder, J. D.; Li, D.; Herron, J. A.; Mavrikakis, M.; Chi, M.; More, K. L.; Li, Y.; Markovic, N. M.; Somorjai, G. A.; Yang, P.; Stamenkovic, V. R. Science 2014, 343, 1339–1343.

(16) Khan, M. U.; Wang, L.; Liu, Z.; Gao, Z.; Wang, S.; Li, H.; Zhang, W.; Wang, M.; Wang, Z.; Ma, C.; Zeng, J. Angew. Chemie - Int. Ed. 2016, 55, 9548 –9552.

(17) An, K.; Alayoglu, S.; Ewers, T.; Somorjai, G. A. J. Colloid Interface Sci. 2012, 373, 1-13.

(18) Wang, C.; Daimon, H.; Sun, S. Nano Lett. 2009, 9, 1493–1496.

(19) Sun, X.; Guo, S.; Liu, Y.; Sun, S. Nano Lett. 2012, 12, 4859–4863.

(20) Wang, D.; Xin, H. L.; Hovden, R.; Wang, H.; Yu, Y.; Muller, D. a.; DiSalvo, F. J.; Abruña, H. D. Nat. Mater. 2012, 12, 81–87.

(21) Zhang, X. B.; Yan, J. M.; Han, S.; Shioyama, H.; Xu, Q. J. Am. Chem. Soc. 2009, 131, 2778–2779.

(22) Alayoglu, S.; Nilekar, A. U.; Mavrikakis, M.; Eichhorn, B. Nat. Mater. 2008, 7, 333–338.

(23) Tao, F.; Grass, M. E.; Zhang, Y.; Butcher, D. R.; Renzas, J. R.; Liu, Z.; Chung, J. Y.; Mun, B. S.; Salmeron, M.; Somorjai, G. A. Science 2008, 322, 932–934.

(24) Joo, S. H.; Park, J. Y.; Tsung, C. K.; Yamada, Y.; Yang, P.; Somorjai, G. A. Nat. Mater. 2009, 8, 126–131.

(25) Sasaki, K.; Naohara, H.; Choi, Y.; Cai, Y.; Chen, W.-F.; Liu, P.; Adzic, R. R. Nat. Commun. 2012, 3, 1115–1124.

(26) Liang, W. I.; Zhang, X.; Zan, Y.; Pan, M.; Czarnik, C.; Bustillo, K.; Xu, J.; Chu, Y. H.; Zheng, H. J. Am. Chem. Soc. 2015, 137, 14850–14853.

(27) Gawande, M. B.; Goswami, A.; Asefa, T.; Guo, H.; Biradar, A. V; Peng, D.; Zboril, R.; Varma, R. S. Chem. Soc. Rev. 2015, 44, 7540–7590.

(28) Strasser, P.; Koh, S.; Anniyev, T.; Greeley, J.; More, K.; Yu, C.; Liu, Z.; Kaya, S.; Nordlund, D.; Ogasawara, H.; Toney, M. F.; Nilsson, A. Nat. Chem. 2010, 2, 454–460.

(29) Prabhudev, S.; Bugnet, M.; Bock, C.; Botton, G. A. ACS Nano 2013, 7, 6103–6110.

(30) Jang, J.H.; Lee, E.; Park, J.; Kim, G.; Hong, S.; Kwon, Y.U. Sci. Rep. 2013, 3, 2872–2880.

(31) Zhang, S.; Zhang, X.; Jiang, G.; Zhu, H.; Guo, S.; Su, D.; Lu, G.; Sun, S. J. Am. Chem. Soc. 2014, 136, 7734–7739.

(32) Guo, X.; Brault, P.; Zhi, G.; Caillard, A.; Jin, G.; Guo, X. J. Phys. Chem. C 2011, 115, 24164–24171.

(33) Jagadeesh, R. V.; Surkus, A.-E.; Junge, H.; Pohl, M.-M.; Radnik, J.; Rabeah, J.; Huan, H.; Schunemann, V.; Bruckner, A.; Beller, M. Science 2013, 342, 1073–1076.

(34) Easterday, R.; Leonard, C.; Sanchez-Felix, O.; Losovyj, Y.; Pink, M.; Stein, B. D.; Morgan, D. G.; Lyubimova, N. A.; Nikoshvili, L. Z.; Sulman, E. M.; Mahmoud, W. E.; Al-Ghamdi, A. A.; Bronstein, L. M. ACS Appl. Mater. Interfaces 2014, 6, 21652–21660.

(35) Stamenkovic, V. R.; Mun, B. S.; Mayrhofer, K. J. J.; Ross, P. N.; Markovic, N. M. J. Am. Chem. Soc. 2006, 128, 8813–8819.

(36) Wang, Y.; He, Q.; Guo, J.; Wang, J.; Luo, Z.; Shen, T. D.; Ding, K.; Khasanov, A.; Wei, S.; Guo, Z. ACS Appl. Mater. Interfaces 2015, 7, 23920–23931.

(37) Jiang, G.; Zhu, H.; Zhang, X.; Shen, B.; Wu, L.; Zhang, S.; Lu, G.; Wu, Z.; Sun, S. ACS Nano 2015, 9, 11014–11022.

(38) Guo, S.; Zhang, S.; Sun, X.; Sun, S. J. Am. Chem. Soc. 2011, 133, 15354–15357.

(39) Shao, M. H.; Sasaki, K.; Adzic, R. R. J. Am. Chem. Soc. 2006, 128, 3526–3527.

(40) Liu, L.; Zhou, F.; Wang, L.; Qi, X.; Shi, F.; Deng, Y. J. Catal. 2010, 274, 1–10.

(41) Golubina, E. V.; Lokteva, E. S.; Lunin, V. V.; Telegina, N. S.; Stakheev, A. Y.; Tundo, P. Appl. Catal. A, Gen. 2006, 302, 32–41.

(42) Wu, C.-T.; Yu, K. M. K.; Liao, F.; Young, N.; Nellist, P.; Dent, A.; Kroner, A.; Tsang, S. C. E. Nat. Commun. 2012, 3, 1050–1058.

(43) Kast, P.; Friedrich, M.; Teschner, D.; Girgsdies, F.; Lunkenbein, T.; D'Alnoncourt, R. N.; Behrens, M.; Schlögl, R. Appl. Catal. A, Gen. 2015, 502, 8–17.

(44) Yu, Y.; Sun, K.; Tian, Y.; Li, X. Z.; Kramer, M. J.; Sellmyer, D. J.; Shield, J. E.; Sun, S. Nano Lett. 2013, 13, 4975–4979.

(45) Easterday, R.; Sanchez-Felix, O.; Stein, B. D.; Morgan, D. G.; Pink, M.; Losovyj, Y.; Bronstein, L. M. J. Phys. Chem. C 2014, 118, 24769–24775.

(46) Sun, S.; Murray, C. B.; Weller, D.; Folks, L.; Moser, A. Science 2000, 287, 1989–1992.

(47) Ung, D.; Tung, L. D.; Caruntu, G.; Delaportas, D.; Alexandrou, I.; Prior, I. a.; Thanh, N. T. K. CrystEngComm 2009, 11, 1309–1316.

(48) Schlapka, A.; Lischka, M.; Groß, A.; Kasberger, U.; Jakob, P. Phys. Rev. Lett. 2003, 91, 016101/1-016101/4.

(49) Kwak, J. H.; Hu, J.; Mei, D.; Yi, C.-W.; Kim, D. H.; Peden, C. H. F.; Allard, L. F.; Szanyi, J. Science 2009, 325, 1670–1673.

(50) Chen, M. S.; Goodman, D. W. Science 2004, 306, 252–255.

(51) Kwon, S. G.; Krylova, G.; Phillips, P. J.; Klie, R. F.; Chattopadhyay, S.; Shibata, T.; Bunel, E. E.; Liu, Y.; Prakapenka, V. B.; Lee, B.; Shevchenko, E. V. Nat. Mater. 2015, 14, 215–223.

(52) Yao, Y.; Patzig, C.; Hu, Y.; Scott, R. W. J. J. Phys. Chem. C 2015, 119, 21209–21218.

(53) Zhou, S.; Johnson, M.; Veinot, J. G. C. Chem. Commun. 2010, 46, 2411–2413.

(54) Hermann, N.; Brorson, M.; Topsøe, H. Catal. Letters 2000, 65, 169–174.

(55) Niquille-Röthlisberger, A.; Prins, R. Catal. Today 2007, 123, 198–207.

(56) Li, X.; Wang, A.; Egorova, M.; Prins, R. J. Catal. 2007, 250, 283–293.

(57) Jayne, D.; Zhang, Y.; Haji, S.; Erkey, C. Int. J. Hydrogen Energy 2005, 30, 1287–1293.

(58) Hernández, S.; Solarino, L.; Orsello, G.; Russo, N.; Fino, D.; Saracco, G.; Specchia, V. Int. J. Hydrogen Energy 2008, 33, 3209–3214.

(59) Ma, X.; Sun, L.; Song, C. Catal. Today 2002, 77, 107–116.

(60) Ziaei-Azad, H.; Semagina, N. Appl. Catal. B, Environ. 2016, 191, 138–146.

(61) Prins R. Handbook of heterogeneous catalysis; Ertl, G., Knozinger, H., Schuth, F., Weitkamp, J.,; Wiley-VCH, 2008, 2965-2718.

(62) Song, C.; Ma, X. Appl. Catal. B, Environ. 2003, 41, 207–238.

(63) Ito, E.; van Veen, J. A. R. Catal. Today 2006, 116, 446–460.

(64) Ma, X.; Sakanishi, K.; Isoda, T.; Mochida, I. Energy & Fuels 1995, 9, 33–37.

(65) Ma, X.; Sakanishi, K.; Mochida, I. Ind. Eng. Chem. Res. 1996, 35, 2487–2494.

(66) Qian, E. W.; Otani, K.; Li, L.; Ishihara, A.; Kabe, T. J. Catal. 2004, 221, 294–301.

(67) Niquille-Röthlisberger, A.; Prins, R. J. Catal. 2006, 242, 207–216.

(68) Zdražil, M. Catal. Today 1988, 3, 269–365.

(69) Bertolini, J.C.; Rousset, J.L.; Miegge, P.; Massardier, J.; Tardy, B. Surf. Sci. 1993, 287/288, 346-349.

(70) Teranishi, T.; Miyake, M. Chem. Mater. 1998, 10, 594–600.

(71) Pérez-Ramírez, J.; Berger, R. J.; Mul, G.; Kapteijn, F.; Moulijn, J. A. Catal. Today 2000, 60, 93–109.

(72) George, C.; Genovese, A.; Casu, A.; Prato, M.; Povia, M.; Manna, L.; Montanari, T. Nano Lett. 2013, 13, 752–757.

(73) Ahn, T.; Kim, J. H.; Yang, H. M.; Lee, J. W.; Kim, J. D. J. Phys. Chem. C 2012, 116, 6069–6076.

(74) McIntyre, N. S.; Zetaruk, D. G. Anal. Chem. 1977, 49, 1521–1529.

(75) Grosvenor, A. P.; Kobe, B. A.; Biesinger, M. C.; McIntyre, N. S. Surf. Interface Anal. 2004, 36, 1564–1574.

(76) Guerrero-Ruiz, A.; Sepulveda-Escribano, A.; Rodriguez-Ramos, I. Appl. Catal. A 1992, 81, 101-112.

(77) Farag, H.; Whitehurst, D. D.; Sakanishi, K.; Mochida, I. Catal. Today 1999, 50, 9–17.

(78) Koussathana, M.; Vamvouka, D.; Economou, H.; Verykios, X. Appl. Catal. 1991, 77, 283-301.

(79) Cristol, S.; Paul, J.-F.; Payen, E.; Bougeard, D.; Hutschka, F.; Clemendot, S. J. Catal. 2004, 224, 138-147.

(80) Shesterkina, A.A.; Kirichenko, O.A.; Kozlova, L.M.; Kapustin, G.I.; Mishin, I.V.; Strelkova, A.A.; Kustov, L.M. Mendeleev Commun. 2016, 26, 228-230.

(81) Dominguez-Dominguez, S.; Berenguer-Murcia, A.; Cazorla-Amoros, D.; Linares-Solano, A. J. Catal. 2006, 243, 74-81.

(82) Shen, J.; Semagina, N. ChemCatChem 2016, 8, 2565-2571.

Chapter 5. Unsupported $Cu_{0.65}NbS_2$ as Hydrodesulfurization Catalyst

5.1 Introduction

Nanostructured transition metal sulfides (TMS) demonstrated a promising performance in a wide variety of applications, in particular, as heterogeneous catalysts in the production of clean fuels from petroleum-based feedstocks, renewable bio-oils, and recently from syngas.[1] The tunable structural and electronic properties of TMS make them attractive and versatile for optoelectronic,[2] energy storage materials,[3–5] solar cells,[6,7] and as photo- and electrocatalyst for hydrogen evolution[8–10] and CO_2 reduction[11,12]. For instance, ultrathin layered niobium disulfide (NbS_2) behaved as a semiconductor[13] while bulk NbS_2 is known for its superconductivity at low temperature.[14]

Historically, the interest on TMS has been ignited for the purpose of fuel upgrading and coal liquefaction.[15] Since then, for decades, conventional nickel- and cobalt-promoted molybdenum disulfide (MoS_2) catalysts have been used in petroleum hydrotreating units for heteroatoms removal such as nitrogen, oxygen, and more importantly sulfur.[1,16–18] Nonetheless, the existing hydrodesulfurization (HDS) catalysts are not efficient enough to deliver the high-quality fuels under non-severe operating conditions to meet the stringent environmental regulations.[16,19–24] Accordingly, vast efforts have been devoted to designing more efficient HDS catalysts and technologies.[17] Noble metals catalysts have shown excellent HDS performance especially toward refractory sulfur compounds but the performance does not compensate the catalyst price.[18] Therefore, finding a highly active and inexpensive hydrotreating catalyst based on earth-abundant elements remains as a scientific and technological challenge.

Pecoraro and Chianelli[25] reported that the HDS catalytic activity of unsupported TMS varied over three orders of magnitude across the periodic table from Group IVB to Group VIIIB following a typical "volcano" trend. The First-row TMS were found relatively inactive in HDS of dibenzothiophene (DBT) while the second- and the third-row metal sulfides exhibited the highest activities. Lacroix et. al.[26] investigated the HDS and hydrogenation properties of first- and second-row unsupported transition metal sulfides. Following noble metal sulfides on top, niobium sulfides structure (NbS_x) was the highest intrinsically active structures in HDS of DBT and biphenyl (BP) hydrogenation, even more active than MoS_2 and WS_2 catalysts. However,

among the TMS examined, BP was hydrocracked over NbS_x to single ring products revealing the particular cracking and isomerization properties of Nb species.[26,27] In fact, Nb-based catalysts are intrinsically acidic in both sulfide and oxide states.[26,28] The bulk and supported niobia (Nb_2O_5) catalysts were found exclusively acidic (100 % acidic character). The surface of supported niobium oxide serves as coordinatively unsaturated Lewis acid sites.[29] The higher HDS intrinsic activity of niobium sulfides was further verified in several studies.[23,30] Niobium as dopant improved the DBT HDS and Tetralin hydrogenation activities of industrial $NiMo/Al_2O_3$ catalyst.[31] Opposed to the strong inhibition effects of H_2S on the performance of conventional HDS catalysts, activity and durability of NbS_2 catalyst were not diminished by H_2S.[21,27,32] Moreover, Nb made MoS_2/Al_2O_3 catalyst insensitive to the H_2S partial pressure as compared to $NiMo/Al_2O_3$.[24] Note that Nb is 15-times more abundant than Mo in the earth crust. Nonetheless, the literature on Nb-based catalysts is rare.

NbS_2 and NbS_3 are the most important and stable structures of niobium sulfides. NbS_2 exhibited the same structural features as MoS_2; a lamellar arrangement of trigonal prisms $[NbS_6]$[33,34] in which metal layers sandwiched between two sulfur layers (by Van der Waals force) within a hexagonal cell.[35] However, the *d*-band filling is different from MoS_2 leading to a unique catalytic activity.[36] NbS_3 has a completely different structure although it is made from the same prismatic units. The infinite fiber Nb-S slabs formed by sharing the triangular face of $[NbS_6]$ prisms.[23] NbS_3 is more active in HDS than NbS_2 likely due to the presence of anionic vacancies functioning as active sites.[26,27,23,37] However, in general, the thermal stability of trisulfides structures (NbS_3, MoS_3, WS_3) is low and transforms to disulfides (NbS_2, MoS_2, WS_2) under hydrotreatment conditions.[26,27] This structural transformation strongly depends on temperature, H_2S partial pressure, and the textural properties of the material.[27]

Despite the above-mentioned benefits of NbS_x-based catalysts, formation of niobium sulfides via sulfidation of niobium oxides is not facile as sulfidation of MoO_3 and WO_3.[23,28,38] The high affinity of niobium to oxygen results in extremely stable Nb_2O_5 and NbO_2 compounds with the heats of formation of -380 and -395 kJ/mol, respectively, which are greater than MoO_3 (-248 kJ/mol) and WO_3 (-279 kJ/mol).[13] It was reported that the hydrogen reduction of bulk Nb_2O_5 initiates at 800 °C and reduces to bulk Nb_2O_4 at 1300 °C.[39] From the thermodynamic perspective, the Gibbs free energies for the sulfidation of NbO_2 and Nb_2O_5 with H_2S at 600 K are positive,

$\Delta G°$= +82 and +108 kJ/mol, respectively, as compared to MoO_3 ($\Delta G°$= -119 kJ/mol).[38] Note that bulk NbS_x can be obtained from the elemental mixture of niobium and sulfur at elevated temperatures, i.e. 700 °C for NbS_3 and above 800 °C for NbS_2, which leads to a severe thermal sintering and very low surface area (less than 3 m^2/g).[13,27,33,37] Such a high reduction/sulfidation temperature in a reductive atmosphere is not feasible and even operable industrially that simply hinders the usage of NbS_x-based catalysts in many applications. Noteworthy that a strong metal-support interaction further impedes the sulfidation of Nb_2O_5.[23,37,38,40] Allali et al.[23] reported that a higher sulfidation of Nb was obtained when supported on carbon compared to alumina as a support that also promoted the formation of NbS_3.

Herein, we report for the first time that the addition of copper to niobium oxide (Nb_2O_5) dramatically reduces the sulfidation/reduction temperature of Nb_2O_5 and consequently enhance its HDS activity. A series of bmietallic $NbCu_x$ catalysts where "x" is the molar ratio of Cu to Nb were prepared by a facile coprecipitation technique. Niobium oxalate was used as Nb precursor because of the higher HDS activity showed in a previous study.[37] In addition, copper is precipitated with oxalic species of Nb precursor without using external precipitating agent.[41] The synthesized catalysts were evaluated in HDS of dibenzothiophene at 325 °C and 3 MPa. The objective of the present work was to increase the sulfidation extent of Nb at practically relevant temperatures by addition of a promoter. Our thermodynamic calculation with experimental data showed that copper facilitates reduction and sulfidation of niobium oxides, which at the same time functions as a promoter to improve the reaction selectivity. Copper promoted the formation of desired direct desulfurization (DDS path) and hydrogenation (HYD path) products while suppressing hydrocracking reaction pathway (Scheme 5.1). The HDS activity was maximized at a threshold Cu/Nb molar ratio.

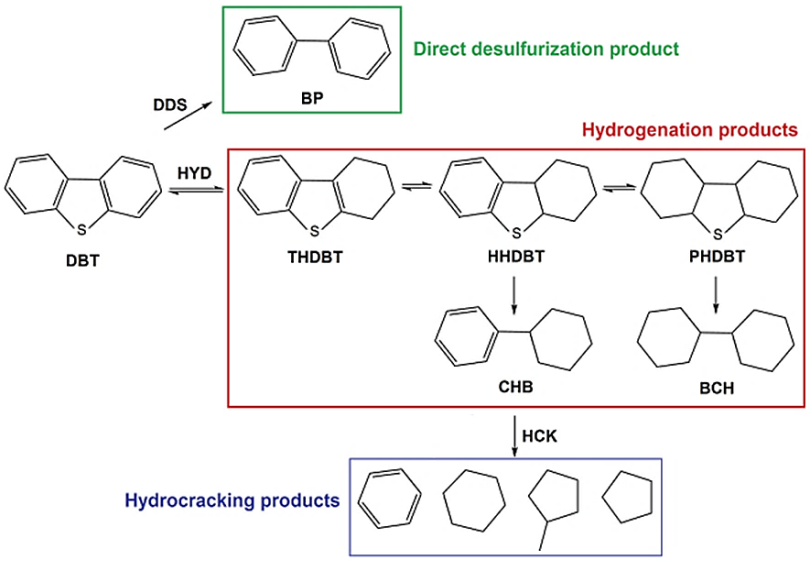

Scheme 5.1. DBT hydrodesulfurization pathways.

5.2 Experimental

5.2.1 Materials

Copper nitrate hexahydrate ($CuNO_3.6H_2O$), ammonium niobate (V) oxalate hydrate ($C_4H_4NNbO_9 \cdot xH_2O$), and ammonium heptamolybdate tetrahydrate ($H_{24}Mo_7N_6O_{24}.4H_2O$) all from Sigma–Aldrich were used for catalyst preparation. Oxalic acid ($(COOH)_2.2H_2O$, from Caledon) and distiled water were used as received. 1000 ppmw sulfur as dibenzothiophene (DBT, $C_{12}H_8S$, Sigma-Aldrich) was dissolved in *n*-decane (Fisher Scientific) as a solvent containing 3.5 wt% *n*-dodecane (Sigma-Aldrich) as the internal standard and was used as a model fuel for HDS reaction. Carbon disulfide (CS_2, Sigma-Aldrich) was dissolved in *n*-decane at 10 wt% and used as a sulfidation agent. Ultra-high purity (99.999%) argon and hydrogen gases were purchased from Praxair.

5.2.2 Catalyst preparation

A series of bimetallic $NbCu_x$ (x represents the molar ratio of Cu to Nb) catalysts were prepared via coprecipitation method at room temperature in which copper and niobium precipitated by

oxalate and acetone, respectively, without using external precipitant. Typically, to synthesize $NbCu_{0.5}$, about 5.7 g of Nb precursor was dissolved in 10 ml of distilled water to reach a clear solution at a pH level of 1.0. The copper-containing solution was prepared by dissolving 2.21 g of $CuNO_3.6H_2O$ in excess acetone. Next, the Nb solution was quickly injected into the Cu solution while mixing vigorously leading to the formation of a blue precipitate of Cu and Nb species. The slurry was mixed for 30 min to achieve a homogeneous mixture and then dried at 110 °C for 24 h. All the synthesized catalysts were calcined in static air at 400 °C for 4 h before characterization and reaction (based on the TGA profile, Figure S1 in Supporting Information). Monometallic Nb, Cu, and Mo catalysts were prepared by calcination of dried precursor (110 °C, overnight) at 400 °C for 4 h. The calcined catalysts were crushed and sieved before HDS experiment.

5.2.3 Catalyst characterization

Field Emission Scanning Electron Microscopy (FESEM) images coupled with energy dispersive X-ray spectroscopy (EDS) were recorded using a scanning electron microscope (Zeiss Sigma FESEM/ EDS & EBSD). Silicon wafer was used for EDS analysis. High-resolution transmission electron microscopy (HRTEM) images were recorded using a JEOL JEM-ARM200CF (probe aberration-corrected S/TEM with a cold field emission gun (cFEG)) operating at 200 kV. X-ray diffraction (XRD) patterns of calcined and sulfided catalysts were recorded using ex-situ Rigaku Ultima IV diffractometer equipped with a D/Tex detector, an Fe Filter, and Co Kα radiation (λ = 1.78899 Å). The diffraction patterns were collected over 5° to 90° on a continuous scan at 2 degrees 2θ per minute with a step size of 0.02°. Data interpretation was done using JADE 9.6 with the 2016 ICDD and 2016 ICSD databases. X-ray photoelectron spectroscopy (XPS) of the calcined and sulfided catalysts (after the sulfidation at 400 °C) was performed using Kratos Axis 165 X-ray photoelectron spectrometer using Mono Al Kα source operating at 14 kV and15 mA. Background subtraction and peaks analysis were performed using CasaXPS software package. All the XPS core–level spectra were corrected with C 1s at 284.8 eV. Specific surface area (BET) and pore size distribution (BJH) analyses were conducted using an Autosorb-iQ Quantachrome. About 0.3 g of sample was degassed with Ar at 120 °C for 2 h before each analysis. Temperature-programmed reduction (TPR) was performed using Micromeritics

Autochem II 2920 apparatus equipped with a TCD detector. About 100 mg of the calcined catalysts were degassed by He at 200 °C for 1 h. TPR analysis was performed after cooling down the sample to room temperature using a 10 ml/min of 10 mol% H_2/Ar at the heating rate of 10 °C/min from room temperature up to 900 °C. Thermogravimetric analysis (TGA) were performed using a Mettler Toledo TGA/DSC1 stare system. About 20 mg of the dried sample was loaded in an alumina crucible and the temperature increased up to 700 °C at a heating rate of 10 °C/min under 50 ml/min nitrogen gas. Diffuse-reflectance infrared Fourier-transform (DRIFTS) spectra of the calcined samplese were collected using NEXUS 670 FT-IR fitted with a smart diffuse reflectance accessory. About 50 mg of the sample was mixed with 500 mg of dried KBr for each measurement. DRIFT spectra were recorded three times against a KBr standard with 256 scans and a resolution of 4 cm^{-1}. The resolution enhancement and data processing were performed with OMNIC software.

5.2.4 Catalytic experiments

Hydrodesulfurization of dibenzothiophene (DBT) was conducted at 325 °C and 3 MPa hydrogen pressure using a fixed-bed plug-flow reactor (stainless steel, L=22", i.d.=0.5"). The catalysts were diluted with silicon carbide (mesh 120, 15:1 weight ratio) to achieve isothermal plug-flow conditions in the reactor. The effects of reactor wall and axial dispersion were negligible.[42] The absence of external and internal mass transfer limitations was verified by Mears and Weisz-Prater criterion, respectively. The heat transfer limitations were found to be negligible by Mears criterion. The calculated values of $6.9x10^{-4}$ for heat transfer and $6.9x10^{-9}$ for external mass transfer limitations are much lower than Mears criterion of 0.15. The calculated Thiele modulus of $9.8x10^{-5}$ reveals that internal mass transfer limitation was absent in the system.

The catalysts were sulfided *in situ* before each HDS reaction. The sulfidation method was optimized to achieve the highest HDS activity possible at practical conditions. Typically, the pressurized reactor (with pure hydrogen gas at 3 MPa) was heated up to 175 °C at a heating rate of 8 °C/min where the sulfidation feed (10 wt% CS_2 in *n*-decane) was introduced into the reactor downward at 0.05 ml/min using a Series II high-pressure pump. The amount of CS_2 in *n*-decane during sulfidation corresponded to pH_2S/pH_2 of 0.01. The liquid feed was pre-mixed with 100 ml/min hydrogen gas before feeding into the reactor. Then, the temperature ramped at 5 °C/min

up to 400 °C where maintained for additional 20 h. After cooling down the system to 325 °C naturally in flowing CS_2 feed stream and hydrogen, a model liquid fuel containing 1000 ppmw sulfur as DBT with 3.5 wt% *n*-dodecane as the internal standard in *n*-decane (as solvent) was then introduced into the reactor at 0.05 ml/min. The liquid feed was mixed with 100 ml/min hydrogen gas to reach the hydrogen-to-liquid molar ratio of 16. All the HDS experiments were performed for 24 h on-stream including overnight stabilization to reach the steady-state conditions. During HDS reaction, the pH_2S/pH_2 was adjusted at $2.55x10^{-4}$ using the concentration of DBT in the feed stream to stabilize the structure in its sulfide state. This ratio is seven orders of magnitude higher than the required thermodynamic value.[38]

Identification of the reaction products was carried out off-line by a gas chromatography coupled with mass spectrometry (GC-MS) using a Thermo Scientific Trace GC Ultra, equipped with a Thermo Scientific TR-5 column (30m, 0.25mm, 0.25um, μm film thickness) as described previously. As shown in Scheme 5.1 the reaction products are categorized into direct desulfurization (DDS), hydrogenation (HYD), and hydrocracking (HCK). The selectivity to the direct desulfurization (DDS) path was calculated based on the amount of biphenyl (BP) formation divided by the amount of converted DBT. Selectivity to hydrogenation (HYD) path is the summation of selectivities to cyclohexylbenzene (CHB), bicyclohexyl (BCH), perhydro-dibenzothiophene (PHDBT), hexahydro-dibenzothiophene (HHDBT), and tetrahydrodibenzothiophene (THDBT). Hydrocracking selectivity (HCK) includes single-ring products such as benzene, cyclohexane, cyclopentane, and methylcyclopentane. The reported conversions are subject to 15% experimental error. Two standard deviations in selectivities are 3%. The carbon mass balance was above 95%.

5.3 Results and Discussion

5.3.1 Thermodynamics of niobium oxide sulfidation

The target is to overcome the thermodynamic limitations of NbS_x phase formation by alloying with another metal sulfide in a way that the resulting alloy will maintain similar catalytically active NbS_x. However, the synergistic or anti-synergistic effects of the second metal on the

performance of NbS_x are unavoidable. To achieve this, the second metal should have negative and significantly lower Gibbs free energy ($\Delta G°$) of sulfidation than niobium oxide to offset the high positive $\Delta G°$ of Nb_2O_5 sulfidation. Furthermore, the sulfidation promoter should possess lower surface free energy (heat of fusion) than niobium with a less stable sulfide phase than NbS_x. Therefore, the less heat of fusion concentrates the second metal on the surface of Nb_2O_5 providing active sites for sulfur adsorption through H_2S dissociation. Once the sulfur is adsorbed on the second metal, it will migrate to niobium if its sulfide free energy is higher than that of niobium sulfide. For example, when sulfur adsorbs on pure platinum (Pt) surface, it stays on Pt surface instead of migrating into the bulk because of much lower surface free energy of sulfur than Pt. On the other hand, both Cu and Zinc (Zn) have lower surface free energies than Pt concentrating on the surface but Zn does not promote Pt sulfidation. This is due to the much stronger Zn-S bond than Pt-S prohibiting the migration of sulfur from the surface into the bulk of Pt, whereas Cu-S bond is less strong than Pt-S bond facilitating sulfur migration into Pt bulk.[43]
According to the above-mentioned criteria, we investigated 35 different metal sulfides as an alloying component for niobium including copper (Cu), iron (Fe), cobalt (Co), molybdenum (Mo), vanadium (V), cadmium (Cd), chromium (Cr), zinc (Zn), manganese (Mn), and tungsten (W). We excluded noble metals in this study for their high price and limited availability in nature. Based on the thermodynamic data[38], Fe, Co, Ni, Cr, Zn, and Mn have positive or not low enough negative $\Delta G°$ of sulfidation to promote Nb_2O_5 sulfidation. On the other hand, vanadium sulfide was found more stable than niobium sulfide. The stability of MoS_2 and WS_2 are slightly lower than that of NbS_2[38], which may not provide sufficient driving force for sulfur migration from Mo or W to niobium. Overall, only Cu and Cd satisfied the three mentioned criteria. However, Cd is one of the six hazardous materials listed in the Restriction of Hazardous Substances Directive adopted in 2003 by the European Union, which leaves Cu as the potential candidate to promote niobium oxides sulfidation. The Gibbs free energies for the formation of individual CuS and NbS_2 from oxides at 600 K are -119 kJ/mol and +108 kJ/mol, respectively.[38] Literature indicates that $Cu_{0.65}NbS_2$ is the most abundant Cu-Nb-S species.[44] Its preparation from individual oxides can be described as below:

$$0.65\ CuO + 0.5\ Nb_2O_5 + 2H_2S + 1.15\ H_2 \Rightarrow Cu_{0.65}NbS_2 + 3.15\ H_2O \quad (5.1)$$

The Gibbs energy of formation of $Cu_{0.65}NbS_2$ from elements can be calculated based on the approach proposed for mixed sulfides from individual sulfides (i) based on the assumption of ideal mixing. N_i is the mole fraction of a component sulfide in the formation reaction, which are 0.65/2 for Cu_2S and 1 for NbS_2.[45]

$$\Delta G_f^o = \sum[N_i \, \Delta G_{f,i}^o] + 5.02 \, R \, T \, \sum[N_i \, \ln N_i \,] \quad (5.2)$$

Figure 5.1a shows the Gibbs free energies of formation of mono- and bimetallic sulfides from corresponding oxide structures using H_2S and H_2 as a function of temperature in the range of 300-650 °C. The thermochemical analysis clearly reveals that addition of Cu to Nb_2O_5 removes the thermodynamic limitation for sulfidation of Nb_2O_5. The large difference between the stability of NbS_2 ($\Delta G^o_{(f),\ 600\ K}$ = -330 kJ/mol) and Cu_2S ($\Delta G^o_{(f),\ 600\ K}$ = -56 kJ/mol) promotes sulfur migration from CuS to NbO_x species. Thermal stability of bimetallic sulfide is very important. Figure 5.1b displays the stability of formed structure as a function of temperature and partial pressure of H_2S to H_2. As can be seen, there is an exponential relation between pH_2S/pH_2 and temperatures to keep the structure is its sulfide phase. The structure exhibits stability within the range of reaction temperature.

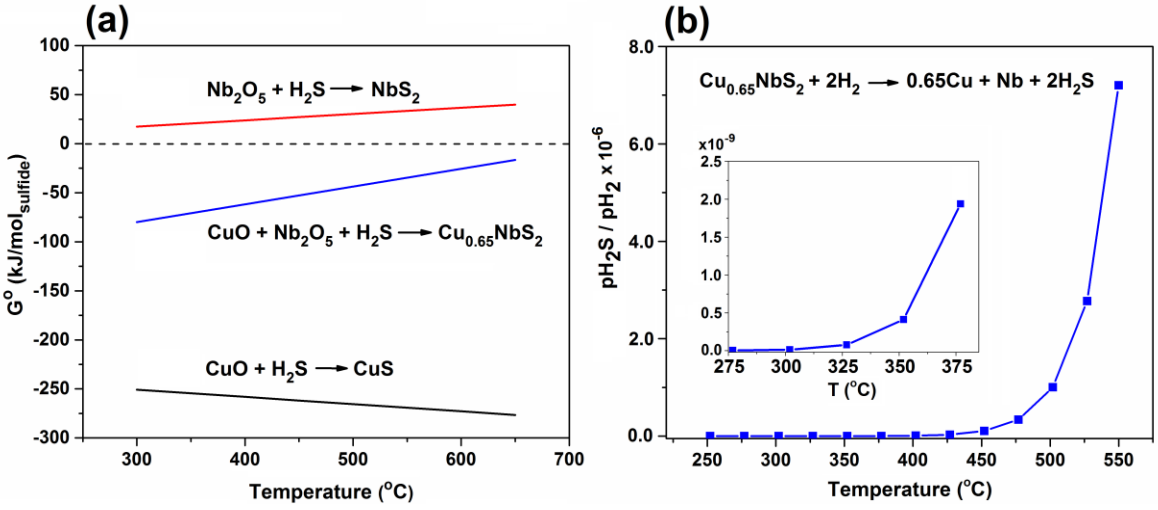

Figure 5.1. (a) Gibbs free energy of formation of metal sulfides from oxide structures using H_2S and H_2; (b) stability of bimetallic NbCu sulfide as a function of temperature and H_2S/H_2 partial pressure.

5.3.2 Catalysts characterization

Table 5.1 illustrates the physicochemical properties of bulk monometallic Nb and bimetallic $NbCu_x$ catalysts (x represents the molar ratio of Cu/Nb). The BET surface areas of the bimetallic samples after sulfidation (under pH_2S/pH_2 of 0.01 and 400 °C for 20 h) are below 10 m^2/g and the pore size diameter determined by BJH are in the range of 4 Å, which is in agreement with previous studies (adsorption-desorption isotherms and pore size distribution graphs in SI, Figure S2).[13,27,33,37] This reveals that the addition of copper did not decrease the surface areas and pore diameters but improved the pore volume of the bimetallic catalysts compared to monometallic Nb. This reveals the morphological changes in the presence of copper.

Table 5.1. Physicochemical characteristic of synthesized bulk catalysts.

Catalyst	Cu/Nb loading (wt%)	BET surface area (m^2/g)	Pore volume (cm^3/g)	Pore diameter (Å)
Nb	0.0/100.0	3.3	0.01	4.0
$NbCu_{0.1}$	7.7/92.3	3.4	0.03	4.0
$NbCu_{0.3}$	14.3/85.7	6.5	0.06	4.0
$NbCu_{0.5}$	25.0/75.0	4.3	0.04	4.0
Mo	–	10.1	0.07	4.0

Figure 5.2 shows the typical surface views of the mono- and bimetallic bulk catalysts after calcination and sulfidation. Copper changed the surface morphology of oxide and sulfide catalysts. For instance, the smooth surface morphology of Nb changed to a sponge-like structure in $NbCu_{0.5}$ with smaller particle size. Sulfidation itself led to the structural changes as well. Figure 5.3 displays the FESEM-EDS images of calcined and sulfide materials. Although calcined $NbCu_{0.5}$ showed a homogeneous structure (Figure 5.3a), copper seems to be segregated on the surface of the sulfide samples most likely during sulfidation in the reducing atmosphere (Figure 5.3b, c). This is more significant in the sample with a higher copper content, which could be due to the higher surface free energy of copper with respect to niobium. This could also cover niobium active sites suggesting that an optimum Cu/Nb ratio is required to reach the highest

niobium sulfidation ratio and HDS activity possible. Note that EDS is not an accurate technique to quantify the surface concentration of the elements because sulfur and niobium peaks overlapped in the EDS map. For oxygen, EDS is not reliable and XPS should be used to probe surface oxygen concentration. Electron energy-loss spectroscopy (EELS) and Auger electron spectroscopy can be used for the quantification of the surface.

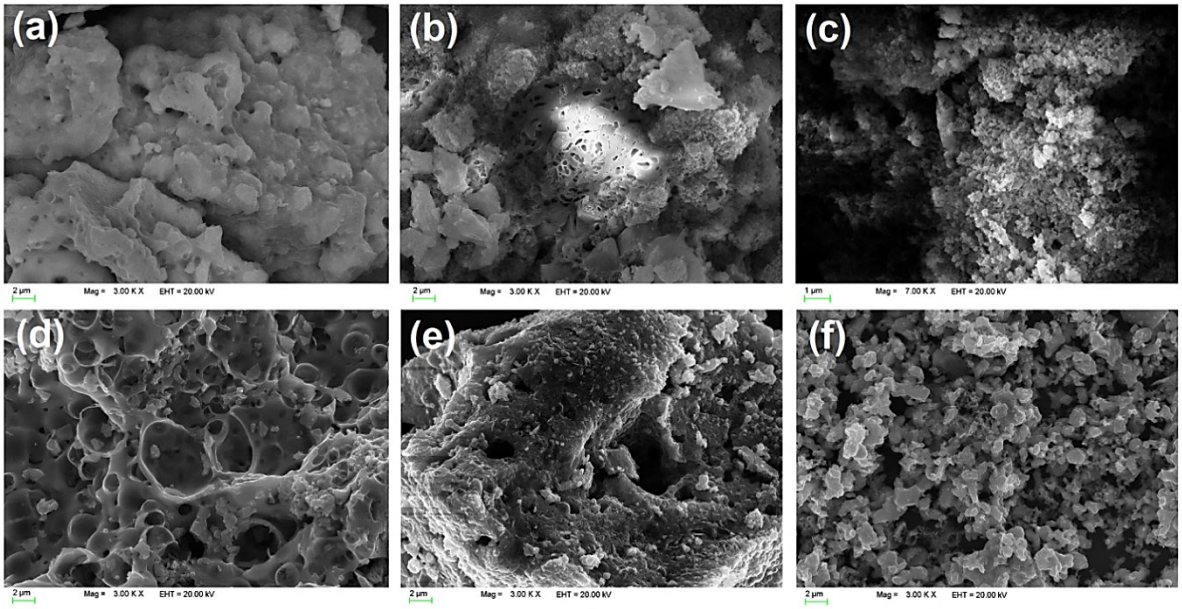

Figure 5.2. FESEM images of bulk calcined: (a) Nb_2O_5, (b) $NbCu_{0.3}$, (c) $NbCu_{0.5}$ catalysts and sulfided (d) Nb_2O_5, (e) $NbCu_{0.3}$, and (f) $NbCu_{0.5}$ catalysts; slfidation performed at 400 °C for 20 h.

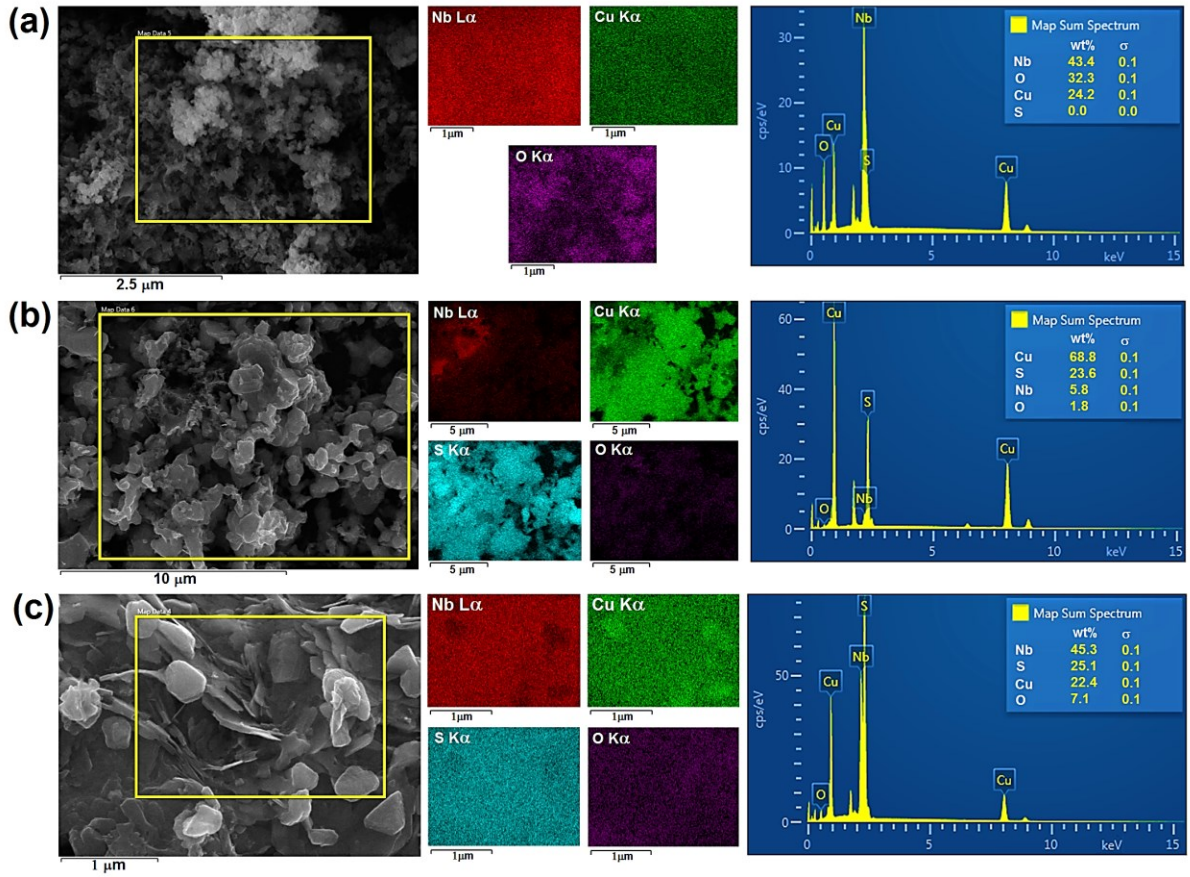

Figure 5.3. FESEM images (on the left); EDS images (on the middle), and elemental mapping (on the right) of (a) calcined $NbCu_{0.5}$, (b) sulfided $NbCu_{0.5}$, and (c) sulfided $NbCu_{0.3}$.

Figure 5.4 exhibits the TPR profile of the calcined catalysts. The amounts of monometallic Nb and Cu catalysts in the TPR profiles correspond to the niobium and copper content of $NbCu_{0.5}$. The reduction of monometallic bulk niobium oxide (Nb_2O_5) and copper oxide (CuO) occur at around 730 °C and 350 °C, respectively, which is in agreement with previous studies.[39,46] For bimetallic catalysts, the reduction peak of Nb_2O_5 shifted to lower temperatures in the presence of copper and merged with the CuO reduction peak. In addition, the small peak at 585 °C disappeared by increasing the Cu loading, indicating the facilitative effect of Cu on the reduction of Nb_2O_5. This also suggests the formation of a bimetallic structure as $Cu_xNb_yO_z$. Table 5.2 lists the normalized areas (per mole of monometallic Nb and Cu catalysts) of the reduction peaks occurred at high and low temperatures. The low-temperature reduction peaks (<300 °C) showed an enhancement in the area revealing the reduction of niobium oxides in a bimetallic structure

with copper oxide. On the other hand, the normalized area corresponding to the reduction of Nb_2O_5 at high temperature (585 °C) decreased in the bimetallic samples. This suggests the formation of two niobium-rich and copper-rich phases with a limited solid solubility of the elements in each other that is consistent with Nb-Cu phase diagram.[47] A decrease in the reduction temperature of CuO in bimetallic catalyst that is lower than bulk Cu could be due to the formation of dispersed CuO species in the presence of niobium.[48]

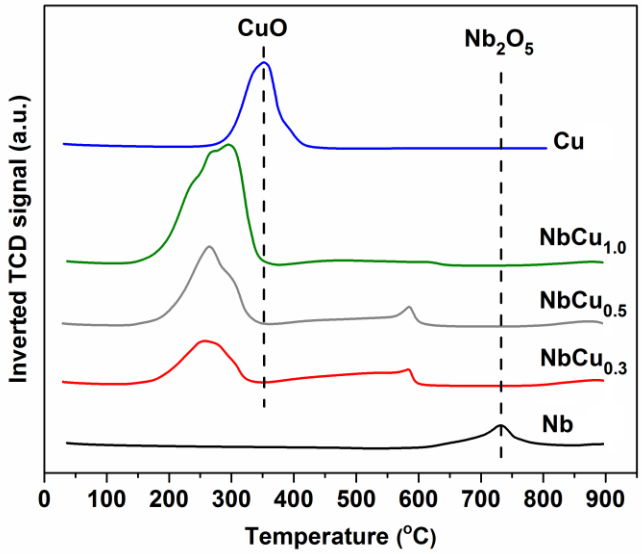

Figure 5.4. TPR profiles of calcined catalysts. The inverted TCD signal reflects hydrogen consumption. The amounts of monometallic Nb and Cu catalysts correspond to the Nb and Cu content of $NbCu_{0.5}$.

Table 5.2. Normalized areas of the reduction peaks per mole of monometallic Nb and Cu.

Catalyst	cat. (mg)	wt % Nb_2O_5	wt % CuO	mmol Nb_2O_5	mmol CuO	Low-T area	High-T area	area/mmol CuO	area/mmol Nb_2O_5	Normalized CuO area enhancement (%)	Normalized Nb_2O_5 area decreasement (%)
Nb	75	100	-	0.28	0.0	-	9.8	-	35	-	0.0
$NbCu_{0.3}$	100	87.3	12.7	0.33	0.16	21.1	6.9	131.7	20.9	47.3	-40.3
$NbCu_{0.5}$	100	77.4	22.6	0.29	0.28	32.3	4.5	115.4	15.5	29.0	-55.7
$NbCu_{1.0}$	100	42.2	57.8	0.16	0.73	60.6	2	83.1	12.5	0.0	-64.3
Cu	25	-	100	0.0	0.31	27.7	-	89.4	-	0.0	-

The interactions of niobium with copper in the calcined samples were investigated using DRIFTS (Figure 5.5). The spectra of bimetallic samples clearly distinguished from the spectra of the monometallic Nb and Cu catalysts. The band at 2056 and 2200.2 cm^{-1} are the first surface niobium sites that reacted with copper oxide species. The intensity of the latter and the peak located at 2344.2 cm^{-1} decreased by the copper content of the material. The DRIFTS spectra in the hydroxyl region (3000–4000 cm^{-1}) show the presence of different type bands of OH groups with various stretching frequencies (Figure 5.5b). Three peaks appear in the spectrum of Nb catalyst at 3700, 3595, and 3480 cm^{-1}. The most intense peak at 3700 cm^{-1} is attributed to the terminal OH groups and two last peaks corresponded to the bridge and multicenter OH groups.[49] For bimetallic materials, the intensities of intermediate frequency peak (3595 cm^{-1}) increased, revealing the formation of bridged OH groups in the presence of copper. Furthermore, a new shoulder a higher frequency of 3748 cm^{-1} appeared. The occurrence of different frequencies of OH groups in metal oxide indicates a different degree of coordination[49] probably because of the interactions between copper and niobium species.

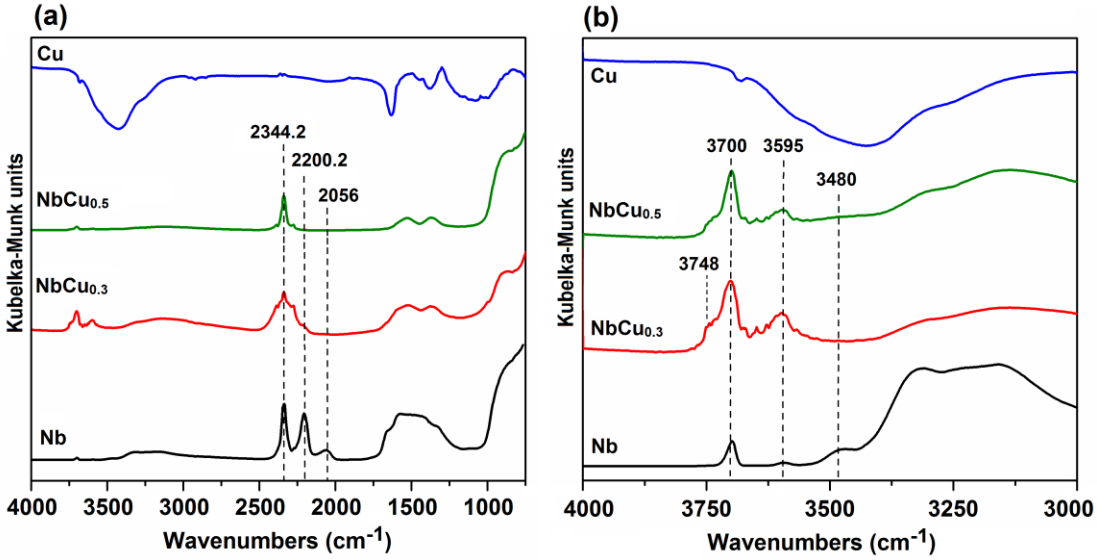

Figure 5.5. (a) DRIFTS spectra of calcined catalysts; (b) hydroxyl region.

XPS analyses were performed on the fresh catalysts after calcination in air at 400 °C and sulfided catalysts (after calcination and then sulfidation at desired temperature and duration) (Figure 5.6

and Table 5.3). The high-resolution XPS spectrum of bulk Nb shows two strong peaks at the binding energies (BEs) of 207.3 and 210.1 eV, respectively, corresponding to the Nb $3d_{5/2}$ and Nb $3d_{3/2}$ core levels of Nb(+5) in Nb_2O_5.[50,51] These peaks shifted to the lower BEs in the calcined copper-containing samples, correlating to the copper content in the catalysts (Figure 5.6a). For instance, Nb $3d_{5/2}$ peak moved from 207.3 eV (in Nb_2O_5) to 207.0 and 206.7 eV in the case of $NbCu_{0.5}$ and $NbCu_{1.0}$ samples, respectively. On the other hand, the Cu 2p core levels in bimetallic materials shifted to the higher BEs compared to bulk Cu (Figure 5.6c). This reveals the charge transfer between niobium and copper and formation of bimetallic structures. Compared to the calcined samples, the Nb 3d peaks of sulfided catalysts shifted to the lower BEs of 203.7 eV and 206.5 eV where the BEs of niobium disulfide (NbS_2) are located[13,52] (Figure 5.6b and Table 5.3). This correlates with Cu/Nb ratio implying the facilitative effects of copper on niobium oxide sulfidation. Cu 2p doublets in the XPS spectra of sulfided samples negatively shifted to the BEs of copper sulfide (Figure 5.6d). The S $2p_{3/2}$ and S $2p_{1/2}$ peaks at BEs of 162.0 and 163.1 eV further confirm the formation of NbS_2 (Figure 5.6e).[52] The XPS spectrum acquired on the reduced $NbCu_{0.5}$ catalyst (using hydrogen gas at 400 °C for 20 h) is a typical feature of Nb_2O_5 in which Nb $3d_{5/2}$ still centered at 207.3 eV while Cu 2p moved toward lower oxidation states. This verifies the formation of niobium and copper sulfide structures during sulfidation process, not reduced species. Indeed, Nb $3d_{5/2}$ peak of niobium carbide and metallic niobium at BEs of 202.5 eV and 202.2 eV, respectively, were not observed in the XPS spectra of the sulfided materials.[50,53]

Table 5.3. Binding energy values of Nb 3d and Cu 2p in the sulfided catalysts.

sample	**Binding Energy (eV)**							
	NbS_2		**NbO_x**		**Nb_2O_5**		**Cu $2p_{3/2}$**	**Cu $2p_{1/2}$**
	Nb $3d_{5/2}$	**Nb $3d_{3/2}$**	**Nb $3d_{5/2}$**	**Nb $3d_{3/2}$**	**Nb $3d_{5/2}$**	**Nb $3d_{3/2}$**		
Nb	203.9	206.7	205.2	207.9	208.0	210.7	–	–
$NbCu_{0.3}$	203.8	206.5	204.7	207.6	207.0	209.6	932.7	952.6
$NbCu_{0.5}$	203.7	206.4	204.6	207.4	206.8	209.5	932.6	952.5
$NbCu_{1.0}$	203.7	206.4	204.5	207.3	206.6	209.3	932.5	952.4

* Mo sulfidation degree is 74.4 % as MoS_2

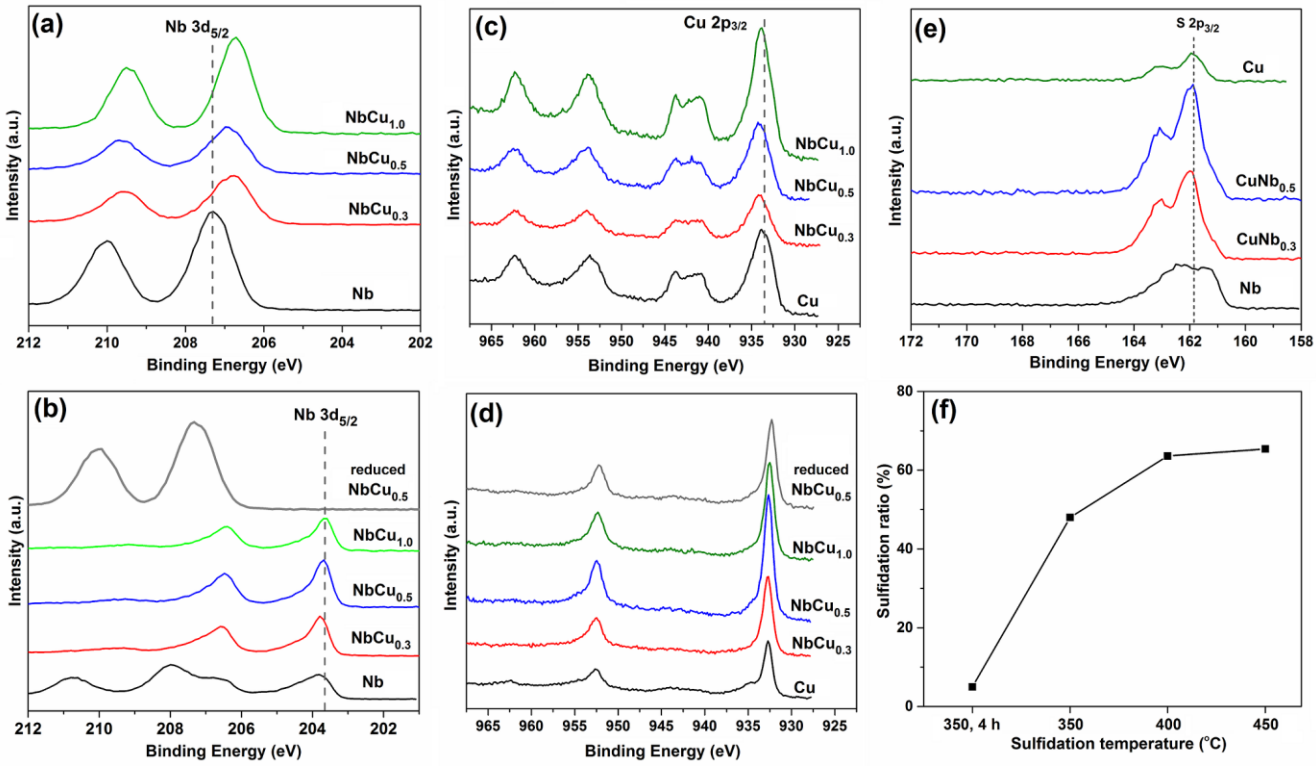

Figure 5.6. XPS spectra: Nb 3d core levels of (a) calcined and (b) sulfided samples (sulfidation at 400 °C for 20 h); Cu 2p core levels of (c) calcined and (d) sulfided materials; (e) S 2p core levels of sulfided samples, and (f) effect of sulfidation temperature on Nb sulfidation ratio.

Deconvolution of XPS spectra revealed that both oxide and sulfide phases are simultaneously present in the sulfided samples (Figure 5.7 and Table 5.3). The sulfidation ratio of niobium (% NbS_2) was calculated based on the area of deconvoluted peaks corresponding to NbS_2, unreduced Nb_2O_5, and partially reduced Nb_2O_5 shown as NbO_x (Figure 5.7 and Table 5.4). The niobium sulfidation degree increases by the sulfidation temperature and duration (Figure 5.6f) as well as operating pressure. For example, a 50-degree increase in the sulfidation temperature from 350 to 400 °C led to 33% enhancement in niobium sulfidation ratio. The highest Nb sulfidation was obtained above 400 °C in agreement with a previous study[23] in which the highest HDS activity of carbon-supported niobium catalyst was obtained by sulfidation at 400 °C. The sulfidation ratio of bulk Mo under identical conditions was 74.4% (Figure S3, Supporting Information). On the other hand, pressurizing the system from 0.1 to 3 MPa at 400 °C promoted niobium sulfidation by 17 %. Allali et. al.[23] reported that the highest niobium sulfidation ratio at 400 °C using H_2S

was obtained over the Nb-based catalyst that dried at room temperature. Here we found that dried $NbCu_{0.5}$ sample exhibited negligible sulfidation ratio. Figure 5.7 and Table 5.4 reveal the presence of oxide and sulfide species in $NbCu_{0.3}$ after sulfidation. Most likely Nb_2O_5 undergoes a reduction process to form niobium oxides with lower oxidation states (shown as NbO_x), which is a mixture of NbO_2 and NbO, and then transforms to the NbS_2 structure.

The fraction of niobium sulfide (NbS_2) increased with increasing copper content of the materials. It maximized at around 64 % for the Cu/Nb molar ratio of 0.5 and then leveled off for higher Cu content in the catalysts (Figure 5.7b and Table 5.4). The calculated elemental surface concentration (Table 5.4) reveals the surface tendency of Cu, which is in agreement with the EDS mapping. In addition, the normalized molar ratios of Cu/Nb and S/Nb are in the range of 0.63-0.86 and 2.2-2.7, respectively, which is consistent with the stoichiometry of $Cu_{0.65}NbS_2$ compound. The XRD patterns of sulfided bimetallic samples in Figure 5.8 prove the formation of $Cu_{0.65}NbS_2$ structure in addition to the presence of a small fraction of copper sulfide. However, the counterpart-oxidized compound ($Cu_{0.65}NbO_2$) was not identified in the XRD patterns of calcined samples. Only crystalline copper oxide and amorphous niobium oxides were formed during calcination in air at 400 °C. The same amorphous Nb_2O_5 structure was reported for the calcination temperature of 400 °C.[54] The HRTEM images in Figure 5.8 showed the amorphous and crystalline structures of sulfided Nb and $NbCu_{0.3}$, respectively. In contrast to $NbCu_{0.3}$, layered NbS_2 phase only partially formed in Nb catalyst after sulfidation (Figure 5.8c). The fringe size of 0.29 and 0.32 nm can be attributed to the (004) and (100) planes of $Cu_{0.65}NbO_2$ (Figure 5.8d). However, distinguishing between (100) and (101) planes in difficult because of very close fringe sizes 0.29 and 0.28 nm, respectively ((PDF no.00-015-0409).

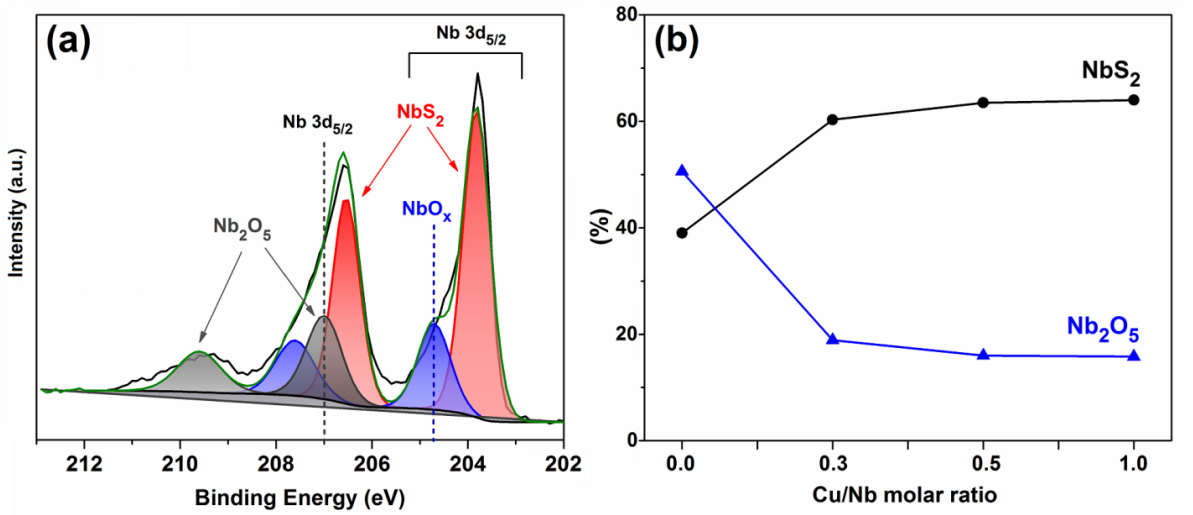

Figure 5.7. (a) Deconvoluted XPS spectra of sulfided $NbCu_{0.3}$; (b) fraction of NbS_2 and Nb_2O_5 in sulfided samples as a function of Cu/Nb ratio.

Table 5.4. Amount of sulfided, partially reduced and unreacted Nb_2O_5 present in the sulfided catalysts calculated by the areas of corresponding deconvoluted peaks; elemental surface composition of the sulfided samples.

sample	**presented amount in the sample (%)**			**surface composition (atomic %)**		
	NbS_2	**NbO_x**	**Nb_2O_5**	**Nb**	**Cu**	**S**
Nb	39.0	10.3	50.7	48.7	–	51.3
$NbCu_{0.3}$	60.3	20.8	18.9	26.0	16.4	57.6
$NbCu_{0.5}$	63.6	20.4	16.0	24.2	16.9	58.9
$NbCu_{1.0}$	64.0	20.2	15.8	22.1	19.1	58.8

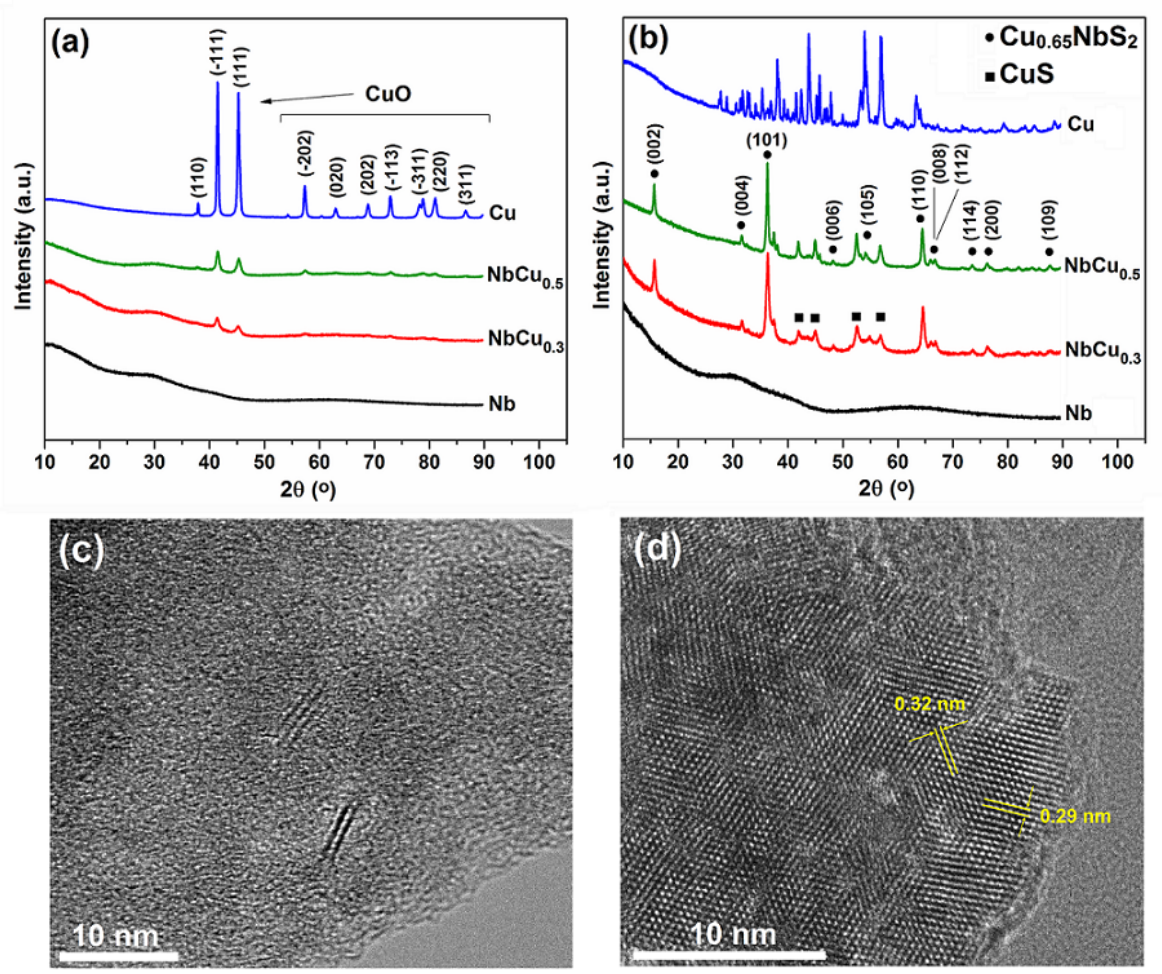

Figure 5.8. XRD patterns of (a) calcined and (b) sulfided samples at 400 °C for 20 h. The peaks were assigned based on the powder diffraction file numbers of 00-015-0409 for $Cu_{0.65}NbS_2$ and 97-008-7123 for CuO. HRTEM images of (c) sulfided Nb and (d) sulfided $NbCu_{0.3}$.

5.3.3 Catalytic performance in hydrodesulfurization of DBT

The catalytic properties of the synthesized catalysts were assessed in the continuous hydrodesulfurization of DBT at 325 °C and 3 MPa for 24 hours on stream. The catalysts were sulfided *in situ* before the reaction at 400 °C for 20 h under 3 MPa H_2. The amount of sulfur in the feed was seven orders of magnitude higher that the required partial pressures of $p(H_2S)/p(H_2)$ to stabilize NbS_2.[38] Figure 5.9 shows the DBT conversion and activities of the monometallic Nb and bimetallic NbCu catalysts. We also measured the activity of bulk molybdenum (Mo) catalyst under identical conditions as a reference material with almost the same sulfidation ratio of 74.4%

(Figure S4). A negligible conversion obtained over reduced Nb catalyst (around 1% DBT conversion after 24 h) verifies the necessity of sulfidation pretreatment for HDS catalysis. Sulfided Nb exhibited higher DBT conversion than the sulfided Mo catalyst consistent with previous studies.[26,30] Monometallic Cu catalyst tested under identical conditions was found inactive as expected since first-row TMS are inactive in HDS. Compared to the monometallic Nb, the addition of copper promoted the HDS activities of the catalysts. The DBT conversions depend on the Cu/Nb molar ratio following a volcano trend; the DBT conversion increased by copper loading in the sample, maximized at Cu/Nb molar ratio of 0.3, and then decreased for the higher Cu/Nb ratio of 0.5 (Figure 5.9a). However, both $CuNb_{0.3}$ and $CuNb_{0.5}$ have the same level of NbS_2, as determined by XPS. Therefore, a decrease in the DBT conversion by increasing Cu/Nb ratio could be attributed to the surface coverage of active sites by Cu species as shown by EDS mapping. The activities of the mono- and bimetallic catalysts showed different trends over time-on-stream (Figure 5.9b). Both monometallic Nb and Mo catalysts exhibited a decreasing conversion trend over reaction time, while bimetallic NbCu conversions improved except for $NbCu_{0.5}$. We attributed the decreasing trend of $NbCu_{0.5}$ to the higher copper content in this sample.

Figure 5.9c illustrates the activities of the catalysts per mole of the active metal (Nb or Mo) and per total mass of the catalyst. The mass activities of bimetallic NbCu catalysts were higher than Nb catalyst. However, a high Cu/Nb molar ratio above 0.3 suppressed the activity per mole of niobium even to below the activity obtained by Nb catalyst. This implies the optimized Cu/Nb ratios of 0.3 for HDS catalysis and deactivation effect of copper for higher ratios. This is further proved in Figure 5.9d demonstrating the activities per BET surface areas of the sulfided catalysts and the surface fraction of NbS_2. As seen, increasing Cu/Nb ratio from 0.3 to 0.5, results in a substantial decrease in the activity per surface NbS_2 (red dashed line). This implies that copper coverage deactivates the active sites although improved the sulfidation degree of niobium. The greatest activity per BET was also obtained for the bimetallic catalyst as Cu/Nb ratio of 0.1 However, in general, the HDS activities of the sulfides do not correlate with the BET surface areas.[55]

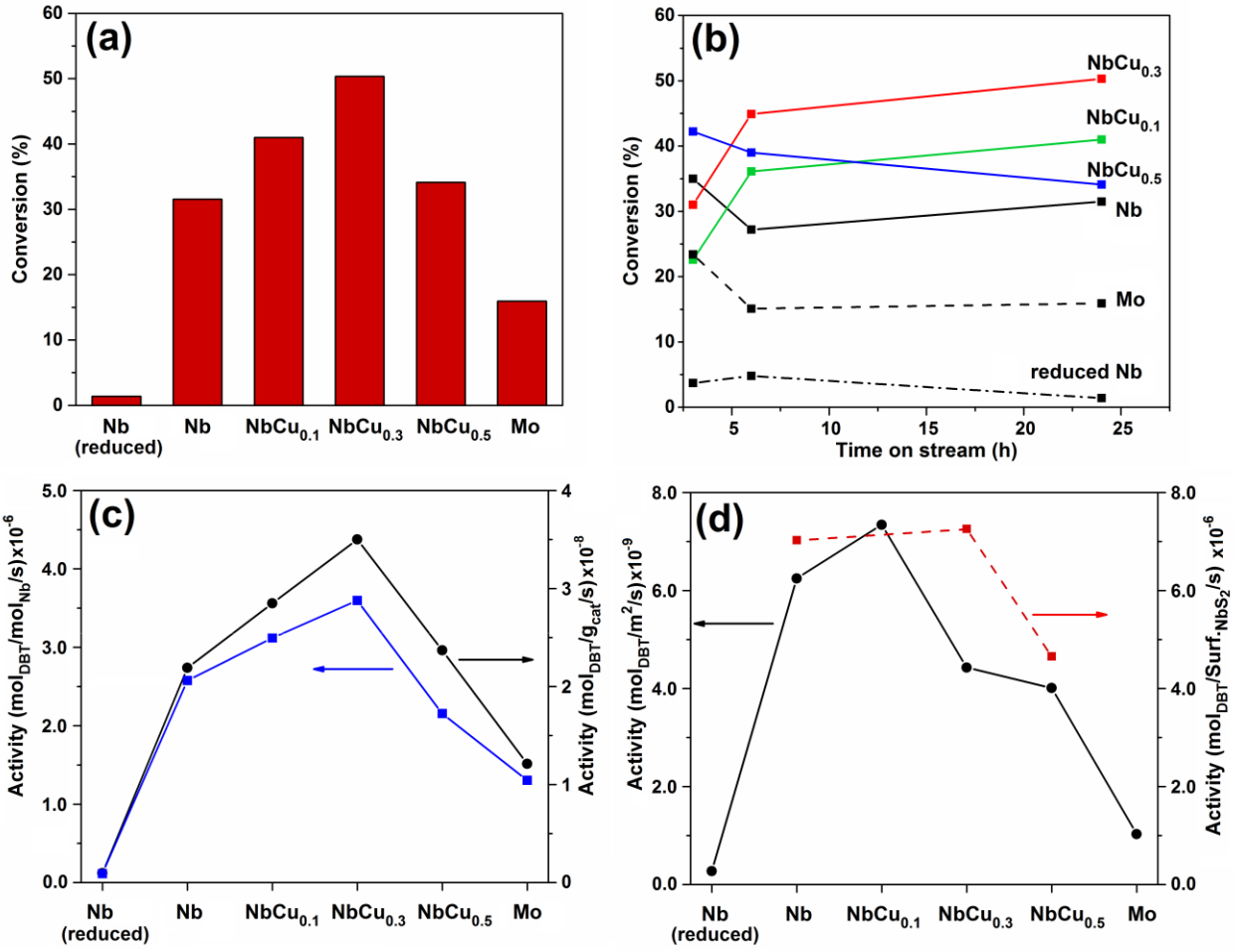

Figure 5.9. (a) DBT conversion at 325 °C and 3MPa after 24 h on stream, and (b) at different time-on-stream; (c) activities after 24 h on-stream per mole of Nb and total mass of catalyst; (d) activities after 24 h normalized per BET surface area of the sulfided materials and surface fraction of NbS_2. The amount of catalyst was adjusted to keep 2.26 mmol Nb (Mo) in all reactions. All the catalysts were pre-sulfided (reduced) *in situ* at 400 °C for 20 h.

Figure 5.10 shows the selectivities and products distribution as a function of Cu/Nb molar ratios. According to the HDS reaction mechanism (Scheme 5.1), the reaction products include biphenyl as direct desulfurization (DDS) route, hydrogenation products, and sulfur-free hydrocracking compounds with 5- and 6-membered rings. Within the same range of DBT conversion (32 ± 9%), Nb catalyst showed 37.9% selectivity to BP (DDS route), while it increased to 54% in the case of $NbCu_{0.5}$ catalyst, both higher than that of Mo catalyst. The higher intrinsic activity and DDS selectivity of the Nb catalyst than that of Mo were already reported in HDS of thiophene.[37]

Hydrocracking (HCK) selectivity showed a decreasing trend by increasing the Cu/Nb ratio. It was 26.9% in the case of Nb and minimized to 7.7% for $NbCu_{0.5}$ catalyst. Although the hydrogenation (HYD) selectivities slightly improved in bimetallic catalysts, distribution of HYD products significantly changed (Figure 5.10b). The selectivities towards CHB enhanced for bimetallic catalysts as compared to Nb and Mo catalysts. On the other hand, the selectivity to BCH declined for NbCu catalysts. The selectivities to sulfur-containing molecules such as HHDBT and THDBT (from HYD route) decreased in bimetallic NbCu catalysts suggesting that copper improved the sulfur tolerance of hydrogenation active sites. This is due to the lower Gibbs free energy of sulfidation of copper than niobium using H_2S.[38] We also found that HCK selectivity is correlated to the fraction of Nb_2O_5 in the sample whereas NbS_2 promotes DDS products (Figure 5.10c). Therefore, the cracking activity can be attributed to the unreduced niobium oxides. Figure 5.11 shows the yields of HDS products per mole of niobium and mass of catalysts. As can be seen, the higher yields of DDS and HYD products were achieved in the case of bimetallic NbCu samples, 100% greater than Nb and Mo catalysts.

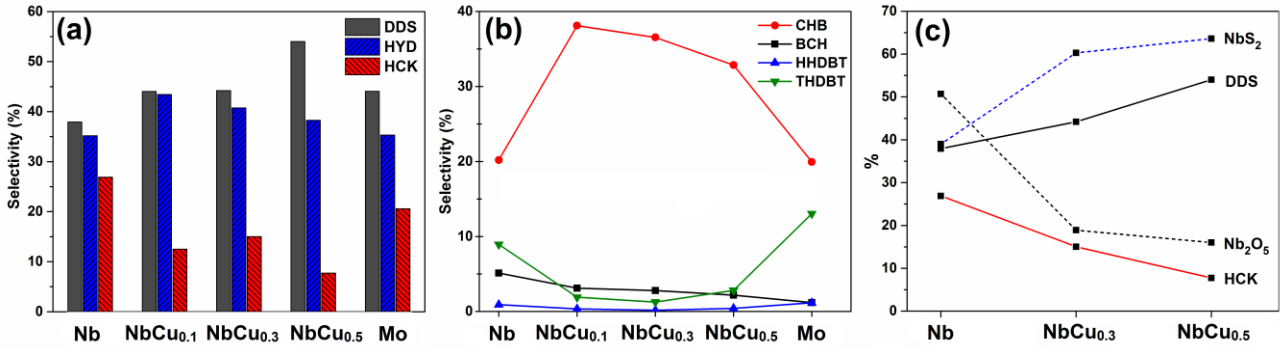

Figure 5.10. (a, b) Selectivity as a function of Cu/Nb molar ratio at 32 ± 9% DBT conversion (except for 50% conversion of $NbCu_{0.3}$ and 16% for Mo), and (c) DDS and HCK selectivities and fraction of Nb_2O_5 and NbS_2 in the catalysts determined by XPS; all after 24 h on stream at 325 °C and 3 MPa

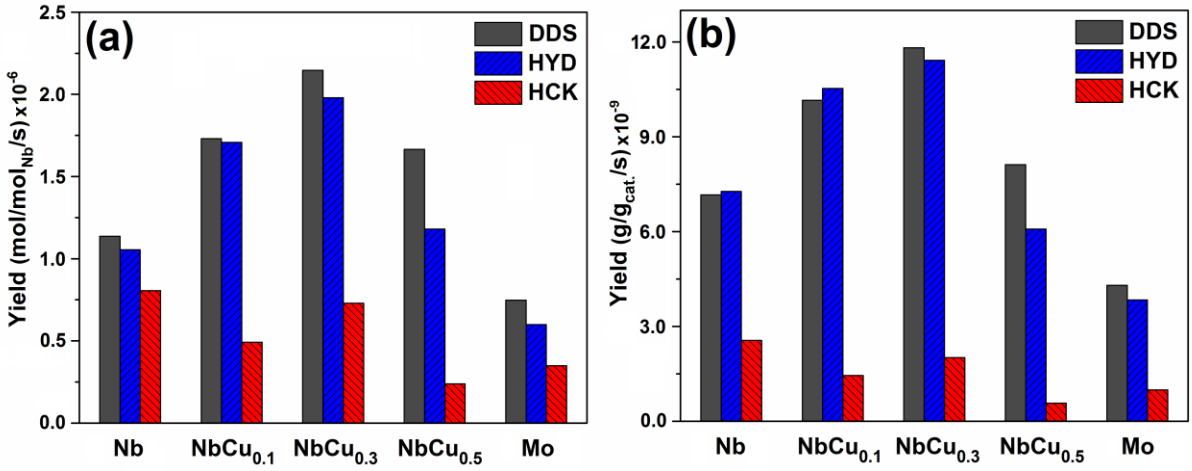

Figure 5.11. Product yields as a function of Cu/Nb molar ratio: (a) mole of products per mole of active metal; (b) mass of products per mass of catalyst; all after 24 h on stream at 325 °C and 3 MPa.

5.4 Conclusions

A series of bimetallic NbCu catalysts at different Cu/Nb molar ratios were prepared via coprecipitation method at room temperature. Copper nitrate precipitates using oxalate species of niobium precursor without using external precipitant. The synthesized catalysts were sulfided at 400 °C and then evaluated in the HDS of DBT at 325 °C and 3 MPa. Adding copper to the Nb-based catalyst led to a significant decrease in the reduction/sulfidation temperature of niobium oxides correlating to the Cu/Nb ratio. DBT conversion depended on the Cu/Nb molar ratios and the presence of Nb sulfides as active sites for HDS reaction. However, there is a threshold Cu/Nb of 0.3 to maximize the activity. At higher Cu/Nb, copper coverage deactivates the NbS_2 active sites. Nb and NbCu catalysts delivered higher DBT conversions and activities than the Mo catalyst. Compared to the Nb catalyst, the activity per mole of niobium and per mass of catalyst enhanced in the bimetallic catalyst (at Cu/Nb of 0.3) by 60% and 40%, respectively. Copper also improved and suppressed the DDS and hydrocracking selectivities, respectively. The cracking selectivity correlated with the fraction of niobium oxide (Nb_2O_5) in the sample. In addition, selectivities to sulfur-containing molecules such as HHDBT and THDBT decreased in the presence of copper. Bimetallic catalysts enhanced the DDS and HYD products yields, with respective to monometallic Nb sample. The study demonstrates that NbCu structures could be a promising candidate as HDS catalyst.

Acknowledgements

Financial support from NSERC CRD and Imperial Oil is acknowledged. Dr. Anqiang He, Dr. Shihong Xu, and Diane Caird are gratefully acknowledged for SEM, XPS, and XRD data acquisition at the U of A.

5.5 Supporting information

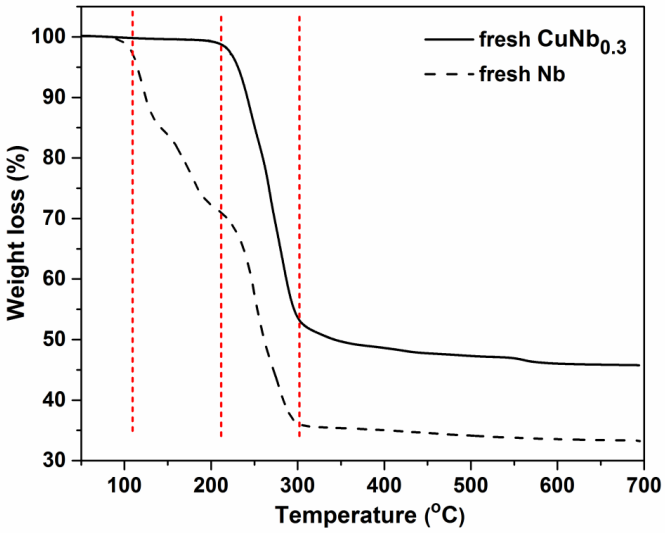

Figure S1. TGA profiles of Nb oxalate hydrate (fresh Nb) and dried $CuNb_{0.3}$ material performed under 50 ml/min N_2 from 30 °C to 700 °C on 10 °C/min.

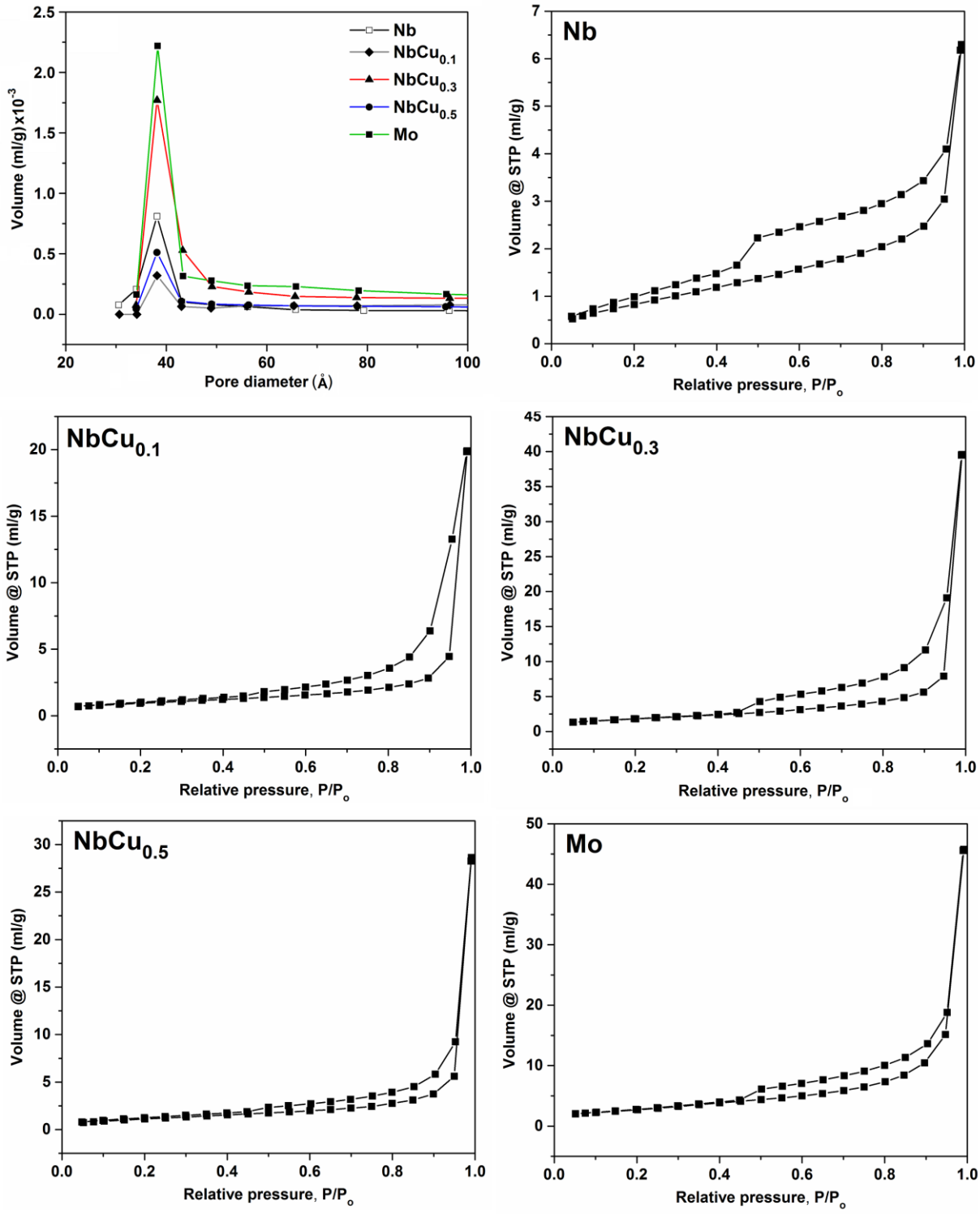

Figure S2. Pore size distribution and nitrogen adsorption-desorption isotherms of the sulfided catalysts; sulfidation at 400 °C for 20 h.

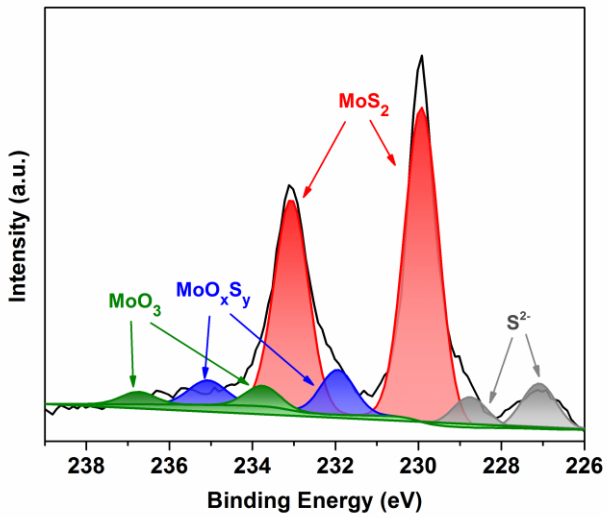

Figure S3. Deconvoluted XPS spectrum of Mo after sulfidation at 400 °C for 20 h.

5.6 References

(1) Bara, C.; Plais, L.; Larmier, K.; Devers, E.; Digne, M.; Lamic-Humblot, A. F.; Pirngruber, G. D.; Carrier, X. J. Am. Chem. Soc. 2015, 137, 15915–15928.

(2) Wang, Q. H.; Kalantar-Zadeh, K.; Kis, A.; Coleman, J. N.; Strano, M. S. Nat. Nanotechnol. 2012, 7, 699–712.

(3) Pang, Q.; Liang, X.; Kwok, C. Y.; Nazar, L. F. Nat. Energy 2016, 1, 16132.

(4) Lai, C.-H.; Lu, M.-Y.; Chen, L.-J. J. Mater. Chem. 2012, 22, 19–30.

(5) Ou, X.; Xiong, X.; Zheng, F.; Yang, C.; Lin, Z.; Hu, R.; Jin, C.; Chen, Y.; Liu, M. J. Power Sources 2016, 325, 410–416.

(6) Montoya, J. H.; Seitz, L. C.; Chakthranont, P.; Vojvodic, A.; Jaramillo, T. F.; Nørskov, J. K. Nat. Mater. 2016, 16, 70–81.

(7) Tsai, M.-L.; Su, S.-H.; Chang, J.-K.; Tsai, D.-S.; Chen, C.-H.; Wu, C.-I.; Li, L.-J.; Chen, L.-J.; He, J.-H. ACS Nano 2014, 8, 8317–8322.

(8) Kibsgaard, J.; Chen, Z.; Reinecke, B. N.; Jaramillo, T. F. Nat. Mater. 2012, 11, 963–969.

(9) Ha, E.; Liu, W.; Wang, L.; Man, H.-W.; Hu, L.; Tsang, S. C. E.; Chan, C. T.-L.; Kwok, W.-M.; Lee, L. Y. S.; Wong, K.-Y. Sci. Rep. 2017, 7, 39411-39419.

(10) Staszak-Jirkovský, J.; Malliakas, C. D.; Lopes, P. P.; Danilovic, N.; Kota, S. S.; Chang, K.-C.; Genorio, B.; Strmcnik, D.; Stamenkovic, V. R.; Kanatzidis, M. G.; Markovic, N. M. Nat. Mater. 2015, 15, 197–203.

(11) Asadi, M.; Kumar, B.; Behranginia, A.; Rosen, B. a; Baskin, A.; Repnin, N.; Pisasale, D.; Phillips, P.; Zhu, W.; Haasch, R.; Klie, R. F.; Král, P.; Abiade, J.; Salehi-Khojin, A. Nat. Com. 2014, 5, 4470-4478.

(12) Asadi, M.; Kim, K.; Liu, C.; Addepalli, A. V.; Abbasi, P.; Yasaei, P.; Phillips, P.; Behranginia, A.; Cerrato, J. M.; Haasch, R.; Zapol, P.; Kumar, B.; Klie, R. F.; Abiade, J.; Curtiss, L. A.; Salehi-Khojin, A. Science 2016, 353, 467–470.

(13) Dash, J. K.; Chen, L.; Dinolfo, P. H.; Lu, T. M.; Wang, G. C. J. Phys. Chem. C 2015, 119, 19763–19771.

(14) Chhowalla, M.; Shin, H. S.; Eda, G.; Li, L.-J.; Loh, K. P.; Zhang, H. Nat. Chem. 2013, 5, 263–275.

(15) Chianelli, R. R. Oil Gas Sci. Technol. - Rev. l'IFP 2006, 61, 503–513.

(16) Aray, Y.; Zambrano, D.; Cornejo, M.; Ludeña, E. V.; Iza, P.; Vidal, A. B.; Coll, D. S.; Jímenez, D. M.; Henriquez, F.; Paredes, C. J. Phys. Chem. C 2014, 118, 27823–27832.

(17) Gutiérrez, O. Y.; Singh, S.; Schachtl, E.; Kim, J.; Kondratieva, E.; Hein, J.; Lercher, J. A. ACS Catal. 2014, 4, 1487–1499.

(18) Eijsbouts, S.; Anderson, G. H.; Bergwerff, J. A.; Jacobi, S. Appl. Catal. A Gen. 2013, 458, 169–182.

(19) Shafi, R.; Hutchings, G. J. Catal. Today 2000, 59, 423–442.

(20) Babich, I. V.; Moulijn, J. A. Fuel 2003, 82, 607–631.

(21) Stanislaus, A.; Marafi, A.; Rana, M. S. Catal. Today 2010, 153, 1–68.

(22) Song, C. Catal. Today 2003, 86, 211–263.

(23) Allali, N.; Marie, A. M.; Danot, M.; Geantet, C.; Breysse, M. J. Catal. 1995, 156, 279–289.

(24) Gaborit, V.; Allali, N.; Danot, M.; Geantet, C.; Cattenot, M.; Breysse, M.; Diehl, F. Catal. Today 2003, 78, 499–505.

(25) Pecoraro, T. A.; Chianelli, R. R. J. Catal. 1981, 67, 430–445.

(26) Lacroix, M.; Boutarfa, N.; Guillard, C.; Vrinat, M.; Breysse, M. J. Catal. 1989, 120, 473–477.

(27) Danot, M.; Afonso, J.; Des, C. T.; Portefaix, J. L.; Breysse, M. Catal. Today 1991, 10, 629–643.

(28) Ziolek, M. Catal. Today 2003, 78, 47–64.

(29) Jehng, J. M.; Wachs, I. E. Catal. Today 1990, 8, 37–55.

(30) Hermann, N.; Brorson, M.; Topsøe, H. Catal. Letters 2000, 65, 169–174.

(31) Gaborit, V.; Allali, N.; Geantet, C.; Breysse, M.; Vrinat, M.; Danot, M. Catal. Today 2000, 57, 267–273.

(32) Egorova, M.; Prins, R. , J. Catal. 2004, 225, 417–427.

(33) Kadijk, F.; Jellinek, F. J. Less Common Met. 1969, 19, 421–430.

(34) Liu, Z. L.; Cai, L. C.; Zhang, X. L. J. Alloys Compd. 2014, 610, 472–477.

(35) Jellinek, F.; Brauer, G.; Müller, H. Nature 1960, 185, 376–377.

(36) Afanasiev, P.; Bezverkhyy, I. Appl. Catal. A, Gen. 2007, 322, 129–141.

(37) Geantet, C.; Afonso, J.; Breysse, M.; Allali, N.; Danot, M. Catal. Today 1996, 28, 23–30.

(38) Zdražil, M. Catal. Today 1988, 3, 269–365.

(39) Wachs, I. E.; Briand, L. E.; Jehng, J.-M.; Burcham, L.; Gao, X. Catal. Today 2000, 57,

323–330.

(40) Wachs, I. E.; Jehng, J. M.; Deo, G.; Hu, H.; Arora, H. Catal. Today 1996, 28, 199–205.

(41) Jongen, N.; Bowen, P.; Lemaître, J.; Valmalette, J.-C.; Hofmann, H. J. Colloid Interface Sci. 2000, 226, 189–198.

(42) Pérez-Ramírez, J.; Berger, R. J.; Mul, G.; Kapteijn, F.; Moulijn, J. A. Catal. Today 2000, 60, 93–109.

(43) Kuhn, M.; Rodriguez, J. A. Catal. Letters 1995, 32, 345–355.

(44) Ridder, R. De; Tendeloo, G. Van; Landuty, J. Van; Dyck, D. Van; Amelince, S. phys. stat. sol. 1976, 37, 591–606.

(45) Craig, J. R.; Barton, P. B. Econ. Geol. 1973, 68, 493–506.

(46) Mansouri, A.; Khodadadi, A. A.; Mortazavi, Y. J. Hazard. Mater. 2014, 271, 120–130.

(47) Chakrabarti, D. J.; Laughlin, D. E. Bull. Alloy Phase Diagrams 1982, 2, 455–460.

(48) Xiang, Y.; Barbosa, R.; Li, X.; Kruse, N. ACS Catal. 2015, 5, 2929-2934.

(49) Braga, V. S.; Dias, J. a; Dias, S. C. L.; De Macedo, J. L. Chem. Mater. 2005, 17, 690–695.

(50) Teixeira da Silva, V. L. S.; Schmal, M.; Oyama, S. T. J. Solid State Chem. 1996, 123, 168–182.

(51) Izawa, K.; Ida, S.; Unal, U.; Yamaguchi, T.; Kang, J. H.; Choy, J. H.; Matsumoto, Y. J. Solid State Chem. 2008, 181, 319–324.

(52) Wu, X.; Tao, Y.; Ke, X.; Zhu, J.; Hong, J. Mater. Res. Bull. 2004, 39, 901–908.

(53) Badrinarayanan S.; Sinha, S. Appl. Phys. 1991, 69, 1141.

(54) Paulis, M.; Martín, M.; Soria, D. B.; Díazb, A.; Odriozola, J. A.; Montes, M. Appl. Catal. A, Gen. 1999, 180, 411–420.

(55) Harris, S.; Chianelli, R. R. J. Catal. 1984, 86, 400–412.

Chapter 6. Supported Copper-Niobium Sulfide Layered Structure as Hydrodesulfurization Catalyst

6.1 Introduction

Two-dimensional transition metal sulfides (TMS) with a general formula of MS_2 have attracted significant attentions for their versatile striking properties in catalysis, energy storage, and electronic devices.[1–9] In contrast to graphene that is chemically inert, TMS exhibited activities in a wide range of applications while providing the benefits of dimensionality and tunable electronic structure simultaneously.[8] TMS are dominant as layered structures in which packed layer of earth-abundant metal atoms such as Mo, W, and Nb covalently sandwiched between two layers of sulfur atoms.[8,10] The weak van der Waals forces between the layers allow the stabilization of single layers as in graphene.[8]

TMS can catalyze a wide range of reactions such as oil hydroprocessing[11–14], hydrogenation of olefins, ketones, and aromatics, dealkylation, ring opening of aromatics, isomerization of paraffins, Fischer–Tropsch, alcohol synthesis, and direct coal liquefaction.[15] In addition, the tunable structural and electronic properties of layered TMS make them attractive in optoelectronic,[16] energy storage materials,[3–5] solar cells,[17,18] and recently as photo- and electrocatalyst for hydrogen evolution[9,19,20] and CO_2 reduction[6,7]. Molybdenum sulfide (MoS_2) as the most commonly used TMS also exhibited a promising performance in bio-oil upgrading.[21] However, to maintain the catalysts active during the reaction, an appropriate amount of sulfur (i.e., H_2S) should be added to the feed, which deprives the advantage of bio-oil low-sulfur content.[21] Therefore, the research for alternative TMS delivering a higher activity while requires lower sulfur in the feed is always underway.

Niobium sulfide (NbS_2) with similar layered feature as MoS_2 but different *d*-band filling could be a promising candidate. The required pH_2S/pH_2 to stabilized NbS_2 is around 10^{-11}, three orders of magnitude lower than the required value for MoS_2 (10^{-8}).[22] NbS_2 has also exhibited exotic properties not shown by other TMS.[10,23–25] For instance, previous studies revealed that NbS_2 is intrinsically more active than MoS_2 and WS_2 in HDS of dibenzothiophene (DBT)[26–29] and hydrogenation of biphenyl (BP)[27]. It should be noted that MoS_2 it is not able to meet the current

stringent environmental regulations, minimizing the sulfur content of fuels to 10 ppmw, even after being promoted with either cobalt or nickel species.[11,12,26,30–36] Moreover, in contrast to the conventional NiMo HDS catalysts, the activity and durability of Nb-based catalyst were not diminished by H_2S as a side product of HDS reaction.[32,37,38] Nonetheless, NbS_2 catalysts have not found many catalytic applications because of stability of niobium oxides, Nb_2O_5 and NbO_2, against reduction/sulfidation with the heats of formation of –380 and –395 kJ/mol, respectively.[39] The Gibbs free energies of sulfidation of NbO_2 and Nb_2O_5 using H_2S at 600 K are +82 and +108 kJ/mol, respectively.[22] This causes the reduction/sulfidation of niobium oxides occurring above 800 °C, which is not feasible industrially.[39–41]

We showed in Chapter 5 that copper facilitates the reduction and sulfidation of niobium oxides. However, for the supported niobium oxides, the sulfidation and reduction behavior (kinetic and thermodynamic) are strongly influenced by the nature of the support material.[26,22,42,43] In particular, in the case of basic materials in which Nb^{5+} strongly incorporates into the support.[43] For instance, Nb_2O_5 supported on Al_2O_3 and ZrO_2 showed no redox properties whereas trace and significant redox products were observed in the case of TiO_2 and SiO_2, respectively.[43,44] A higher degrees of niobium oxides sulfidation and thus HDS activity was achieved when carbon employed as a support instead of alumina.[26,42] These behaviors are due to the weak metal-support interactions between niobium species and supports such as silica and carbon. Furthermore, niobium trisulfide (NbS_3) that is more active but less stable than NbS_2 under hydrotreatment conditions only detected on a carbon support using , not alumina.[26,27,37] Carbon-supported NbS_2 catalyst exhibited higher thiophene HDS activity than MoS_2 on the same support revealing higher intrinsic activity of supported NbS_2 than MoS_2.[26]

Cracking is an intrinsic property of oxidized and sulfided Nb-based catalysts.[27,45] Lacroix et. al.[27] observed that among the first- and second-row transition metal sulfides, only NbS_2 promoted the hydrocracking reaction in the low-temperature hydrogenation of biphenyl. Bulk and supported niobia (Nb_2O_5) were found exclusively acidic. Bulk Nb_2O_5 is well known for its Brønsted acid sites but when supported on oxides exhibited Lewis acid properties as coordinatively unsaturated sites.[2] Besides the effects of support material, the surface coverage of Nb species on the support strongly affects the formation of different types of niobium oxides with various acidic and catalytic characters.[41,43,46–48] Jehng and Wachs[2] reported that niobium oxides at low loading

behaved as coordinatively unsaturated Lewis acid sites (CUS). The number of these Lewis acid sites decreased by surface coverage of the niobium oxide overlayers achieved at increased Nb loadings.[49,50] At a very high loading above monolayer coverage, bulk niobia with Brønsted acid sites forms on the surface. This also affects the reduction and sulfidation properties of layered transition metal oxides. For example, an increased metal loading (number of layers) promoted sulfidation and reduction of tungsten and nickel oxides.[51] The structure of niobia on oxide supports has been studied extensively. Nonetheless, the literature on niobium supported on carbon-based materials is rare.

In this contribution, we present the sulfidation and HDS performances of niobium supported on mesoporous carbon via impregnation at different Nb loading of 2.0, 6.0, and 12.0 wt%. The catalysts were also promoted with copper at various Cu/Nb ratios. We observed that addition of copper facilitated the reduction and sulfidation of niobium oxides over the entire range of metal loadings and Nb sulfidation increased by Cu/Nb ratio. Nb sulfidation varied by Nb loading and a high sulfidation degree was only obtained at the highest Nb loading of 12.0 wt%. Raman spectroscopy showed that various niobium oxide species formed at different Nb loadings; distorted NbO_6 at low loading (2.0 wt% as Nb_2/C) and bulk-like niobia (amorphous with some degrees of crystallinity) at the highest Nb loading (12.0 wt% as Nb_{12}/C). These structures showed different catalytic performance. The former compound with the lowest degree of sulfidation functioned as coordinatively unsaturated Lewis acid sites in the HDS of DBT and delivered the highest activity per mole of Nb as compared to Nb species in Nb_6/C and Nb_{12}/C catalysts. The high acidity of Nb_2/C catalyst resulted in an unprecedented hydrocracking (HCK) selectivity of around 70 % while Nb_6/C and Nb_{12}/C showed 40 % and 25 % at similar conversions, respectively (Scheme 6.1). Copper enhanced the DDS selectivity and reduced the HCK selectivity in all synthesized catalysts at different loadings. However, it was more pronounced in the case of Nb_2/C in which HCK selectivity was reduced from 70 % to around 15 % and DDS improved from about 18 % to more than 60 %. Kinetic studies at different weight times showed that bimetallic NbCu catalyst performed better, in terms of DDS selectivity and sulfur removal, under severe conditions (high feed flow rates).

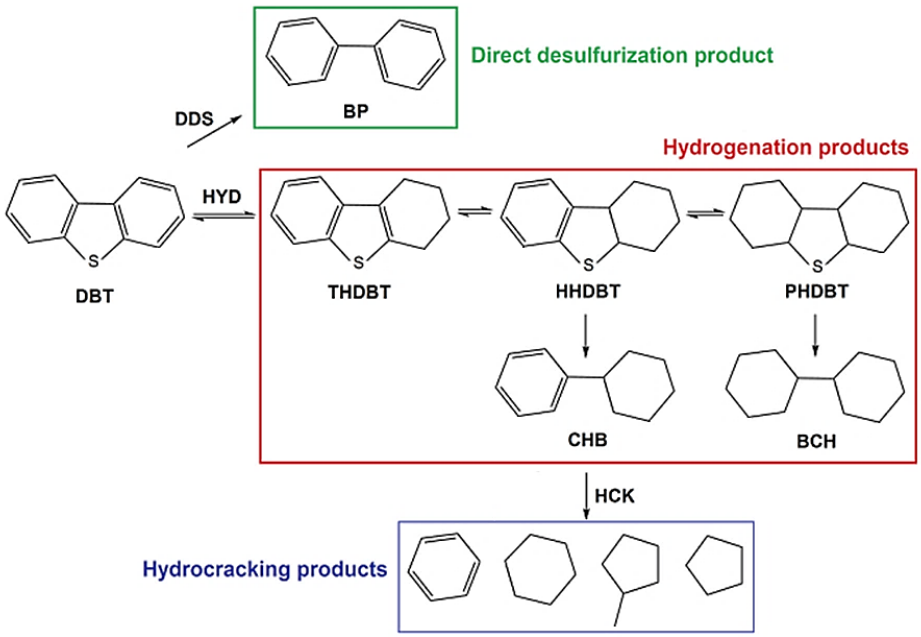

Scheme 6.1. Reaction pathway and product distribution of DBT hydrodesulfurization.

6.2 Experimental

6.2.1 Materials

Copper (II) nitrate trihydrate ($Cu(NO_3)_2.3H_2O$), ammonium niobate (V) oxalate hydrate ($C_4H_4NNbO_9 \cdot xH_2O$), nickel (II) nitrate hexahydrate ($Ni(NO_3)_2.6H_2O$), and ammonium heptamolybdate tetrahydrate ($(NH_4)_6Mo_7O_{24}.4H_2O$) all from Sigma–Aldrich were used as precursors. Oxalic acid ($(COOH)_2.2H_2O$, from Caledon) and distilled water were used as received. Mesoporous carbon (Nano powder, <500 nm particle size, from Sigma-Aldrich) and alumina were used as the catalyst support. Different types of alumina such as gamma-alumina (γ-Al_2O_3, CATALOX SBa-200, BET=200 m^2/), theta-alumina (θ-Al_2O_3, PURALOX TH 100/90, BET=103 m^2/g), and alpha-alumina (α-Al_2O_3, PURALOX SCCa-25/5, BET=7 m^2/g) were provided by Sasol. delta-alumina (δ-Al_2O_3) was prepared by calcination of γ-Al_2O_3 in static air at 950 °C for 5 h. 1000 ppmw sulfur as dibenzothiophene (DBT, $C_{12}H_8S$, Sigma-Aldrich) was dissolved in *n*-decane (Fisher Scientific) as a solvent containing 3.5 wt% *n*-dodecane (Fisher Scientific) as the internal standard and was used as a model fuel for HDS reactions. Carbon disulfide (CS_2, Sigma-Aldrich) was dissolved in *n*-decane at 10 wt% and used for sulfidation of

the catalysts. Ultra-high purity (99.999%) argon and hydrogen gases were purchased from Praxair.

6.2.2 Catalyst preparation

Mono- and bimetallic NbCu catalyst supported on either mesoporous carbon (C) or different phases of alumina (Al_2O_3) were synthesized using incipient wetness impregnation (IWI) method. For a typical synthesis of bimetallic catalyst, niobium and copper solution were prepared separately in two vials to prevent precipitation of copper with oxalate species of niobium precursor. The total volume of both solutions together equals to the support pore volume except for the mesoporous carbon support. Next, niobium and copper solutions were added dropwise to the support simultaneously. For monometallic catalysts supported on carbon at the metal loading of below 2 wt%, the pH of impregnation solution was adjusted at 1.0 using oxalic acid, similar to the concentrated solution used for higher loadings. The synthesized catalysts were dried at room temperature for 2 h and then in static air at 70 °C overnight followed by calcination in a continuous flow system using pure helium at 400 °C for 4 h.

6.2.3 Catalyst characterization

High-resolution (scanning) transmission electron microscopy (HRSTEM) images coupled with energy dispersive X-ray spectroscopy (EDS) were recorded using a JEOL JEM-ARM200CF (probe aberration-corrected S/TEM with a cold field emission gun (cFEG)) operating at 200 kV. Nickel TEM grid was used for EDS analysis. Powder X-ray diffraction (XRD) patterns of calcined and sulfided catalysts were recorded using ex-situ Rigaku Ultima IV diffractometer equipped with a D/Tex detector, an Fe Filter, and Co Kα radiation (λ = 1.78899 Å). The diffraction patterns were collected over 5° to 90° on a continuous scan at 2 degrees 2θ per minute with a step size of 0.02°. Data interpretation was done using JADE 9.6 with the 2016 ICDD and 2016 ICSD databases. X-ray photoelectron spectroscopy (XPS) of the calcined and sulfided catalysts (after the sulfidation at 400 °C) was performed using Kratos Axis 165 X-ray photoelectron spectrometer using Mono Al Kα source operating at 14 kV and15 mA. Background subtraction and peaks analysis were performed using CasaXPS software package.

All the XPS core–level spectra were corrected with C 1s at 284.8 eV. Specific surface area (BET) and pore size distribution (BJH) analyses were conducted using an Autosorb-iQ Quantachrome. About 0.3 g of sample was degassed with Ar at 120 °C for 2 h before each analysis. Temperature-programmed reduction (TPR) was performed using Micromeritics Autochem II 2920 apparatus equipped with a TCD detector. About 100 mg of the calcined catalysts were degassed by helium at 350 °C for 1 h. TPR analysis was performed after cooling down the sample to room temperature using a 10 ml/min of 10 mol% H_2/Ar at the heating rate of 10 °C/min from room temperature up to 900 °C where remained for 10 min. Raman spectra were recorded using a Thermo Scientific DXR2 Raman microscope at 532 nm laser with a high-resolution grating (wavenumber resolution is about 2 cm^{-1}). The spectra were taken using 10-times exposures and 10 second exposure time.

6.2.4 Catalytic experiments

Hydrodesulfurization of dibenzothiophene (DBT) was conducted at 325 °C and 3 MPa hydrogen pressure using a fixed-bed plug flow reactor (stainless steel, L=22", i.d.=0.5"). The catalysts were diluted with silicon carbide (mesh 120, 15:1 weight ratio) to achieve isothermal plug-flow conditions in the reactor. The effects of reactor wall and axial dispersion were negligible.[52] Heat transfer limitations, external and internal mass transfer limitations were not present as verified by Mears and Weisz-Prater criterion. The calculated values of $6.9x10^{-4}$ for heat transfer and $6.9x10^{-9}$ for external mass transfer limitations are much lower than Mears criterion of 0.15.

The catalysts were sulfided *in situ* before each HDS reaction as described in Chapter 5. Briefly, the pressurized reactor under pure hydrogen gas at 3 MPa was heated up to 175 °C at a heating rate of 8 °C/min where the sulfidation feed (10 wt% CS_2 in *n*-decane) at 0.05 ml/min pre-mixed with 100 ml/min hydrogen was introduced into the reactor using a Series II high-pressure pump. Then, the temperature ramped at 5 °C/min up to 400 °C for 20 h. Next, the system cooled down to 325 °C while flowing sulfidation feed and hydrogen. A model liquid fuel containing 1000 ppmw sulfur as DBT with 3.5 wt% *n*-dodecane as the internal standard in *n*-decane (as solvent) was then introduced into the reactor at 0.05 ml/min. The liquid feed was mixed with 100 ml/min hydrogen gas to reach the hydrogen-to-liquid molar ratio of 16. All the HDS experiments were performed for 24 h on-stream including overnight stabilization to reach the steady-state

conditions. During the HDS reactions, the pH_2S/pH_2 was adjusted at $2.55x10^{-4}$ using the concentration of DBT in the feed stream to stabilize the structure in its sulfide state. This ratio is seven orders of magnitude higher than the required thermodynamic value.[22]

A series of HDS experiments were performed over sulfided catalysts at different weight-times but at a constant ratio of liquid to hydrogen flow rates similar to what reported previously with some modifications.[53] Weight time in this study is the ratio of the catalyst weight to the liquid molar flow. Right after sulfidation, the catalyst was subjected to 24 h stabilization at the highest weight time (5.7 g h/mol) which was the lowest flow rate. Then, experimental data were collected at different points while decreasing the weight times (increasing liquid and hydrogen flow rates at a constant ratio). Each sample point was taken after reaching steady state conditions within several hours. Although the system stabilized in 4-5 h after changing the weight time, we let the system to treat 45 ml of sulfur-containing feed for each point and then started collecting the samples. This is to ensure that the off-line sample represents the new weight time. Several samples were collected for each measuring point at different times. During the sampling, a parallel condenser was used in order to prevent pressure fluctuations and disruption of the steady state conditions.

The reaction products were identified out off-line by gas chromatography-mass spectrometry (GC-MS) using a Thermo Scientific Trace GC Ultra, equipped with a Thermo Scientific TR-5 column (30m, 0.25mm, 0.25um, μm film thickness) as described previously. DBT and reaction products were quantified using a calibrated flame ionization detector (Agilent 7890A gas chromatograph) equipped with a H-PONA Agilent capillary column (50 m, 0.25 mm, 0.25 μm film thickness) using the internal standard present in the feed. As shown in Scheme 6.1, the molar selectivity to the direct desulfurization (DDS) path was calculated based on the amount of biphenyl (BP) formation divided by the amount of converted DBT. Selectivity to hydrogenation (HYD) path is the summation of selectivities to cyclohexylbenzene (CHB), bicyclohexyl (BCH), perhydro-dibenzothiophene (PHDBT), hexahydro-dibenzothiophene (HHDBT), and tetrahydrodibenzothiophene (THDBT). Hydrocracking selectivity (HCK) includes single-ring products such as benzene, cyclohexane, cyclopentane, and methylcyclopentane. The reported conversions are subject to 15% experimental error. Two standard deviations in selectivities are

3%. The carbon mass balance was above 95%. Integral activity refers to the activity based on conversion and flow rate, which is different from the reaction rate.

6.3 Results and Discussion

6.3.1 Catalyst characterization

Table 6.1 shows the physicochemical properties of the synthesized catalysts. The BET surface areas were measured after calcination and sulfidation at 400 °C. As can be seen, the surface areas of sulfided catalysts dramatically decreased compared to the area of the carbon support, correlating with the total metal loading (Nb and Cu). However, the pore diameter did not change (adsorption-desorption data in Figure S1, Supporting Inofrmation).

Table 6.1. Textural properties of the synthesized catalysts.

Catalyst	Metal loading (wt%)		BET (m^2/g)	average pore diameter (nm)
	Nb	Cu		
Nb_{12}/C	12.0	0.0	–	–
$Nb_{12}Cu_1/C$	12.0	1.0	–	–
$Nb_{12}Cu_2/C$	12.0	2.0	98	7.0
$Nb_{12}Cu_4/C$	12.0	4.0	–	–
$Nb_{12}Cu_8/C$	12.0	8.0	–	–
Nb_6Cu_1/C	6.0	1.0	119	7.0
$Nb_2Cu_{0.3}/C$	2.0	0.3	135	7.0

BET surface area of mesoporous carbon = 205 nm^2/g

Figure 6.1 shows the electron microscopy analyses of sulfided $Nb_{12}Cu_2/C$ and $Nb_2Cu_{0.3}/C$ catalysts (sulfidation at 400 °C for 20 h). The bright-field TEM image in Figure 6.1a shows the homogeneous distribution of carbon particles supporting non-spherical nanostructures as shown in the dark-field image of Figure 6.1a. The EDS mapping analysis acquired on the sulfided

$Nb_{12}Cu_2$/C catalyst confirmed the spatial association of niobium, copper, and sulfur elements on the carbon support (Figure 6.1b). However, EELS or Auger electron spectroscopy analysis should be used for a detailed surface quantification. A typical layered structure including disordered stacked planes was observed in the HRTEM images of both low- and high-loading samples (Figure 6.1a, c). Similar stacking slabs structure of NbS_2 supported on alumina was observed in a previous study[26] analogous to WS_2 and MoS_2. The number of overlayers in $Nb_{12}Cu_2$/C was higher than that of $Nb_2Cu_{0.3}$/C catalyst. The maximum stacking number in $Nb_{12}Cu_2$/C catalyst was 13 and the longest slab was around 15 nm (Figure S2a, Supporting Information). On the other hand, the number of slabs decreased remarkably in $Nb_2Cu_{0.3}$/C to a maximum of seven (Figure S2b, Supporting Information).

The interplanar spacing of 0.65 nm seen in the HRTEM images of both samples can be assigned to the (002) basal plane of $Cu_{0.65}NbS_2$ (according to the PDF no. 00-015-0409). This value is higher than that of (002) plane in monometallic NbS_2 (0.59 nm, PDF no. 00-041-0980) suggesting the incorporation of copper atoms in niobium structure (Cu intercalated NbS_2 as $Cu_{0.65}NbS_2$).[54] Accordingly, the fringe size of 0.28 nm can be attributed to the (101) plane of $Cu_{0.65}NbS_2$. For $Nb_2Cu_{0.3}$/C, the fringe size of 0.33 nm can be assigned to the (004) plane of $Cu_{0.65}NbS_2$ (PDF no. 00-015-0409). The formation of such crystalline bimetallic phases was further confirmed by XRD analyses (Figure 6.1d). However, Nb_{12}/C was mostly amorphous even after sulfidation. We also identified the d-spacing of 0.25 nm and 0.32 nm in a close proximity of the layered Nb structure of both catalysts. Unambiguous assignment of these fringes is difficult since they can be attributed to the bimetallic $Cu_{0.65}NbS_2$ structure or residual copper species unreacted with niobium and present as copper sulfide (CuS).

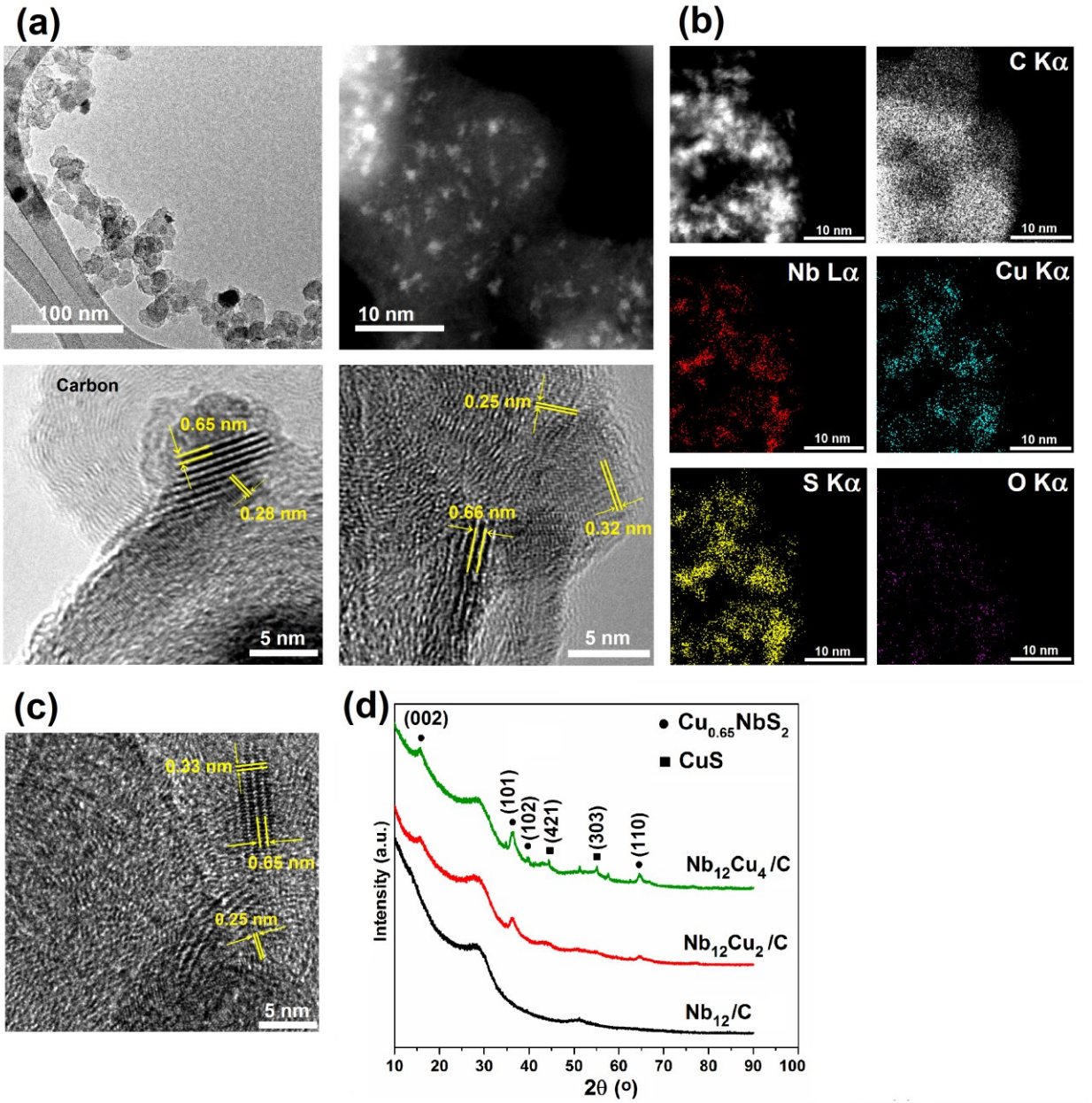

Figure 6.1. Textural analyses; (a) TEM and HRTEM images (bright- and dark-field TEM images on top left and righ, respectively); (b) STEM-EDS mapping of sulfided $Nb_{12}Cu_2/C$; (c) HRTEM image of $Nb_2Cu_{0.3}/C$, and (d) XRD patterns of monometallic Nb_{12}/C and bimetallic NbCu sulfide catalysts at different Cu/Nb ratios; all samples were sulfided at 400 °C for 20 h before analysis.

Figure 6.2 shows the TPR profiles of calcined mono- and bimetallic catalysts supported on carbon and different phases of alumina. The ratios of Nb loading to BET surface area were

constant for all the samples. The reduction temperature of alumina-supported Nb was higher than that of bulk niobia (730 °C)[40], which is due to the strong metal-support interactions. Except for the alpha phase of alumina (α-Al_2O_3), no reduction peak was observed below 800 °C on oxide supports. Note that spinel $AlNbO_4$ structure did not form as its formation occurs beyond 850 °C.[55] The reduction profiles of carbon-supported catalysts are shown in Figure 6.2b. The reduction of monometallic catalyst (Nb_{12}/C) occurred at around 650 °C, which is lower than the reduction temperature of bulk niobia. Nevertheless, the temperature is still very high for many applications.[41] Addition of copper to Nb catalysts shifted the reduction peak of Nb_2O_5 to lower temperaturesto around 350-450 °C suggesting the formation of bimetallic NbCu structures. Increasing the Cu/Nb ratio reduced more niobia species as its reduction peak merged with the reduction peak of CuO at a high Cu content.

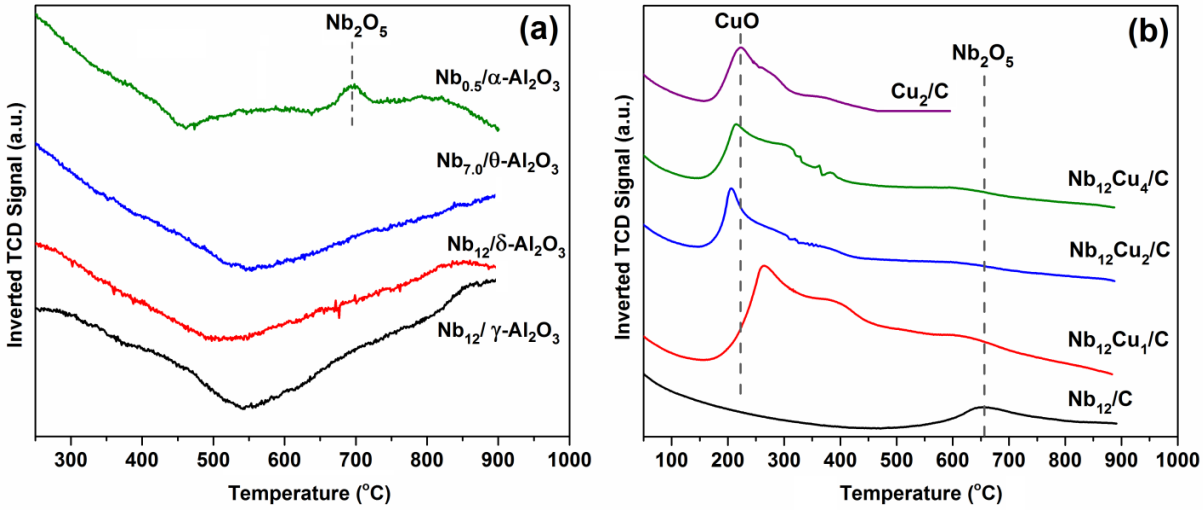

Figure 6.2. TPR profiles: (a) calcined Nb catalyst supported on different alumina phases, and (b) carbon-supported mono- and bimetallic catalysts.

XPS spectra were acquired on the fresh calcined and sulfided catalysts in which the effects of Cu/Nb ratios and total metal loading on the sulfidation behavior of Nb were investigated (Figure 6.3). The Nb 3d binding energies (BEs) of the monometallic Nb_{12}/C catalyst at 208.2 and 211.0 eV, corresponding to niobia[56], negatively shifted by around 0.7 eV in bimetallic CuNb samples (Figure 6.3a). The same amount of shift was observed when the Nb loading in the

bimetallic catalysts decreased to 6.0 and 2.0 wt% (Figure 6.3b). This indicates the charge transfer between copper and niobium species and formation of bimetallic structures irrespective of the metal loading. Compared to the calcined fresh samples, the Nb 3d peaks in the XPS spectra of the sulfided catalysts (at 12.0 wt% Nb loading) shifted to the lower BEs (Figure 6.3c) and a new peak at around 204.1 eV appeared. This new peak corresponds to the formation of niobium disulfide (NbS_2).[39,57] The area and intensity of this peak increased by an addition of copper to the catalyst correlating with the Cu content (Figure 6.3c, Figure 6.4a, and Table 6.3). Surprisingly, the same behavior was not observed when the total metal loading decreased to 7.0 wt% (Nb_6Cu_1/C) and 2.3 wt% ($Nb_2Cu_{0.3}$/C) at the same Cu/Nb ratio of $Nb_{12}Cu_2$/C sample. Only a negligible shift in niobia BEs was detected besides the formation of a very low amount of NbS_2 (less than 5 % as shown in Table 6.3). S 2p core levels in Figure 6.3e showed the different type of sulfur-niobium interaction at high and low metal loadings. The BE of 162.2 eV, corresponding to NbS_2,[57] only observed in the XPS of $Nb_{12}Cu_2$/C. Nevertheless, copper species were found in their reduced state in all samples at different loadings (Figure 6.3f). The XPS data clearly reveal that Nb sulfidation directly depends on the Nb loading in the catalyst. A higher Nb sulfidation was only obtained at a high Nb loading. The same behavior was reported in the literature in the case of supported tungsten (W) and nickel (Ni) layered structures in which higher W and Ni sulfidation was achieved at increased metal loading.[51]

Table 6.2. Binding energy values of Nb 3d in the sulfided catalysts.

Sample	**Binding Energy (eV)**					
	NbS_2		**NbO_x**		**Nb_2O_5**	
	Nb $3d_{5/2}$	**Nb $3d_{3/2}$**	**Nb $3d_{5/2}$**	**Nb $3d_{3/2}$**	**Nb $3d_{5/2}$**	**Nb $3d_{3/2}$**
Nb_{12}/C	204.2	206.9	206.0	208.8	207.9	210.7
$Nb_{12}Cu_2$/C	204.1	206.8	205.6	208.3	207.9	210.7
$Nb_{12}Cu_4$/C	204.0	206.8	205.1	205.8	208.0	210.7

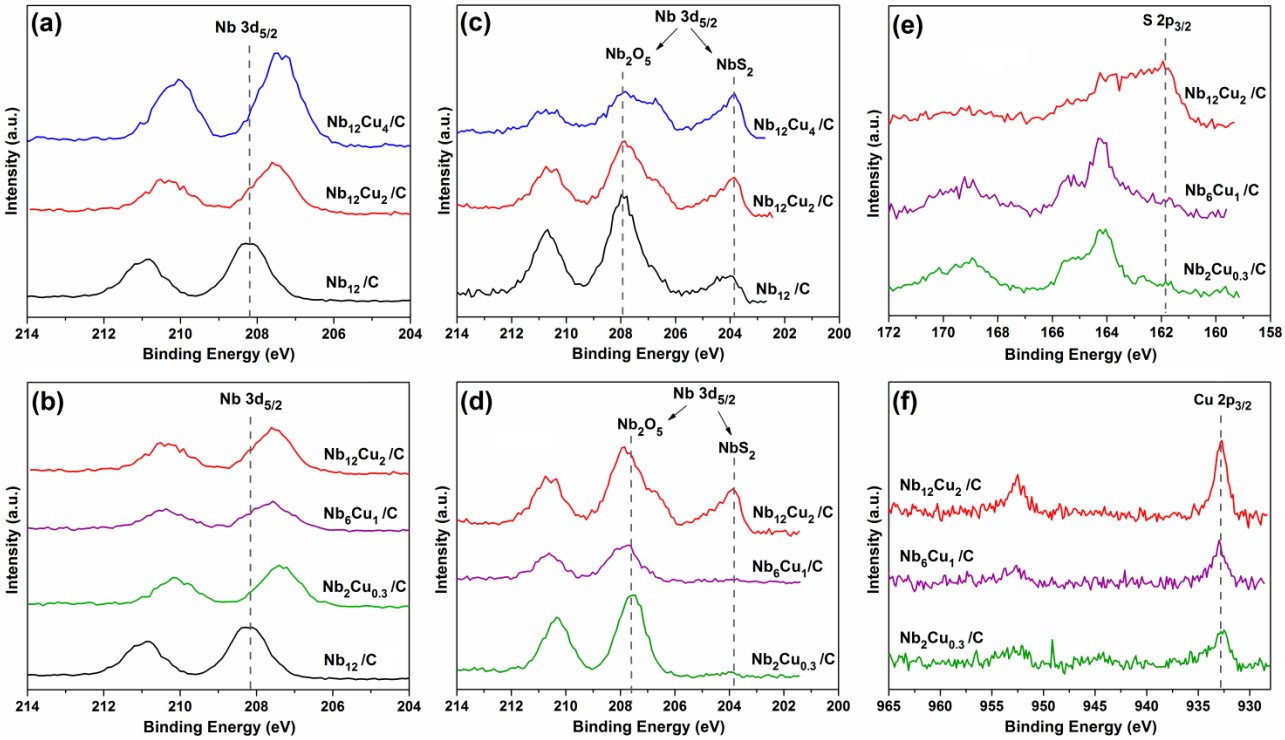

Figure 6.3. XPS spectra: Nb 3d core levels of (a) fresh calcined samples at different Cu/Nb ratios, and (b) at different total metal loading at constant Nb/Cu ratio; (c, d) Nb 3d core levels after sulfidation at 400 °C for 20 h; (e) S 2p core levels of sulfided samples; (f) Cu 2p core levels of the sulfided materials.

Deconvoluted XPS spectra of bimetallic catalysts (12.0 wt% Nb) at different Cu/Nb molar ratios revealed that Nb sulfidation (fraction of NbS_2 in the sample) linearly increased with the copper content of the catalyst (Figure 6.4a,b and Table 6.3). The surface concentration of copper also enhanced by the Cu/Nb ratio. In addition, copper enhanced the fraction of partially reduced niobium oxide (NbO_x), which is a mixture of NbO_2 and NbO (Table 6.3). However, in contrast to the bulk materials, niobium oxides are dominated in the sulfided samples, especially in the case of low loading materials, which are highly resistant to sulfidation (Figure 6.4c and Table 6.3). These findings suggest the presence of different niobium oxide species at low and high Nb loadings that exhibited various sulfidation behaviors. In fact, there is a threshold Nb loading (number of overlayers) that essentially requires achieving a considerable level of Nb sulfidation.

Table 6.3. Amount of sulfided, partially reduced and unreacted Nb_2O_5 in the sulfided catalysts calculated by the areas of corresponding deconvoluted peaks; elemental surface composition of the sulfided samples.

sample	fraction in the sample (%)			surface composition (atomic %)		
	NbS_2	NbO_x	Nb_2O_5	Nb	Cu	S
Nb_{12}/C	20	7	73	41	–	59
$Nb_{12}Cu_2/C$	32	5	63	33	6	61
$Nb_{12}Cu_4/C$	47	11	42	26	9	65
Nb_6Cu_1/C	4	0	96	23	8	69
$Nb_2Cu_{0.3}/C$	2	0	98	44	6	50

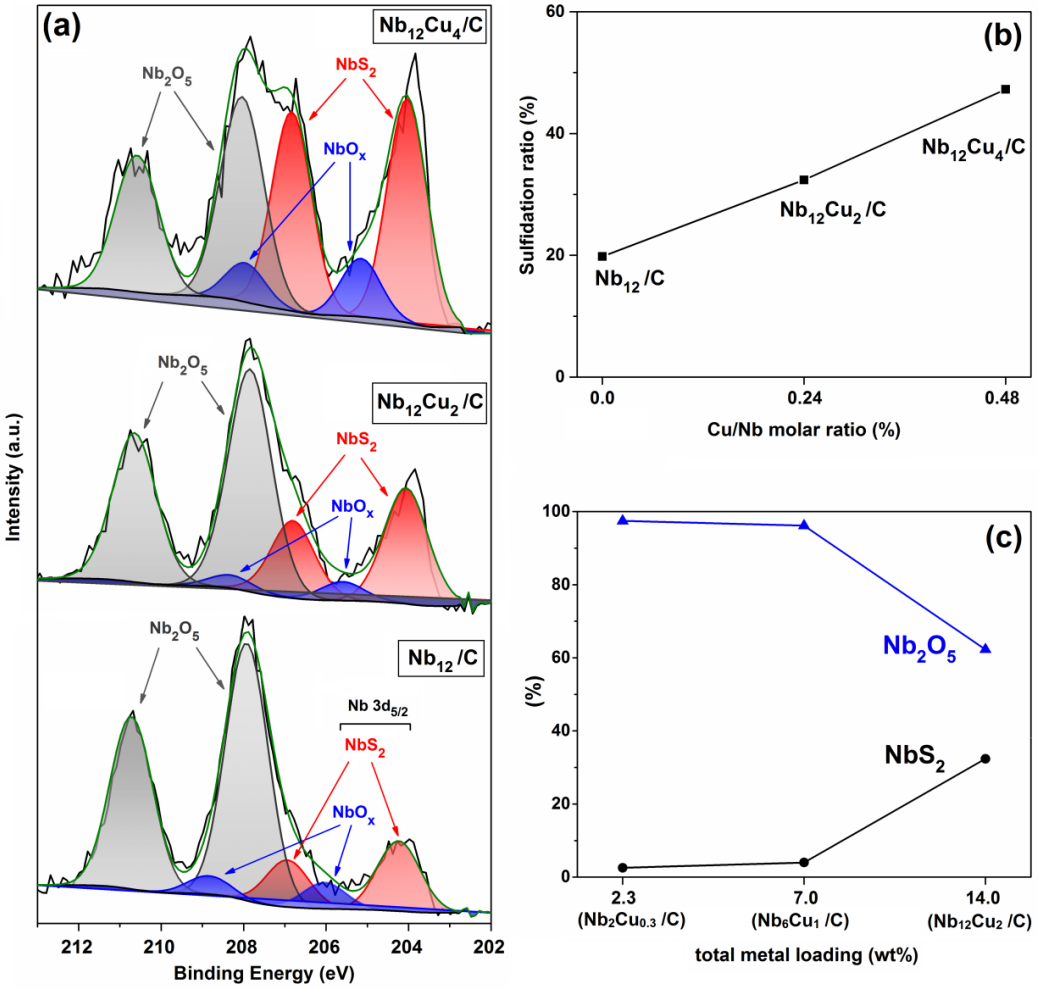

Figure 6.4. (a) Deconvoluted XPS spectra of the sulfided catalysts; (b) effect of Cu/Nb molar ratio on Nb sulfidation ratio; (c) fraction of NbS_2 and Nb_2O_5 in the sulfided samples as a function of total metal (Nb+Cu) loading at constant Nb/Cu ratio; sulfidation of all samples at 400 °C for 20 h.

The ambient Raman spectroscopy was performed on calcined and sulfided catalysts at different metal loadings to obtain fundamental information on the molecular structures of surface species (Figure 6.5). Raman spectra of calcined monometallic catalysts are presented in Figure 6.5a. The spectrum of bulk amorphous niobia was also shown for comparison in which three strong bands exhibited at 257, 630, and 980 cm^{-1} consistent with a previous work.[58] Such multiple Raman bands indictes the presence of various niobia species with different reactivities in the reaction.[2] The Raman spectra of supported catalysts were clearly distinguished from bulk niobia revealing the formation of surface two-dimensional niobium oxide species.[59] As-received carbon support did not show any Raman bands within the measured range but the carbon impregnated with oxalic acid followed by annealing in inert at 400 °C exhibited two strong bands at 558 and 1095 cm^{-1}. No significant difference was identified in the Raman spectra of the monometallic Nb_2/C and Nb_6/C (Figure 6.5a). A major Raman band at around 803 cm^{-1} besides two weak peaks at ~950 and ~990 cm^{-1} occurred in the spectra of both Nb_2/C and Nb_6/C samples. In contrast, increasing the Nb loading to 12.0 wt% (Nb_{12}/C) resulted in additional Raman bands at ~235 and ~675 cm^{-1} besides a shoulder at ~315 cm^{-1}. However, the peak at 558 cm^{-1} overlapped with the one at 675 cm^{-1} difficult to discriminate any peaks within this region. Almost the same peak positions were observed in the case of niobia supported on alumina and silica.[59] In addition, increasing Nb loading on alumina and silica resulted in a new peak at ~680 cm^{-1} and ~647 cm^{-1}, respectively.[59]

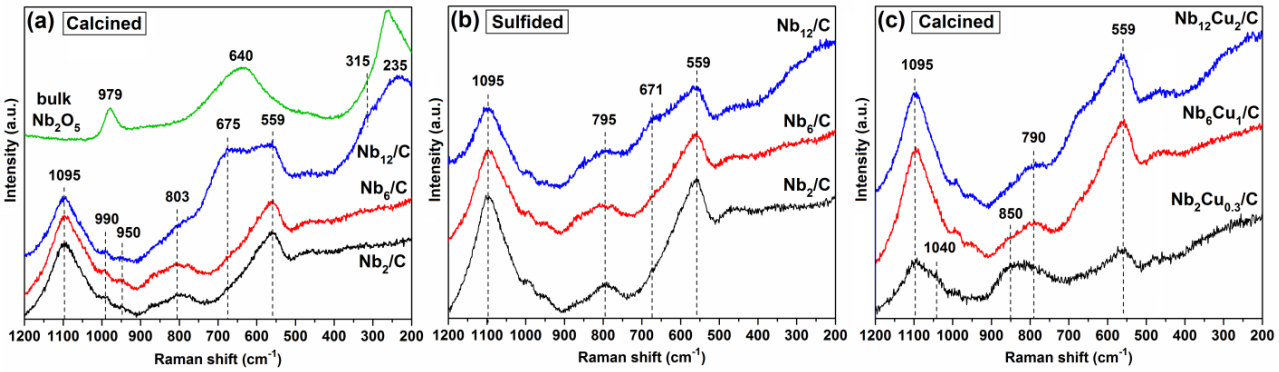

Figure 6.5. Raman spectra of (a) calcined and (b) sulfided monometallic catalysts at different Nb loadings; (c) calcined bimetallic catalysts at different metal loadings (at constant Cu/Nb ratio).

In literature, the Raman bands above 800 cm^{-1} were assigned to the surface niobium oxide and the ones between 600-700 cm^{-1} corresponed to either bulk or hydroxyl-coordinated niobium oxide surface species.[2] Terminal Nb=O bond occurs at around 850-1000 cm^{-1} and Nb–O bonds between 500-700 cm^{-1}.[43] The Raman spectra of the synthesized catalysts are different from fully hydrated niobia (Nb_2O_5 . nH_2O).[60,61] Accordingly, the weak bands at ~950 and ~990 cm^{-1} can be attributed to mono-oxo Nb=O stretching mode of highly distorted octahedra NbO_6 species with different niobium–oxygen bond lengths.[2,43,59] NbO_6 occurs at low Nb loading in which each Nb atom is coordinated with six ogygen atoms and one oxygen atom in the corner connects two adjacent NbO_6.[61] A weak metal-support interaction between Nb and carbon especially at high Nb loading might have promoted the level of distortions through tilting two adjacent NbO_6.[2,59] The Raman band of Nb_{12}/C was not perfectly matched with amorphous niobia with some changes toward crystalline niobia consistent with the formation of T or TT-Nb_2O_5. Therefore, the bands at ~235 and ~675 cm^{-1} in the spectrum of Nb_{12}/C can be assigned to the amourphos niobia with bending mode of Nb–O–Nb linkages that partially transformed to T or TT-Nb_2O_5 (low-temperature crystal phase of Nb_2O_5).[2,58,61–64] These bands occured at high loading on oxide supports when Nb exceeds monolayer surface coverage.[58,59]

After sulfidation (Figure 6.5b), the peaks at ~803 cm^{-1} in the spectra of calcined Nb_2/C and Nb_6/C slightly shifted to the lower wavenumber at 795 cm^{-1} with no significant changes in the position of other bands. A weak peak at this position also appeared in the spectrum of Nb_{12}/C. This negative shift could be due to the partial reduction or sulfidation of niobium oxides leading to a lower metal–oxygen bond order (i.e. from Nb=O to Nb–O).[61] Furthermore, the intensities of the peaks assigned to bulk niobia at 675 and 235 cm^{-1} greatly decreased upon sulfidation suggesting that niobia sulfidation was more significant at enhanced Nb loading, which is consistent with the XPS data. The addition of copper to calcined Nb_2/C changed the Raman feature in the region above 750 cm^{-1} (Figure 6.5c). The peak at ~803 cm^{-1} shifted to a higher wavenumber (~850 cm^{-1}) in $Nb_2Cu_{0.3}$/C and the weak peak at 950 cm^{-1} disappeared while a new shoulder at 1040 cm^{-1} appeared. Nb_6Cu_1/C only exhibited a negative shift from 803 to 790 cm^{-1}. The peaks at 675 and 235 cm^{-1} were not observed in the spectrum of $Nb_{12}Cu_2$/C. The peaks corresponding to copper (oxides)[65] were not identified in the Raman spectra of bimetallic samples. These changes in the presence of copper can be attributed to the incorporation of acidic Nb^{+5} into basic copper oxide species and formation of bimetallic CuNb structures.[59]

Accordingly, there are different types of niobium oxides on the carbon surface at different Nb loadings. Jehng and Wachs[2] reported that niobium oxides at low loading (distorted NbO_6 possessing Nb=O bonds) exhibited Lewis acid properties serving as coordinatively unsaturated acid sites (CUS). These Lewis acid sites on the oxide supports only formed below ~1/3 monolayer coverage.[64] The HDS performance of catalyst towards alkyl DBTs was improved through increasing the concentration and intensity of Lewis acid sites.[66] CUS of CoMo sulfide also exhibited Lewis acidity, changed by metal loading, and promoted hydrocracking and HDS activity.[67] Therefore, an increased HDS activity and hydrocracking selectivity at low Nb loadings is expected. It was also found that the most active acid sites on the oxide supports were the ones highly resistant to reduction.[64] A decreased in the number of Lewis acid sites by increasing the Nb loading on oxide supports (above 5.0 wt%) was observed in previous works attributed to the surface coverage of the metal oxide overlayer, not strucutral changes.[49,50] However, on the other hand, increasing niobia overlayers to the bulk niobia increases the number Brønsted acid sites (–OH).

6.3.2 Catalytic Performance

The synthesized catalysts were evaluated in HDS of DBT at 325 °C and 3 MPa. The catalysts were sulfided *in situ* before the HDS reaction at 400 °C for 20 h. The amount of sulfur in the feed as DBT was adjusted to achieve a partial pressure $p(H_2S)/p(H_2)$ of $2.55x10^{-4}$ stabilizing Nb and Cu in their sulfide phases (required $p(H_2S)/p(H_2)$ for Nb and Cu are 10^{-11} and 10^{-5}, respectively).[22] Figure 6.6a shows the DBT conversions and activities of the carbon-supported Nb-based catalysts. We also measured the activity of monometallic molybdenum (Mo) catalyst supported on carbon at 12.0 wt% Mo loading (Mo_{12}/C). DBT conversion on reduced Nb-based catalyst without prior sulfidation (400 °C, 20 h) was only 6.3 % revealing the importance of sulfidation pretreatment for Nb. Sulfided Nb_{12}/C exhibited a higher DBT conversion than Mo_{12}/C catalyst consistent with previous studies[27,29] and bulk catalysts discussed in Chapter 5. In contrast, copper did not improve the activity of Nb as opposed to the bulk materials. The DBT conversion decreased from 78 % for Nb_{12}/C to 69 % for $Nb_{12}Cu_2/C$ (with 3% experimental deviation in conversion). However, the conversion at the highest Cu content (8.0 wt%)

suppressed dramatically to around 35 % likely due to the surface segregation of inactive copper sulfide that cover Nb active sites.

We also investigated the HDS performance of Nb supported on different phases of alumina, carbon nanotube (CNT), and graphene (Table S1, Supporting Information). Nb supported on mesoporous carbon delivered the highest HDS activity (per mole of Nb and mass of catalyst) due to the weak metal-support interactions between Nb and carbon. In addition, Nb supported on alpha-alumina (α-Al_2O_3) showed more activity (per mole of Nb) than other phases of alumina. However, the activity per mass of catalyst was lower than γ-Al_2O_3 and carbon-supported catalysts. The activities of Nb-based catalysts supported on carbon and γ-Al_2O_3 showed different trends over time-on-stream (Figure 6.6b). Carbon-supported Nb catalysts (mono- and bimetallic catalysts) exhibited an increasing conversion over time, while γ-Al_2O_3-supported catalysts gradually deactivated especially in the presence of copper. The activity of Nb-based samples per mass of catalyst, per mole of Nb, and per BET surface area were higher than Mo-based (Mo_{12}/C) except for the bimetallic NbCu with 8.0 wt% Cu (Figure 6.6c).

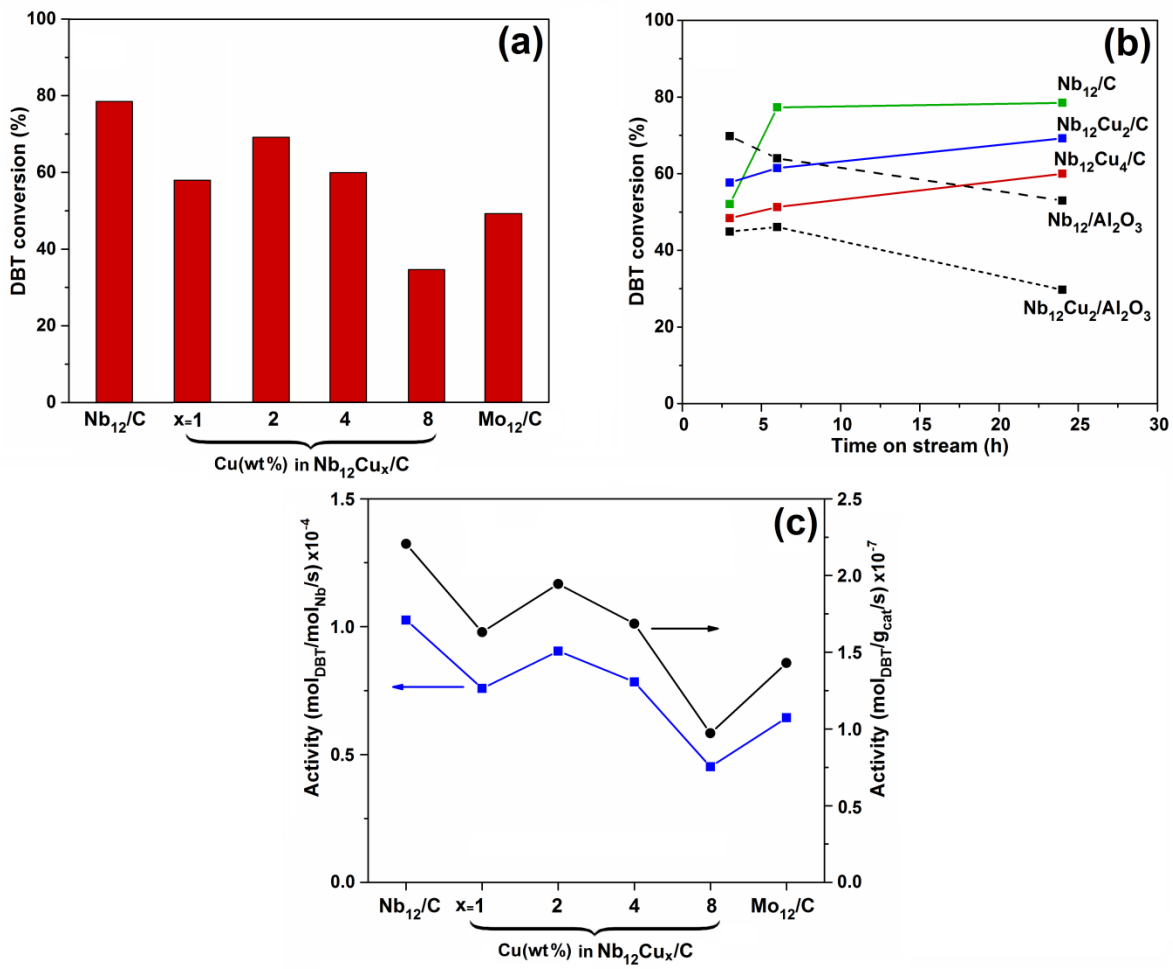

Figure 6.6. (a) DBT conversion after 24 h on stream for carbon-supported catalysts, and (b) at different time-on-stream and support materials; (c) integral activities after 24 h on-stream per mole of Nb (Mo) and total mass of catalyst; (d) activities per BET surface area of the sulfided catalysts The catalysts were pre-sulfided *in situ* at 400 °C for 20 h.

According to the HDS reaction mechanism (Scheme 6.1), there are three major reaction products including biphenyl as direct desulfurization (DDS) route, hydrogenation products, and sulfur-free hydrocracking compounds with 5- and 6-membered rings. Figure 6.7 shows the selectivities and products yields obtained at 325 °C and 3MPa. In contrast to Mo_{12}/C with a high HYD selectivity of 53 %, monometallic Nb_{12}/C was more selective to HCK and DDS (Figure 6.7a). The higher intrinsic activity and DDS selectivity of the Nb catalyst than Mo one were already reported in HDS of thiophene.[42] In addition, Nb catalysts in both oxide and sulfide phases are acidic.[27,45] According to the fraction of Nb_2O_5 determined by XPS (Table 6.3), one can find a correlation

between the HCK selectivity and unreduced niobium oxides in the sample. Adding copper to Nb_{12}/C changed the selectivity significantly. Similar to the bulk catalysts, DDS selectivity increased by the Cu content, from ~39 % in Nb_{12}/C to 66 % in $Nb_{12}Cu_8$/C for the DBT conversions of ~78% and ~35 %, respectively. On the other hand, HCK selectivity decreased from 25.1 to 8.5 % for the same materials. In addition, copper decreased HYD selectivity from 36.2 to 25.3 %. Accordingly, the selectivity towards CHB, as one of the main HYD products, decreased for bimetallic NbCu catalysts as compared to monometallic Nb_{12}/C and Mo_{12}/C (Figure 6.7b). This behavior is different from what observed for the bulk catalysts in which there was a volcano trend versus Cu/Nb ratio for the HYD selectivities and CHB formation. However, a decreasing trend of BCH selectivity is similar to the bulk catalysts. The selectivities to sulfur-containing molecules such as HHDBT and THDBT (from HYD route) were almost unchanged in the presence of copper. On the contrary, the selectivities toward these compounds over Mo_{12}/C were one order of magnitude higher than Nb-based samples. The S-free selectivity was 87 % on Mo_{12}/C as compared to around 98 % for the Nb-based sample. This reveals a higher H_2S resistance of the Nb catalysts that delivered a higher level of sulfur removal.[32,37,38] Among different Cu/Nb ratios, the catalysts with 2.0 and 4.0 wt% copper loading delivered a better performance; however, $Nb_{12}Cu_2$/C showed the highest activity. Therefore, we chose this sample for additional experiments.

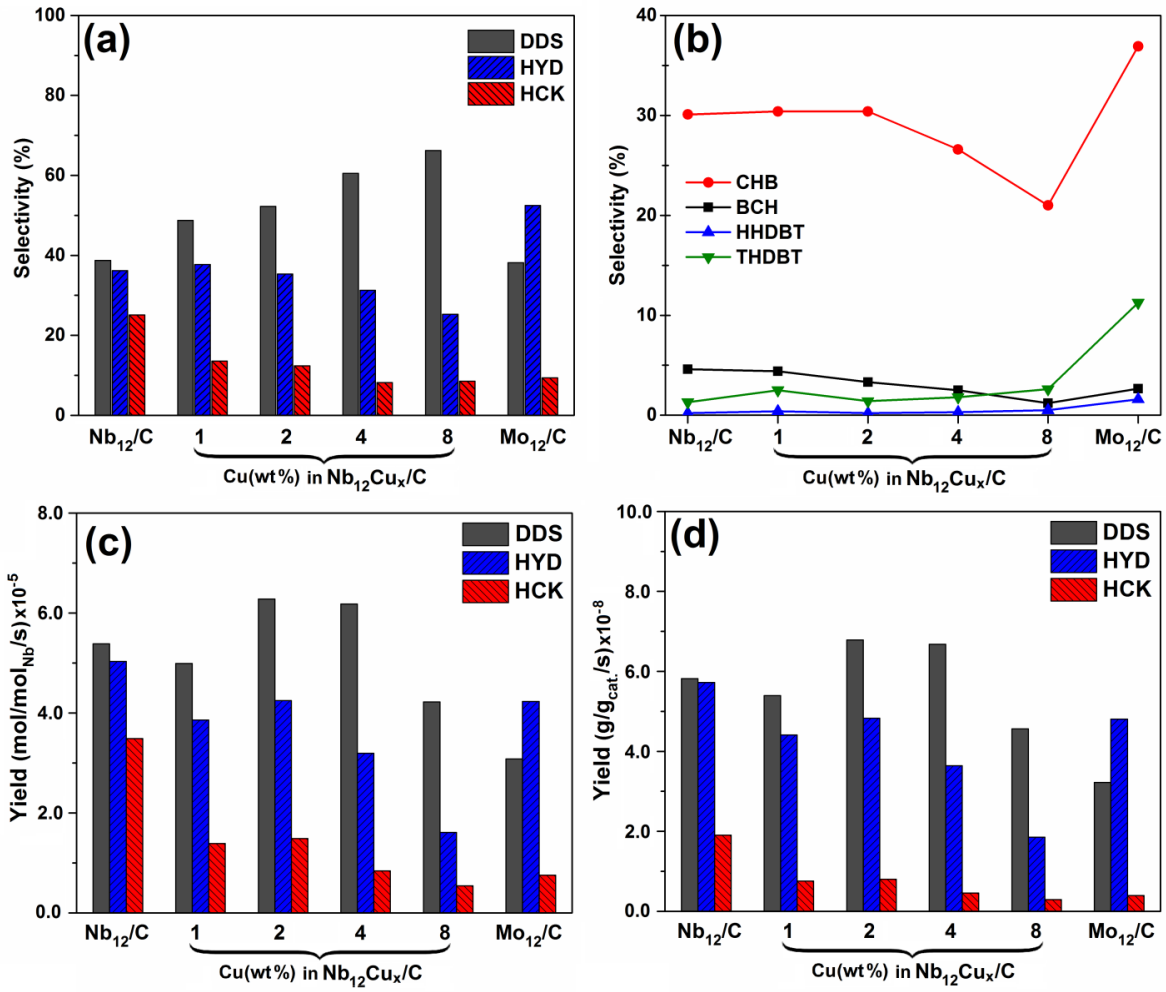

Figure 6.7. Selectivity and yields: (a, b) selectivity as a function of Cu/Nb molar ratio at the conversions reported in Figure 6.6a (in range between 61 and 79% except 35 % for $Nb_{12}Cu_8/C$ and 49 % for Mo_{12}/C); (c) yield (mole of products per mole of active metal), and (d) mass of products per mass of catalyst; all after 24 h on stream at 325 °C and 3 MPa; the catalysts were sulfided *in situ* at 400 °C for 20 h.

A series of HDS reactions were performed at different weight times (catalyst weight to the total liquid molar flow rate) over Nb_{12}/C, $Nb_{12}Cu_2/C$, Mo_{12}/C, and nickel-promoted Mo_{12}/C catalysts ($Mo_{12}Ni_2/C$). Each sample point was taken after reaching steady state conditions within several hours which correspond to treating 45 ml of sulfur-containing feed. Figure 6.8 displays the DBT conversion at different weight times. As can be seen, the activities of Nb-based catalysts outperformed monometallic Mo-based catalyst (Mo_{12}/C) over the entire range of weight times, however, lower than that of NiMo catalyst supported on carbon ($Mo_{12}Ni_2/C$). Considering 3 %

error in the conversion, Nb_{12}/C and $Nb_{12}Cu_2/C$ both delivered the same level of catalytic activities.

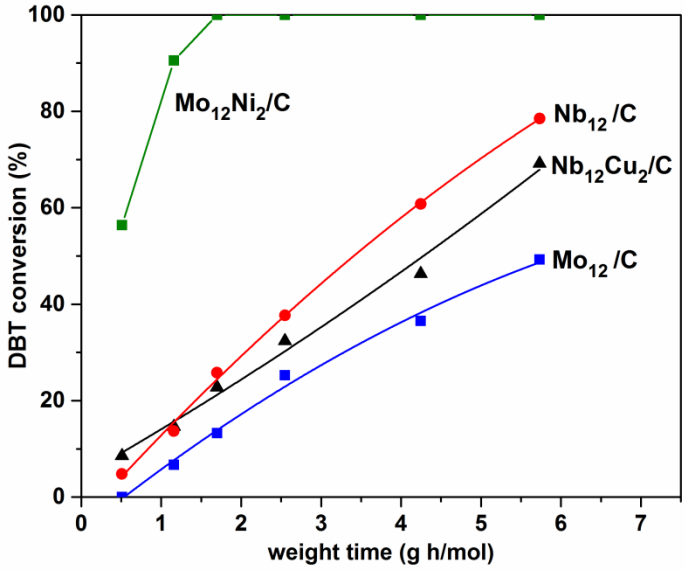

Figure 6.8. DBT conversion at different weight times at 325 °C and 3MPa.

Figure 6.9 exhibits the selectivities at different weight times. Nb_{12}/C and Mo_{12}/C catalysts showed the same level of DDS selectivities. The copper addition as $Nb_{12}Cu_2/C$ improved the DDS selectivity over the whole weight time range with an increasing trend by lowering the weight time. On the contrary, Mo_{12}/C showed higher HYD selectivities than Nb-based catalysts at the weight times higher than 1.16 g h/mol. HYD selectivity is defined as the summation of selectivities to BCH, CHB, and sulfur containing intermediates such as THDBT and HHDBT, termed as S-HYD Figure 6.9. The fully hydrogenated intermediate perhydro-dibenzothiophene (PH-DBT) was not detected most likely because of its slow formation and high reactivity. As can be seen, in contrast to Nb-based catalysts, Mo_{12}/C is highly selective to S-HYD products especially at low weight times. This implies the weaker capability of Mo for sulfur removal compared to Nb. Furthermore, Mo_{12}/C showed the lowest BCH selectivity among the measured catalysts revealing the poisoning of hydrogenation active sites by H_2S. On the other hand, Nb_{12}/C showed the highest BCH selectivity that decreased by feed flow rates. This reveals the presence

of hydrogenation active sites that poisoned at low weight times. However, a high intrinsic acidity of Nb promoted the transformation of HYD products to HCK species over the whole range of measurement with a similar trend to BCH vs. decreasing the weight time.

Besides improving the DDS selectivity of Nb, copper remarkably changed the hydrogenation and hydrocracking activity of Nb. It suppressed the HCK selectivity of Nb_{12}/C, i.e. from 25.1 to 12.4 % at the highest weight time. With no significant changes at high weight times, copper reduced the HYD selectivity of Nb_{12}/C from 35.7 to 24.6 % when we increased the feed flow rate to the maximum value. Various behaviors were observed for HYD products at different weight times. Similar HCK, copper reduced BCH selectivities. More importantly, the selectivity of Nb_{12}/C to sulfur-containing hydrogenation intermediates (S-HYD) sharply increased by decreasing the weight time whereas $Nb_{12}Cu_2$/C showed a significant improvement, i.e. from 22.2 to 10.0 % at the highest feed flow rate.

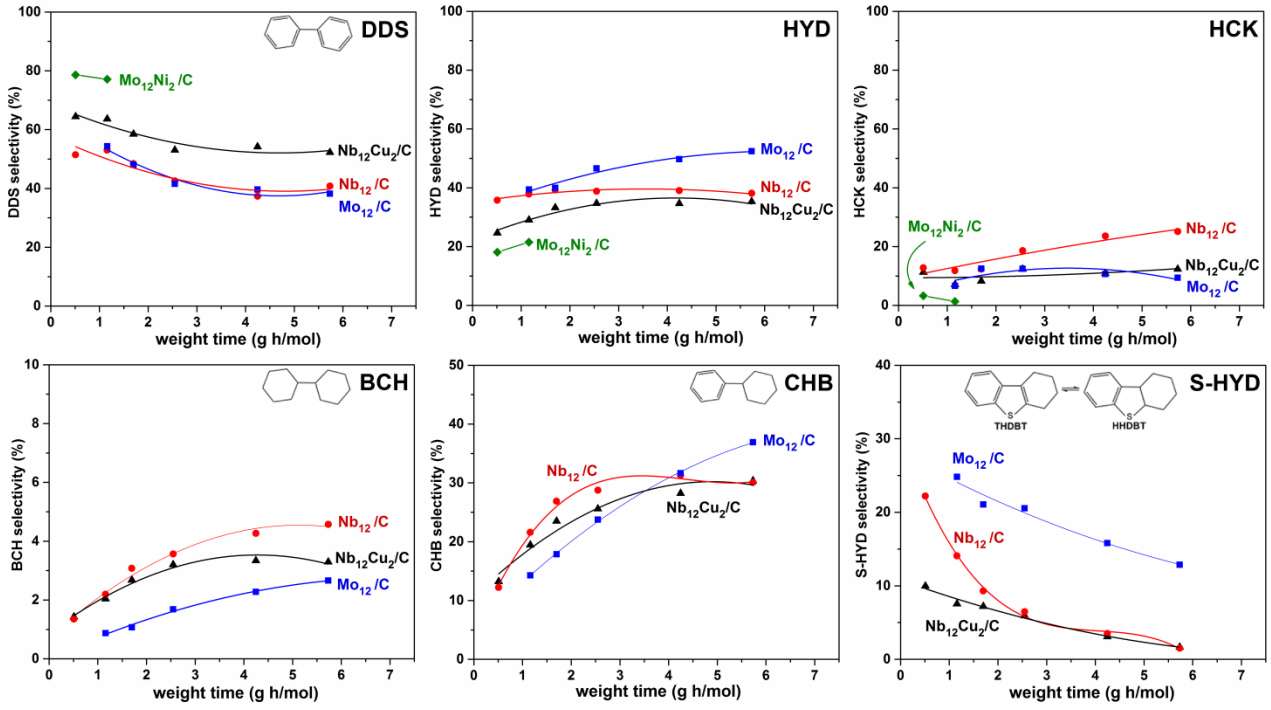

Figure 6.9. Selectivities at different weight times; all at 325 °C and 3 MPa.

The yields of reaction products at different weight times are shown in Figure 6.10. In general, bimetallic NbCu performed better than Nb_{12}/C at low weight times. Biphenyl (BP) as the DDS

product was the major product over all the catalysts. The formation of BP occurred easily as the yield increased at the low weight times. The DDS yields of Nb-based catalysts were higher than Mo_{12}/C. Moreover, the addition of copper to Nb_{12}/C enhanced the formation of BP, especially when the feed flow rate increased. However, in contrast to the bulk catalysts, copper did not improve the hydrogenation performance of Nb supported on carbon. The second major product was cyclohexylbenzene (CHB) followed by bicyclohexyl (BCH). The superior formation of DDS and CHB than BCH suggests that the synthesized catalysts are highly active and selective to DDS instead of HYD, which facilitates the low-pressure operation of HDS reaction. $Nb_{12}Cu_2$/C diminished the formation of hydrogenated intermediate (CHB and BCH) as compared to Nb_{12}/C, except for the lowest weight time. HYD and DDS occur via two different chemisorption modes of σ and π in which DBT adsorbs on the active site through the sulfur atom and flat-lying benzene ring, respectively.[68] Accordingly, this difference suggests that copper changed the adsorption mode of DBT on Nb active sites probably by changing the *d*-band filling of Nb.

As discussed before, Mo_{12}/C showed the highest S-HYD selectivity. Accordingly, Mo highly yielded S-HYD compounds over the measured weight times increased exponentially by feed flow rate. Nb-based catalysts showed an increasing trend as well. However, excluding the highest weight time, $Nb_{12}Cu_2$/C decreased the S-HYD yields. The yield of sulfur free products (S-free) was enhanced on Nb-based catalysts compared to Mo_{12}/C revealing the better performance of Nb catalysts in desulfurization than Mo. $Nb_{12}Cu_2$/C catalyst yielded slightly lower than Nb_{12}/C at high weight times, while surpassed Nb_{12}/C when feed flow rates increased.

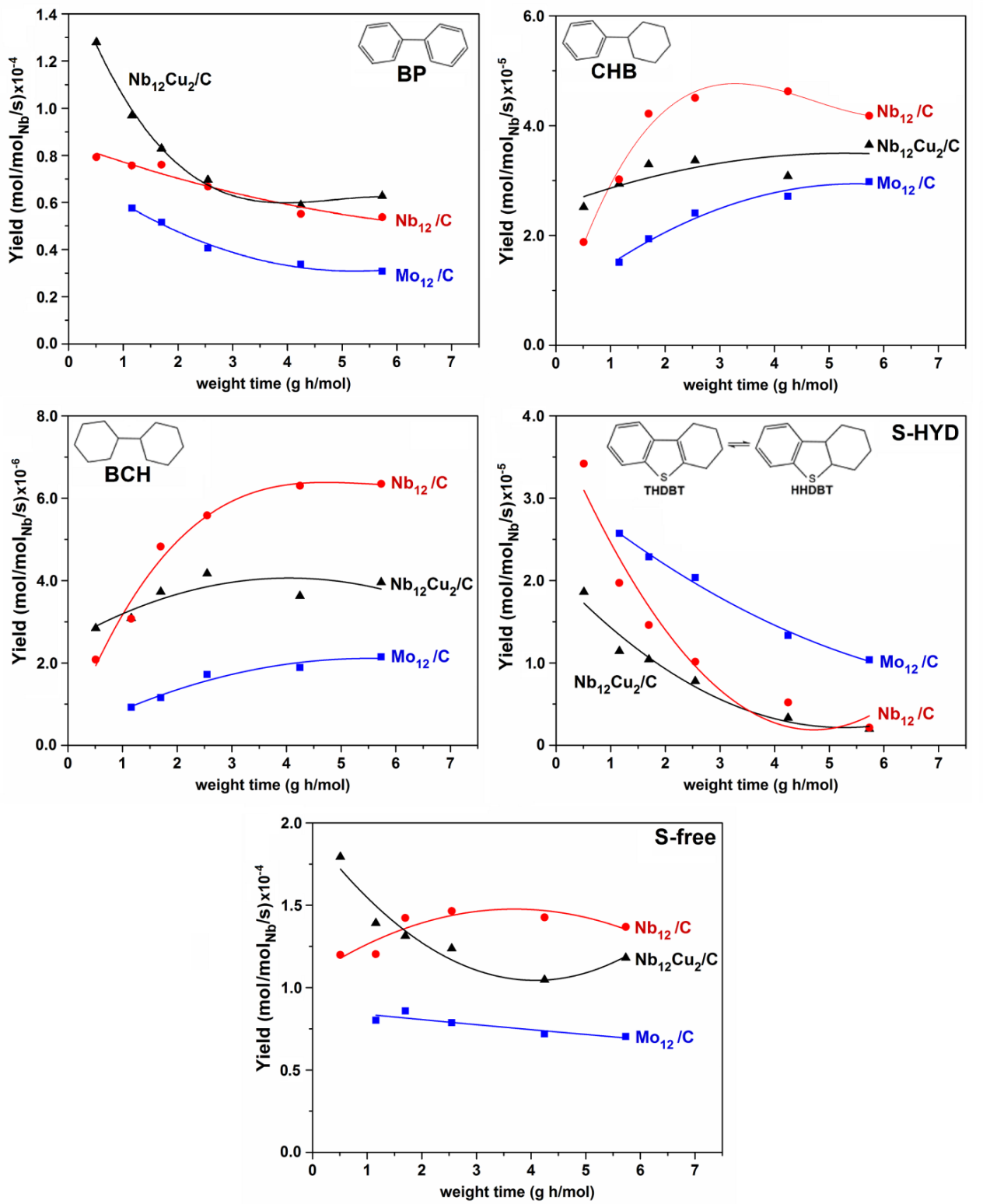

Figure 6.10. Product yields at different weight times at 325 °C and 3 MPa.

We also studied the effect of metal loadings on the HDS performance of the synthesized catalysts. As explained in the Experimental part, we prepared monometallic Nb/C at Nb loading of 2.0 wt% (Nb_2/C) and 6.0 wt% (Nb_6/C). In addition, we synthesized bimetallic Nb_6Cu_1/C and $Nb_2Cu_{0.3}$/C counterparts at constant Cu/Nb ratio analogous to $Nb_{12}Cu_2$/C. Figure 6.11 shows the performance of the catalysts. Different amount of catalyst was loaded into the reactor to achieve comparable DBT conversions for a reliable comparison of the selectivities. As can be seen, the catalytic activity per mole of Nb increased by when the Nb loading decreased from 12.0 to 2.0 wt%. Copper slightly reduced the activities and conversions but remarkably improved the selectivities. In general, the effects of copper on selectivities were greater at the lower Nb loadings. For example, the DDS selectivity in the case of Nb_2/C catalyst increased from ~15 % to ~60 % by adding 0.3 wt% of copper ($Nb_2Cu_{0.3}$/C catalyst), while increased from 34.8 in Nb_6/C to ~52 % in Nb_6Cu_1/C, and from 39 in Nb_{12}/C to 52 % in $Nb_{12}Cu_2$/C. With no improvement in the HYD selectivity at 12.0 wt% Nb loading ($Nb_{12}Cu_2$/C vs. Nb_{12}/C), copper enhanced the HYD selectivities of low loading catalysts. For instance, the HYD selectivity of Nb_2/C increased from ~14 % to ~27 % in $Nb_2Cu_{0.3}$/C. More importantly, the HCK selectivity of Nb_2/C reduced from ~72 % to 13 % in the presence of copper. Interestingly, the HCK selectivity did not exceed 15 % in the bimetallic CuNb even at different weight times. This indicates that copper deactivated the HCK active sites. The HCK product distribution exhibited a significant difference at different Nb loadings. As shown in Table 6.4, high Nb loading (both 6 and 12 wt% Nb) promoted the formation of six-member-ring products such as benzene. On the other hand, low-loaing Nb (2 wt%) remarkably enhaned the formation of (alkyl-substituted) five-member-rings such as cyclopentane and methylcyclopentane. Interestingly, the selectivity to benzene decreased from ~19 % in the case of Nb_6/C to less than 1 % in Nb_2/C. This suggests the higher acidity of the active sites in Nb_2/C rather than other samples promoted the isomerization of benzene to CP and MCP.

According to the Raman data, niobium oxides at low Nb loading (highly distorted NbO_6) functioned as coordinatively unsaturated Lewis acid sites $(CUS)^2$ that promoted hydrocracking and HDS activity.[66,67] They were highly resistant to sulfidation as the sulfidation ratios of less than 5 % were obtained in the case of $Nb_2Cu_{0.3}$/C and Nb_6Cu_1/C as compared to 32 % in $Nb_{12}Cu_2$/C. Note that the DBT conversions on reduced $Nb_2Cu_{0.3}$/C and $Nb_{12}Cu_2$/C samples (only reduction at 400 °C for 20 h) were below 10 %, implying the importance of sulfidation

pretreatment before HDS reaction irrespective of Nb loading. The higher HDS activity of $Nb_2Cu_{0.3}$/C than Nb_6Cu_1/C can be attributed to the higher dispersion of Nb species (increased fraction of corners and edges). Copper reduced the HCK selectivity probably through an acid-base interaction with highly acidic Nb species which also changed the electronic properties of Nb active sites (*d*-band filling) that led to a DDS selectivity improvement. Sulfidation of high loading catalyst resulted in a high stacking of NbS_2 slabs as showed by HRTEM which could reduce the accessibility of the active sites.

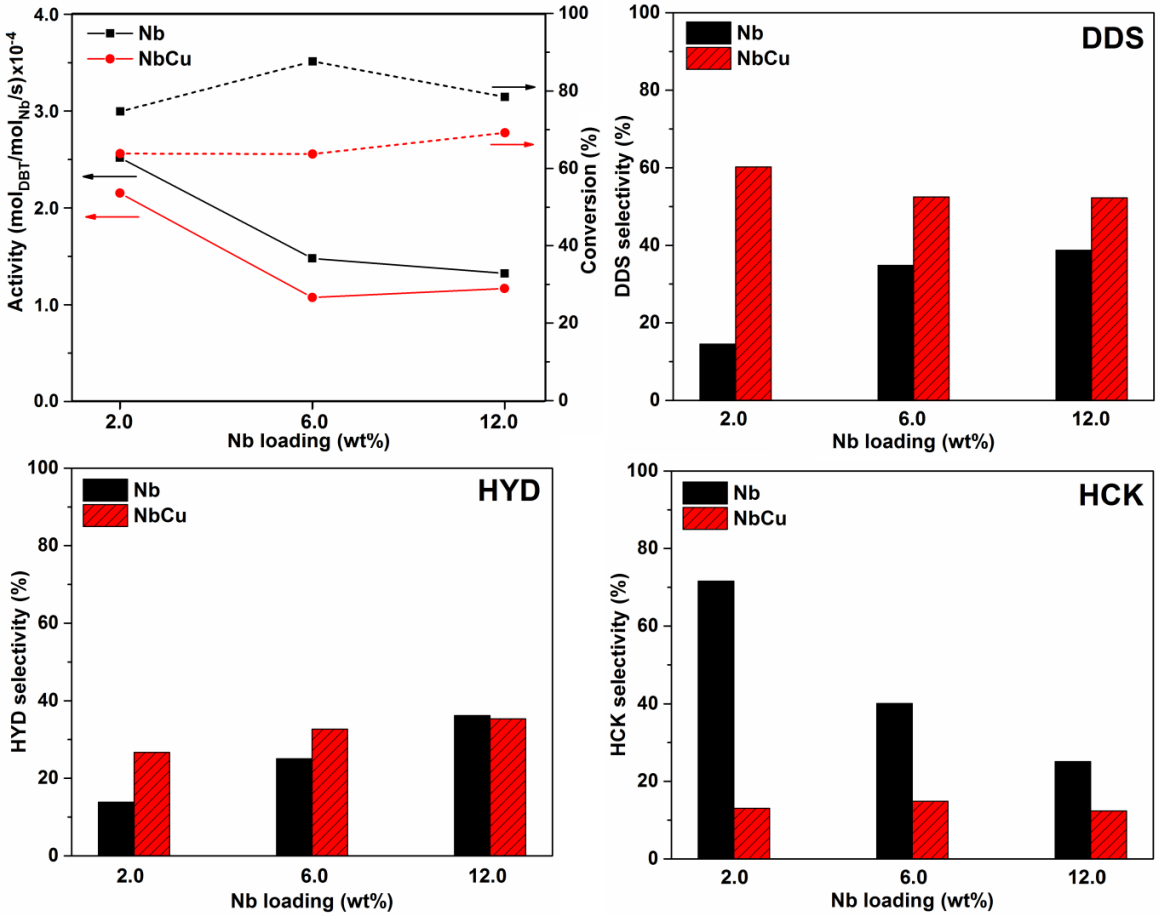

Figure 6.11. Activity and selectivities at different metal loadings (constant Cu/Nb ratio) of $Nb_2Cu_{0.3}$/C, Nb_6Cu_1/C, and $Nb_{12}Cu_2$/C; all after 24 h on stream at 325 °C and MPa; the catalyst were sulfided at 400 °C for 20 h; the amount of the catalysts in the reactor was adjusted to achieve comparable conversions in a range between 64 % to 87 %. We loaded 0.09 g, 0.18 g, and 0.27 g for respectively Nb_{12}/C, Nb_6/C, and Nb_2/C and their bimetallic counterparts.

Table 6.4. Product distribution (mol. %) of the catalysts at different Nb loadings; X represents DBT conversion; the amount of the catalysts in the reactor was adjusted to achieve comparable conversions.

catalyst	X (%)	CP	MCP	Benzene	CH	BCH	CHB	BP	HHDBT	THDBT
Nb_{12}/C	78.5	5	4	14	2	5	30	39	<0.1	1
$Nb_{12}Cu_2/C$	69.2	4	2	5	1	3	31	53	<0.1	1
Nb_6/C	87.6	8	6	19	7	5	19	35	<0.1	1
Nb_6Cu_1/C	63.7	4	1	7	3	3	27	53	<0.1	2
Nb_2/C	74.7	41	28	1	2	<1	12	15	<0.1	1
$Nb_2Cu_{0.3}/C$	63.8	5	4	4	1	2	23	60	<0.1	1

6.4 Conclusions

A series of bimetallic NbCu catalysts at different Cu/Nb ratios were supported on mesoporous carbon and different phases of alumina via incipient wetness impregnation method. The synthesized catalysts were assessed in HDS of DBT at 325 °C and 3 MPa. Electron microscopy data showed that copper and niobium sulfide species formed layered structures as $Cu_{0.65}NbS_2$, as revealed by XRD. Copper decreased the reduction and sulfidation temperature of niobium oxide species correlating with the copper content. However, copper segregated on the surface at a high Cu/Nb ratio reduced the catalytic activity. Raman spectroscopy showed that various niobium oxide species formed on the carbon support at different Nb loadings with different sulfidation and catalytic behaviors. Niobium species at low loading of 2.0 wt% showed the least sulfidation degree (less than 5 %) which increased to 20 % at the Nb loading of 12.0 wt%. The former compound with the lowest degree of sulfidation functioned as coordinatively unsaturated Lewis acid sites in the HDS of DBT and delivered a higher HDS activity as compared to Nb_6/C and Nb_{12}/C catalysts. The high acidity of Nb_2/C catalyst resulted in an unprecedented hydrocracking (HCK) selectivity of around 70 % while Nb_6/C and Nb_{12}/C showed 40 % and 25 %, respectively. Low-loading Nb (Nb_2/C) promoted five-member-ring products such as (methyl) cyclopentane through isomerization of six-member ring as benzene. Copper significantly improved the direct desulfurization selectivity and reduced the hydrocracking selectivity in all synthesized catalysts at different loadings.

6.5 Supporting Information

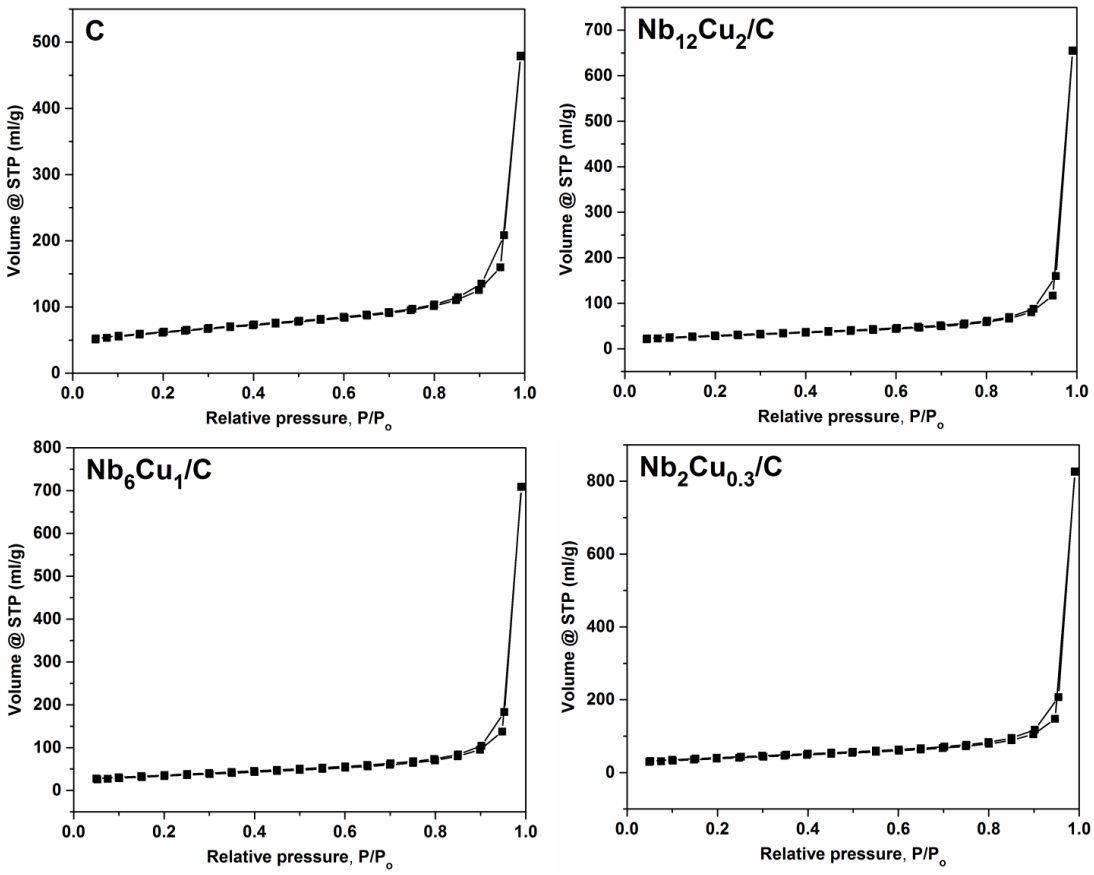

Figure S1. Adsorption-desorption data on sulfided catalyst.

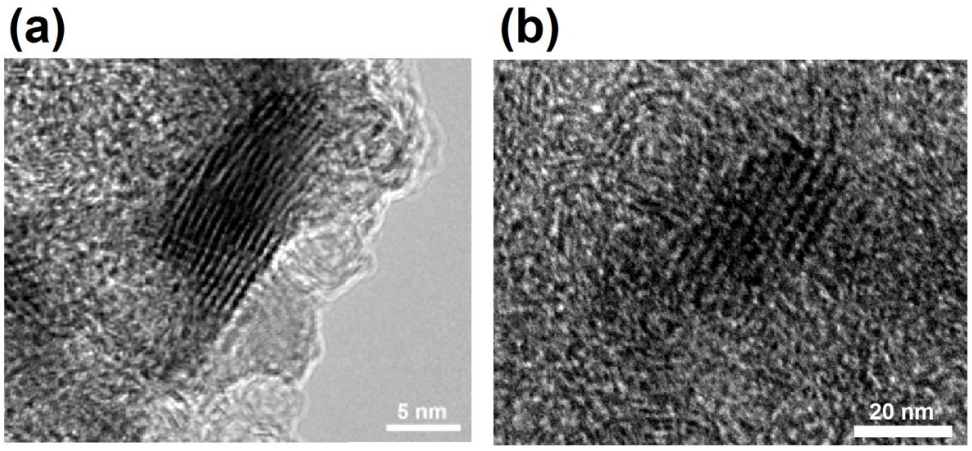

Figure S2. HRTEM image of sulfided (a) $Nb_{12}Cu_2$/C and (b) $Nb_2Cu_{0.3}$/C with the highest length and stacking number.

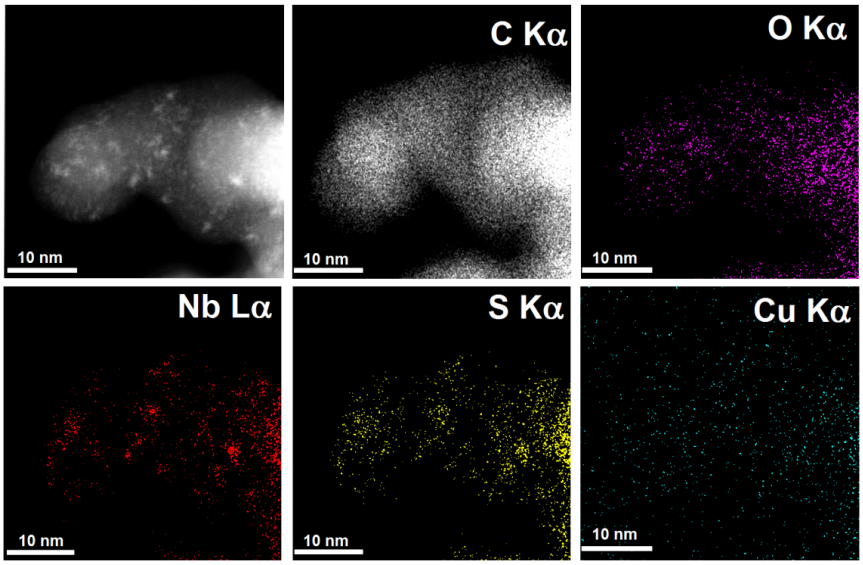

Figure S3. STEM-EDS of sulfided $Nb_{12}Cu_2/C$; second region.

Table S1. Catalytic activity of Nb catalysts supported on γ-Al_2O_3, θ-Al_2O_3, and α-Al_2O_3 (at constant Nb loading/BET ratio) in HDS of DBT at 300 °C and 30 bar H_2 after 24 h on stream. Sulfidation at 300 °C for 4 h. Dried samples were used without calcination.

Catalyst	**cat. (g)**	**Nb (mg)**	**Conversion (%)**	**Activity ($\mu mol_{DBT}/mol_{Nb}/s$)**	**Selectivity (mol %)**		
					DDS	**HYD**	**HCK**
Nb_{12}/γ-Al_2O_3 - dried	0.34	40.8	17.4	7.7	69.2	21.4	9.4
Nb_{12}/γ-Al_2O_3 - calcined	0.29	34.8	11.4	6.0	65.1	22.6	12.3
$Nb_{6.8}/\theta$-Al_2O_3- dried	0.6	40.8	30.2	13.5	59.6	26.2	14.2
$Nb_{0.4}/\alpha$-Al_2O_3- dried	2.0	8.0	18.2	41.5	60.7	26.3	13.0
$Nb_{1.5}/\alpha$-Al_2O_3- dried	2.0	30	45.2	27.4	50.8	35.2	14.0
$Nb_{1.5}/\alpha$-Al_2O_3- dried	2.0	30	28.2	17.2	43.7	41.4	13.9
Nb_{12}/MesC-dried	0.15	18.0	37.6	38.0	45.6	36.2	18.2
Nb_{12}/CNT-dried	0.15	18.0	23.6	23.8	47.5	28.7	23.8
Nb_{12}/Graphene-dried	0.15	18.0	19.3	19.5	52.5	19.7	27.7

6.6 References

(1) Seh, Z. W.; Yu, J. H.; Li, W.; Hsu, P.-C.; Wang, H.; Sun, Y.; Yao, H.; Zhang, Q.; Cui, Y. Nat. Commun. 2014, 5, 5017.

(2) Jehng, J. M.; Wachs, I. E. Catal. Today 1990, 8, 37–55.

(3) Pang, Q.; Liang, X.; Kwok, C. Y.; Nazar, L. F. Nat. Energy 2016, 1, 16132.

(4) Lai, C.-H.; Lu, M.-Y.; Chen, L.-J. J. Mater. Chem. 2012, 22, 19–30.

(5) Ou, X.; Xiong, X.; Zheng, F.; Yang, C.; Lin, Z.; Hu, R.; Jin, C.; Chen, Y.; Liu, M. J. Power Sources 2016, 325, 410–416.

(6) Asadi, M.; Kumar, B.; Behranginia, A.; Rosen, B. a; Baskin, A.; Repnin, N.; Pisasale, D.; Phillips, P.; Zhu, W.; Haasch, R.; Klie, R. F.; Král, P.; Abiade, J.; Salehi-Khojin, A. Nat. Com. 2014, 5, 4470.

(7) Asadi, M.; Kim, K.; Liu, C.; Addepalli, A. V.; Abbasi, P.; Yasaei, P.; Phillips, P.; Behranginia, A.; Cerrato, J. M.; Haasch, R.; Zapol, P.; Kumar, B.; Klie, R. F.; Abiade, J.; Curtiss, L. A.; Salehi-Khojin, A. Science 2016, 353, 467–470.

(8) Chhowalla, M.; Shin, H. S.; Eda, G.; Li, L.-J.; Loh, K. P.; Zhang, H. Nat. Chem. 2013, 5, 263–275.

(9) Kibsgaard, J.; Chen, Z.; Reinecke, B. N.; Jaramillo, T. F. Nat. Mater. 2012, 11, 963–969.

(10) Jellinek, F.; Brauer, G.; Müller, H. Nature 1960, 185, 376–377.

(11) Aray, Y.; Zambrano, D.; Cornejo, M.; Ludeña, E. V.; Iza, P.; Vidal, A. B.; Coll, D. S.; Jímenez, D. M.; Henriquez, F.; Paredes, C. J. Phys. Chem. C 2014, 118, 27823–27832.

(12) Gutiérrez, O. Y.; Singh, S.; Schachtl, E.; Kim, J.; Kondratieva, E.; Hein, J.; Lercher, J. A. ACS Catal. 2014, 4, 1487–1499.

(13) Bara, C.; Plais, L.; Larmier, K.; Devers, E.; Digne, M.; Lamic-Humblot, A. F.; Pirngruber, G. D.; Carrier, X. J. Am. Chem. Soc. 2015, 137, 15915–15928.

(14) Eijsbouts, S.; Anderson, G. H.; Bergwerff, J. A.; Jacobi, S. Appl. Catal. A, Gen. 2013,

458, 169–182.

(15) Chianelli, R. R.; Berhault, G.; Torres, B. Catal. Today 2009, 147, 275–286.

(16) Wang, Q. H.; Kalantar-Zadeh, K.; Kis, A.; Coleman, J. N.; Strano, M. S. Nat. Nanotechnol. 2012, 7, 699–712.

(17) Montoya, J. H.; Seitz, L. C.; Chakthranont, P.; Vojvodic, A.; Jaramillo, T. F.; Nørskov, J. K. Nat. Mater. 2016, 16, 70–81.

(18) Tsai, M.-L.; Su, S.-H.; Chang, J.-K.; Tsai, D.-S.; Chen, C.-H.; Wu, C.-I.; Li, L.-J.; Chen, L.-J.; He, J.-H. ACS Nano 2014, 8, 8317–8322.

(19) Ha, E.; Liu, W.; Wang, L.; Man, H.-W.; Hu, L.; Tsang, S. C. E.; Chan, C. T.-L.; Kwok, W.-M.; Lee, L. Y. S.; Wong, K.-Y. Sci. Rep. 2017, 7, 39411-39419.

(20) Staszak-Jirkovský, J.; Malliakas, C. D.; Lopes, P. P.; Danilovic, N.; Kota, S. S.; Chang, K.-C.; Genorio, B.; Strmcnik, D.; Stamenkovic, V. R.; Kanatzidis, M. G.; Markovic, N. M. Nat. Mater. 2015, 15, 197–203.

(21) Wang, H.; Male, J.; Wang, Y. ACS Catal. 2013, 3, 1047–1070.

(22) Zdražil, M. Catal. Today 1988, 3, 269–365.

(23) Kadijk, F.; Jellinek, F. J. Less Common Met. 1969, 19, 421–430.

(24) Liu, Z. L.; Cai, L. C.; Zhang, X. L. J. Alloys Compd. 2014, 610, 472–477.

(25) Afanasiev, P.; Bezverkhyy, I. Appl. Catal. A, Gen. 2007, 322, 129–141.

(26) Allali, N.; Marie, A. M.; Danot, M.; Geantet, C.; Breysse, M. J. Catal. 1995, 156, 279–289.

(27) Lacroix, M.; Boutarfa, N.; Guillard, C.; Vrinat, M.; Breysse, M. J. Catal. 1989, 120, 473–477.

(28) Allali, N.; Leblanc, A.; Danot, M.; Geantet, C.; Vrinat, M.; Breysse, M. Catal. Today 1996, 27, 137–144.

(29) Hermann, N.; Brorson, M.; Topsøe, H. Catal. Letters 2000, 65, 169–174.

(30) Shafi, R.; Hutchings, G. J. Catal. Today 2000, 59, 423–442.

(31) Babich, I. V.; Moulijn, J. A. Fuel 2003, 82, 607–631.

(32) Stanislaus, A.; Marafi, A.; Rana, M. S. Catal. Today 2010, 153, 1–68.

(33) Song, C. Catal. Today 2003, 86, 211–263.

(34) Allali, N.; Marie, A. M.; Danot, M.; Geantet, C.; Breysee, M. J. Catal. 1995, 156, 279–289.

(35) Gaborit, V.; Allali, N.; Danot, M.; Geantet, C.; Cattenot, M.; Breysse, M.; Diehl, F. Catal. Today 2003, 78, 499–505.

(36) Mansouri, A.; Khodadadi, A. A.; Mortazavi, Y. J. Hazard. Mater. 2014, 271, 120–130.

(37) Danot, M.; Afonso, J.; Des, C. T.; Portefaix, J. L.; Breysse, M. Catal. Today 1991, 10, 629–643.

(38) Egorova, M.; Prins, R. , J. Catal. 2004, 225, 417–427.

(39) Dash, J. K.; Chen, L.; Dinolfo, P. H.; Lu, T. M.; Wang, G. C. J. Phys. Chem. C 2015, 119, 19763–19771.

(40) Wachs, I. E.; Briand, L. E.; Jehng, J.-M.; Burcham, L.; Gao, X. Catal. Today 2000, 57, 323–330.

(41) Wachs, I. E.; Chen, Y.; Jehng, J.M.; Briand, L. E.; Tanaka, T.; Catal. Today 2003, 78, 13–24.

(42) Geantet, C.; Afonso, J.; Breysse, M.; Allali, N.; Danot, M. Catal. Today 1996, 28, 23–30.

(43) Wachs, I. E.; Jehng, J. M.; Deo, G.; Hu, H.; Arora, H. Catal. Today 1996, 28, 199–205.

(44) Jehng, J.-M.; Wachs, I. E. J. Mol. Catal. A Chem. 1991, 67, 369–387.

(45) Ziolek, M. Catal. Today 2003, 78, 47–64.

(46) Tanaka, T.; Yoshida, T.; Yoshida, H.; Aritani, H.; Funabiki, T.; Yoshida, S.; Jehng, J.-M.; Wachs, I. E. Catal. Today 1996, 28, 71–78.

(47) Yoshida, S.; Tanaka, T.; Hanada, T.; Hiraiwa, T.; Kanai, H.; Funabiki, T. Catal. Letters 1992, 12, 277–285.

(48) Gao, X.; Wachs, I. E.; Wong, M. S.; Ying, J. Y. Catal. 2001, 203, 18–24.

(49) Datka, J.; Turek, A. M.; Jehng, J. M.; Wachs, I. E. J. Catal. 1992, 135, 186–199.

(50) Turek, A. M.; Wachs, I. E.; DeCanio, E. J. Phys. Chem. 1992, 96, 5000–5007.

(51) Cui, G.; Wang, J.; Fan, H.; Sun, X.; Jiang, Y.; Wang, S.; Liu, D.; Gui, J. Fuel Process. Technol. 2011, 92, 2320–2327.

(52) Pérez-Ramírez, J.; Berger, R. J.; Mul, G.; Kapteijn, F.; Moulijn, J. A. Catal. Today 2000, 60, 93–109.

(53) Niquille-Röthlisberger, A.; Prins, R. J. Catal. 2006, 242, 207–216.

(54) De Rridder, R.; Van Tendeloo, G.; Van Landuty, J.; Van Dyck, D.; Amelinckx S. phys. stat. sol. 1976, 37, 591–606.

(55) Papulovskiy, E.; Khabibulin, D. F.; Terskikh, V. V.; Paukshtis, E. A.; Bondareva, V. M.; Shubin, A. A.; Andreev, A. S.; Lapina, O. J. Phys. Chem. C 2015, 119, 10400–10411.

(56) Sarma, D. D.; Rao, C. N. R. J. Electron Spectros. Relat. Phenomena 1980, 20, 25–45.

(57) Wu, X.; Tao, Y.; Ke, X.; Zhu, J.; Hong, J. Mater. Res. Bull. 2004, 39, 901–908.

(58) Pittman, R. M.; Bell, A. T. J. Phys. Chem. 1993, 97, 12178–12185.

(59) Jehng, J.-M.; Wacbs, I. E. J. Phys. Chem. 1991, 95, 7373–7379.

(60) Gao, X.; Wachs, I. E.; Wong, M. S.; Ying, J. Y. J. Catal. 2001, 203, 18–24.

(61) Jehng, J.-M.; Wachs, I. E. Chem. Mater. 1991, 3, 100–107.

(62) Burcham, L. J.; Datka, J.; Wachs, I. E. J. Phys. Chem. B 1999, 103, 6015–6024.

(63) Jehng, J.-M.; Turek, A. M.; Wachs, I. E. Appl. Catal. A Gen. 1992, 83, 179–200.

(64) Jehng, J.-M.; Wachs, I. E. Catal. Today 1993, 16, 417–426.

(65) Deng, Y.; Handoko, A. D.; Du, Y.; Xi, S.; Yeo, B. S. ACS Catal. 2016, 6, 2473–2481.

(66) Zhang, Z.; Zhou, Y.; Zhang, S.; Xu, C. Energy and Fuels 2006, 20, 2293–2298.

(67) Huo, Q.; Dou, T.; Zhao, Z.; Pan, H. Appl. Catal. A Gen. 2010, 381, 101–108.

(68) Mansouri, A.; Semagina, N. Appl. Catal. A Gen. 2017, 543, 43–50.

Chapter 7. Shape-controlled Colloidal Niobium Sulfide Nanostructures and their Hydrodesulfurization Activities

7.1 Introduction

The numerous exotic properties of two-dimensional (2D) layered materials have attracted a substantial attention.[1–6] Transition-metal dichalcogenides (TMDC) are of particular interest among the 2D materials for their unique properties, especially when thinning them down to an atomically single layer.[1,2,4,6] In contrast to graphene that is inert in chemistry, TMDC exhibited a tunable chemical versatility in catalysis, energy storage materials, and (opto)electronics.[7] A TMDC monolayer consists of a metal atoms layer covalently bonded between two chalcogenide planar structures. A weak van der Waals force between the lamellar layers allows stabilization of anisotropic single layers.[7,8]

Synthesis of single layer TMDC nanosheets is challenging particularly in solution phase. They can easily form multilayers or aggregate into closed structures with different dimensionalities such as 0D fullerene-like or 1D tubular structures, altering their electronic characteristics as well.[3,9] Mechanical exfoliation and chemical vapor deposition (CVD) techniques as the most common routes for the preparation of layered TMDC have not yet delivered a sufficient control over the size and thickness of nanosheets.[6] Instead, solution-based synthesis methods have demonstrated promising advantageous such as relative simplicity, a good control over size and crystallinity, as well as uniform structural distribution of colloidal TMDC.[1,2,6,10] However, despite a great progress, size- and shape-controlled preparation of 2D and 3D TMDC nanostructure such as single layer 2D nanosheets with a large lateral size remains as a challenge of paramount importance. Shape-controlled nanomaterials play an important role in functional applications such as piezoelectric, light harvesting, photocatalysis, transistors, and the light-emitting diode.[16] As discussed in the previous chapters, HDS activity and selectivity of active sites depend on their positions (coordination) in the catalytic nanoparticles. For example, the active sites located in edges and corners are more active and selective to DDS. Based on this, we aimed to enhance the fraction of these active sites by changing the shape of nanostructures through adjusting the type and amounts of solvent, ligand, and sulfur source.

It was reported that a slow and continuous delivery of chalcogen source into the synthesis solution led to the formation of single-layer group IV TMDC.[6] Analogous to the ligand-directed anisotropic growth of 0D and 1D nanostructures[11–13], Jung et al.[14] controlled the number of layers of molybdenum and tungsten selenide ($MoSe_2$ and WSe_2) nanosheets by changing the functional groups of the capping ligands. Oleic acid (OAc) resulted in an anisotropic lateral growth of single layer as compared to multilayers in oleyamine (OAm) and oleyl alcohol. This was attributed to the lower binding affinity of carboxylic acid to the reactive edge facets of TMDC than amine and alcohol.[14] Ligands with strong anchoring groups do not maintain a dynamic bonding on the surface of crystals, therefore, have been eliminated in the synthesis of nanocrystals.[15]

It is well established that electronic and geometric properties of capping ligands affect thermodynamics and kinetics of nanocrystals' growth, which yields different sizes and morphologies.[16] Coordinating ligands preferentially bind distinctive crystallographic facets and thereby determine the shape and lateral dimension of nanocrystals by controlling the extent of precursor supersaturation and crystal growth.[16,17] For example, different coordinating ligands led to the formation of GdOCl nanosheets and nanodiscs with different thickness through mediating the crystal growth kinetics.[16] Similarly, Mahler et al.[2] synthesized colloidal WS_2 monolayer in two different crystalline structures using hexamethyldisilazane in the presence of OAm and OAc. On the other hand, varying the concentration of ligands in the reaction solution tunes the reactivity of the monomers during the nucleation and growth period.[18,19] For instance, decreasing the initial concentration of OAc enhanced the number of nuclei (reactivity of monomers) significantly.[19] This leads to the aggregation of monomers and formation of different shapes. The amount of chalcogen source can also kinetically control the growth of different crystallographic planes.[28,29]

In this study, we developed a reproducible solution-based technique for a selective growth of 2D and 3D size- and shape-confined TMDC colloids. We chose NbS_2 as a representative case because of its difficult gas-solid sulfidation and dimensionally sensitive performance; a superconductive bulk NbS_2 behaves as a semiconductor when structured as a ultrathin layer.[20,21] To the best of our knowledge, this is the first report on ligand-directed synthesis protocol of shape-controlled NbS_2 that can be generalizable to other TMDC. We discovered that the type of

capping ligands, solvent, and the amount of chalcogen source (sulfur) significantly influenced the structural properties of NbS_2. We tested oleylamine (OAm) as a coordinating solvent and 1-octadecene (ODE) as a non-coordinating solvent in the presence of oleic acid (OAc) as a natural capping ligand (Scheme 7.1). Depending on the ratio of OAc/OAm/S, NbS_2 in different shapes and structures were formed. 2D single layer NbS_2 nanosheets were formed in OAm with a large lateral size of ~1.0 μm at 300 °C, which transformed into multilayers and flower-like structures at a prolonged sulfidation. On the other hand, OAc stabilized single layer nanosheets. Apart from the effects of capping ligand, we found that the amount of chalcogen source promoted the preferential growth of specific crystallographic facets. Increasing the amount of sulfur led to the formation of corners- and edges-abundant nanohexagons and nanobars with different crystalline structures. In contrast to the formation of 2D NbS_2 in OAm, ODE as a non-coordinating solvent boosted nanoparticles growth as a 3D NbS_2. The synthesized materials were evaluated in hydrodesulfurization (HDS) reaction. We found that decreasing the number of layers and lateral size in nanosheets enhanced their catalytic activities. However, higher activities were obtained on nanohexagons and nanoparticles most likely due to the higher fraction of edge and corner atoms.

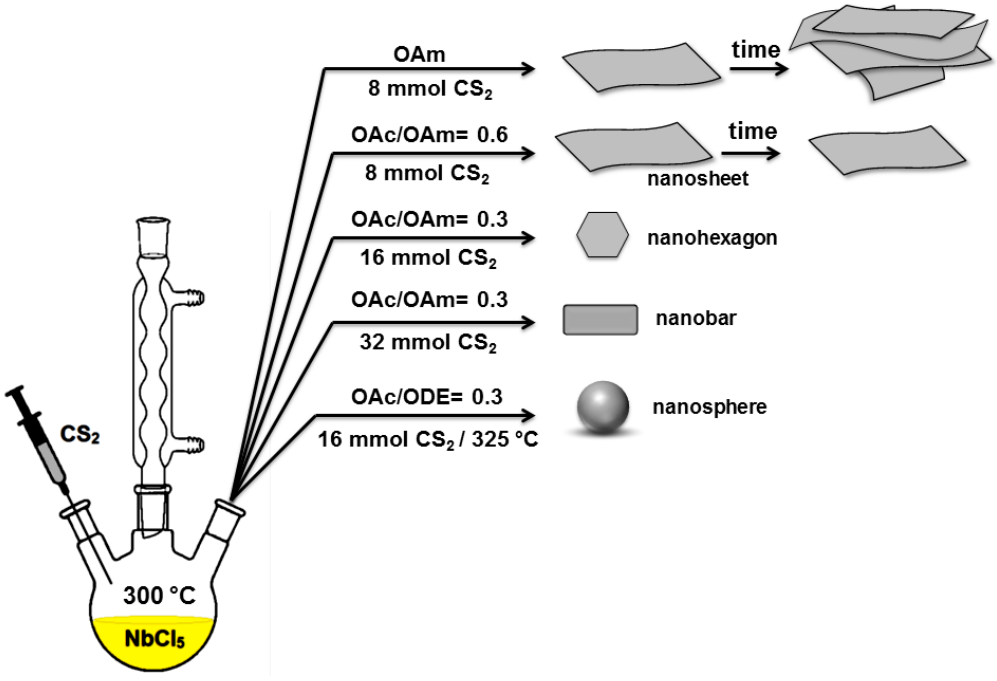

Scheme 7.1. Synthesis protocol of shape-controlled NbS_2 nanostructures.

7.2 Experimental

7.2.1 Materials

Niobium (V) chloride ($NbCl_5$, 99%), copper (II) chloride ($CuCl_2$, 97%), oleylamine (OAm, ≥98 %), oleic acid (OAc, Technical grade, 90%), 1-octadecene (ODE, Technical grade, 90%), tetraethylene glycol, and carbon disulfide (CS_2, ≥99.9%) all from Sigma–Aldrich were used as received. 2-propanol (anhydrous 99.5%), ethanol (anhydrous, 90%), and *n*-hexane were purchased from Fisher Scientific. Gamma-alumina (γ-Al_2O_3 powder (Sasol CATALOX SBa-200, BET=200 m^2/g) was used as a support material. Dibenzothiophene (DBT, $C_{12}H_8S$, Sigma-Aldrich), *n*-dodecane (Sigma-Aldrich), and *n*-decane (Fisher Scientific) were used as a model fuel for HDS reaction. Ultra-high purity (99.999%) argon and hydrogen gases were purchased from Praxair.

7.2.2 Synthesis of NbS_2 Nanosheets

0.23 mmol $NbCl_5$ was dissolved in 20 mL of oleylamine in a three-neck flask. The solution was degassed by ultra-high purity nitrogen gas at 100 °C for 15 min while mixing rigorously. Next, the mixture was heated up to 300 °C at 5 °C/min, where 8 mmol pure carbon disulfide (CS_2) was injected into the solution generating hydrogen sulfide (H_2S) *in situ* that forms NbS_2 nanosheets. This indicated by an instant color change from yellow to dark-brown. The sulfidation reaction was prolonged up to 0.5-3 h. The obtained solution became thickened during the synthesis procedure; initiated after 30 min correlating with the synthesis duration. The NbS_2 nanosheets were isolated by centrifugation with a mixture of ethanol and 2-propanol (1:3 volume ratio). For bimetallic NbCu nanosheets, required amount of $CuCl_2$ (0.0018 or 0.0036 g) were dissolved in the solution with $NbCl_5$. At 300 °C, the color of the solution was bluish which turned to dark-brown after CS_2 injection.

7.2.3 Synthesis of NbS_2 nanohexagon

5 mL oleic acid was mixed with 15 mL oleylamine containing 0.23 mmol $NbCl_5$. The solution was degassed by nitrogen gas at 100 °C for 15 min. 16 mmol CS_2 was injected into the stirring

solution at 300 °C while purging with nitrogen gas. The color of the solution slowly changed to brown. The difference in the color of the solutions between nanosheet and nanohexagon indicates a different coordination of Nb ions. After 2 h, the mixture was cooled down to room temperature and then nanohexagons were collected by centrifuging the mixture of ethanol and 2-propanol (1:3 volume ratio). The obtained colloids were clear and macroscopically homogeneous with no precipitation at the end of the synthesis procedure.

7.2.4 Synthesis of NbS_2 nanobars

0.23 mmol $NbCl_5$ was dissolved in a mixture of oleic acid and oleylamine (5:15 mL) and then purged at 100 °C. Next, once the temperature of the stirring solution reached 300 °C, 32 mmol pure CS_2 was injected into the stirring solution changed the color to brown. After 2 h at 300 °C, the nanobars were isolated by centrifuge. The obtained colloids were clear and macroscopically homogeneous with no precipitation at the end of the synthesis procedure.

7.2.5 Synthesis of NbS_2 nanospheres

0.23 mmol $NbCl_5$ was dissolved in 3 mL oleic acid and then mixed with 15 mL 1-octadecene. After degassing at 100 °C for 15 min, the solution was heated up to the boiling temperature (325 °C) at which 16 mmol CS_2 was injected in the mixture changing the color to dark-red. After refluxing for 2 h, the nanospheres were collected by centrifuge at room temperature. The obtained colloids were clear and macroscopically homogeneous with no precipitation at the end of the synthesis procedure.

7.2.6 Alumina-supported NbS_2 nanostructures

The solution of nanostructures and 2 g of alumina were mixed with a mixture of ethanol and 2-propanol (1:3 volume ratio) at room temperature. The nanostructures were extraxted from the synthesis solution and homogeneously deposited on the support. The obtained materials were dried at 80 °C overnight under vaccuum before catalytic experiments.

7.2.7 Catalyst characterization

Transmission electron microscopy (TEM) images were recorded using a JEOL JEM2100 device operating at 200 kV. Scanning transmission electron microscopy (STEM) coupled with energy dispersive X-ray spectroscopy (EDS) was performed using a a JEOL JEM-ARM200CF (probe aberration-corrected S/TEM with a cold field emission gun (cFEG) operating at 200 kV. Powder X-ray diffraction (XRD) patterns of the sulfided NPs were recorded using Rigaku Ultima IV diffractometer equipped with a D/Tex detector, an Fe Filter, and Co Kα radiation (λ = 1.78899 Å). The diffraction patterns were collected over 5° to 90° on continuous scan at 2 degrees 2θ per minute with a step size of 0.02°. Data interpretation was done using JADE 9.6 with the 2016 ICDD and 2016 ICSD databases. X-ray photoelectron spectroscopy (XPS) analyses were performed using Kratos Axis 165 X-ray photoelectron spectrometer using Mono Al Kα source operating at 14 kV and15 mA. CasaXPS software was used for spectra analysis. The measured XPS doublets were calibrated with C 1s at 284.8 eV. Raman spectra were recorded using a Thermo Scientific DXR2 Raman microscope at 532 nm laser with a high-resolution grating (wavenumber resolution is about 2 cm^{-1}). The spectra were taken using 10-times exposures and 10 second exposure time. The elemental analyses of the supported catalysts were performed using an ICP-MS Perkin Elmer's Elan 6000 at ICP RF power of 1300 W.

7.2.8 Catalytic experiments

The synthesized catalysts were evaluated in hydrodesulfurization (HDS) of dibenzothiophene (DBT) at 325 °C and 3 MPa hydrogen pressure in a continuous-flow fixed bed reactor (Stainless steel, L=22”, i.d.=0.5”). About 0.25 g catalyst diluted with silicon carbide (mesh 120, 22:1 weight ratio) was used for each HDS test. Before each HDS test, the catalysts were sulfided *in situ* for 3 h at either 325 °C under 3MPa hydrogen. The reactor was heated up to 175 °C (at 8 °C/min) where the sulfidation feed (10 wt% CS_2 in *n*-decane) was introduced into the reactor downward at 0.05 ml/min flow using a Series II high pressure pump. The feed was pre-mixed with 100 ml/min hydrogen gas before feeding into the reactor. Next, a model feed containing 1000 ppmw sulfur as DBT with 3.5 wt% *n*-dodecane as the internal standard in *n*-decane as solvent was introduced into the reactor at 0.05 ml/min. The liquid feed was mixed with 100

ml/min hydrogen gas to reach the hydrogen-to-liquid molar ratio of 16. All the HDS experiments were performed for 24 h including overnight stablization period. Quantification of DBT and the reaction products was performed using a calibrated Agilent 7890A gas chromatograph equipped with a flame ionization detector, as described in the previous Chapters.

7.3 Results and Discussion

Similar to the previous reports on the synthesis of TMDC, we used oleylamine as a coordinating solvent.[1,2,4–6] Carbon disulfide (CS_2) was used as the source of sulfur for *in situ* production of hydrogen disulfide (H_2S). Injection of CS_2 into the oleylamine solution containing niobium (V) chloride at 300 °C resulted in the formation of niobium sulfide (NbS_2) nanosheets (Figure 7.1a), indicating by a color change from yellow to dark-brown during synthesis. The TEM images in Figure 7.1a show a structural transformation as the sulfidation reaction proceeds. The nanosheet collected after 15 min of sulfidation (after CS_2 injection) exhibited a lateral size of ~1 μm with a low number of layers, likey monolayer nanosheets overlapping with each other. However, atomic force microscopy (AFM) technique is required to prove single layer formation. Prolonging the synthesis duration to 30 min led to the stacking of single layers to form multilayers nanosheets with an increased lateral size up to ~2-3 μm. As the sulfidation further continued up to 3 h, the nanosheets aggregated to a flower-like structure. However, monolayer sheets were still observed at the edges of the structure. The same structure was observed in a previous work on WS_2 nanosheets.[2] The TEM image in Figure 7.1a also exhibits the lamellar structure of the synthesized NbS_2. STEM-EDS mapping of a sheet revealed a uniform association of niobium species with sulfur (Figure 7.1b). The Nb 3d binding energies (BE) in the XPS spectra of nanosheets centered at 203.0 eV and 205.8 eV confirming the formation of NbS_2 (Figure 7.1c).[20,23] The quantified surface ratio of Nb to S, determined by XPS, was 1.03/2.0 consistent with the stoichiometric ratio of NbS_2.

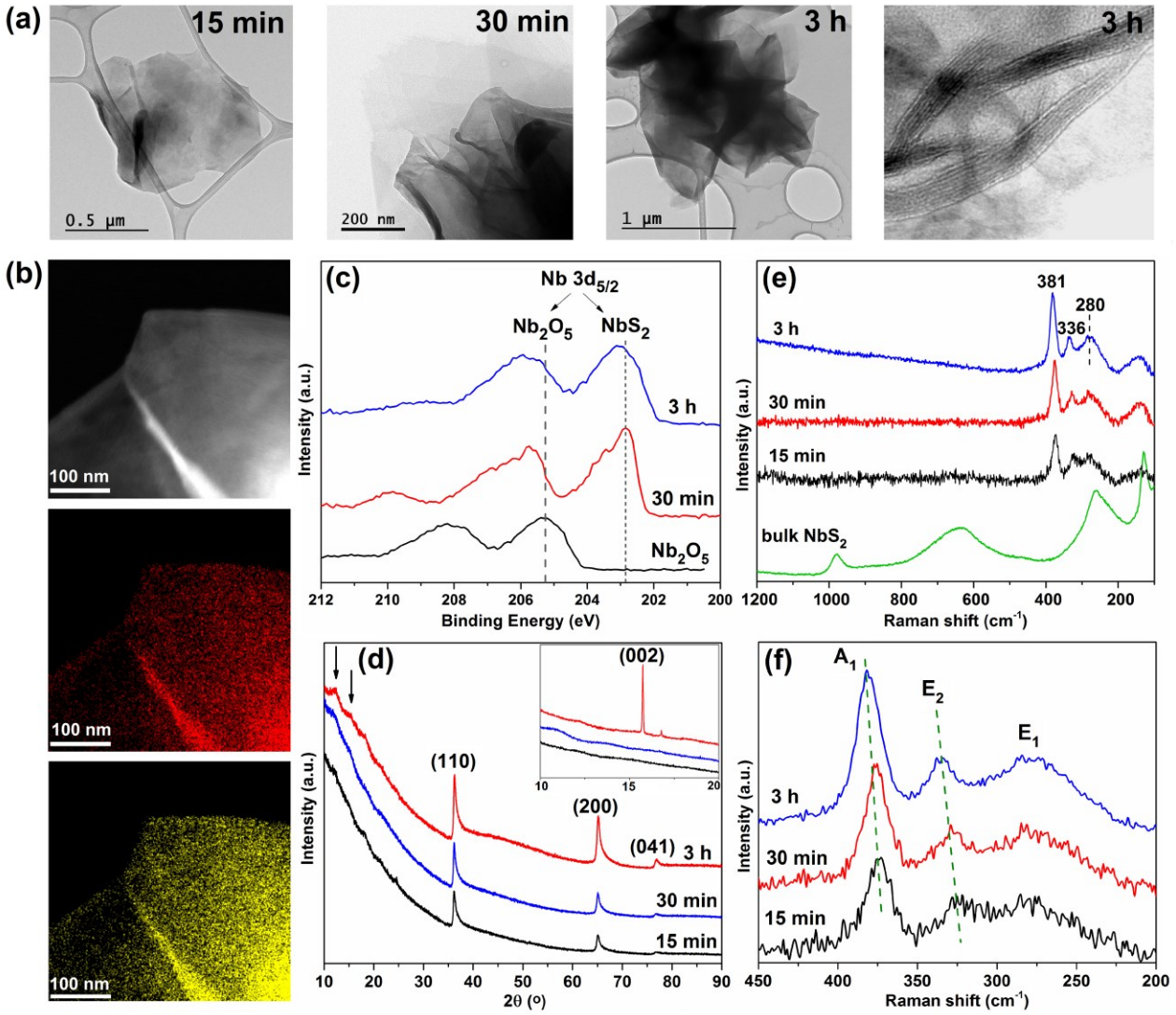

Figure 7.1. (a) TEM images of NbS_2 nanosheets collected at different sulfidation times; (b) STEM-EDS images of nanosheet collected after 30 min sulfidation; (c) XPS spectra of bulk Nb_2O_5 and NbS_2 nanosheets collected at different sulfidation times; (d) XRD patterns of NbS_2 nanosheets prepared at different sulfidation times assigned by PDF # 97-005-0648 (inset is the patterns collected at a lower scan rate); (e) Raman spectra of the NbS_2 bulk and nanosheets; (f) a close-up view of the Raman spectra.

Figure 7.1d displays the XRD patterns of the nanosheets collected at different sulfidation times. The XRD peaks were asymmetric that is a typical feature of 2D nanosheets[3,22], which also intensified by sulfidation time. In contrast to the XRD pattern of the sample collected after 15 min, new peaks appeared (at 2θ below 20°) in the pattern of multilayers nanosheets (indicated by

arrows in Figure 7.1d). The XRD patterns collected at a lower scan rate showed a sharp peak in the case of 3 h sulfidation (inset in Figure 7.1d). This peak can be assigned to the (002) plane revealing the *c*-axis growth of nanosheet at increased sulfidation time.[3,14] This finding suggests that the crystalline NbS_2 were initially generated as monolayer sheets (or with a low number of layers) with a strong dimensional confinement along the *c*-axis, then gradually stacked into multilayers sheets with a partial aggregation as sulfidation continues.

Raman spectroscopy as a sensitive tool to layer thickness was performed at ambient temperature for further structural investigation. The Raman spectra of the nanosheets collected at various sulfidation durations exhibited a different feature than that of bulk NbS_2 (Figure 7.1e, f). The Raman bands at 280 cm^{-1}, 336 cm^{-1}, and 381 cm^{-1} can be attributed to the E_1, E_2, and A_1 modes of layered NbS_2 (3R-NbS_2).[24,25] Similar to the reported Raman spectrum for 3R-NbS_2, the out-of-plane vibrational mode A_1 showed a higher intensity than in-plane E_2.[25] However, we did not detect the A_2 mode. The thickness dependence of the Raman frequency modes was already established.[26,27] Therefore, since no variations were observed in the Raman spectra of different locations within a sample, they can be used as a layer thickness indicator. As shown in the Raman close-up view in Figure 7.1f, the intensities of the Raman peaks increased by the number of layers. Moreover, the E_2 and A_1 bands shifted toward higher wavenumbers. For instance, the E_2 peak at 373 cm^{-1} for the sample collected after 15 min moved to 381 cm^{-1} for the multilayer nanosheets (collected after and 3 h).

Adding oleic acid (OAc) to the oleylamine (OAm) solution led to the significant structural changes depending on the OAc/OAm molar ratio. We tested two OAc/OAm molar ratios of 0.3 and 0.6. At both ratios, OAc suppressed the formation of flower-like aggregates. At the high OAc/OAm ratio of 0.6, the number of layer reduced with a confined lateral size of ~1 μm even after 3 h sulfidation (Figure 7.2a). The (002) peak corresponding to the *c*-axis growth was not observed in the XRD pattern indicating the absence of multilayer nanosheets (Figure 7.2b). Furthermore, the peaks' intensities were lower than those in the XRD pattern of single layer nanosheet obtained after 15 min sulfidation in OAm. Figure 7.2c shows that the E_2 and A_1 Raman modes shifted to the lower wavenumbers as compared to the multilayer nanosheets. Moreover, E_1 vibrational mode appeared as a shoulder. This suggests that OAc caused a diffusion barrier and a slow growth of active monomers that prevented the vertical growth and

aggregation of NbS_2 nanosheets. This is in agreement with a former study in which oleic acid afforded single layer WSe_2 nanosheets with the lateral size of 200-300 nm.[2]

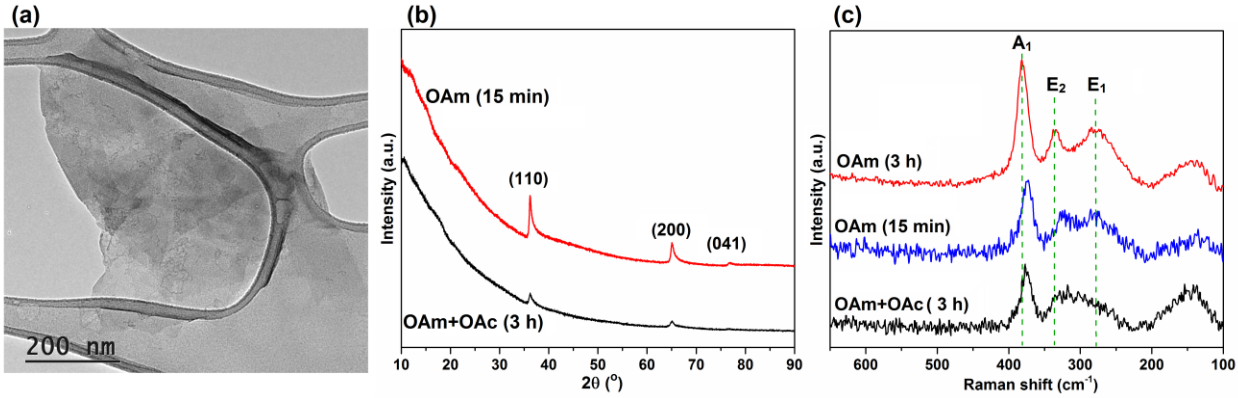

Figure 7.2. (a) TEM image of NbS_2 nanosheet collected after 3 h sulfidation at 300 °C prepared at OAc/OAm molar ratio of 0.6; (b) XRD pattern assigned by PDF # 97-005-0648; and (c) high-resolution Raman spectra of the nanosheets prepared at OAc/OAm of 0.6.

It is known that varying the concentration of ligands in the reaction solution tunes the reactivity of the monomers during the nucleation and growth period.[18,19] The influence of the concentration of OAc on the growth kinetics of semiconductor nanocrystals such as CdS and their size distribution was found significant.[19] Accordingly, we reduced th OAc/OAm ratio to 0.3 under identical synthesis conditions. As expected, a different morphology was obtained at the reduced OAc. A spherically rounded surface that partially collapsed were developed in the edge areas of the 2D nanosheet (Figure 7.3). The formation of this poorly defined agglomerates can be attributed to the reaction with a low concentration of ligands.[16]

We discovered that the amount of CS_2 injected into the synthesis solution led to a shape change and selective growth of NbS_2 (Figure 7.3). In the case of oleylamine solution, injection of a higher amount CS_2 (32 mmol instead of 8 mmol) resulted in the formation of multilayers and aggregates in the early stages of sulfidation (30 min of sulfidation) (Figure S1, Supporting Information). Similarly, the number of the layer was increased without the formation of aggregates when 32 mmol CS_2 was injected into the mixture oleylamine and oleic acid at the

OAc/OAm molar ratio of 0.6. Surprisingly, a completely different structure was formed when the OAc/OAm molar ratio decreased to 0.3. Injection of 16 mmol CS_2 resulted in the formation of ultrathin nanohexagons with a narrow lateral size of ~50 nm. Increasing CS_2 up to 32 mmol resulted in the formation of nanobars (Figure 7.3 and Figure 7.5). A similar behavior was observed in the previous works in which concentration of selenium (Se) as a chalcogen source changed the shape of indium selenide (InSe) nanocrystals.[28,29]

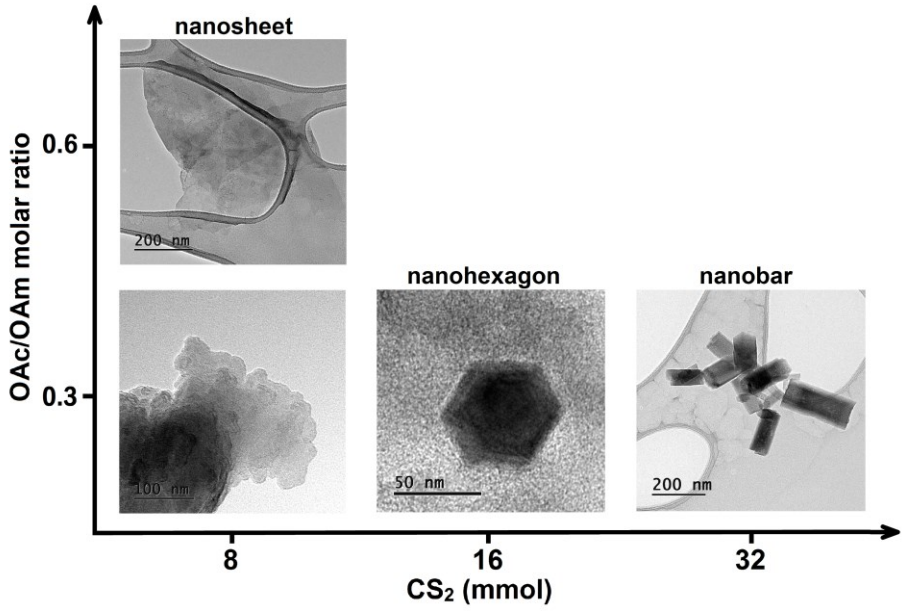

Figure 7.3. NbS_2 shape dependence on OAc/OAm molar ratio and the amount of injected CS_2.

TEM image in Figure 7.4 shows that Nb species nucleated first as spherically-shaped structures (inset, taken after 15 min of sulfidation) and then grew up as dispersed nanohexagons. The *d*-spacing of 0.29 nm determined in the HRTEM image can be attributed to (110) plane of NbS_2, consistent with the XRD PDF # 97-005-0648. In contrast to the in-plane growth of nanosheets, the nanoplates grew in the vertical (*c*-axis) direction as indicated by the (003) plane in the XRD pattern. The Raman E_1, E_2, and A_1 modes occurred at the wavenumbers similar to the single sheet. Increasing the CS_2 to 32 mmol resulted in 2D nanobars (Figure 7.5). Interestingly, the fringe size of 0.35 nm was different from that of nanohexagons that can be attributed to the (004) plane of NbS_2. This reveals the presence of different crystallographic planes in the 2D structure

with various reactivities toward sulfur, similar to what observed in the case of InSe.[28,29] We also investigated the effects of a non-coordinating solvent such as 1-octadecene (ODE). We followed the synthesis conditions used for nanohexagons except using ODE instead of OAm. We found that a higher temperature of ~325 °C is required for sulfidation and formation of nanoparticles. As can be seen in Figure 7.6, 3D spherical particles were obtained after 2 h sulfidation using 16 mmol CS_2. The obtained particles were crystalline with a fringe size of 0.32 nm.

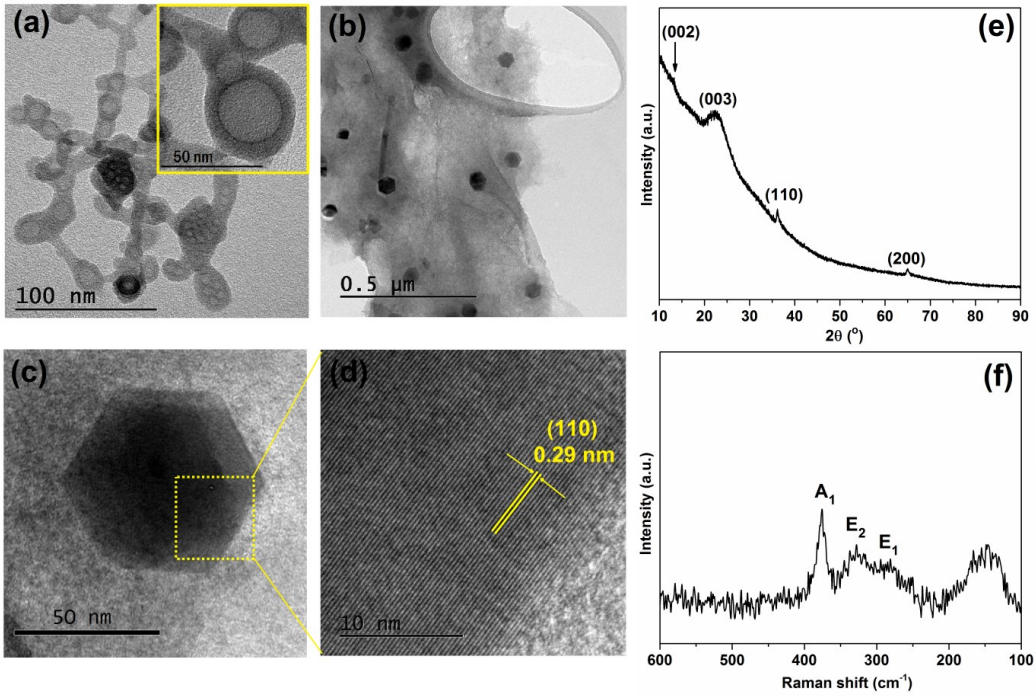

Figure 7.4. (a) TEM image of NbS_2 nanohexagons collected after 15 min sulfidation at 300 °C shows the nucleation of nanostructures; (b) TEM images of 2D nanohexagons; (c, d) HTREM images of nanohexagons; (e) XRD pattern assigned with PD F# 97-005-0648 NbS_2; and (f) High-resolution Raman spectrum.

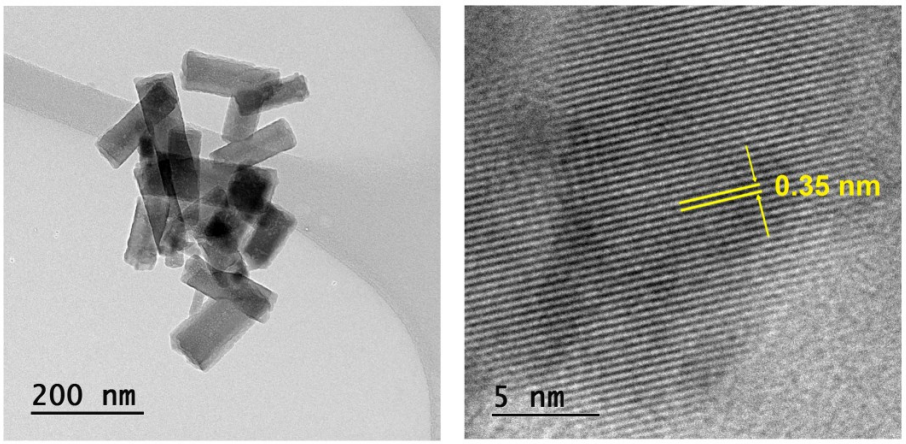

Figure 7.5. TEM and HRTEM images of NbS_2 nanobars.

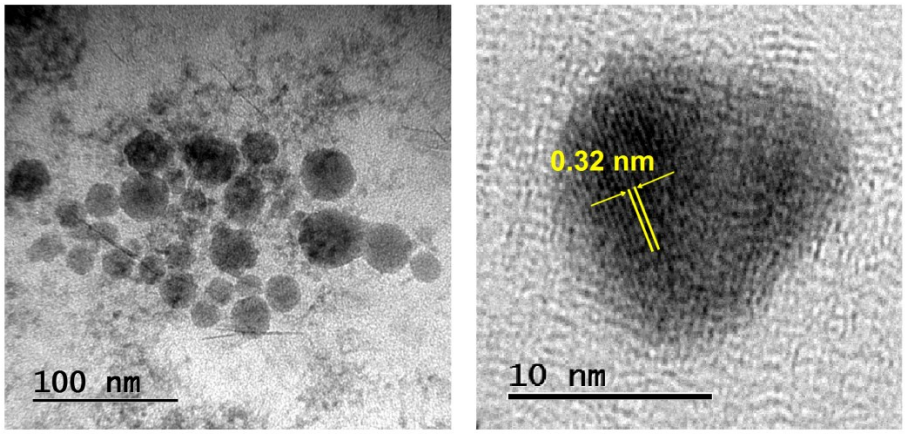

Figure 7.6. TEM and HRTEM images of NbS_2 nanospheres.

Copper-doped NbS_2 nanosheets were prepared by sulfidation of Nb and Cu precursors in oleylamine at 300 °C using 8 mmol CS_2. Two samples with Cu/Nb molar ratio of 0.1 and 0.3 were prepared. HRTEM-EDS was employed to determine the structural properties of the synthesized materials. As can be seen in Figure 7.7, bimetallic NbCu nanosheets with a Cu/Nb molar ratio of 0.1 was formed 30 min after CS_2 injection. The TEM images revealed the absence of aggregated nanosheets (Figure 7.7a). Furthermore, copper sulfides were not present as single particles. However, at higher Cu/Nb molar ratio, Cu presented as individual particles out of nanosheets (Figure S2, Supporting Information). This suggests that there is a threshold Cu/Nb

molar ratio at which Cu substituted in NbS_2 nanosheet. This limitation could be due to the p-type and n-type semiconducting natures of copper and niobium sulfide, respectively. The XPS Nb 3d and Cu 2p core levels exhibited clear positive and negative shifts as compared to the monometallic NbS_2 and CuS, respectively. This suggests the charge transfer between Cu and Nb species in the nanosheets. The XRD pattern showed similar feature as NbS_2 nanosheets. However, a shift in the peak position and an increase in the peak width were observed in the XRD pattern of CuNb nanosheets as compared to NbS_2. In comparison with that of NbS_2, the Raman bands of bimetallic NbCu nanosheets at 336 and 285 cm^{-1} slightly shifted to lower and higher wavenumbers, respectively. Moreover, new weak peaks appeared at 438 and 482 cm^{-1}. This negative shift has been attributed to the decreased interlayer van der Waals forces, which consequently increased the presence of single sheets. Note that copper is not needed during liquid-phase formation of NbS_2.

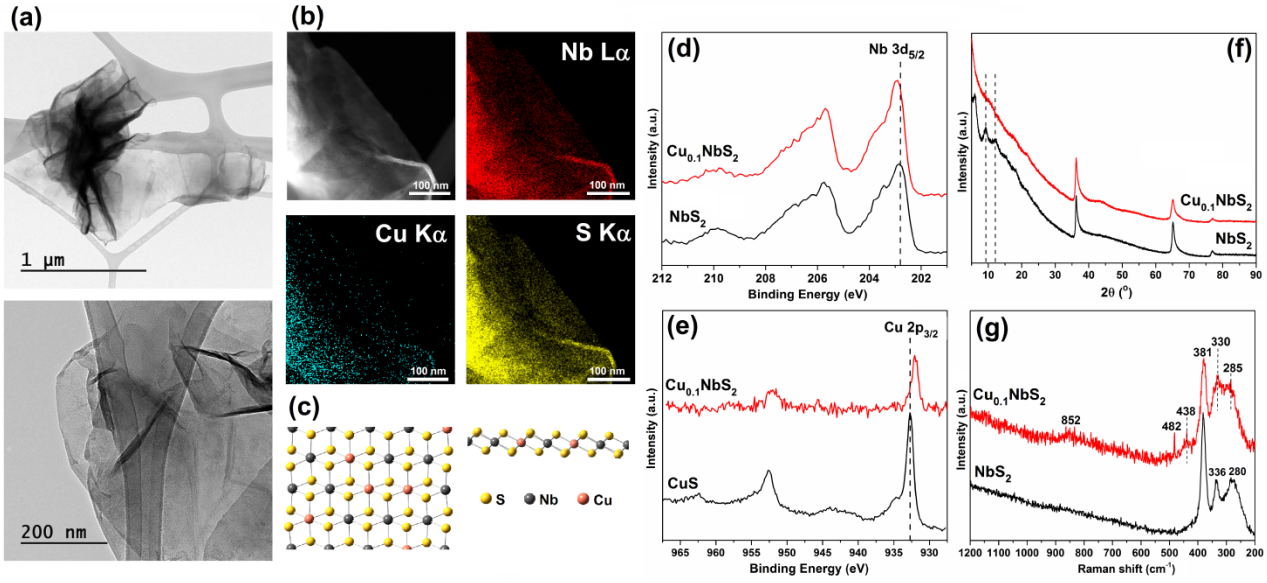

Figure 7.7. NbCu nanosheet: (a) TEM images, (b) STEM-EDS images, (c) random substitution of Cu in NbS_2 nanosheet, (d) Nb 3d core level and (e) Cu 2p core level XPS spectra; (f) XRD pattern; (g) Raman spectra at ambient temperature; all after 30 min sulfidation at 300 °C.

The alumina-supported nanostructures were evaluated in HDS of DBT at 325 °C and 3 MPa in a continuous flow system. Table 7.1 shows the performance of the catalysts after 24 h on-stream

including stabilization period. The Nb loadings of different samples, measured by ICP-MS, were in the same range. To complete the sulfidation and to remove remaining ligands, the synthesized catalysts were treated before HDS reaction at 325 °C in a flow of 100 ml/min hydrogen gas and 0.05 ml/min CS_2 diluted in *n*-decane (10 wt% CS_2) for 3 h. The stabilizers used in the synthesis can be removed during deposition on the support followed by the heat treatment since their boiling points are in the range of 350 °C. In contrast to the bulk niobia (Nb_2O_5) that requires a high temperature (≥750 °C) sulfidation, colloidal NbS_2 supported on alumina exhibited a better performance at the lower treatment temperature of 325 °C, irrespective of the shape and the structure of the nanomaterials (Table 7.1 and Table S1 in Supporting Information). This reveals that a complete sulfidation of Nb occurred in the liquid phase, as verified by XPS, eliminating a high-temperature pretreatment.

The single- and multilayers nanosheets prepared in oleylamine after 15 min and 3 h sulfidation, respectively, showed different catalytic performance. Increasing the layer number and formation of aggregates decreased the DBT conversion by ~100 %. The same behavior was observed when the single layer nanosheet treated at 400 °C. Accordingly, the lower conversion of multilayers nanosheets could be due to lower accessible active sites as well as aggregation of the nanostructures. Increasing the number of layers promoted the hydrocracking (HCK) selectivity from 35 to 56 %. Substitution of Cu in the nanosheets at Cu/Nb molar ratio of 0.1 reduced the DBT conversion from ~10 to below 2 % with no significant change in selectivity.

Shape-confined NbS_2 2D nanostructures and 3D nanoparticles exhibited different catalytic activities and selectivities. The highest conversion was obtained in the case of nanohexagons, even higher than that of NbS_2 nanoparticles. We also found that controlling the shape and structure of the NbS_2 improved the DDS selectivity in cost of HCK selectivity. The lowest HCK selectivity of 8 % and the highest DDS selectivity of 76 % were achieved on nanohexagons at DBT conversion of 74 %. We attributed this behavior to the higher fraction of active sites at corners and edges.

Table 7.1. Catalytic performance of the synthesized materials in HDS of DBT at 325 °C and 3MPa. Pretreatment at 325 °C for 3 h.

catalyst	Nb loading (wt%)	DBT conversion (%)	Activity ($mmol_{DBT}/mol_{Nb}/s$)	Selectivity		
				DDS	HYD	HCK
Monolayer nanosheet	0.97	9.6	0.07	42	23	35
Multilayer nanosheet	0.94	4.6	0.03	33	11	56
NbCu nanosheet	0.76	1.6	0.01	38	11	51
nanohexagons	0.96	74.0	0.54	76	16	8
nanobars	1.00	7.1	0.04	45	11	44
nanoparticle	1.0	36.5	0.26	64	20	16

7.4 Conclusions

Ligand-directed 2D and 3D size- and shape-confined NbS_2 colloids were synthesized in this work at ~300 °C by CS_2. Oleylamine as a coordinating solvent formed monolayer nanosheet in the early stage of synthesis, which then transformed into multilayers and flower-like structures as the sulfidation proceeds. Addition of oleic acid reduced the number of layers. Increasing the amount of sulfur led to the formation of corners- and edges-abundant nanohexagons and nanobars with different crystalline structures. In contrast to the formation of 2D NbS_2 in OAm, ODE as a non-coordinating solvent boosted nanospheres (3D NbS_2) growth. The synthesized materials were supported on alumina and then evaluated in hydrodesulfurization (HDS) of DBT at 325 °C. We found that decreasing the number layers and lateral size of the nanostructures enhanced the catalytic activities. The highest activity and direct desulfurization selectivity (DDS) was obtained on the nanohexagons most likely because of its increased fraction of corner and edge active sites. The synthesis protocol developed in this study can be generalizable to other TMDC.

7.5 Supporting Information

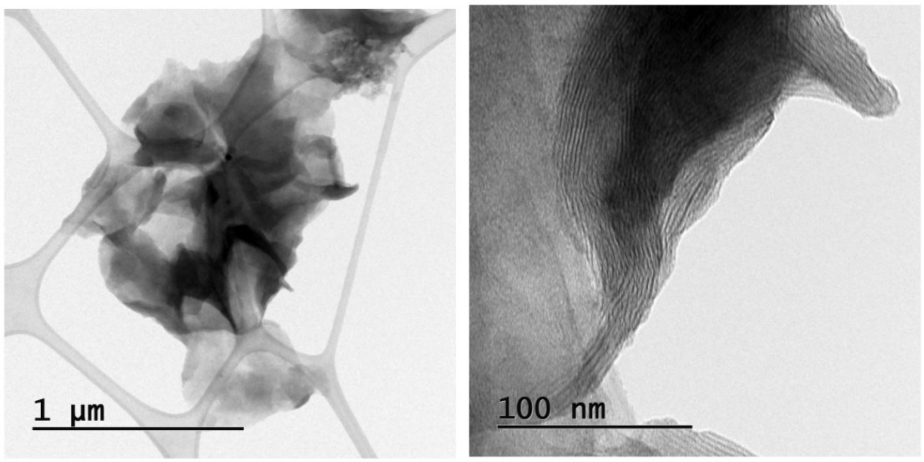

Figure S1. TEM images of nanosheet collected after 30 min sulfidation at 300 °C with 32 mmol CS_2. The number of layers increased and aggregates formed as compared to the lower amount of injected CS_2.

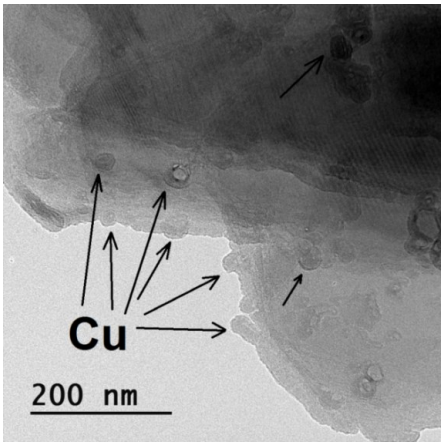

Figure S2. TEM image of NbCu nanosheet at Cu/Nb molar ratio of 0.2 revealing the formation of copper nanoparticles out of sheets.

7.6 References

(1) Jeong, S.; Yoo, D.; Jang, J.; Kim, M.; Cheon, J. J. Am. Chem. Soc. 2012, 134, 18233-18236.

(2) Mahler, B.; Hoepfner, V.; Liao, K.; Ozin, G. A. J. Am. Chem. Soc. 2014, 136, 14121-14127.

(3) Seo, J. W.; Jun, Y. W.; Park, S. W.; Nah, H.; Moon, T.; Park, B.; Kim, J. G.; Kim, Y. J.; Cheon, J. Angew. Chemie - Int. Ed. 2007, 46, 8828-8831.

(4) Jang, J. T.; Jeong, S.; Seo, J. W.; Kim, M. C.; Sim, E.; Oh, Y.; Nam, S.; Park, B.; Cheon, J. J. Am. Chem. Soc. 2011, 133, 7636-7639.

(5) Jeong, S.; Han, J. H.; Jang, J. T.; Seo, J. W.; Kim, J. G.; Cheon, J. J. Am. Chem. Soc. 2011, 133, 14500-14503.

(6) Yoo, D.; Kim, M.; Jeong, S.; Han, J.; Cheon, J. J. Am. Chem. Soc. 2014, 136, 14670-14673.

(7) Chhowalla, M.; Shin, H. S.; Eda, G.; Li, L.-J.; Loh, K. P.; Zhang, H. Nat. Chem. 2013, 5, 263-275.

(8) Jellinek, F.; Brauer, G.; Müller, H. Nature 1960, 185, 376-377.

(9) Zak, A.; Feldman, Y.; Alperovich, V.; Rosentsveig, R.; Tenne, R. J. Am. Chem. Soc. 2000, 122, 11108-11116.

(10) Han, J. H.; Lee, S.; Cheon, J. Chem Soc Rev 2013, 42, 2581-2591.

(11) Zhang, Z.; Tang, Z.; Kotov, N. A.; Glotzer, S. C. Nano Lett. 2007, 7, 1670-1673.

(12) Pradhan, N.; Xu, H.; Peng, X. Nano Lett. 2006, 6, 720-724.

(13) Polleux, J.; Pinna, N.; Antonietti, M.; Niederberger, M. Adv. Mater. 2004, 16, 436-439.

(14) Jung, W.; Lee, S.; Yoo, D.; Jeong, S.; Miro, P.; Kuc, A.; Heine, T.; Cheon, J. J. Am. Chem. Soc. 2015, 137, 7266-7269.

(15) Pradhan, N.; Reifsnyder, D.; Xie, R.; Aldana, J.; Peng, X. J. Am. Chem. Soc. 2007, 129, 9500-9509.

(16) Kort, K. R.; Banerjee, S. Small 2015, 11, 329-334.

(17) Meng, F.; Morin, S. A.; Jin, S. Acc. Chem. Res. 2013, 46, 1616-1626.

(18) Peng, X.; Thessing, J. Struc Bond 2005, 118, 79-119.

(19) Yu, W. W.; Peng, X. Angew. Chemie - Int. Ed. 2002, 41, 2368-2371.

(20) Dash, J. K.; Chen, L.; Dinolfo, P. H.; Lu, T. M.; Wang, G. C. J. Phys. Chem. C 2015, 119 , 19763-19771.

(21) Chhowalla, M.; Shin, H. S.; Eda, G.; Li, L.-J.; Loh, K. P.; Zhang, H. Nat. Chem. 2013, 5, 263-275.

(22) Yang, D.; Jimenez Sandoval, S.; Divigalpitiya, W. M. R.; Irwin, J. C.; Frindt, R. F. Phys. Rev. B 1991, 43, 12053-12056.

(23) Wu, X.; Tao, Y.; Ke, X.; Zhu, J.; Hong, J. Mater. Res. Bull. 2004, 39, 901-908.

(24) Onari, S.; Arai, T.; Aoki, R.; Nakamura, S. Solid State Commun. 1979, 31, 577-579.

(25) McMullan, W. G.; Irwin, J. C. Solid State Commun. 1983, 45, 557-560.

(26) Lee, C.; Yan, H.; Brus, L. E.; Heinz, T. F.; Hone, J.; Ryu, S. ACS Nano 2010, 4, 2695-2700.

(27) Zhao, S. H.; Hotta, T.; Koretsune, T.; Watanabe, K.; Taniguchi, T.; Sugawara, K.; Takahashi, T.; Shinohara, H.; Kitaura, R. 2D Mater. 2016, 3, 025027.

(28) Hayashi, T.; Keiji Ueno; Saiki, K.; Koma, A. J. Cryst. Growth 2000, 219, 115-122.

(29) Hyun Park, K.; Jang, K.; Kim, S.; Jin Kim, H.; Uk Son, S. J. Am. Chem. Soc. 2006, 128, 14780-14781.

(30) Zhou, J.; Pu, C.; Jiao, T.; Hou, X.; Peng, X. J. Am. Chem. Soc. 2016, 138, 6475-6483.

Chapter 8. Concluding remarks and future works

8.1 Conclusions

This thesis focuses on design and development of high-performance catalysts for a two-stage hydrodesulfurization (HDS) units using earth-abundant metals and reduced amounts of noble metals. Two types of catalysts based on palladium and niobium sulfide have been developed in this work. Palladium as the second stage HDS catalyst has shown an outstanding performance in HDS of refractory sulfur compounds but it is scarce and suffers from sintering in high-temperature applications. The objective of this research was to improve Pd thermal stability and catalytic performance (activity and selectivity) and to reduce Pd usage in the catalyst formulation. It was hypothesized that addition of a sintering-resistant element to palladium or dispersing palladium on the surface of a cheap metal as a core could promote its electronic and textural properties for a higher catalytic performance. Accordingly, bimetallic palladium-yttrium and palladium-iron nanostructures were developed using colloidal chemistry. In contrast to the conventional impregnation method, the addition of yttrium to palladium via hydrogen sacrificial technique improved its thermal stability against sintering and enhanced the carbon monoxide (CO) chemisorption on Pd species with modified adsorption mode and strength. In a low-pressure (1 MPa) HDS of 4,6-DMDBT at 350 °C, yttrium doubled the ratio of direct desulfurization to hydrogenation selectivities and suppressed hydrocracking selectivity twice with no changes in activity. On the other hand, decoration of palladium as nanosized islands on the surface of iron cores using galvanic exchange reaction increased Pd dispersion by an order of magnitude. This resulted in a four-fold enhancement in Pd mass-based HDS activity at 350 °C and 3 MPa at a reduced Pd content in the catalyst (Pd/Fe molar ratio of 0.2). Iron also improved the sulfur resistance of hydrogenation sites due to the higher affinity of sulfur to Fe as compared to Pd.

Niobium sulfide (NbS_2) is intrinsically more active than molybdenum sulfide (MoS_2) in the first stage HDS but its usage is hindered because of a very high temperature (more than 700 °C) required for sulfidation of niobium oxide (Nb_2O_5), which is impractical at industrial scales. The hypothesis was that the synergism between copper and niobium species facilitates the reduction/sulfidation of niobium oxide to much lower temperatures. Accordingly, a series of bimetallic NbCu bulk catalysts at different Cu/Nb molar ratios were developed via

coprecipitation method. XPS and TPR data verified the facilitative effects of copper on sulfidation and reduction of niobium oxide correlating with the copper content in the catalyst. XRD showed the formation of $Cu_{0.65}NbS_2$ structure after sulfidation at 400 °C. In HDS of DBT at 325 °C and 3 MPa, copper enhanced the HDS activity maximizing at a threshold Cu/Nb molar ratio of 0.3. Copper also improved DDS and HYD selectivities and suppressed hydrocracking selectivity. DDS selectivity correlated with the fraction of NbS_2 in the sample and hydrocracking selectivity correlated with the fraction of Nb_2O_5.

The performance of supported Nb and NbCu structures are strongly influenced by the nature of the support materials. Niobium species strongly interact with oxide supports making its sulfidation/reduction more difficult. Carbon as a support showed the highest mass-based activity among other types of support such as carbon nanotube and graphene as well as different phases of alumina. Despite the facilitative effect of copper on reduction and sulfidation of niobium oxide, HDS activities of supported catalysts were not improved but the selectivities changed significantly. Nb sulfidation enhanced by Nb loading in the carbon-supported catalysts. In contrast to this trend, the low loading catalyst (2.0 wt% Nb) with the least sulfidation degree (less than 10 %) functioned as coordinatively unsaturated Lewis acid sites in the HDS of DBT and delivered the highest HDS activity per mole of Nb. However, this sample delivered a high hydrocracking selectivity of around 70 % at 74 % conversion. The addition of copper enhanced DDS selectivity and reduced hydrocracking selectivity to around 15 % over the whole range of Nb loadings without suppressing/improving HDS activity.

Colloidal chemistry is a powerful technique for liquid phase sulfidation of transition metals at low temperature (~300 °C) that also offers a possibility of controlling the structure of nanoparticles. In addition, it minimizes the metal-support interactions between niobium species and oxide supports as compared to the impregnation method. Colloidal NbS_2 nanostructures were synthesized in different shapes and structures using a coordinating solvent and capping ligands. NbS_2 was formed as thin nanosheets in oleylamine as a coordinating solvent. Increasing the sulfidation time, increased the number of layers and then finally aggregated as a flower-like structure after 3 h sulfidation. Adding oleic acid as a capping ligand into the oleylamine solution prevented the formation of aggregates and stabilized thin layer even after 3 h sulfidation. The amount of capping ligand as well as sulfur content affected the structural properties of NbS_2.

Injection of an increased amount of CS_2 formed nanohexagons instead of nanosheets. Further CS_2 led to the formation of nanobars. A non-coordinating solvent such as 1-octadecene resulted in the formation of three-dimensional NbS_2 nanospheres. The synthesized nanostructures supported on Al_2O_3 exhibited different HDS activities depending on the shape of nanostructures. The developed materials did not require a high-temperature pre-sulfidation in contrast to the bulk and supported catalysts. Increasing the number of layers in nanosheets reduced the HDS activity. Nanohexagons exhibited the highest activity per mole of Nb and DDS selectivity with a minimum cracking selectivity (less than 10 %). This activity was twice more than that of low loading carbon-supported catalyst (2.0 wt% Nb) most likely due to the higher fraction of corners and edges active sites.

8.2 Future works

Both developed catalysts for the first and the second stage HDS units have a great potential for further research on their own. For the first stage HDS unit, two research approaches are recommended:

1- A real feedstock contains a wide range of heteroatom-containing compounds such as nitrogen and polycyclic aromatics. Niobium sulfide is known for its promising hydrodenitrogenation and hydrocracking activities. Therefore, one approach for both bulk and supported Nb(Cu) catalysts (prepared by impregnation or colloidal nanohexagons) would be measuring the performance and stability of the catalysts in simultaneous nitrogen, sulfur, and aromatic removal especially from heavy feedstocks.

2- Although Nb(Cu) sulfide outperformed molybdenum sulfide, the activity is still lower than that of Ni(Co)Mo catalyst. Therefore, an interesting approach to future research would be determining the probable synergism between Nb(Cu) structure and one of nickel, cobalt, molybdenum, or tungsten metals in hydrotreating reaction.

For the second stage HDS catalyst, palladium can be doped with a second metal such as platinum or dope iron with nickel or cobalt in order to further enhance the activity and control the selectivity. Doping either Pd or Fe with a second metal will affect the electronic and crystal properties of active sites.

Bibliography

(1) Stanislaus, A.; Marafi, A.; Rana, M. S. Catal. Today 2010, 153, 1–68.

(2) Mariq, M. M.; Chase, R. E.; Xu, N.; P.M. Laing. Environ. Sci. Technol. 2002, 36, 283-289.

(3) Corro, G. Catal. Lett. 2002, 75, 89-106.

(4) Ziaei-Azad, H.; Semagina, N. Appl. Catal. B, Environ. 2016, 191, 138–146.

(5) Song, C. Catal. Today 2003, 86, 211–263.

(6) Ho, T. C. Catal. Today 2004, 98, 3–18.

(7) Song, C.; Ma, X. Appl. Catal. B, Environ. 2003, 41 207–238.

(8) Kabe, T.; Ishihara, A.; Zhang, Q. Appl. Catal. A, Gen. 1993, 97, L1-L9.

(9) Prins R. In Handbook of heterogeneous catalysis; Ertl, G., Knozinger, H., Schuth, F., Weitkamp, J., Eds.; Wiley-VCH, 2008, 2695–2718.

(10) Song, C.; Ma, X. Appl. Catal. B, Environ. 2003, 41, 207–238.

(11) Ito, E.; van Veen, J. A. R. Catal. Today 2006, 116, 446–460.

(12) Ma, X.; Sakanishi, K.; Isoda, T.; Mochida, I. Energy & Fuels 1995, 9, 33–37.

(13) Ma, X.; Sakanishi, K.; Mochida, I. Eng. Chem. Res. 1996, 35, 2487–2494.

(14) Andari, M. K.; Abu-Seedo, F.; Stanislaus, A.; Qabazard, H. M. Fuel 1996, 75, 1664–1670.

(15) Knudsen, K. G.; Cooper, B. H.; Topsøe, H. Appl. Catal. A, Gen. 1999, 189, 205–215.

(16) Chianelli, R. R.; Berhault, G.; Torres, B. Catal. Today 2009, 147, 275–286.

(17) Aray, Y.; Zambrano, D.; Cornejo, M.; Ludeña, E. V.; Iza, P.; Vidal, A. B.; Coll, D. S.; Jímenez, D. M.; Henriquez, F.; Paredes, C. J. Phys. Chem. C 2014, 118, 27823–27832.

(18) Gutiérrez, O. Y.; Singh, S.; Schachtl, E.; Kim, J.; Kondratieva, E.; Hein, J.; Lercher, J. A. ACS Catal. 2014, 4, 1487–1499.

(19) Bara, C.; Plais, L.; Larmier, K.; Devers, E.; Digne, M.; Lamic-Humblot, A. F.; Pirngruber, G. D.; Carrier, X. J. Am. Chem. Soc. 2015, 137, 15915–15928.

(20) Eijsbouts, S.; Anderson, G. H.; Bergwerff, J. A.; Jacobi, S. Appl. Catal. A, Gen. 2013, 458, 169–182.

(21) Wang, Q. H.; Kalantar-Zadeh, K.; Kis, A.; Coleman, J. N.; Strano, M. S. Nat. Nanotechnol. 2012, 7, 699–712.

(22) Pang, Q.; Liang, X.; Kwok, C. Y.; Nazar, L. F. Nat. Energy 2016, 1, 16132-16143.

(23) Lai, C.-H.; Lu, M.-Y.; Chen, L.-J. J. Mater. Chem. 2012, 22, 19–30.

(24) Ou, X.; Xiong, X.; Zheng, F.; Yang, C.; Lin, Z.; Hu, R.; Jin, C.; Chen, Y.; Liu, M. J. Power Sources 2016, 325, 410–416.

(25) Montoya, J. H.; Seitz, L. C.; Chakthranont, P.; Vojvodic, A.; Jaramillo, T. F.; Nørskov, J. K. Nat. Mater. 2016, 16, 70–81.

(26) Tsai, M.L.; Su, S.H.; Chang, J.K.; Tsai, D.S.; Chen, C.H.; Wu, C.I.; Li, L.J.; Chen, L.J.; He, J.H. ACS Nano 2014, 8, 8317–8322.

(27) Kibsgaard, J.; Chen, Z.; Reinecke, B. N.; Jaramillo, T. F. Nat. Mater. 2012, 11, 963–969.

(28) Ha, E.; Liu, W.; Wang, L.; Man, H.W.; Hu, L.; Tsang, S. C. E.; Chan, C. T.L.; Kwok, W.M.; Lee, L. Y. S.; Wong, K.Y. Sci. Rep. 2017, 7, 39411-39419.

(29) Staszak-Jirkovský, J.; Malliakas, C. D.; Lopes, P. P.; Danilovic, N.; Kota, S. S.; Chang, K.-C.; Genorio, B.; Strmcnik, D.; Stamenkovic, V. R.; Kanatzidis, M. G.; Markovic, N. M. Nat. Mater. 2015, 15, 197–203.

(30) Asadi, M.; Kumar, B.; Behranginia, A.; Rosen, B. a; Baskin, A.; Repnin, N.; Pisasale, D.; Phillips, P.; Zhu, W.; Haasch, R.; Klie, R. F.; Král, P.; Abiade, J.; Salehi-Khojin, A. Nat. Commun. 2014, 5, 4470-4478.

(31) Asadi, M.; Kim, K.; Liu, C.; Addepalli, A. V.; Abbasi, P.; Yasaei, P.; Phillips, P.; Behranginia, A.; Cerrato, J. M.; Haasch, R.; Zapol, P.; Kumar, B.; Klie, R. F.; Abiade, J.; Curtiss, L. A.; Salehi-Khojin, A. Science 2016, 353, 467–470.

(32) H. Topsøe, B.S. Clausen, F.E. Massoth, in: J.R. Anderson, M. B. (Eds.Springer-Verlag: New York, 1996.

(33) Shafi, R.; Hutchings, G. J. Catal. Today 2000, 59, 423–442.

(34) Babich, I. V.; Moulijn, J. A. Fuel 2003, 82, 607–631.

(35) Allali, N.; Leblanc, A.; Danot, M.; Geantet, C,; Vrinat, M.; Breysse, M. Catal. Today 1996, 27, 137–144.

(36) Allali, N.; Marie, A.M.; Danot, M.; Geantet, C.; Breysse, M. J. Catal. 1995, 156, 279–289.

(37) Gaborit, V.; Allali, N.; Danot, M.; Geantet, C.; Cattenot, M.; Breysse, M.; Diehl, F. Catal. Today 2003, 78, 499–505.

(38) Lauritsen, J. V.; Kibsgaard, J.; Olesen, G. H.; Moses, P. G.; Hinnemann, B.; Helveg, S.; Nørskov, J. K.; Clausen, B. S.; Topsøe, H.; Lægsgaard, E.; Besenbacher, F. J. Catal. 2007, 249, 220–233.

(39) Walton, A. S.; Lauritsen, J. V.; Topsøe, H.; Besenbacher, F. J. Catal. 2013, 308, 306–318.

(40) Ted Oyama, S.; Zhao, H.; Freund, H. J.; Asakura, K.; Włodarczyk, R.; Sierka, M. J. Catal. 2012, 285, 1–5.

(41) Plantenga, F. L.; Cerfontain, R.; Eijsbouts, S.; van Houtert, F.; Anderson, G. H.; Miseo, S.; Soled, S.; Riley, K.; Fujita, K.; Inoue, Y. Stud. Surf. Sci. Catal. 2003, 145, 407–410.

(42) Eijsbouts, S.; Plantenga, F.; Leliveld, B.; Inoue, Y.; Fujita, K. ACS Div. Fuel Chem. Prepr. 2003, 48, 494–495.

(43) Eijsbouts, S.; Mayo, S. W.; Fujita, K. Appl. Catal. A Gen. 2007, 322, 58–66.

(44) Pecoraro, T. A.; Chianelli, R. R. J. Catal. 1981, 67, 430–445.

(45) Chianelli, R. R. Catal. Rev. 1984, 26, 361–393.

(46) Lacroix, M.; Boutarfa, N.; Guillard, C.; Vrinat, M.; Breysse, M. J. Catal. 1989, 120, 473–477.

(47) Benard, J.; Oudar, J.; Barbouth, N.; Margot, E.; Berthier, Y. Surf. Sci., 1979, 88, L35-L41 .

(48) Chianelli, R. R.; Berhault, G.; Raybaud, P.; Kasztelan, S.; Hafner, J.; Toulhoat, H. Appl. Catal. A, Gen. 2002, 227, 83–96.

(49) Toulhoat, H.; Raybaud, P.; Kasztelan, S.; Kresse, G.; Hafner, J. Catal. Today 1999, 50, 629–636.

(50) Raybaud, P.; Kresse, G.; Hafner, J.; Toulhoat, H. J. Phys. Condens. Matter 1999, 9, 11085–11106.

(51) Chianelli, R. R.; Pecoraro, T. A.; Halbert, T. R.; Pan, W. H.; Stiefel, E. I. J. Catal. 1984, 86, 226–230.

(52) Tanaka, K. I. Adv. Catal. 1985, 33, 99–158.

(53) Karroua, M.; Ladrie`re, J.; Matralis, H.; Grange, P.; Delmon, B. J. Catal. 1992, 138, 640–658.

(54) Afanasiev, P.; Fischer, L.; Beauchesne, F.; Danot, M.; Gaborit, V.; Breysse, M. Catal. Lett. 2000, 64, 59.

(55) Hermann, N.; Brorson, M.; Topsøe, H. Catal. Letters 2000, 65, 169–174.

(56) Danot, M.; Afonso, J.; Des, C. T.; Portefaix, J. L.; Breysse, M. Catal. Today 1991, 10, 629–643.

(57) Egorova, M.; Prins, R. J. Catal. 2004, 225, 417–427.

(58) Gaborit, V.; Allali, N.; Geantet, C.; Breysse, M.; Vrinat, M.; Danot, M. Catal. Today 2000, 57, 267–273.

(59) Geantet, C.; Afonso, J.; Breysse, M.; Allali, N.; Danot, M. Catal. Today 1996, 28, 23–30.

(60) Haxel, G. B.; Hedrick, J. B.; Orris, G. J. Rare Earth Elements-Critical Resources for High Technology; 2002.

(61) WebElements.com. Archived from the original on 9 March 2007. Retrieved 2007-04-14.

(62) Ziolek, M. Catal. Today 2003, 78, 47–64.

(63) Zdražil, M. Catal. Today 1988, 3, 269–365.

(64) Dash, J. K.; Chen, L.; Dinolfo, P. H.; Lu, T. M.; Wang, G. C. J. Phys. Chem. C 2015, 119 , 19763–19771.

(65) Wachs, I. E.; Briand, L. E.; Jehng, J.M.; Burcham, L.; Gao, X. Catal. Today 2000, 57, 323–330.

(66) Kadijk, F.; Jellinek, F. J. Less Common Met. 1969, 19, 421–430.

(67) Allali, N.; Prouzet, E.; Michalowicz, A.; Gaborit, V.; Nadiri, A.; Danot, M. Appl. Catal. A, Gen. 1997, 159, 333–354.

(68) Breysse, M.; Courieres, T. D.; Danot, M.; Geantet, M.; Portefaix, J.-L., US patent, 1992, US5157009 A.

(69) Gissy, H.; Bartsch, R.; Tanielian, C. J. Catal. 1980, 65, 150–157.

(70) de Beer, V. H. J.; Bevelander, C.; van Sint Fiet, T. H. M.; Werter, P. G. A. J.; Amberg, C. H. J. Catal. 1976, 43, 68–77.

(71) Rao, C. N. R.; Pisharody, K. P. R. Prog. Solid State Chem. 1976, 10, 207–270.

(72) Liu, Z. L.; Cai, L. C.; Zhang, X. L. J. Alloys Compd. 2014, 610, 472–477.

(73) Jellinek, F.; Brauer, G.; Müller, H. Nature 1960, 185, 376–377.

(74) Afanasiev, P.; Bezverkhyy, I. Appl. Catal. A, Gen. 2007, 322, 129–141.

(75) Rijnsdorp, J.; Jellinek, F. J. Solid State Chem. 1978, 25, 325–328.

(76) Bullett, D. W. J. Solid State Chem. 1980, 33, 13–16.

(77) McCarty, K. F.; Anderegg, J. W.; Schrader, G. L. J. Catal. 1985, 93, 375–387.

(78) De Ridder, R.; Van Tendeloo, G.; Van Landuty, J.; Van Dyck, D.; Amelinckx, S.; phys. stat. sol. 1976, 37, 591–606.

(79) Schuit, G. C. A; Gates, B. C. AIChE J. 1973, 19, 417–438.

(80) Voorhoeve, R. J. H.; Stuiver, J. C. M. J. Catal. 1971, 23, 243–252.

(81) Hagenbach, G.; Courty, P.; Delmon, B. J. Catal. 1973, 31, 264–273.

(82) Topsøe, H.; Clausen, B. S.; Candia, R.; Wivel, C.; Morup, S. J. Catal. 1981, 68, 433–452.

(83) Sorensen, O.; Clausen, B. S.; Candia, R.; Topsøe, H. Appl. Catal. 1985, 13, 363–372.

(84) Topsøe, H. Appl. Catal. A, Gen. 2007, 322, 3–8.

(85) Breysse, M.; Bennett, B. A.; Chadwick, D.; Vrinat, M. Bull. Soc. Chim. Belg. 1981, 90, 1271.

(86) Topsøe, H.; Clausen, B. S. Appl. Catal. 1986, 25, 273–293.

(87) Daage, M.; Chianelli, R. R. J. Catal. 1994, 149, 414–427.

(88) Lauritsen, J. V; Nyberg, M.; Nørskov, J. K.; Clausen, B. S.; Topsøe, H.; Laegsgaard, E.; Besenbacher, F. J. Catal. 2004, 224, 94–106.

(89) Lauritsen, J. V.; Helveg, S.; Lægsgaard, E.; Stensgaard, I.; Clausen, B. S.; Topsøe, H.; Besenbacher, F. J. Catal. 2001, 197, 1–5.

(90) Helveg, S.; Lauritsen, J. V; Laegsgaard, E.; Stensgaard, I.; Nørskov, J. K.; Clausen, B. S.; Topsøe, H.; Besenbacher, F. Phys. Rev. Lett. 2000, 84, 951.

(91) Besenbacher, F.; Brorson, M.; Clausen, B. S.; Helveg, S.; Hinnemann, B.; Kibsgaard, J.; Lauritsen, J. V.; Moses, P. G.; Nørskov, J. K.; Topsøe, H. Catal. Today 2008, 130, 86–96.

(92) Kabe, T.; Ishihara, A.; Qian, W.; Godo, M. Catal. Today 1998, 45, 285–291.

(93) Kabe, T.; Qian, W.; Ishihara, A. Catal. Today 39 1997, 39, 3–12.

(94) Qian, W.; Ishihara, A.; Wang, G.; Tsuzuki, T.; Godo, M.; Kabe, T. J. Catal. 1997, 170, 286–294.

(95) Kabe, T.; Qian, W.; Hirai, Y.; Li, L.; Ishihara, A. J. Catal. 2000, 190, 191–198.

(96) Nørskov, J. K.; Clausen, B. S.; Topsøe, H. Catal. Letters 1992, 13, 1–8.

(97) Yoshimura, Y.; Toba, M.; Matsui, T.; Harada, M.; Ichihashi, Y.; Bando, K. K.; Yasuda, H.; Ishihara, H.; Morita, Y.; Kameoka, T. Appl. Catal. A, Gen. 2007, 322, 152–171.

(98) Bej, S. K.; Maity, S. K.; Turaga, U. T. Energy & Fuels 2005, 18, 1227–1237.

(99) Landau, M. V.; Berger, D.; Herskowitz, M. J. Catal. 1996, 159, 236–245.

(100) Qian, E. W.; Otani, K.; Li, L.; Ishihara, A.; Kabe, T. J. Catal. 2004, 221, 294–301.

(101) Niquille-Röthlisberger, A.; Prins, R. J. Catal. 2006, 242, 207–216.

(102) Yu, Y.; Gutiérrez, O. Y.; Haller, G. L.; Colby, R.; Kabius, B.; Rob Van Veen, J. A.; Jentys, A.; Lercher, J. A. J. Catal. 2013, 304, 135–148.

(103) Niquille-Röthlisberger, A.; Prins, R. J. Catal. 2005, 235, 229–240.

(104) Kabe, T.; Qian, W.; Hirai, Y.; Li, L.; Ishihara, A. J. Catal. 2000, 190, 191–198.

(105) Ishihara, A.; Dumeignil, F.; Lee, J.; Mitsuhashi, K.; Qian, E. W.; Kabe, T. Appl. Catal. A, Gen. 2005, 289, 163–173.

(106) Shen, J.; Semagina, N. ChemCatChem 2016, 8, 2565–2571.

(107) Niquille-Röthlisberger, A.; Prins, R. Catal. Today 2007, 123, 198–207.

(108) Girgis, M. J.; Gates, B. C. Ind. Eng. Chem. Res. 1991, 30, 2021–2058.

(109) D.D. Whitehurst, T. Isoda, I. M. Adv. Catal. 1998, 42, 345.

(110) Houalla, M.; Broderick, D. H.; Sapre, A. V.; Nag, N. K.; de Beer, V. H. J.; Gates, B. C.; Kwart, H. J. Catal. 1980, 61, 523–527.

(111) Ishihara, A.; Tajima, H.; Kabe, T. Chem. Lett. 1992, 21, 669–670.

(112) Ma, X.; Sakanishi, K.; Mochida, I. Ind. Eng. Chem. Res. 1996, 2487–2494.

(113) Wang, H.; Iglesia, E. ChemCatChem 2011, 3, 1166–1175.

(114) Zhu, W.; Michalsky, R.; Metin, Ö.; Lv, H.; Guo, S.; Wright, C. J.; Sun, X.; Peterson, A. a; Sun, S. J. Am. Chem. Soc. 2013, 135, 16833–16836.

(115) Wang, H.; Iglesia, E. J. Catal. 2010, 273, 245–256.

(116) Jackson, S. D.; Willis, J.; Mclellan, G. D.; Webb, G.; Keegan, M. B. T.; Moyes, R. B.; Simpson, S.; Wells, P. B.; Whyman, R. J. Catal. 1993, 139, 191–206.

(117) Matsui, T.; Harada, M.; Ichihashi, Y.; Bando, K. K.; Matsubayashi, N.; Toba, M.; Yoshimura, Y. Appl. Catal. A, Gen. 2005, 286, 249–257.

(118) Betta, R. A. D.; Boudart, M.; Gallezot, P.; Weber, R. S. J. Catal. 1981, 69, 514–515.

(119) Figueras, F.; Mencier, B.; De Mourgues, L.; Naccache, C.; Trambouze, Y. J. Catal. 1970, 19, 315–321.

(120) Gallezot, P. Catal. Rev. 1979, 20, 121–154.

(121) Guo, H.; Sun, Y.; Prins, R. Catal. Today 2008, 130, 249–253.

(122) Sachtler, W. M. H.; Stakheev, A. Y. Catal. Today 1992, 12, 283–295.

(123) Sun, Y.; Prins, R. Angew. Chemie - Int. Ed. 2008, 47, 8478–8481.

(124) Cooper, B. H.; Donnis, B. B. L. Appl. Catal. A, Gen. 1996, 137, 203–223.

(125) Qiao, B.; Wang, A.; Yang, X.; Allard, L. F.; Jiang, Z.; Cui, Y.; Liu, J.; Li, J.; Zhang, T. Nat. Chem. 2011, 3, 634–641.

(126) Choi, C. H.; Kim, M.; Kwon, H. C.; Cho, S. J.; Yun, S.; Kim, H.-T.; Mayrhofer, K. J. J.; Kim, H.; Choi, M. Nat. Commun. 2016, 7, 10922–10931.

(127) Hunt, S. T.; Milina, M.; Alba-rubio, A. C.; Hendon, C. H.; Dumesic, J. A.; Román-leshkov, Y. Science 2015, 352, 974–978.

(128) Hu, G.; Nitze, F.; Gracia-Espino, E.; Ma, J.; Barzegar, H. R.; Sharifi, T.; Jia, X.; Shchukarev, A.; Lu, L.; Ma, C.; Yang, G.; Wågberg, T. Nat. Commun. 2014, 5, 1–9.

(129) Eric Marceau, Xavier Carrier, and M. C. Synthesis of solid catalysts; de Jong, K. P., Ed.; Wiley-VCH, 2009.

(130) Coq, B.; Figueras, F. J. Mol. Catal. A Chem. 2001, 173, 117–134.

(131) Ziaei-Azad, H. Bimetallic Ir-based Catalysts for Ring Opening and Hydrodesulfurization Reactions, University of Alberta, Edmonton, Canada, PhD thesis, 2014.

(132) Lei, Y.; Mehmood, F.; Lee, S.; Greeley, J.; Lee, B.; Seifert, S.; Winans, R. E.; Elam, J. W.; Meyer, R. J.; Redfern, P. C.; Teschner, D.; Schloegl, R.; Pellin, M. J.; Curtiss, L. A.; Vajda, S. Science 2010, 328, 224–228.

(133) Herzing, A. a; Kiely, C. J.; Carley, A. F.; Landon, P.; Hutchings, G. J. Science 2008, 321, 1331–1335.

(134) Turner, M.; Golovko, V. B.; Vaughan, O. P. H.; Abdulkin, P.; Berenguer-Murcia, A.; Tikhov, M. S.; Johnson, B. F. G.; Lambert, R. M. Nature 2008, 454, 981–983.

(135) Wei, H.; Liu, X.; Wang, A.; Zhang, L.; Qiao, B.; Yang, X.; Huang, Y.; Miao, S.; Liu, J.; Zhang, T. Nat. Commun. 2014, 5, 5634–5642.

(136) Vilé, G.; Albani, D.; Nachtegaal, M.; Chen, Z.; Dontsova, D.; Antonietti, M.; López, N.; Pérez-Ramírez, J. Angew. Chemie - Int. Ed. 2015, 54, 11265–11269.

(137) Liu, P.; Zhao, Y.; Qin, R.; Mo, S.; Chen, G.; Gu, L.; Chevrier, D. M.; Zhang, P.; Guo, Q.; Zang, D.; Wu, B.; Fu, G.; Zheng, N. Science 2016, 352, 797–801.

(138) Ranocchiari, M.; Lothschutz, C.; Grolimund, D.; van Bokhoven, J. A. Proc. R. Soc. A Math. Phys. Eng. Sci. 2012, 468, 1985–1999.

(139) Duarte, R. B.; Krumeich, F.; Van Bokhoven, J. A. ACS Catal. 2014, 4, 1279–1286.

(140) Fujiwara, K.; Müller, U.; Pratsinis, S. E. ACS Catal. 2016, 6, 1887–1893.

(141) Tian, N.; Zhou, Z.-Y.; Sun, S.-G.; Ding, Y.; Wang, Z. L. Science 2007, 316, 732–735.

(142) Chen, C.; Kang, Y.; Huo, Z.; Zhu, Z.; Huang, W.; Xin, H. L.; Snyder, J. D.; Li, D.; Herron, J. A.; Mavrikakis, M.; Chi, M.; More, K. L.; Li, Y.; Markovic, N. M.; Somorjai, G. A.; Yang, P.; Stamenkovic, V. R. Science 2014, 343, 1339–1343.

(143) Khan, M. U.; Wang, L.; Liu, Z.; Gao, Z.; Wang, S.; Li, H.; Zhang, W.; Wang, M.; Wang, Z.; Ma, C.; Zeng, J. Angew. Chemie - Int. Ed. 2016, 55, 9548 –9552.

(144) An, K.; Alayoglu, S.; Ewers, T.; Somorjai, G. A. J. Colloid Interface Sci. 2012, 373, 1–13.

(145) Wang, C.; Daimon, H.; Sun, S. Nano Lett. 2009, 9, 1493–1496.

(146) Sun, X.; Guo, S.; Liu, Y.; Sun, S. Nano Lett. 2012, 12, 4859–4863.

(147) Wang, D.; Xin, H. L.; Hovden, R.; Wang, H.; Yu, Y.; Muller, D. a.; DiSalvo, F. J.; Abruña, H. D. Nat. Mater. 2012, 12, 81–87.

(148) Zhang, X. B.; Yan, J. M.; Han, S.; Shioyama, H.; Xu, Q. J. Am. Chem. Soc. 2009, 131, 2778–2779.

(149) Alayoglu, S.; Nilekar, A. U.; Mavrikakis, M.; Eichhorn, B. Nat. Mater. 2008, 7, 333–338.

(150) Tao, F.; Grass, M. E.; Zhang, Y.; Butcher, D. R.; Renzas, J. R.; Liu, Z.; Chung, J. Y.; Mun, B. S.; Salmeron, M.; Somorjai, G. A. Science 2008, 322, 932–934.

(151) Joo, S. H.; Park, J. Y.; Tsung, C. K.; Yamada, Y.; Yang, P.; Somorjai, G. A. Nat Mater. 2009, 8, 126–131.

(152) Sasaki, K.; Naohara, H.; Choi, Y.; Cai, Y.; Chen, W.-F.; Liu, P.; Adzic, R. R. Nat. Commun. 2012, 3, 1115–1124.

(153) Liang, W. I.; Zhang, X.; Zan, Y.; Pan, M.; Czarnik, C.; Bustillo, K.; Xu, J.; Chu, Y. H.; Zheng, H. J. Am. Chem. Soc. 2015, 137, 14850–14853.

(154) Gawande, M. B.; Goswami, A.; Asefa, T.; Guo, H.; Biradar, A. V; Peng, D.; Zboril, R.; Varma, R. S. Chem. Soc. Rev. 2015, 44, 7540–7590.

(155) Strasser, P.; Koh, S.; Anniyev, T.; Greeley, J.; More, K.; Yu, C.; Liu, Z.; Kaya, S.; Nordlund, D.; Ogasawara, H.; Toney, M. F.; Nilsson, A. Nat. Chem. 2010, 2, 454–460.

(156) Schlapka, A.; Lischka, M.; Groß, A.; Kasberger, U.; Jakob, P. Phys. Rev. Lett. 2003, 91, 016101/1-016101/4.

(157) Zhang, S.; Zhang, X.; Jiang, G.; Zhu, H.; Guo, S.; Su, D.; Lu, G.; Sun, S. J. Am. Chem. Soc. 2014, 136, 7734–7739.

(158) Kwak, J. H.; Hu, J.; Mei, D.; Yi, C.-W.; Kim, D. H.; Peden, C. H. F.; Allard, L. F.; Szanyi, J. Science 2009, 325, 1670–1673.

(159) Chen, M. S.; Goodman, D. W. Science 2004, 306, 252–255.

(160) Kwon, S. G.; Krylova, G.; Phillips, P. J.; Klie, R. F.; Chattopadhyay, S.; Shibata, T.; Bunel, E. E.; Liu, Y.; Prakapenka, V. B.; Lee, B.; Shevchenko, E. V. Nat. Mater. 2015, 14, 215–223.

(161) Wei, S.; Wang, Q.; Zhu, J.; Sun, L.; Lin, H.; Guo, Z. Nanoscale 2011, 3, 4474.

(162) Tschöpe, A.; Birringer, R. Acta. Metall. Mater. 1993, 41, 2791–2796.

(163) Bryden, K. J.; Ying, J. Y. Acta Mater. 1996, 44, 3847–3854.

(164) Hansen, T. W.; Delariva, A. T.; Challa, S. R.; Datye, A. K. Acc. Chem. Res. 2012, 46, 1720–1730.

(165) Campbell, C. T. Acc. Chem. Res. 2013, 46, 1712–1719.

(166) An, K.; Zhang, Q.; Alayoglu, S.; Musselwhite, N.; Shin, J. Y.; Somorjai, G. A. Nano Lett. 2014, 14, 4907–4912.

(167) Weissmiiller, J.; Loffler, J.; Martin, K. NanoStructured Mater. 1995, 6, 105–114.

(168) Hansen, T. W.; Delariva, A. T.; Challa, S. R.; Datye, A. K. Acc. Chem. Res. 2013, 46, 1720–1730.

(169) Ge, J.; Zhang, Q.; Zhang, T.; Yin, Y. Angew. Chemie - Int. Ed. 2008, 47, 8924–8928.

(170) Wang, Y.; Biradar, A. V.; Duncan, C. T.; Asefa, T. J. Mater. Chem. 2010, 20, 7834.

(171) Zhang, W.; Chi, Z. X.; Mao, W. X.; Lv, R. W.; Cao, A. M.; Wan, L. J. Angew. Chemie - Int. Ed. 2014, 53, 12776–12780.

(172) Wang, Y.; Tseng, W. J. J. Am. Ceram. Soc. 2009, 92, 32–37.

(173) Fodor, D.; Ishikawa, T.; Krumeich, F.; van Bokhoven, J. A. Adv. Mater. 2015, 27, 1919–1923.

(174) Cao, A.; Veser, G. Nat. Matter. 2010, 9, 75-81

(175) Courtin, E.; Boy, P.; Rouhet, C.; Bianchi, L.; Bruneton, E.; Poirot, N.; Laberty-Robert, C.; Sanchez, C. Chem. Mater. 2012, 24, 4540–4548.

(176) Fort, D.; Farr, J. P. G.; Harris, I. R. J. Less-Common Met. 1975, 39, 293–308.

(177) Semagina, N.; Kiwi-Minsker, L. Catal. Review 2009, 51, 147-217.

(178) H. Bonnemann, K. S. Nagabhushana, in: G. Schmid, N. Toshima, B. Corain (Eds.). Metal Nanoclusters in Catalysis and Material Science: The Issue of Size Control, Elsevier Science, Amesterdam, 2008, 21–48.

(179) Shi, G.; Franzke, T.; Sánchez, M. D.; Xia, W.; Weis, F.; Seipenbusch, M.; Kasper, G.; Muhler, M. ChemCatChem 2012, 4, 760–765.

(180) LaMer, V.; Dinegar, R. J. Am. Chem. Soc. 1950, 72, 4847–4854.

(181) Teranishi, T.; Kurita, R.; Miyake, M. J. Inorg. Organomet. Polym. 2000, 10, 145–156.

(182) Mpourmpakis, G.; Caratzoulas, S.; Vlachos, D. G. Nano Lett. 2010, 10, 3408–3413.

(183) Jana, N. R.; Chen, Y.; Peng, X. Chem. Mater. 2004, 16, 3931–3935.

(184) Banholzer, W. F.; R.I. Masel. J. Catal. 1984, 85, 127–134.

(185) Somorjai, G. a.; Blakely, D. W. Nature 1975, 258, 580–583.

(186) Sun, S. G.; Chen, A. C.; Huang, T. S.; Li, J. B.; Tian, Z. W. J. Electroanal. Chem. 1992, 340, 213–226.

(187) Wang, Y.; Toshima, N. J. Phys. Chem. B 1997, 101, 5301–5306.

(188) Kleperis, J.; Wójcik, G.; Czerwinski, A.; Skowronski, J.; Kopczyk, M.; Beltowska-Brzezinska, M. J. Solid State Electrochem. 2001, 5, 229–249.

(189) Xia, X.; Wang, Y.; Ruditskiy, A.; Xia, Y. Adv. Mater. 2013, 25, 6313–6332.

(190) Park, T.H.; Lee, H.; Lee, J.; Jang, D.J. RSC Adv. 2017, 7, 7718–7724

(191) Alia, S. M.; Yan, Y.; Pivovar, B. Catal. Sci. Technol. 2014, 4, 3589–3600.

(192) Tracy, B. D. A. J. B. Nanoscale 2014, 6, 12195–12216.

(193) Gross, E.; Liu, J. H.-C.; Toste, F. D.; Somorjai, G. a. Nat. Chem. 2012, 4, 947–952.

(194) Lee, I.; Delbecq, F.; Morales, R.; Albiter, M. a; Zaera, F. Nat. Mater. 2009, 8, 132–138.

(195) Chen, G.; Xu, C.; Huang, X.; Ye, J.; Gu, L.; Li, G.; Tang, Z.; Wu, B.; Yang, H.; Zhao, Z.; Zhou, Z.; Fu, G.; Zheng, N. Nat. Mater. 2016, 15, 564–569.

(196) Wu, J.; Li, P.; Pan, Y.-T. F.; Warren, S.; Yin, X.; Yang, H. Chem. Soc. Rev. 2012, 41, 8066–8074.

(197) Yang, R. T.; Hernández-Maldonado, A. J.; Yang, F. H. Science 2003, 301, 79–81.

(198) Prins, R.; Egorova, M.; Niquille-Röthlisberger, A.; Zhao, Y.; Sivasankar, N.; Kukula, P. Catal. Today 2006, 111, 84–93.

(199) Ma, X.; Sakanishi, K.; Mochida, I. Ind. Eng. Chem. Res. 1996, 2487–2494.

(200) Alsolami, B.; Carneiro, J. T.; Moulijn, J. A.; Makkee, M. Fuel 2011, 90, 3021–3027.

(201) Navarro, R.; Pawelec, B.; Fierro, J. L. G.; Vasudevan, P. T.; Cambra, J. F.; Arias, P. L. Appl. Catal. A Gen. 1996, 137, 269–286.

(202) Ziaei-Azad, H.; Yin, C. X.; Shen, J.; Hu, Y.; Karpuzov, D.; Semagina, N. J. Catal. 2013, 300, 113–124.

(203) Reinhoudt, H. R.; Troost, R.; Van Schalkwijk, S.; Van Langeveld, A. D.; Sie, S. T.; Van Veen, J. A. R.; Moulijn, J. A. Fuel Process. Technol. 1999, 61, 117–131.

(204) Vít, Z.; Gulková, D.; Kaluža, L.; Kupčík, J. Appl. Catal. B, Environ. 2015, 179, 44–53.

(205) ASM Handbook, Volume 3: Alloy Phase Diagrams; 2004.

(206) Doyle, B. M. L.; Harris, I. R. Platin. Met. Rev., 1988, 32, 130–140.

(207) Seo, M. H.; Choi, S. M.; Seo, J. K.; Noh, S. H.; Kim, W. B.; Han, B. Appl. Catal. B, Environ. 2013, 129, 163–171.

(208) Harris, I. R.; M. Norman. J. Less-Common Met. 1970, 22, 127–130.

(209) Vitos, L.; Ruban, A. V.; Skriver, H. L.; Kollár, J. Surf. Sci. 1998, 411, 186–202.

(210) Passos, F. B.; Oliveira, E. R.; Mattos, L. V.; Noronhe, F. B. Catal. Letters 2006, 110, 261–267.

(211) Shi, C.; Zhang, P. Appl. Catal. B Environ. 2012, 115–116, 190–200.

(212) Santos, D. C. R. M.; Madeira, L.; Passos, F. B. Catal. Today 2010, 149, 401–406.

(213) Jeon, M. K.; McGinn, P. J. J. Power Sources 2011, 196, 1127–1131.

(214) Liu, X.; Yu, E. H.; Scott, K. Appl. Catal. B, Environ. 2015, 162, 593–601.

(215) Greeley, J.; Stephens, I. E. L.; Bondarenko, a S.; Johansson, T. P.; Hansen, H. a; Jaramillo, T. F.; Rossmeisl, J.; Chorkendorff, I.; Nørskov, J. K. Nat. Chem. 2009, 1, 552–556.

(216) Song, H.; Xu, X. W.; Song, H. L.; Jiang, N.; Zhang, F. Y. Catal. Commun. 2015, 63, 52–55.

(217) Teranishi, T.; Miyake, M. Chem. Mater. 1998, 10, 594–600.

(218) Pérez-Ramírez, J.; Berger, R. J.; Mul, G.; Kapteijn, F.; Moulijn, J. A. Catal. Today 2000, 60, 93–109.

(219) Guo, X.; Brault, P.; Zhi, G.; Caillard, A.; Jin, G.; Guo, X. J. Phys. Chem. C 2011, 115, 24164–24171.

(220) Niemantsverdriet, J. W.; van Kaam, J. A. C.; Flipse, C. F. J.; van der Kraan, A. M. J. Catal. 1985, 96, 58–71.

(221) Pillo, T.; Zimmermann, R.; Steiner, P.; Hüfner, S. J. Phys. Condens. Matter 1999, 9, 3987–3999.

(222) Otto, K.; Haack, L. P.; deVries, J. E. Appl. Catal. B, Environ. 1992, 1, 1–12.

(223) Oemar, U.; Hidajat, K.; Kawi, S. Int. J. Hydrogen Energy 2015, 40, 12227–12238.

(224) Köck, E.-M.; Kogler, M.; Bielz, T.; Klötzer, B.; Penner, S. J. Phys. Chem. C 2013, 117, 17666–17673.

(225) Zhao, W.; Li, X.; Shao, X.; Xu, B.; Yao, J. Eur. Phys. J. D 2013, 67, 1–8.

(226) Scheffler, M. Surf. Sci. 1979, 81, 562–570.

(227) Shen, J.; Semagina, N. ACS Catal. 2014, 4, 268–279.

(228) Zeinalipour-Yazdi, C. D.; Willock, D. J.; Thomas, L.; Wilson, K.; Lee, A. F. Surf. Sci. 2016, 646, 210–220.

(229) George, C.; Genovese, A.; Casu, A.; Prato, M.; Povia, M.; Manna, L.; Montanari, T. Nano Lett. 2013, 13, 752–757.

(230) Lear, T.; Marshall, R.; Lopez-Sanchez, J. A.; Jackson, S. D.; Klapötke, T. M.; Bäumer, M.; Rupprechter, G.; Freund, H. J.; Lennon, D. J. Chem. Phys. 2006, 124.

(231) Wagman, D. D.; Evans, W. H.; Parker, V. B.; Schumm, R. H.; Halow, I.; Bailey, S. M.; Churney, K. L.; Nuttall, R. L. Journal of Physical and Chemical Reference Data. 1982, 1–407.

(232) Richard, F.; Boita, T.; Pérot, G. Appl. Catal. A, Gen. 2007, 320, 69–79.

(233) Prabhudev, S.; Bugnet, M.; Bock, C.; Botton, G. A. ACS Nano 2013, 7, 6103–6110.

(234) Jang, J.-H.; Lee, E.; Park, J.; Kim, G.; Hong, S.; Kwon, Y.-U. Sci. Rep. 2013, 3, 2872–2880.

(235) Jagadeesh, R. V.; Surkus, A.-E.; Junge, H.; Pohl, M.-M.; Radnik, J.; Rabeah, J.; Huan, H.; Schunemann, V.; Bruckner, A.; Beller, M. Science 2013, 342, 1073–1076.

(236) Easterday, R.; Leonard, C.; Sanchez-Felix, O.; Losovyj, Y.; Pink, M.; Stein, B. D.; Morgan, D. G.; Lyubimova, N. A.; Nikoshvili, L. Z.; Sulman, E. M.; Mahmoud, W. E.; Al-Ghamdi, A. A.; Bronstein, L. M. ACS Appl. Mater. Interfaces 2014, 6, 21652–21660.

(237) Stamenkovic, V. R.; Mun, B. S.; Mayrhofer, K. J. J.; Ross, P. N.; Markovic, N. M. J. Am. Chem. Soc. 2006, 128, 8813–8819.

(238) Wang, Y.; He, Q.; Guo, J.; Wang, J.; Luo, Z.; Shen, T. D.; Ding, K.; Khasanov, A.; Wei, S.; Guo, Z. ACS Appl. Mater. Interfaces 2015, 7, 23920–23931.

(239) Jiang, G.; Zhu, H.; Zhang, X.; Shen, B.; Wu, L.; Zhang, S.; Lu, G.; Wu, Z.; Sun, S. ACS Nano 2015, 9, 11014–11022.

(240) Guo, S.; Zhang, S.; Sun, X.; Sun, S. J. Am. Chem. Soc. 2011, 133, 15354–15357.

(241) Shao, M. H.; Sasaki, K.; Adzic, R. R. J. Am. Chem. Soc. 2006, 128, 3526–3527.

(242) Liu, L.; Zhou, F.; Wang, L.; Qi, X.; Shi, F.; Deng, Y. J. Catal. 2010, 274, 1–10.

(243) Golubina, E. V.; Lokteva, E. S.; Lunin, V. V.; Telegina, N. S.; Stakheev, A. Y.; Tundo, P. Appl. Catal. A, Gen. 2006, 302, 32–41.

(244) Wu, C.-T.; Yu, K. M. K.; Liao, F.; Young, N.; Nellist, P.; Dent, A.; Kroner, A.; Tsang, S. C. E. Nat. Commun. 2012, 3, 1050–1058.

(245) Kast, P.; Friedrich, M.; Teschner, D.; Girgsdies, F.; Lunkenbein, T.; D'Alnoncourt, R. N.; Behrens, M.; Schlögl, R. Appl. Catal. A, Gen. 2015, 502, 8–17.

(246) Yu, Y.; Sun, K.; Tian, Y.; Li, X. Z.; Kramer, M. J.; Sellmyer, D. J.; Shield, J. E.; Sun, S. Nano Lett. 2013, 13, 4975–4979.

(247) Easterday, R.; Sanchez-Felix, O.; Stein, B. D.; Morgan, D. G.; Pink, M.; Losovyj, Y.; Bronstein, L. M. J. Phys. Chem. C 2014, 118, 24769–24775.

(248) Sun, S.; Murray, C. B.; Weller, D.; Folks, L.; Moser, A. Science 2000, 287, 1989–1992.

(249) Ung, D.; Tung, L. D.; Caruntu, G.; Delaportas, D.; Alexandrou, I.; Prior, I. a.; Thanh, N. T. K. CrystEngComm 2009, 11, 1309–1316.

(250) Yao, Y.; Patzig, C.; Hu, Y.; Scott, R. W. J. J. Phys. Chem. C 2015, 119, 21209–21218.

(251) Zhou, S.; Johnson, M.; Veinot, J. G. C. Chem. Commun. 2010, 46, 2411–2413.

(252) Li, X.; Wang, A.; Egorova, M.; Prins, R. J. Catal. 2007, 250, 283–293.

(253) Jayne, D.; Zhang, Y.; Haji, S.; Erkey, C. Int. J. Hydrogen Energy 2005, 30, 1287–1293.

(254) Hernández, S.; Solarino, L.; Orsello, G.; Russo, N.; Fino, D.; Saracco, G.; Specchia, V. Int. J. Hydrogen Energy 2008, 33, 3209–3214.

(255) Ma, X.; Sun, L.; Song, C. Catal. Today 2002, 77, 107–116.

(256) Zdražil, M. Catal. Today 1988, 3, 269–365.

(257) Ahn, T.; Kim, J. H.; Yang, H. M.; Lee, J. W.; Kim, J. D. J. Phys. Chem. C 2012, 116, 6069–6076.

(258) McIntyre, N. S.; Zetaruk, D. G. Anal. Chem. 1977, 49, 1521–1529.

(259) Grosvenor, A. P.; Kobe, B. A.; Biesinger, M. C.; McIntyre, N. S. Surf. Interface Anal. 2004, 36, 1564–1574.

(260) Farag, H.; Whitehurst, D. .; Sakanishi, K.; Mochida, I. Catal. Today 1999, 50, 9–17.

(261) Chhowalla, M.; Shin, H. S.; Eda, G.; Li, L.-J.; Loh, K. P.; Zhang, H. Nat. Chem. 2013, 5, 263–275.

(262) Chianelli, R. R. Oil & Gas Sci. Technol. - Rev. IFP 2006, 61, 503–513.

(263) Jehng, J. M.; Wachs, I. E. Catal. Today 1990, 8, 37–55.

(264) Allali, N.; Leblanc, A.; Danot, M.; Geantet, C.; Vrinat, M.; Breysse, M. Catal. Today 1996, 27, 137–144.

(265) Wachs, I. E.; Jehng, J. M.; Deo, G.; Hu, H.; Arora, H. Catal. Today 1996, 28, 199–205.

(266) Jongen, N.; Bowen, P.; Lemaître, J.; Valmalette, J.-C.; Hofmann, H. J. Colloid Interface Sci. 2000, 226, 189–198.

(267) Kuhn, M.; Rodriguez, J. A. Catal. Letters 1995, 32, 345–355.

(268) Craig, J. R.; Barton, P. B. Econ. Geol. 1973, 68, 493–506.

(269) Mansouri, A.; Khodadadi, A. A.; Mortazavi, Y. J. Hazard. Mater. 2014, 271, 120–130.

(270) Chakrabarti, D. J.; Laughlin, D. E. Bull. Alloy Phase Diagrams 1982, 2, 455–460.

(271) Xiang, Y.; Barbosa, R.; Li, X.; Kruse, N. ACS Catal. 2015, 5, 2929−2934

(272) Braga, V. S.; Dias, J. a; Dias, S. C. L.; De Macedo, J. L. Chem. Mater. 2005, 17, 690–695.

(273) Teixeira da Silva, V. L. S.; Schmal, M.; Oyama, S. T. J. Solid State Chem. 1996, 123, 168–182.

(274) Izawa, K.; Ida, S.; Unal, U.; Yamaguchi, T.; Kang, J. H.; Choy, J. H.; Matsumoto, Y. J. Solid State Chem. 2008, 181, 319–324.

(275) Wu, X.; Tao, Y.; Ke, X.; Zhu, J.; Hong, J. Mater. Res. Bull. 2004, 39, 901–908.

(276) Badrinarayanan S.; Sinha, S. Appl. Phys. 1991, 69, 1141.

(277) Paulis, M.; Martín, M.; Soria, D. .; Díaz, A.; Odriozola, J. .; Montes, M. Appl. Catal. A, Gen. 1999, 180, 411–420.

(278) Harris, S.; Chianelli, R. R. J. Catal. 1984, 86, 400–412.

(279) Seh, Z. W.; Yu, J. H.; Li, W.; Hsu, P.-C.; Wang, H.; Sun, Y.; Yao, H.; Zhang, Q.; Cui, Y. Nat. Commun. 2014, 5, 5017.

(280) Chhowalla, M.; Shin, H. S.; Eda, G.; Li, L.-J.; Loh, K. P.; Zhang, H. Nat. Chem. 2013, 5, 263–275.

(281) Wang, H.; Male, J.; Wang, Y. ACS Catal. 2013, 3, 1047–1070.

(282) Wachs, I.E.; Chen, Y.; Jehng, J.M.; Briand, L. E.; Tanaka T. Catal. Today 2003, 78, 13–24.

(283) Jehng, J.-M.; Wachs, I. E. J. Mol. Catal. A, Chem. 1991, 67, 369–387.

(284) Tanaka, T.; Yoshida, T.; Yoshida, H.; Aritani, H.; Funabiki, T.; Yoshida, S.; Jehng, J.-M.; Wachs, I. E. Catal. Today 1996, 28, 71–78.

(285) Yoshida, S.; Tanaka, T.; Hanada, T.; Hiraiwa, T.; Kanai, H.; Funabiki, T. Catal. Letters 1992, 12, 277–285.

(286) Xingtao Gao, Israel E. Wachs, Michael S. Wong, and J. Y. Y. J. Catal. 2001, 203, 18–24.

(287) Datka, J.; Turek, A. M.; Jehng, J. M.; Wachs, I. E. J. Catal. 1992, 135, 186–199.

(288) Turek, A. M.; Wachs, I. E.; DeCanio, E. J. Phys. Chem. 1992, 96, 5000–5007.

(289) Cui, G.; Wang, J.; Fan, H.; Sun, X.; Jiang, Y.; Wang, S.; Liu, D.; Gui, J. Fuel Process. Technol. 2011, 92, 2320–2327.

(290) Papulovskiy, E.; Khabibulin, D. F.; Terskikh, V. V.; Paukshtis, E. A.; Bondareva, V. M.; Shubin, A. A.; Andreev, A. S.; Lapina, O. J. Phys. Chem. C 2015, 119, 10400–10411.

(291) Sarma, D. D.; Rao, C. N. R. J. Electron Spectros. Relat. Phenomena 1980, 20, 25–45.

(292) Pittman, R. M.; Bell, A. T. J. Phys. Chem. 1993, 97, 12178–12185.

(293) Jehng, J.-M.; Wacbs, I. E. J. Phys. Chem. 1991, 95, 7373–7379.

(294) Gao, X.; Wachs, I. E.; Wong, M. S.; Ying, J. Y. J. Catal. 2001, 203, 18–24.

(295) Jehng, J.-M.; Wachs, I. E. Chem. Mater. 1991, 3, 100–107.

(296) Burcham, L. J.; Datka, J.; Wachs, I. E. J. Phys. Chem. B 1999, 103, 6015–6024.

(297) Jehng, J.-M.; Turek, A. M.; Wachs, I. E. Appl. Catal. A, Gen. 1992, 83, 179–200.

(298) Jehng, J.-M.; Wachs, I. E. Catal. Today 1993, 16, 417–426.

(299) Deng, Y.; Handoko, A. D.; Du, Y.; Xi, S.; Yeo, B. S. ACS Catal. 2016, 6, 2473–2481.

(300) Zhang, Z.; Zhou, Y.; Zhang, S.; Xu, C. Energy and Fuels 2006, 20, 2293–2298.

(301) Huo, Q.; Dou, T.; Zhao, Z.; Pan, H. Appl. Catal. A, Gen. 2010, 381, 101–108.

(302) Mansouri, A.; Semagina, N. Appl. Catal. A, Gen. 2017, 543, 43–50.

(303) Jeong, S.; Yoo, D.; Jang, J.; Kim, M.; Cheon, J. J. Am. Chem. Soc. 2012, 134, 18233–18236.

(304) Mahler, B.; Hoepfner, V.; Liao, K.; Ozin, G. A. J. Am. Chem. Soc. 2014, 136, 14121–14127.

(305) Seo, J. W.; Jun, Y. W.; Park, S. W.; Nah, H.; Moon, T.; Park, B.; Kim, J. G.; Kim, Y. J.; Cheon, J. Angew. Chemie - Int. Ed. 2007, 46, 8828–8831.

(306) Jang, J. T.; Jeong, S.; Seo, J. W.; Kim, M. C.; Sim, E.; Oh, Y.; Nam, S.; Park, B.; Cheon, J. J. Am. Chem. Soc. 2011, 133, 7636–7639.

(307) Jeong, S.; Han, J. H.; Jang, J. T.; Seo, J. W.; Kim, J. G.; Cheon, J. J. Am. Chem. Soc. 2011, 133, 14500–14503.

(308) Yoo, D.; Kim, M.; Jeong, S.; Han, J.; Cheon, J. J. Am. Chem. Soc. 2014, 136, 14670–14673.

(309) Zak, A.; Feldman, Y.; Alperovich, V.; Rosentsveig, R.; Tenne, R. J. Am. Chem. Soc. 2000, 122, 11108-11116.

(310) Han, J. H.; Lee, S.; Cheon, J. Chem Soc Rev 2013, 42, 2581–2591.

(311) Kort, K. R.; Banerjee, S. Small 2015, 11, 329–334.

(312) Zhang, Z.; Tang, Z.; Kotov, N. A.; Glotzer, S. C. Nano Lett. 2007, 7, 1670–1675.

(313) Pradhan, N.; Xu, H.; Peng, X. Nano Lett. 2006, 6, 720–724.

(314) Polleux, J.; Pinna, N.; Antonietti, M.; Niederberger, M. Adv. Mater. 2004, 16, 436-439.

(315) Jung, W.; Lee, S.; Yoo, D.; Jeong, S.; Miro, P.; Kuc, A.; Heine, T.; Cheon, J. J. Am. Chem. Soc. 2015, 137, 7266–7269.

(316) Pradhan, N.; Reifsnyder, D.; Xie, R.; Aldana, J.; Peng, X. J. Am. Chem. Soc. 2007, 129, 9500–9509.

(317) Meng, F.; Morin, S. A.; Jin, S. Acc. Chem. Res. 2013, 46, 1616–1626.

(318) Peng, X.; Thessing, J. Struc Bond 2005, 118, 79–119.

(319) Yu, W. W.; Peng, X. Angew. Chemie - Int. Ed. 2002, 41, 2368–2371.

(320) Hayashi, T.; Keiji Ueno; Saiki, K.; Koma, A. J. Cryst. Growth 2000, 219, 115–122.

(321) Hyun Park, K.; Jang, K.; Kim, S.; Jin Kim, H.; Uk Son, S. J. Am. Chem. Soc. 2006, 128, 14780–14781.

(322) Yang, D.; Jimenez Sandoval, S.; Divigalpitiya, W. M. R.; Irwin, J. C.; Frindt, R. F. Phys. Rev. B 1991, 43.

(323) Onari, S.; Arai, T.; Aoki, R.; Nakamura, S. Solid State Commun. 1979, 31, 577–579.

(324) McMullan, W. G.; Irwin, J. C. Solid State Commun. 1983, 45, 557–560.

(325) Lee, C.; Yan, H.; Brus, L. E.; Heinz, T. F.; Hone, J.; Ryu, S. ACS Nano 2010, 4, 2695–2700.

(326) Zhao, S. H.; Hotta, T.; Koretsune, T.; Watanabe, K.; Taniguchi, T.; Sugawara, K.; Takahashi, T.; Shinohara, H.; Kitaura, R. 2D Mater. 2016, 3, 025027.

(327) Fogler, H.S. Elements of chemical reaction engineering, 4th Ed., Prentice Hall, 2005.R.E.

(328) Le Page, J.F. Applied heterogeneous catalysis, TechniP, 1987.

(329) Yu, Q.; Zhang, L.; Guo, R.; Sun, J.; Fu, W.; Tang, T.; Tang, T. Fuel Process. Technol. 2017, 159, 76-87.